



**HAL**  
open science

# Direct writing of micro and nanostructures via two-photon stereolithography for the design of molecularly imprinted polymer-based sensing elements

Ernesto Iii Paruli

► **To cite this version:**

Ernesto Iii Paruli. Direct writing of micro and nanostructures via two-photon stereolithography for the design of molecularly imprinted polymer-based sensing elements. *Polymers*. Université de Technologie de Compiègne, 2021. English. NNT : 2021COMP2629 . tel-03963936

**HAL Id: tel-03963936**

**<https://theses.hal.science/tel-03963936v1>**

Submitted on 30 Jan 2023

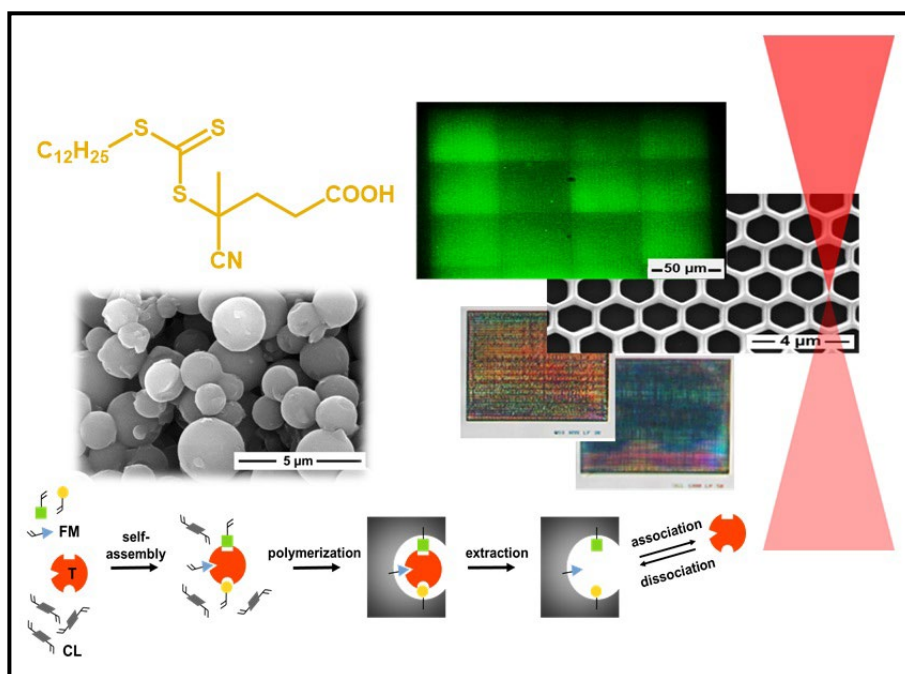
**HAL** is a multi-disciplinary open access archive for the deposit and dissemination of scientific research documents, whether they are published or not. The documents may come from teaching and research institutions in France or abroad, or from public or private research centers.

L'archive ouverte pluridisciplinaire **HAL**, est destinée au dépôt et à la diffusion de documents scientifiques de niveau recherche, publiés ou non, émanant des établissements d'enseignement et de recherche français ou étrangers, des laboratoires publics ou privés.

Par Ernesto III PARULI

*Direct writing of micro and nanostructures via two-photon stereolithography for the design of molecularly imprinted polymer-based sensing elements*

Thèse présentée  
pour l'obtention du grade  
de Docteur de l'UTC



Soutenue le 24 septembre 2021  
**Spécialité :** Biotechnologie, Ingénierie Moléculaire et Interactions : Unité de recherche en Génie Enzymatique et Cellulaire - GEC (UMR-7025)  
 D2629



Le projet POLYSENSE est cofinancé dans le cadre du Fonds Européen de Développement Economique et Régional (FEDER) 2014/2020.



philfrance  
scholarships

SCHOLARSHIP PROGRAM OF THE EMBASSY OF FRANCE TO THE PHILIPPINES

## DOCTORAL THESIS

submitted for graduation as

**DOCTEUR de l'Université de Technologie de Compiègne**

Spécialité : Biotechnologie, Ingénierie Moléculaire et Interactions

Field: Biotechnology, Molecular Engineering and Interactions

by

**Ernesto III PARULI**

## **Direct writing of micro and nanostructures via two-photon stereolithography for the design of molecularly imprinted polymer-based sensing elements**

Thesis supervised by Prof. Karsten HAUPT and Dr. Carlo GONZATO

Disputation on the 24<sup>th</sup> of September 2021, in front of the jury composed of:

- |   |                                |   |            |
|---|--------------------------------|---|------------|
| ▪ | María Cruz MORENO-BONDI, Prof. | Universidad Complutense de Madrid, <i>Spain</i>       | Reviewer   |
| ▪ | Sandra SCHLÖGL, Dr.            | Polymer Competence Center, <i>Austria</i>             | Reviewer   |
| ▪ | Cédric AYELA, Dr.              | IMS, Bordeaux, <i>France</i>                          | Examiner   |
| ▪ | Fortunato III SEVILLA, Prof.   | University of Santo Tomas, <i>Philippines</i>         | Examiner   |
| ▪ | Bérangère AVALLE-BIHAN, Prof.  | Université de Technologie de Compiègne, <i>France</i> | President  |
| ▪ | Karsten HAUPT, Prof.           | Université de Technologie de Compiègne, <i>France</i> | Supervisor |
| ▪ | Carlo GONZATO, Dr.             | Université de Technologie de Compiègne, <i>France</i> | Supervisor |



« Ton cœur est là où se trouve ton trésor.  
Et ton trésor doit être trouvé  
pour que tout ce que tu as découvert en chemin  
puisse avoir un sens. »

*L'Alchimiste (Paulo Coelho)*

## *Acknowledgments*

---

First of all, let me take this opportunity to acknowledge the jury members: Prof. Bérangère Avelle-Bihan (president), Prof. María Cruz Moreno-Bondi (reviewer), Dr. Sandra Schlögl (reviewer), Dr. Cédric Ayela (examiner) and Prof. Fortunato Sevilla III (examiner) for taking the time to read, review and examine my thesis manuscript.

Secondly, I count this thesis as an important milestone in my pursuit of truth and of science. It has been a journey full of exciting discoveries and lifelong learnings. A journey, indeed, that I would have not made without the following beautiful souls:

My dear and respected thesis supervisors, Prof. Karsten Haupt and Dr. Carlo Gonzato. I thank you both for graciously welcoming me as your PhD student. Prof. Karsten, thank you for accepting me into the reputable MIP group of the GEC laboratory, for helping me when I needed it for my thesis or my PhD in general, for your valuable insights, for the opportunity to attend various conferences, and for your warm company outside the laboratory. Dr. Carlo, thank you for your guidance since day one, for your kind mentorship, for your patience, for showing me first the ways of molecular imprinting and imparting to me your knowledge on MIPs and on polymerization, your precious insights and your admirable examples.

My dear previous thesis supervisor, Prof. Fortunato Sevilla III. I thank you for encouraging me to apply for the CHED-PhilFrance scholarship and to pursue my PhD studies in Prof. Haupt's team.

The Commission on Higher Education (CHED) of the Republic of the Philippines and the Embassy of France to the Philippines. I thank you for your joint scholarship program, the CHED-PhilFrance scholarship, by which I have been granted this precious opportunity to pursue a PhD, deepen my knowledge and learn new things in a competent laboratory, as well as the chance to experience the language, culture and people in France. In the same way, I thank the University of Santo Tomas, Manila for being my sending higher education institute (SHEI) as a vital part of my scholarship.

The Génie Enzymatique et Cellulaire (GEC) team. I thank you for having the opportunity to work with you. In particular, I thank Dr. Bernadette Tse Sum Bui for the helpful articles that you shared with us, for your useful input and for your warm hospitality when we were in your place. I also thank Dr. Franck Merlier for the chromatographic analyses of my samples and Elise Prost for helping me with NMR spectroscopy and the Raman microscope. I also thank a previous GEC post-doctoral researcher, Dr. Mariano Garcia-Soto, for helping me understand my early experiments on photopolymerization.

Still in GEC, I send my gratitude to my fellow PhD students (past and present) for their friendship, their readiness to help and for their support, especially to Alejandra, Paulina, Nadja, Raquel (post-doc), Nesrine, Valentina (post-doc), Melissa, Salim, Ye and Dr. Adrián (enseignant-chercheur). I also thank the friends outside GEC who I met during my stay in Europe for their enjoyable company and support, particularly, Ding Dong, Sergio, Guoqiang, Álvaro and Yonatan.

I also thank Frédéric Nadaud of the Service Analyses Physico-chimiques (SAPC) for all the SEM images of my samples.

My dear and beloved family. I thank my mother, Amalia; my brother, Paolo; my father, Ernesto; my aunts Olivia and Grace; and my relatives, who have always been there cheering for me, supporting me, understanding me and praying for me with all their love. I also thank my long-time friends Dennis, Kimberly, JP and Mariden for their support, meaningful exchange and for the little glimpses of how we used to be.

Above all, I lift up my sincerest and greatest gratitude to God Who is Truth and the Author of All for granting me this opportunity to go out of my comfort zone and for standing by me always until the end.

MARAMING SALAMAT!

MERCI BEAUCOUP !

# Contents

---

Acknowledgments.....	2
List of Figures.....	8
List of Tables.....	15
List of Abbreviations.....	16
Abstract: Direct writing of micro and nanostructures via two-photon stereolithography for the design of molecularly imprinted polymer-based sensing elements.....	19
Résumé : Écriture directe de micro et nanostructures via stéréolithographie à deux photons pour la conception d'éléments de detection à base de polymères à empreinte moléculaire.....	21
GENERAL INTRODUCTION.....	23
Chapter 1: PHOTOPOLYMERIZATION AND PHOTOSTRUCTURING OF MOLECULARLY IMPRINTED POLYMERS.....	25
1. Molecular recognition.....	26
2. Molecularly imprinted polymers.....	27
2.1. Introduction.....	27
2.2. Early history.....	27
2.3. Principles of molecular recognition in MIPs.....	29
2.4. Components and their influence for the synthesis of MIPs.....	31
2.5. Conventional methods for preparing MIPs.....	35
2.6. Approaches for triggering the polymerization of MIPs.....	37
3. Photopolymerization of MIPs.....	39
3.1. Introduction to photopolymerization.....	39
3.2. UV mediated photopolymerization of MIPs.....	46
3.3. Visible and NIR light mediated photopolymerization.....	48
3.4. Limitations of photopolymerization of MIPs.....	52
4. Photostructuring MIPs.....	53
4.1. Introduction to photolithography.....	54
4.2. Mask lithography of MIPs.....	58
a. Contact and proximity photolithography.....	58
b. Projection photolithography.....	61
4.3. Photon-based, maskless lithography.....	62



a. Interference lithography.....	62
b. One-photon stereolithography.....	63
c. Multiphoton stereolithography.....	64
d. Near-field assisted optical lithography.....	65
5. Conclusions.....	66
6. References.....	68
Chapter 2: THIOL-YNE CHEMISTRY FOR MOLECULAR IMPRINTING.....	91
1. Introduction.....	92
2. Experimental.....	96
2.1. Chemicals.....	96
2.2. Synthesis of thiol-yne polymers.....	96
2.3. Synthesis of reference (meth)acrylic scaffolds.....	96
2.4. Characterization of the thiol-yne MIPs.....	97
2.5. Equilibrium binding assays.....	98
2.6. Hydrolytic degradation of the thiol-yne MIPs.....	98
3. Results and discussion.....	98
3.1. Affinity and selectivity of thiol-yne MIPs.....	102
3.2. Hydrolytic degradation of ester-based, thiol-yne MIPs.....	103
4. Conclusions.....	107
5. References.....	108
Chapter 3: TWO-PHOTON STEREOGRAPHY AND PHOTOSTRUCTURATION FOR MOLECULAR RECOGNITION.....	111
1. Introduction.....	112
1.1 Rapid Prototyping.....	112
1.2 Stereolithography.....	114
1.3 Two-photon stereolithography.....	116
1.4 Photonic crystals.....	118
1.5 Photonic crystals based on molecularly imprinted polymers.....	121
2. Experimental.....	124
2.1 Materials.....	124
2.2 Equipment and software.....	125

2.3 Methods.....	125
2.3.1. TPS for the fabrication of opal photonic crystals.....	125
2.3.2. Woodpiles based on functionalized IP-Dip.....	127
2.3.3. Woodpiles based on thiol-containing formulations.....	128
3. Results and Discussion.....	129
3.1. TPS for the fabrication of opal photonic crystals.....	129
3.1.1. Fabrication of opal crystals via TPS.....	130
3.2. TPS for the fabrication of woodpile photonic crystals.....	133
3.2.1. Fabrication of woodpiles via TPS.....	134
3.2.1.1. Woodpiles based on commercial formulation.....	135
3.2.1.2. Woodpiles based on thiol-containing formulation.....	149
4. Conclusions.....	154
5. References.....	156
Chapter 4: TPS OF MICROSTRUCTURES AND THEIR FUNCTIONALIZATION WITH MIP.....	166
1. Introduction.....	167
2. Experimental.....	169
2.1. Materials.....	169
2.2. Equipment and software.....	169
2.3. Determination of the smallest lateral and axial printable feature.....	170
2.4. Writing of 2.5D honeycomb microstructures via TPS.....	171
2.5. Assessment of C=C bonds on TPS-written microstructures.....	171
2.6. Assessment of C=C bonds on conventionally photopolymerized photoresists.....	171
2.7. CDTPA decoration of the 2.5D honeycomb microstructure.....	172
2.8. Growing of a fluorescent polymer on CDTPA-decorated 2.5D honeycomb microstructures.....	172
2.9. Growing of a MIP/NIP on CDTPA-decorated 2.5D honeycomb microstructures.....	173
2.10. Binding and selectivity studies on the MIP (or NIP)-decorated honeycombs.....	173
3. Determination of the smallest voxel lateral and axial feature sizes.....	174
3.1. Using IP-Dip.....	174
3.2. Using IP-S.....	174
4. Fabrication via TPS of 2.5D honeycomb microstructures.....	175

5. Decorating 2.5D honeycomb microstructures with CDTPA.....	177
5.1. Residual C=C bonds at the surface of the 2.5D honeycomb microstructures.....	177
5.2. Grafting of CDTPA on the honeycomb via unreacted C=C.....	180
6. Honeycomb functionalization with a fluorescent polymer via a photoiniferter.....	181
7. Honeycomb functionalization with MIP via a photoiniferter.....	184
7.1. SEM characterization of the 2.5D honeycomb microstructures.....	185
7.2. Fluorescent binding test.....	186
7.3. Selectivity study.....	188
8. Conclusions.....	189
9. References.....	191
General Conclusions and Perspectives.....	194
GENERAL CONCLUSIONS.....	195
PERSPECTIVES.....	197
Appendices.....	198
Appendix A.....	199
Appendix B.....	207
Appendix C.....	218
Appendix D: Achievements.....	221

## List of Figures

---

### Chapter 1: PHOTOPOLYMERIZATION AND PHOTOSTRUCTURING OF MOLECULARLY IMPRINTED POLYMERS

- Figure 1.1. Graphical representations of the “lock-and-key” and the “hand-in-a-glove” (or “induced fit”) models that are used to explain the mode of action for the specificity of enzymes for their substrates.....26
- Figure 1.2. General scheme for the molecular imprinting of polymers : Functional monomers (FM) self-assemble around a template (T) to form a pre-polymerization complex which undergoes polymerization in presence of a cross-linker (CL). Upon template extraction, binding sites are made available for the template uptake.....30
- Figure 1.3. Chemical structures of some functional monomers commonly used in the synthesis of MIPs. The functional monomers are grouped here according to their acidic, neutral and basic properties. Under the neutral group, the monomers are further classified as able to form H-bond, dipole-dipole interaction or  $\pi$ - $\pi$  stacking (4-acrylamidophenyl(amino)methanimine and 4-vinyl pyridine) with a template.....32
- Figure 1. 4. A pseudo-phase diagram serving as a general guide on the influence of relative amounts of the cross-linker and of the solvent on the morphology of the synthesized MIP. Reprinted from Ref. 63.....33
- Figure 1.5. Chemical structures of some cross-linkers commonly used in the synthesis of MIPs.....34
- Figure 1.6. The initiating mechanism of a representative (A) Type I photoinitiator (dimethoxy-2-phenylacetophenone, DMPA) and (B) Type II photoinitiator. Figure 1.6(B) reprinted with permission from Wiley-VCH Verlag GmbH & Co. KGaA. Reprinted from Ref. 95.....40
- Figure 1.7. The fabrication process of an imprinted microtip by guiding UV through an optical fiber to the MIP precursor drop. Reprinted from Ref. 114.....47
- Figure 1.8. General scheme for the synthesis of a polymer shell around red and green InP/ZnS emitting QDs. Excitation with UV light allows sequentially polymerizing (A) a hydrophilic shell, and (B) the MIP layer. Reprinted from Ref. 164.....51
- Figure 1.9. Schematic representation of the fabrication of the MIP magnetic upconverting particles (MUCP). Reprinted from Ref. 104.....52
- Figure 1.10. Classification of different lithographic techniques.....54
- Figure 1.11. Comparison of different conventional photolithographic technique (LS=light source, OS=optical system, M=mask, PR=photoresist, SW=silicon wafer).....55
- Figure 1.12. (A) Jablonski diagram showing electronic excitation via two-photon absorption. (B-C) Spatial and temporal compression of photons for increasing the probability of two-photon absorption. Reprinted from Ref. 190. (D) Representative SEM images of microstructures with complex geometries printed via TPS.....57
- Figure 1.13. (A) Schematic representation for the preparation of a grid-patterned double-layered MIP2/MIP1 thin film by contact lithography. (B) Fluorescence microscope image of a grid-patterned

double-layer MIP1/MIP2 thin film with the 54  $\mu\text{m}$  x 54  $\mu\text{m}$  raised MIP2 squares selectively binding the fluorescent target N-dansyl-L- phenylalanine. Reprinted from Ref. 204.....60

Figure 1.14. SEM images of (A) a MIP-coated silicon cantilever obtained by photolithography and (B) large-scale arrays of MIP cantilever. Reprinted from Ref. 206.....61

Figure 1.15. Schematic representation of the preparation of (A) porous microdot arrays and (B) nanofilament microdot arrays by microscope projection photolithography. (C) Transparent photomask. (D) Bright-field microscopy image of the polymer array obtained using the photomask by projection photolithography. (E) SEM image of a single nanofilament dot (magnification: 750 x, inset: 20000 x). Reprinted from Ref. 207.....62

Figure 1.16. (A) Scheme showing the in situ MIP microstructuring process by interference lithography with two laser beams at 532 nm. (B) Holographic MIP film supported on a glass slide. (C) AFM image of the surface topography of a holographic MIP film (10  $\mu\text{m}$  x 10  $\mu\text{m}$ ). Reprinted from Ref. 115.....63

Figure 1.17. (A) SEM image of a 3D imprinted microstructure (600  $\mu\text{m}$  x 600  $\mu\text{m}$  x 100  $\mu\text{m}$ ) fabricated by microstereolithography. (B) Magnification of the structure showing a wall thickness of around 10  $\mu\text{m}$ . Reprinted from Ref. 211.....64

Figure 1.18. (A–B) Multiplexed NIP and MIP dots polymerized on the same sample by two-photon stereolithography (TPS): (A) Optical and (B) fluorescence microscopy images after binding of dansyl-L-Phe. (C) SEM images of MIP cantilevers fabricated by TPS. (D) Relative frequency shift of MIP microcantilevers after extraction, incubation in Z-L-Phe and second extraction. Reprinted from Ref. 144.....65

Figure 1.19. (A) Schematic representation of the setup for the polymerization of MIP microdots by evanescent wave. (B) Optical microscope image (20 x) of a MIP microdot. (C) Fluorescence microscope image (20 x) of a MIP microdot. Interferential microscopy images of (D) a MIP microdot and (E) a NIP microdot. Reprinted from Ref.195.....66

## Chapter 2: THIOL-YNE CHEMISTRY FOR MOLECULAR IMPRINTING

Figure 2.1. Schematic representation of the thiol-yne mechanism. Reprinted from Ref. 10.....93

Figure 2. 2. Proposed mechanism for polymerization via the thiol-yne reaction showing its chain growth and step growth cycles.....95

Figure 2. 3. Structures of the template propranolol and the monomers used.....95

Figure 2. 4. Schematic representation of MIP formation via thiol-yne chemistry in the presence of (meth)acrylic functional monomers: (a) formation of the pre-polymerization complex through coordination of functional monomers (blue) around the template (red), (b) addition of thiols (yellow) to alkynes (grey), (c) addition of thiol to vinyl sulfides, (d) template removal.....99

Figure 2. 5. FTIR spectra of the thiol-yne polymers (orange), polythiols (green) and the dialkyne DBC (blue).....100

Figure 2. 6. Representative SEM images of poly(AA-co-PETMP-co-DBC) MIP (A) and NIP (B) and poly(AA-co-diPETMP-co-DBC) MIP (C) and NIP (D).....101

Figure 2. 7. Equilibrium binding for thiol-yne MIPs (empty squares) and NIPs (filled squares) incubated with 1  $\mu$ M of propranolol. (A) poly(AA-co-PETMP-co-DBC). (B) poly(AA-co-diPETMP-co-DBC).....102

Figure 2. 8. (A) The chemical structures of propranolol and atenolol. (B-C) Equilibrium binding of thiol-yne MIPs incubated with 1  $\mu$ M of propranolol (empty squares) or atenolol (filled squares). (B) poly(AA-co-PETMP-co-DBC). (C) poly(AA-co-diPETMP-co-DBC).....103

Figure 2. 9. Hydrolytic degradation of p(AA-co-PETMP-co-DBC) (filled circles) and p(AA-co-diPETMP-co-DBC) (empty circles) over the time in (A) 1.0 M NaOH at room temperature, and (B) in 1.0 M HCl at 60 °C. Inset: aqueous dispersions of p(AA-co-PETMP-co-DBC) (a), p(AA-co-diPETMP-co-DBC) (b), p(AA-co-PETA) (c) and p(MAA-co-EGDMA) (d) before and after 13 minutes of exposure to 1 molar aqueous NaOH.....104

Figure 2. 10. Turbidity measurements over the time for the alkaline hydrolysis of p(AA-co-PETA) (filled circles) and p(MAA-co-EGDMA) (empty circles) in 1.0 M aqueous NaOH.....105

### Chapter 3: TWO-PHOTON STEREO LITHOGRAPHY AND PHOTOSTRUCTURATION FOR MOLECULAR RECOGNITION

Figure 3.1. The three categories of rapid prototyping technology and their examples.....113

Figure 3.2. (A) Charles Hull, inventor of the first commercial 3D printer, holding a small 3D printed bust of himself. (B) SLA-1, the first commercial 3D printer produced in 1987. Reprinted from Ref. 23,24.....115

Figure 3.3. Several examples of 3D objects manufactured by stereolithographic techniques: (A) a poly( $\epsilon$ -caprolactone)-based tissue engineering scaffold, Reprinted from Ref. 25. (B) a microfluidic device with 3D flow channels, Reprinted from Ref. 26. (C) a cellular cube based on alumina ceramic, Reprinted from Ref. 28. and (D) a tiled solar concentrator lens array. Reprinted from Ref. 31.....115

Figure 3.4. Schematic representation of a typical TPS experimental setup. Reprinted from Ref. 32.....117

Figure 3.5. A representation of a voxel projected from an objective of a TPS system.....117

Figure 3.6. Schematic representation of the three classifications of photonic crystals according to the periodicity of their refractive indices (RI). The different colors represent materials of different RI. Reprinted from Ref. 60.....119

Figure 3.7. The Bragg diffraction of an electromagnetic radiation as it interacts with the particles of a crystal whose lattice constant is of the same magnitude as its wavelength. Adapted from Ref. 62.....120

Figure 3.8. The colors exhibited by (A) the MIC array and (B) the NIC array after incubation in increasing concentrations of TNT in 3:2 v/v methanol/water. (C) The red shift in the Bragg wavelength of the MIP as a function of the TNT concentration. Reprinted from Ref. 53.....122

Figure 3. 9. (A) The colors exhibited by the molecularly imprinted inverse opal dots in response to increasing aqueous concentrations of tetracycline (TC). (B) The red shift in the Bragg wavelength of the molecularly imprinted inverse opal as a function of the TC concentration. (C) The molecularly

imprinted inverse opal dots coated on the hydrophobic PDMS substrate. Reprinted from Ref. 80.....	123
Figure 3.10. The colors exhibited by the molecularly imprinted inverse opal hydrogel upon rebinding atrazine in increasing concentrations. Reprinted from Ref. 52.....	124
Figure 3.11. 3D model of an opal crystal with a fcc unit cell that repeats 4.5 times along the x, y and z axes.....	126
Figure 3.12. Scheme of the fabrication of MIP woodpiles via TPS.....	128
Figure 3. 13. Optical microscopy image of TPS-fabricated opal crystals based on spheres of different size (as indicated by the arrows).....	131
Figure 3.14. Top-view and angled-view (left and right, respectively) of opal crystals consisting of (A) 2400-nm, (B) 800-nm and (C) 500-nm spheres.....	132
Figure 3.15. 3D model of a woodpile structure.....	133
Figure 3.16. Optical microscopy images (TL-POL) of 200 x 200 $\mu\text{m}^2$ woodpiles at the center of the field of view (FOV) of a 20x objective (scale bar = 200 $\mu\text{m}$ ). Laser power values expressed in mW. (Outset) Woodpile written at SS = 1000 $\mu\text{m}/\text{s}$ and LP = 15 mW moved across the FOV.....	136
Figure 3.17. Representative SEM images of (A) the MIP woodpile and (B) the NIP woodpile.....	137
Figure 3.18. Microscopy images (TP-POL) of the MIP woodpile (A) before washing, (B) after washing and (C) after incubation with 1.0 mM propranolol in acetonitrile.....	138
Figure 3.19. Microscopy images (TP-POL) of the NIP woodpile (A) before washing, (B) after washing and (C) after incubation with 1.0 mM propranolol in acetonitrile.....	138
Figure 3. 20. Darkness increase for the woodpiles incubated with 1.0 mM propranolol in acetonitrile.....	139
Figure 3. 21. TP-POL microscopy images of IP-Dip MIP woodpile triplicates 3D printed using the experimentally determined “color-generating” parameters. The fiber-like figure on the third replicate at SS7000 LP25 is a contamination.....	141-142
Figure 3.22. TP-POL microscopy images of IP-Dip MIP woodpile triplicates 3D printed using the experimentally determined “color-generating” parameters.....	143-144
Figure 3.23. TP-POL microscopy images of three representative IP-Dip MIP-NIP pairs as they underwent changes through the various steps of processing and incubation experiments.....	146-148
Figure 3.24. Optical microscopy images (TP-POL) of woodpile structures based on the (A) PETMP/DBC, and the (B) diPETMP/DBC thiol-yne formulations fabricated via TPS under various laser power and scan speed values.....	151
Figure 3.25. Optical microscopy images (TP-POL) of the AcryS2-based woodpiles generated at various laser power values and at (A) “higher” scan speeds and (B) “usual” and very low scan speeds.....	153

## Chapter 4: TPS OF MICROSTRUCTURES AND THEIR FUNCTIONALIZATION WITH MIP

- Figure 4. 1. Schematic representation of the functionalization with MIP of a TPS-written microstructure via photoiniferter-mediated polymerization. (a) The microstructure is immersed in a solution of the photoiniferter, which couples to its surface C=C upon activation by light. (b) The photoiniferter-coupled microstructure is washed and placed in a MIP precursor solution, which polymerizes at the microstructure surface, leading to MIP-functionalized microstructures.....168
- Figure 4. 2. The 2.5D honeycomb design (length measurements in  $\mu\text{m}$ ). The design is programmed to extend to an area of  $200 \times 200 \mu\text{m}^2$ .....175
- Figure 4. 3. Absorbance spectra of the unreacted photoresists IP-Dip and IP-S recorded in acetonitrile at a concentration of  $69 \mu\text{g/mL}$ .....176
- Figure 4. 4. Representative SEM images of TPS-written 2.5D honeycomb microstructures based on the commercial photoresists (A) IP-Dip and (B) IP-S.....176
- Figure 4. 5. The truncated cone design for the Raman spectroscopy of the photoresists polymerized via TPS (length measurements in  $\mu\text{m}$ ).....178
- Figure 4. 6. Raman spectra of (A) unreacted photoresists and (B) TPS-written truncated cones based on these photoresists. PETA was used as the C=C bond-containing monomer reference.....178
- Figure 4. 7. The (A) brightfield image and (B) the Raman image of top surface of the TPS-written truncated cone of each photoresist.....179
- Figure 4.8. The FTIR spectra of (A) unreacted photoresists and (B) conventionally photopolymerized photoresists.....180
- Figure 4. 9. Absorption spectra of CDTPA and the structural mimics of its SUMI adducts with acrylic acid (BM1429) and with methacrylic acid (DoMPAT). All the spectra were recorded in acetonitrile at a concentration of  $7.5 \text{ mM}$ .....181
- Figure 4. 10. (A) Brightfield and (B) fluorescence microscopy images of the bare IP-Dip 2.5D honeycomb microstructure. The arrows indicate the borders of the  $200 \mu\text{m} \times 200 \mu\text{m}$  area of the honeycomb.....182
- Figure 4.11. (A) Brightfield and (B) fluorescence microscopy images of the CDTPA-decorated IP-Dip 2.5D honeycomb microstructure after growing a fluorescent polymer. The arrows indicate the borders of the  $200 \mu\text{m} \times 200 \mu\text{m}$  area of the honeycomb. (Image enhanced).....183
- Figure 4. 12. (A) Brightfield and (B) fluorescence microscopy images of the negative control IP-Dip 2.5D honeycomb microstructure after growing a fluorescent polymer. The arrows indicate the borders of the  $200 \mu\text{m} \times 200 \mu\text{m}$  area of the honeycomb. (Image enhanced).....183
- Figure 4. 13. (A, C, E) Brightfield and (B, D, F) fluorescence microscopy images of the (A, B) bare, (C, D) CDTPA-decorated, and (E, F) negative control IP-S 2.5D honeycomb microstructures after growing a fluorescent polymer. The arrows indicate the borders of the  $200 \mu\text{m} \times 200 \mu\text{m}$  area of the honeycomb.....184
- Figure 4. 14. Representative images of the bare, MIP- and NIP-decorated IP-S-based honeycomb microstructures.....185



Figure 4. 15. Representative images of the bare, MIP- and NIP-decorated IP-Dip-based honeycomb microstructures.....	186
Figure 4. 1. Fluorescence microscopy image of the (A-B) MIP layer on the IP-Dip-based honeycomb microstructures (A) before and (B) after incubation, and of the (C-D) NIP layer (C) before and (D) after incubation in 10 $\mu$ M dansyl-(L)-Phe in acetonitrile. (Image enhanced). (E) Background-corrected $\Delta I_f$ of the MIP and NIP layer on the IP-Dip-based honeycomb microstructure after incubation in a solution of dansyl-(L)-Phe in acetonitrile (n = 3). The concentration of polymerizable double bonds in the MIP and NIP precursor formulation was 1.80 M.....	187
Figure 4. 2. Fluorescence microscopy image of the (A-B) MIP layer on the IP-S-based honeycomb microstructures (A) before and (B) after incubation, and of the (C-D) NIP layer (C) before and (D) after incubation in 10 $\mu$ M dansyl-(L)-Phe in acetonitrile. (Image enhanced). (E) Background-corrected $\Delta I_f$ of the MIP and NIP layer on the IP-S-based honeycomb microstructure after incubation in a solution of dansyl-(L)-Phe in acetonitrile (n = 3). The concentration of polymerizable double bonds in the MIP and NIP precursor formulation was 1.80 M.....	187
Figure 4. 18. Background-corrected $\Delta I_f$ of the MIP and NIP layer on (A) the IP-Dip-, and (B) the IP-S-based honeycomb microstructures after incubation in a solution of dansyl-(L)-Phe alone, dansyl-(L)-Phe with Z-(L)-Phe or dansyl-(L)-Phe with Z-(D)-Phe in acetonitrile (n = 3). The concentration of each molecular species in every solution was 10 $\mu$ M.....	189

## APPENDIX A

Figure A 1. Hydrolytic degradation of p(AA-co-PETMP-co-DBC) (filled circles) and p(AA-co-diPETMP-co-DBC) (empty circles) in 0.1 molar aqueous NaOH (A) and in 0.01 molar aqueous NaOH (B) over time.....	199
Figure A 2. Representative SEM images of (A) p(AA-co-PETA) and (B) p(MAA-co-EGDMA).....	200
Figure A3. Major compounds found by SEC/HRMS with positive (A) et negative (B) ionisation for p(AA-co-PETA). Retention time, exact mass and putative formula was reported on Table A3.....	203
Figure A4. Major compounds found by SEC/HRMS with positive (A) et negative (B) ionisation for p(AA-co-diPETMTP-co-DBC). Retention time, exact mass and putative formulae were reported on Table A4.....	206
Figure A5. Major compounds found by SEC/HRMS with positive (A) et negative (B) ionisation for p(AA-co-PETMTP-co-DBC). Retention time, exact mass and putative formulae were reported on Table A5.....	208
Figure A 6. Comparison between the FTIR spectra of the thiol-yne MIPs (blue) and their products of hydrolysis (red) obtained by incubation in 1.0 M NaOH.....	209
Figure A 7. Comparison between the FTIR spectra of the thiol-yne polymer (blue) and their products of hydrolysis (red) for different vibration modes (insets). Wavenumbers are in $\text{cm}^{-1}$ .....	210
Figure A 8. Comparison between the $^1\text{H-NMR}$ spectra (in $d_8\text{-THF}$ ) of (A) the polythiol diPETMP and (B) the products of the alkaline hydrolysis (pH = 14) for p(AA-co-diPETMP-co-DBC). The highlighted peaks in B (1.96 ppm) refer to the $-\text{SH}$ group.....	211

## APPENDIX B

Figure B1. The minimum (A) lateral and (B) axial feature sizes as functions of laser power at a fixed scan speed using the IP-Dip MIP precursor formulation ( $n = 3$ ). Outset of A: SEM image of triplicates of one-voxel-wide line with the smallest average minimum lateral size ( $277 \pm 156$  nm) generated using  $SS = 10000 \mu\text{m/s}$  and  $LP = 50$  mW. Legend shows scan speed values expressed in  $\mu\text{m/s}$ .....212

Figure B2. The minimum (A) lateral and (B) axial feature sizes as functions of laser power at a fixed scan speed using the IP-Dip NIP precursor formulation ( $n = 3$ ). Outset of A: SEM image of triplicates of one-voxel-wide line with the smallest average minimum lateral size ( $304.7 \pm 39.2$  nm) generated using  $SS = 4000 \mu\text{m/s}$  and  $LP = 35$  mW. Legend shows scan speed values expressed in  $\mu\text{m/s}$ .....213

Figure B3. The computer-generated image of the snowflake microstructure.....214

Figure B4. Effect of increasing TPO-L concentration and of increasing laser power at the same scan speed on the resulting written snowflake microstructures of poly(AA-co-PETMP-co-DBC).....215

Figure B5. Effect of increasing TPO-L concentration and of increasing laser power at the same scan speed on the resulting written snowflake microstructures of poly(AA-co-diPETMP-co-DBC).....216

Figure B6. The minimum lateral feature size as a function of laser power at a fixed scan speed using Nanoscribe, 63x NA1.4 objective, DiLL configuration and AcryS2 formulation ( $n = 1$ ). Legend shows scan speed values expressed in  $\mu\text{m/s}$ .....217

Figure B7. SEM image of suspended lines generated by varying scan speed and laser power using the AcryS2 formulation.....217

## APPENDIX C

Figure C 1. The minimum lateral feature size as a function of laser power at a fixed scan speed using the IP-Dip photoresist ( $n = 3$ ). Outset: SEM image of triplicates of one-voxel-wide line with the smallest average minimum lateral feature size ( $147.7 \pm 64.0$  nm) generated using  $SS = 6000 \mu\text{m/s}$ ,  $LP = 20$  mW. Legend shows scan speed values expressed in  $\mu\text{m/s}$ .....218

Figure C 2. The minimum lateral feature size as a function of laser power at a fixed scan speed using the IP-S photoresist ( $n = 3$ ). Outset: SEM images of triplicates of one-voxel-wide line with smallest ( $270.0 \pm 34.8$  nm) average minimum lateral feature size generated using  $SS = 2000 \mu\text{m/s}$ ,  $LP = 34$  mW. Legend shows scan speed values expressed in  $\mu\text{m/s}$ .....219

Figure C 3. Background-corrected  $\Delta I_f$  of the MIP and NIP layer on the (A) IP-Dip- and (B) IP-S-based honeycomb microstructure after incubation in a solution of dansyl-(L)-Phe in acetonitrile ( $n=1$ ). The concentration of the active bonds in the MIP (and NIP) precursor formulation was  $0.99$  M.....220

## List of Tables

---

### Chapter 1: PHOTOPOLYMERIZATION AND PHOTOSTRUCTURING OF MOLECULARLY IMPRINTED POLYMERS

Table 1.1. Non-exhaustive list of recent examples (from 2013 to 2018) of MIPs synthesized via photopolymerization.....	42-43
--	-------

### CHAPTER 2: THIOL-YNE CHEMISTRY FOR MOLECULAR IMPRINTING

Table 2. 1. Gravimetric conversions for p(AA-co-PETMP-co-DBC) and p(AA-co-diPETMP-co-DBC).....	100
--	-----

Table 2. 2. Surface area (in m <sup>2</sup> /g) for p(AA-co-PETMP-co-DBC) and p(AA-co-diPETMP-co-DBC).....	101
--	-----

### APPENDIX A

Table A 1. Alkyne and thiol conversions for thiol-yne polymerized p(AA-co-PETMP-co-DBC) and p(AA-co-diPETMP-co-DBC) as measured by FTIR.....	199
--	-----

Table A 2. Mean particles size of the thiol-yne MIPs and NIPs and the FRP polymers as measured by SEM.....	200
--	-----

Table A3. Exact Mass (Mass), retention time (RT) and putative formula for the compounds identified by the algorithm "Find Bye Molecular Feature" (MASSHunter, Agilent) on signals generating more than 2000 counts, for p(AA-co-PETA). Corresponding chromatograms are presented in Figure A3.....	201-203
--	---------

Table A4. Exact Mass (Mass), retention time (RT) and putative formula for the compounds identified by the algorithm "Find Bye Molecular Feature" (MASSHunter, Agilent) on signals generating more than 2000 counts, for p(AA-co-diPETMP-co-DBC). Corresponding chromatograms are presented in Figure A4.....	204-205
--	---------

Table A5. Exact Mass (Mass), retention time (RT) and putative formula for the compounds identified by the algorithm "Find Bye Molecular Feature" (MASSHunter, Agilent) on signals generating more than 2000 counts, for p(AA-co-PETMP-co-DBC). Corresponding chromatograms are presented in Figure A5.....	207
--	-----

## List of Abbreviations

---

2,4-D	2,4-dichlorophenoxyacetic acid
4-VP	4-vinylpyridine
AA	acrylic acid
Aam	acrylamide
ABDV	azobisdimethylvaleronitrile
AB·HCl	N-acryloyl-p-aminobenzamidine dihydrochloride
ACN	acetonitrile
AFM	atomic force microscopy
AIBN	azobisisobutyronitrile
AM	additive manufacturing
ATR	attenuated total reflection
ATRP	atom-transfer radical polymerization
AuNP	gold nanoparticle
BAPO	bisacylphosphine oxide
BET	Brunauer-Emmett-Teller
BM1429	3-(((1-carboxyethyl)thio)carbonothioyl)thio)propanoic acid
BSA	bovine serum albumin
CAD	computer-aided design
CCA	colloidal crystal array
CDTPA	4-cyano-4-[(dodecylsulfanylthiocarbonyl)sulfanyl]pentanoic acid
CPADB	4-cyano-4-(thiobenzoylthio)pentanoic acid
CPDTC	2-cyano-2-propyldodecyltrithiocarbonate
CETP	4-cyano-4-ethyltrithiopentanoic acid
CETPA	4-(((2-carboxyethyl)thio)thioxomethyl)thio)-4-cyanopentanoic acid
CL	cross-linker
CT	computerized tomography
d8-THF	tetrahydrofuran-d <sub>8</sub>
DABP	4,4'-bis(di-n-butylamino)biphenyl
dansyl-(L)-Phe	dansyl-(L)-phenylalanine
DBC	di(but-1-yn-4-yl)carbonate
DCM	dichloromethane
DEAEM	diethylaminoethyl methacrylate
DEDTC	diethyldithiocarbamate
DiLL	Dip-in Laser Lithography
diPETMP	dipentaerythritol hexa(3-mercaptopropionate)
DMA	N,N-dimethylaniline
DMF	N,N-dimethylformamide
DMPA	2,2-dimethoxy-2-phenylacetophenone
DMSO	dimethylsulfoxide
DoMPAT	2-(dodecylthiocarbonothioylthio)-2-methylpropionic acid
DVB	divinylbenzene

EBAAm	N,N'-ethylenebis(acrylamide)
EBL	electron-beam lithography
ECL	electrochemiluminescence
EDMAT	2-(((ethylthio)carbonothioyl)thio)-2-methylpropanoic acid
EGDMA	ethylene glycol dimethacrylate
EIS	electrochemical impedance spectroscopy
ENRO	enrofloxacin
EtOH	ethanol
fcc	face-centered cubic
FDM	fused deposition modelling
FDTD	finite difference time domain
FEM	finite element method
FIBL	focused-ion-beam lithography
FOV	field of view
FRP	free-radical polymerization
GlcA	glucuronic acid
HEMA	2-hydroxyethyl methacrylate
HOPG	highly ordered pyrolytic graphite
HP/GL	Hewlett-Packards graphics language
IF	imprinting factor
IGES	initial graphics exchange specification
IR	infrared
ITO	indium tin oxide
IUPAC	International Union of Pure and Applied Chemistry
LED	light-emitting diode
LOD	limit of detection
LP	laser power
MAA	methacrylic acid
MAM	methacrylamide
MBAAm	N,N'-methylenebisacrylamide
MBIL	multibeam interference lithography
MEMS	microelectromechanical system
MIC	molecularly imprinted colloidal particle
MIP	molecularly imprinted polymer
MSLA	multiphoton stereolithography
MUCP	magnetic upconverting particle
NANA	N-acetylneuraminic acid
NEMS	nanoelectromechanical system
NIL	nanoimprint lithography
NIP	non-imprinted polymer
NIR	near infrared
NMP	nitroxide mediated polymerization
NMR	nuclear magnetic resonance
NOBE	N,O-bismethacryloyl ethanolamine
PBG	photonic band gap
PDMS	polydimethylsiloxane

PEG200DMA	poly(ethyleneglycol(200))dimethacrylate
PET	photo-electron transfer
PETA	pentaerythritol triacrylate
PETMP	pentaerythritol tetra(3-mercaptopropionate)
PEW	polymerization by evanescent wave
PGMEA	propylene glycol methyl ether acetate
PhC	photonic crystal
PMMA	poly(methyl methacrylate)
PWE	plane wave expansion
QD	quantum dot
RAFT	reversible addition-fragmentation chain-transfer polymerization
RDRP	reversible deactivation radical polymerization
RP	rapid prototyping
SEC/HRMS	size-exclusion chromatography/high-resolution mass spectrometry
SFRP	stable free radical polymeriza
SIP	surface imprinted polymer
SLA	stereolithography
SLC	stereolithography contour
SOI	silicon-on-insulator
SPE	solid-phase extraction
SS	scan speed
STEM	stimulated-emission-depletion microscopy
STL	standard tessellation language
TC	tetracycline
TEA	triethylamine
TED	tetraethylthiuram disulfide
TEM	transmission electron microscopy
TMM	transfer matrix method
TMPM	3-(trimethoxysilyl)propyl methacrylate
TNT	2,4,6-trinitrotoluene
TPO	(2,4,6-trimethylbenzoyl)phosphine oxide
TPO-L	ethyl (2,4,6-trimethylbenzoyl) phenylphosphinate
TPS	two-photon stereolithography
TRIM	trimethylolpropane trimethacrylate
UV	ultraviolet
V-50	2,2'-azobis(2- methylpropionamide) dihydrochloride
VIS	visible
Z-(D)-Phe	N-(carbobenzyloxy)-(D)-phenylalanine
Z-(L)-Phe	carbobenzyloxy-L-phenylalanine
μCP	microcontact printing
μFP	microfluidic printing

## Abstract

### **Direct writing of micro and nanostructures via two-photon stereolithography for the design of molecularly imprinted polymer-based sensing elements**

*Keywords: two-photon stereolithography, molecular imprinting, molecularly imprinted polymers, photopolymerization, photostructuring, photoiniferter polymerization, photonic crystals, microstructures, fluorescence*

---

Molecularly imprinted polymers (MIPs) have emerged as synthetic receptors with excellent affinity and selectivity for their targets on a par with antibodies. For this reason, MIPs have found various applications such as in chemical sensing, separation science, drug delivery, bioimaging, cosmetics and catalysis. These recognition properties originate from the manner by which MIPs are synthesized: by using the target molecule or a derivative as a template around which selected monomers capable of interacting with it are cross-linked. Upon removal of the template, binding cavities with a geometry and functional groups that complement the target are revealed. Traditionally, MIPs are mainly produced in particulate form; however, photolithographic techniques have gained popularity in the recent years allowing to shape MIPs into predetermined structures to better suit certain applications. Still, many photolithographic techniques are rather “passive” and “restrained” in that they rely on the use of stationary masks and/or molds and stationary light sources, which limits the variety and the complexity of the resulting MIP structures. Two-photon stereolithography (TPS) sets itself apart by offering direct and precise fabrication of three-dimensional (3D) structures through the active manipulation of light within the 3D space of a polymerizable material. In this PhD thesis, we shed light on several possibilities that TPS can offer, primarily to the structuring of MIPs, with feature sizes in the sub-micron range. First, we present a rich discussion on photopolymerization and the existing techniques for photostructuring MIPs, including TPS. This is followed by investigating the feasibility of using the thiol-yne chemistry for the synthesis of MIPs, which is known to be resistant to oxygen inhibition and hence, was considered advantageous in open-air setups such as the equipment for TPS. Moreover, it yields highly cross-linked polymers with low shrinkage, which is desirable to maintain structural integrity. Through conventional photopolymerization, MIPs were obtained via the thiol-yne reaction without a preliminary deoxygenation step – a first in the history of MIPs. The thiol-yne MIPs displayed good affinity and selectivity for the target propranolol. This verified the usability of the thiol-yne chemistry in molecular imprinting and possibly, in the TPS of MIPs. The use of TPS for the writing of MIPs is then discussed. TPS was initially used to write MIP photonic crystals (PhCs), which due to

the periodic modulation in space of their refractive index, reflect a certain wavelength of light. The periodic modulation, as well as the refractive index, may be affected by binding a target molecule, which produces a wavelength shift in the MIP PhCs as a visible response to the presence of the target. We used TPS to fabricate PhCs in the form of woodpiles. The commercial photoresist IP-Dip was modified for molecular imprinting and the written structures showed a visible response in the presence of propranolol during preliminary studies. However, modifying the commercial photoresist proved to be detrimental to the integrity of the PhC structure. The thiol-yne formulations, as well as thiol-acrylate formulations, were also used as photoresists, although they did not yield PhCs that functioned in the visible region. A new strategy was therefore adapted: the use of unaltered IP-Dip for the TPS of repeating structures of sub-micron size (honeycomb) that would serve as the support for MIPs. After TPS, the structures were functionalized with a MIP after attaching the photoiniferter 4-cyano-4-((dodecylsulfanylthiocarbonyl) sulfanyl)pentanoic acid (CDTPA) to residual double bonds for surface-initiated controlled polymerization. MIPs imprinted with N-(carbobenzyloxy)-(L)-phenylalanine (Z-(L)-Phe) were grown. SEM images revealed that the post-TPS polymerization did not drastically diminish the resolution of the honeycomb structure. During the binding test, the MIP-decorated structures exhibited affinity toward the fluorescent target dansyl-(L)-phenylalanine (dansyl-(L)-Phe) as shown by a significant increase in their fluorescence intensity, whereas the control honeycomb (decorated with a non-imprinted control polymer) manifested only a small increase. The MIP-decorated structures also displayed a certain selectivity for the target Z-(L)-Phe over its enantiomer Z-(D)-Phe. Overall, several attempts were made to use TPS for molecular imprinting and while several challenges were met along the way, a promising general approach was finally achieved for the generation of arbitrarily designed 3D structures by TPS with molecular recognition capabilities thanks to the MIP decorated on their surface through the aid of a photoiniferter.



## Résumé

### **Écriture directe de micro et nanostructures via stéréolithographie à deux photons pour la conception d'éléments de détection à base de polymères à empreinte moléculaire**

*Mots clés : stéréolithographie à deux photons, empreinte moléculaire, polymères à empreinte moléculaire, photopolymérisation, photostructuration, polymérisation photoinferter, cristaux photoniques, microstructures, fluorescence*

---

Les polymères à empreintes moléculaires (MIP) sont apparus comme des récepteurs synthétiques avec une excellente affinité et sélectivité pour des molécules cibles comparable à celles des anticorps. Pour cette raison, les MIP ont trouvé diverses applications telles que les capteurs chimiques, la séparation moléculaire, la vectorisation de médicaments, la bio-imagerie, les cosmétiques et la catalyse. Ces propriétés de reconnaissance proviennent de la manière dont sont synthétisés les MIP : en utilisant la molécule cible ou un dérivé comme matrice autour de laquelle sont réticulés des monomères capables d'interagir avec elle. Lors du retrait de la molécule matrice, des cavités de liaison avec une géométrie et des groupes fonctionnels complémentaires à la cible sont révélées. Traditionnellement, les MIP ont été surtout produits sous forme de particules; cependant, les techniques photolithographiques ont gagné en popularité ces dernières années, permettant de façonner les MIP en structures prédéterminées pour mieux les adapter à certaines applications. Pourtant, de nombreuses techniques photolithographiques sont plutôt « passives » et « restrictives » dans la mesure où elles reposent sur l'utilisation de masques et/ou moules et de sources lumineuses stationnaires, ce qui limite la variété et la complexité des structures MIP résultantes. La stéréolithographie à deux photons (TPS) se distingue en offrant une fabrication directe et précise de structures tridimensionnelles (3D) grâce à la manipulation active de la lumière dans l'espace 3D d'un matériau polymérisable. Dans cette thèse, nous mettons en lumière plusieurs possibilités que TPS peut offrir, principalement à la structuration de MIP, avec des éléments de tailles submicroniques. Tout d'abord, nous présentons une discussion riche sur la photopolymérisation et les techniques existantes pour la photostructuration des MIP, y compris la TPS. Ceci est suivi par l'étude de la faisabilité de l'utilisation de la chimie thiol-yne pour la synthèse des MIP, qui est connue pour être résistante à l'inhibition de l'oxygène et, par conséquent, a été considérée comme avantageuse dans les installations hors atmosphère inerte telles que l'équipement pour TPS. De plus, elle donne des polymères hautement réticulés avec un faible contraction, ce qui est souhaitable pour maintenir l'intégrité structurelle. Des MIP ont été obtenus via

la réaction thiol-yne par photopolymérisation conventionnelle, sans étape préalable de désoxygénation - une première dans l'histoire des MIP. Les MIP thiol-yne présentaient une bonne affinité et sélectivité pour la cible propranolol. Cela a confirmé l'applicabilité de la chimie thiol-yne dans l'impression moléculaire et possiblement, pour la TPS des MIP. L'utilisation de TPS pour l'écriture de MIP est ensuite discutée. La TPS a été initialement utilisée pour écrire des cristaux photoniques (PhCs) MIP, qui en raison de la modulation périodique dans l'espace de leur indice de réfraction, réfléchissent une certaine longueur d'onde de la lumière. La modulation périodique, ainsi que l'indice de réfraction, peuvent être affectés par la liaison d'une molécule cible, ce qui produit un décalage de longueur d'onde dans les PhC MIP et donc une réponse visible à la présence de la cible. Nous avons utilisé la TPS pour fabriquer des PhC sous forme de structure '*woodpile*'. Le photoresist commercial IP-Dip a été modifié pour l'impression moléculaire et les structures écrites ont montré une réponse visible en présence de propranolol lors d'études préliminaires. Cependant, la modification de la résine photosensible commerciale s'est avérée préjudiciable à l'intégrité de la structure PhC. Les formulations de thiol-yne, ainsi que les formulations de thiol-acrylate, ont également été utilisées comme photoresists, mais elles n'ont pas produit de PhC fonctionnant dans la région visible. Une nouvelle stratégie a donc été adaptée : l'utilisation d'IP-Dip non altéré pour la TPS de structures répétitives de taille submicronique (nid d'abeille) qui serviraient de support au MIP. Après TPS, les structures ont été fonctionnalisées avec un MIP après avoir fixé le photoiniferteur acide 4-cyano-4-((dodécylsulfanylthiocarbonyl) sulfanyl)pentanoïque (CDTPA) aux doubles liaisons résiduelles de la structure pour une polymérisation contrôlée initiée en surface. Des MIP imprimés avec de la N-(carbobenzyloxy)-(L)-phénylalanine (Z-(L)-Phe) ont été synthétisés. Les images SEM ont révélé que la polymérisation post-TPS n'a pas radicalement diminué la résolution de la structure en nid d'abeille. Lors du test de liaison, les structures décorées de MIP ont montré une affinité envers la cible fluorescente dansyl-(L)-phénylalanine (dansyl-(L)-Phe) comme le montre l'augmentation significative de leur intensité de fluorescence, tandis que la structure témoin (décoré avec un polymère témoin non imprimé) n'a manifesté qu'une faible augmentation. Les structures décorées de MIP ont également affiché une certaine sélectivité pour la cible Z-(L)-Phe par rapport à son énantiomère Z-(D)-Phe. Dans l'ensemble, plusieurs tentatives ont été faites pour utiliser la TPS pour l'impression moléculaire et alors que plusieurs défis ont été relevés en cours de route, une approche générale prometteuse a finalement été réalisée pour la génération de structures 3D arbitrairement conçues par TPS avec des capacités de reconnaissance moléculaire grâce au MIP décoré sur leur surface à l'aide d'un photoiniferteur.

## GENERAL INTRODUCTION

---

---

Molecular recognition is the underlying principle of many biochemical processes. In affinity technology, it is employed for applications like bioseparation, bioimaging and biosensors. Originally described in the 1970s, Molecularly Imprinted Polymers (MIPs) were used for the first time as an antibody replacement in an immunoassay for drugs in 1993. This opened a new field of research, and throughout its decades-long history, molecular imprinting of synthetic polymers has produced affinity materials with the aim of mimicking biological receptors, recognizing molecular targets ranging from simple organic molecules and ions to macromolecules and whole cells. The scientific community has witnessed the evolution and the transformation of the techniques involved in the synthesis of MIPs from a polymer and materials chemistry point of view, and their integration into various technological applications. Each transformation has been a response to the challenge of coming up with better MIPs better adapted for a specific use.

In this PhD thesis, we propose several new routes for the synthesis and structuration of MIPs. It is organized in four chapters, one bibliographic chapter and three results chapters.

Chapter 1 offers a literature review on the photopolymerization and photostructuring of MIPs. It opens with a general introduction to MIPs and continues with the polymerization techniques currently used for their synthesis. It then proceeds to highlight the advantages of photopolymerization over other activation techniques and tackles the types of photoinitiators and the various photoinitiation mechanisms, including the different regions of the electromagnetic spectrum employed, with special emphasis on polymerization with visible light. Thereby, both free radical polymerization and controlled-living radical polymerization are addressed. In the second part, different methods used for the micro and nanostructuring of MIPs are described, based on both mask and mask-less approaches. The chapter underlines the importance of two-photon stereolithography in future developments, the method used within this thesis.

Chapter 2 focuses on the application of the thiol-yne chemistry in molecular imprinting. The first part presents thiol-yne chemistry as a new and attractive avenue for synthesizing MIPs. Despite its quasi-absence in the MIP literature, it actually possesses several desirable qualities such as its click nature, compatibility with the existing libraries of vinyl functional monomers, and oxygen tolerance. Results are then presented on MIPs imprinted with the beta-antagonist drug S-propranolol, which

demonstrate that MIPs can be obtained with the functional monomer used in the conventional FRP recipe in a thiol-yne context, in the presence of oxygen.

Chapter 3 deals with two-photon stereolithography (TPS) in molecular imprinting. It starts by introducing the concept of “rapid prototyping”, narrowing the discussion to stereolithography, to enter the subject on two-photon stereolithography. With the aim of producing MIP-based optical sensing elements, materials exhibiting structural colors, such as opal and woodpile lattices are then probed and are finally fabricated via two-photon stereolithography using different formulations. The latter are based on the thiol-yne polymer matrix of Chapter 2, and two commercial photoresists.

Lastly, Chapter 4 describes the development of a general approach to the precise photostructuring with subsequent chemical functionalization, whereby micro/nanostructuring and molecular imprinting are dissociated from each other. This has the advantage of avoiding conflicts concerning the optimal conditions of the two synthesis steps, TPS and MIP synthesis. Fabricating honeycomb microstructures as a model feature for the subsequent synthesis of MIPs by photoiniferter coupling and post-polymerization. The chapter concludes by presenting perspectives on the future applications of two-photon stereolithography in the field of molecular imprinting.

## Chapter 1

# PHOTOPOLYMERIZATION AND PHOTOSTRUCTURING OF MOLECULARLY IMPRINTED POLYMERS

# Chapter 1: PHOTOPOLYMERIZATION AND PHOTOSTRUCTURING OF MOLECULARLY IMPRINTED POLYMERS

---

## 1. Molecular recognition

Molecular recognition is the ability of molecules to interact with one another strongly and specifically due to the high shape complementarity and the noncovalent forces between their interacting surfaces.<sup>1,2</sup> The geometry of these surfaces allows them to fit one another, as represented in several host-guest system models such as the lock-and-key model and the hand-and-glove model (Figure 1.1). Noncovalent forces providing adhesion between interacting molecules may include van der Waals forces, hydrogen bonding, electrostatic forces,  $\pi$ - $\pi$  interactions, metal coordination, as well as the hydrophobic effect.<sup>3-5</sup>

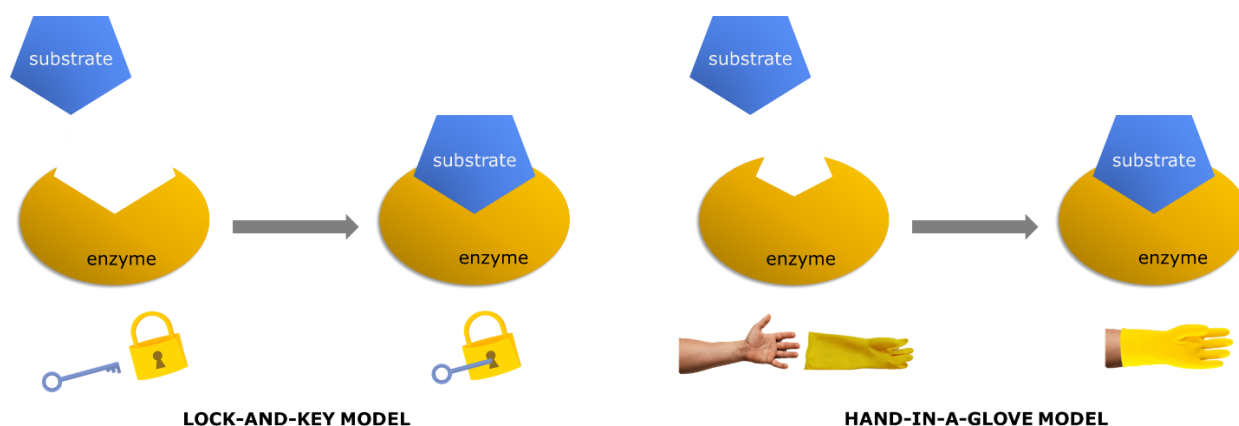


Figure 1.1. Graphical representations of the “lock-and-key” and the “hand-in-a-glove” (or “induced fit”) models that are used to explain the mode of action for the specificity of enzymes for their substrates.

The importance of molecular recognition in nature cannot be understated since it plays a fundamental role in the realization of many biochemical processes such as immune recognition, catalysis and signaling.<sup>2,6</sup> Antibodies, for example, rely on molecular recognition to detect the antigen of a pathogen to neutralize and prevent it from harming the organism. Enzymes, which facilitate biochemical reactions ranging from synthesizing or breaking down sources of energy to genetic information transfer, require recognition of their substrates to catalyze a reaction. In the same way, receptors found on cell membranes must recognize their specific ligands to trigger a cellular response. Without molecular recognition, life as we know it would not exist.

It is crucial to note that these interactions must be strong and specific enough, otherwise detrimental errors may occur. Due to these “high-precision” host-guest interactions, molecular recognition in nature have inspired the design of many synthetic recognition systems for various applications. Examples of these systems include aptamers, metal organic frameworks, dendrimers, crown ethers and molecularly imprinted polymers (MIPs). Among these, MIPs are considered one of the simplest though elegant ways to generate synthetic molecular recognition systems. Their particularity is that they are tailor-made for a given target molecule. In fact, MIPs have been dubbed “plastic antibodies” as they mimic in artificial polymeric matrices the recognition phenomena occurring in natural biomolecules, thus they are an excellent example of biomimicry at the molecular level.

## 2. Molecularly imprinted polymers

### 2.1. Introduction

MIPs are synthetic polymers displaying high affinity and selectivity for analytes ranging from ions,<sup>7-9</sup> to small organic molecules,<sup>10-12</sup> peptides,<sup>13-15</sup> biomolecules<sup>16-18</sup> up to whole cells.<sup>19,20</sup> The principle is that the polymer is synthesized in the presence of the target molecule, or a derivative thereof, which serves as a template around which the polymer is molded. The crucial step in the preparation of MIPs involves the formation of a covalent or a noncovalent pre-polymerization complex between functional monomers and the template. This pre-polymerization complex is then polymerized with an excess of cross-linker in order to “freeze” its structure into a three-dimensional rigid matrix. Thus, after polymerization and template removal, cavities are revealed in the polymer network that are complementary to the template in terms of size, shape and spatial distribution of functional groups. As such, the polymer is effectively “imprinted” and its binding sites locally display a “ligands sphere” able to host its target with affinities often comparable to those of antibodies. At the same time, MIPs surpass their natural counterparts in terms of great stability, physico-chemical resistance, robustness and low-cost, due to their synthetic character. Thanks to these advantages, MIPs have unsurprisingly been exploited in diverse applications requiring molecular recognition such as separation science,<sup>21-24</sup> drug delivery,<sup>25-27</sup> bioimaging,<sup>28-30</sup> cosmetics,<sup>31</sup> catalysis<sup>32-34</sup> and (bio)chemical sensing.<sup>35-37</sup>

## 2.2. Early history

Molecular imprinting has been around already for several decades. The very first evidence of “molecular imprinting” was accidentally reported by Polyakov in 1931, while trying to modify silica for chromatographic purposes.<sup>38</sup> He prepared silica gels by polymerizing sodium silicate in water using  $(\text{NH}_4)_2\text{CO}_3$  as the gelling agent. Two weeks after, he introduced an additive such as benzene, toluene or xylene. When the silica had dried up after 20 to 30 days at room temperature, it was washed extensively in hot water to remove the additive. He then noticed that when a silica gel was placed inside a desiccator containing a beaker with one of the additives, the silica gel exhibited a higher adsorption capacity for the additive with which it had been synthesized than the other two additives. It seemed that the silica gels remembered their respective additives and had a kind of “molecular memory”.<sup>39,40</sup> Later, in the 1940s, Pauling put forward his theory on the formation of antibodies,<sup>41</sup> postulating that the functional groups on the surface of an antigen exerted attractive and repulsive forces on the chains of an antibody, which in turn experienced conformational change to complement its structure. Although proven wrong later on, it reflected nonetheless the general mechanism of molecular imprinting. Meanwhile, there was a rise in the overt development of silica-based materials in the presence of template molecules to empirically test Pauling’s theory at first and to purify certain molecules later on. Dickey<sup>42</sup> was the first to prepare silica gels in the presence of methyl-, ethyl-, propyl- or butyl orange dye. After eluting the dyes from the gels and reincubating them together in a new solution, he measured the ratio of the concentration of the dye adsorbed by the silica gel to the original concentration of the dye in the solution, i.e. the binding capacity, which he then called the “adsorption power” of the silica gel. By showing that their “adsorption powers” were greater than that of a control gel, he proved that the presence of a dye during the formation of the silica gel enhanced the latter’s adsorption properties. He went on to measure what he coined “relative adsorption power”, which was the ratio of the “adsorption power” of an adsorbent gel to that of a control gel, i.e. the formula of today’s “imprinting factor”. He found that the “relative adsorption power” of a particular gel was highest with its template dye and that it decreased dramatically with the other dyes, leading him to call these gels “specific adsorbents”. Haldeman and Emmett<sup>43</sup> observed that the aforementioned orange dyes produced the red coloration of their acid form when adsorbed by specific silica gels even at pH values where their basic forms should dominate. By studying the basic dissociation equilibria of these orange dyes, they reasoned that hydrogen bonding must be an important force of attraction between the azo group of the dye and the surface silanol group of the gel. Stereoselective silica adsorbents also became popular through the works of Curti and Colombo<sup>44</sup> who used them for the chromatographic isolation of the levo stereoisomers of camphorsulfonic acid and mandelic acid. Beckett and Anderson<sup>45</sup> prepared stereoselective adsorbents against levorphanol



and dextrorphan to determine the configurations of morphine, phenazocine and racemorphan and show that their analgesic activities resided in their levo isomers.

Molecular imprinting as we know it today dates back to the 1970s, when Wulff and Sarhan introduced organic vinyl-based polymers that simulated enzyme-driven catalysis of different reactions.<sup>46</sup> These polymers were synthesized based on covalent bonds between the template and the monomers (i.e. covalent imprinting). The use of covalent interactions for catalytic purposes would be the central theme of Wulff's group for the years to come. In 1976, Tsuchida et al. prepared for the first time poly(vinylpyridine) resin for the selective adsorption of metal ions.<sup>47</sup> In 1981, Mosbach and Arshady pioneered the use of free templates for noncovalent bonding with functional organic monomers (i.e. non covalent imprinting), which would copolymerize with crosslinkers. They described the process as "host-guest interaction" instead of "template polymerization".<sup>48</sup> The first explicit mention in literature of "imprinting" (of various molecules in highly cross-linked synthetic polymers) and "imprinted polymers" occurred in 1984 and 1985, respectively, by Mosbach and co-workers.<sup>49,50</sup> The noncovalent approach later became the most widely used approach for the synthesis of MIPs. Since then, MIPs have evolved by taking ingenious routes of fabrication, by assuming various forms (e.g. nanoparticles, nanogels, films, etc.) adapted for diverse applications such as separation science,<sup>21-24</sup> drug delivery,<sup>25-27</sup> bioimaging,<sup>28-30</sup> cosmetics,<sup>31</sup> catalysis<sup>32-34</sup> and (bio)chemical sensing.<sup>35-</sup>

37

### 2.3. Principles of molecular recognition in MIPs

The success of MIPs as molecular recognition elements heavily relies on the manner of their synthesis. As mentioned in the previous section, there are currently two main imprinting strategies, depending on the nature of the monomer-template interaction. The first approach is the so-called "covalent imprinting" which lies on covalent bonds between functional monomers and the template. In this case, a reversible reaction takes place, with bonds being stable during the synthetic step, while breaking after synthesis for template removal. Molecular recognition then occurs by re-forming those bonds between the reactive groups on the cavities and the target. While offering the advantage of relatively stable and stoichiometric interactions with the template, this "covalent" approach is unfortunately restricted to a limited number of bonds, such as for instance, boronic esters,<sup>46</sup> Schiff bases,<sup>51</sup> ketals,<sup>52</sup> esters<sup>53</sup> and disulfides,<sup>54</sup> which prevents its wide application.

The “noncovalent imprinting” on the other hand is based on noncovalent interactions between template and functional monomers such as hydrogen bonding,  $\pi$ - $\pi$  stacking, ionic interactions, van der Waals forces and metal coordination, which today accounts for the large majority of reported MIPs. Noncovalent interactions are less stable than covalent interactions, they are not stoichiometric but they form much more rapidly. Moreover, they disrupt easily by solvent competition and/or temperature change, which facilitates template extraction. A wide variety of functional monomers adapted to diverse templates is commercially available, which makes noncovalent imprinting very versatile. Figure 1.2 shows a schematic representation of the covalent and noncovalent imprinting approaches. There also exists a third, hybrid imprinting approach known as “semi-covalent” imprinting, based on a covalent imprinting step followed by noncovalent binding.<sup>55,56</sup> Despite being conceptually elegant, it is of limited applicability, as it requires the use of sacrificial spacers and polymers able to survive the often harsh template removal.<sup>57,58</sup>

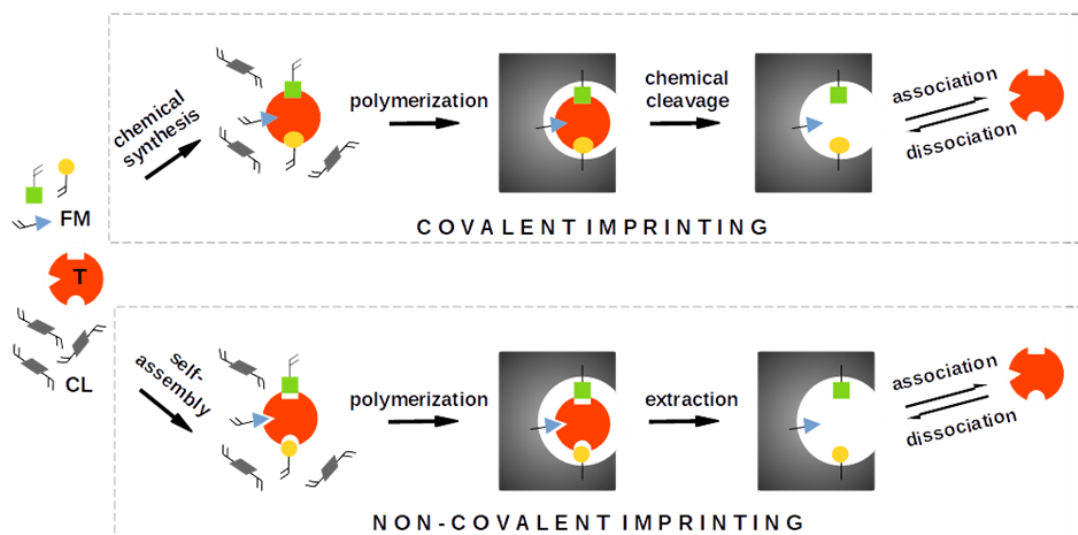


Figure 1.2. General scheme for the molecular imprinting of polymers : Functional monomers (FM) self-assemble around a template (T) to form a pre-polymerization complex which undergoes polymerization in presence of a cross-linker (CL). Upon template extraction, binding sites are made available for the template uptake.

From this point on, the discussion will concern the noncovalent molecular imprinting approach. This approach has been utilized for all the MIPs presented in this manuscript due to its advantages (straightforward nature and reversible binding events) and widespread use.

## 2.4. Components and their influence for the synthesis of MIPs

The quality of the imprinting in MIPs can be described both by the geometry of the binding sites and by the presence of functional groups on these sites that must complement the template molecule. On the same note, the binding sites must be readily accessible to the target molecules to permit the binding event to occur. Both the imprinting quality and the binding site's accessibility largely depend on the nature and the relative amount of constituents in the pre-polymerization solution. In general, these constituents are the **template molecule**, the **functional and the crosslinking monomers**, the **initiator** and the **solvent**. Together, they determine the affinity and the selectivity of the synthesized MIPs toward their target molecules for effective molecular recognition.

The *template* molecule serves as a "functional shape" against which the MIP is imprinted. It may be the actual target, a structural analog or a sub-structure of it. Virtually every chemical species can be imprinted since its functional group/s can potentially interact with the right functional monomers, forming the basis for the molecular recognition of the target molecule by the MIP. However, it has to remain inert and stable under the chosen polymerization conditions.<sup>59</sup> Nevertheless, it should be pointed out that small organic molecules generally tend to be imprinted more easily because they have less complexity in their structures, which makes them relatively stable, and because they favor the formation of well-defined binding cavities. Furthermore, their small size facilitates their removal from the polymer after the MIP synthesis. In contrast, the imprinting of large templates,<sup>59</sup> such as proteins and cells, is more challenging as they are usually unstable under common polymerization conditions, disposed to forming poorly defined binding cavities and can be expensive as high concentrations are needed for imprinting. Moreover, their large size renders their extraction from the polymer network after MIP synthesis rather difficult. A way to circumvent these challenges is the epitope approach, wherein a small fragment of a protein is instead used as a template to give rise to binding cavities that are able to recognize the whole protein itself.<sup>17,60</sup> There may also be limitations on the lower end of molecular sizes, since entities much smaller than the monomers used should be conceptually difficult to imprint.

The most defining characteristic of *functional monomers* is their chemical groups which interact noncovalently with the template. For example, monomers bearing acidic moieties are chosen for the synthesis of MIPs against templates containing basic groups. Common examples of acidic functional monomers include methacrylic acid and acrylic acid. Conversely, basic monomers, such as vinylpyridine, are selected to target acidic moieties on the template. Other monomers enhance complex association by bringing hydrogen bonding and other noncovalent forces like coordination

bonds. Monomers with aromatic groups such as styrene can participate in a  $\pi$ - $\pi$  stacking with an aromatic template. In fact, the strength of the interaction between the functional monomers and the template positively influences the selectivity of the resulting MIP for the target.<sup>59</sup> This interaction results in the formation of a template-monomer complex, which is an equilibrium process. The functional monomers are therefore often added in molar excess compared to the template in order to shift the equilibrium to the complex-formation side.<sup>61</sup> However, caution must be observed since an surplus of functional monomers leads to non-specific binding sites on the MIPs caused by their functional monomer residues being outside of distinct imprinted sites. Likewise, it may result in self-aggregation of the monomers, which reduces the selective binding of the MIP.<sup>62</sup> Historically, the molar ratio of the functional monomers to the template has typically been set at 1:4. Finally, a functional monomer must contain a functional group that will allow it to participate in the designated polymerization reaction (e.g. a vinyl group for a free radical polymerization reaction). Some of the commonly used functional monomers are shown in Figure 1.3.

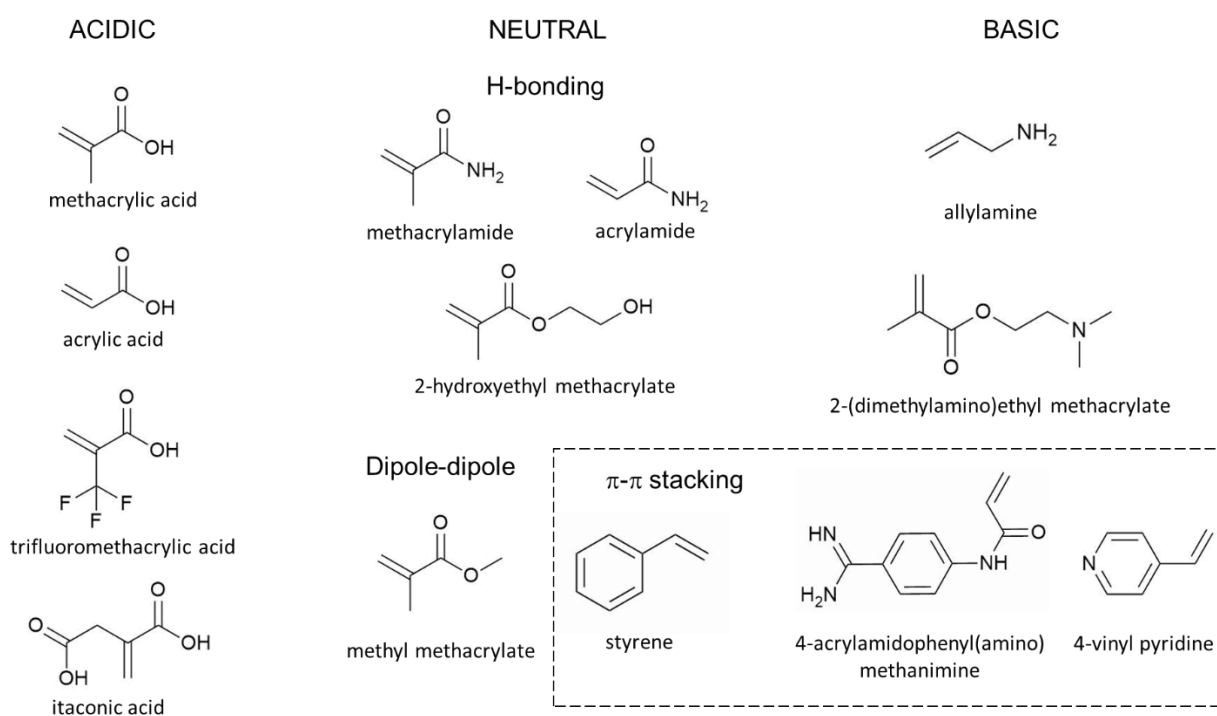


Figure 1.3. Chemical structures of some functional monomers commonly used in the synthesis of MIPs. The functional monomers are grouped here according to their acidic, neutral and basic properties. Under the neutral group, the monomers are further classified as able to form H-bond, dipole-dipole interaction or  $\pi$ - $\pi$  stacking (4-acrylamidophenyl(amino)methanimine and 4-vinyl pyridine) with a template.

*Cross-linkers* (CLs) are polyfunctional (at least bi-functional) monomers responsible for connecting polymer chains to one another in order to form a network. In the synthesis of MIP,

crosslinkers play three important roles: a) they control polymer morphology (e.g. gel-type, macroporous, microgel powder) (Figure 1. 4), b) they provide mechanical stability, and (c) they preserve the structural integrity of the binding cavities of the MIP.<sup>59,62,63</sup> Representing most often the major constituent of MIPs, cross-linkers have an immediate effect on the physical and the chemical properties of the polymer matrix. Ethylene glycol dimethacrylate (EGDMA), which is by far the most widely used CL, is known to promote mechanical and thermal stability, as well as good wettability to the resulting MIP.<sup>61</sup> In fact, its tandem with the functional monomer MAA is the most commonly used polymer system in molecular imprinting.<sup>64</sup> During polymerization, crosslinkers “freeze” the functional monomers around the template molecule and thereby, grant stability to the binding cavities of the MIP even after template removal. For example, EGDMA often represent at least 50% of the total monomers in a pre-polymerization solution.<sup>65</sup> Insufficient cross-linking leads to reduced recognition ability because the cavities cannot sustain itself structurally. On the other hand, higher cross-linking promotes higher selectivity in MIPs. However, an excessive amount of cross-linker means a decrease in the amount of the functional monomer per unit mass, which translates to a reduction in the number of recognition sites per unit of mass. It also results in a more difficult extraction of the template and may hinder rebinding. Aside from EGDMA, other common examples of cross-linkers are divinylbenzene (DVB), trimethylolpropane trimethacrylate (TRIM) and N,N'-methylenebisacrylamide (MBAA) (Figure 1.5).<sup>59,62</sup>

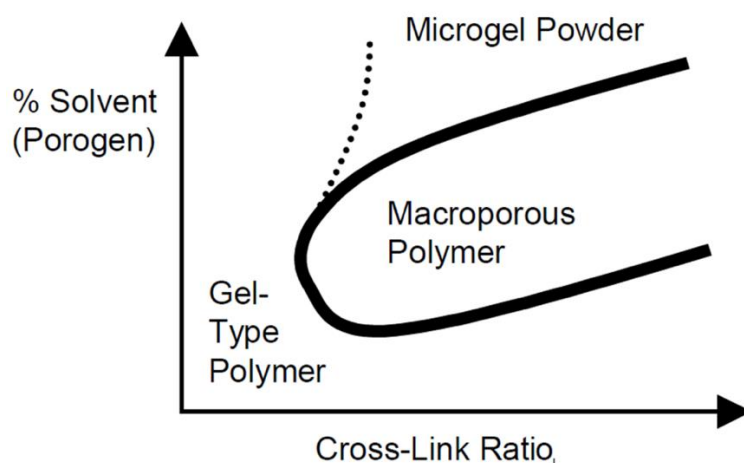


Figure 1. 4. A pseudo-phase diagram serving as a general guide on the influence of relative amounts of the cross-linker and of the solvent on the morphology of the synthesized MIP. Reprinted with permission from Elsevier B.V.<sup>63</sup>

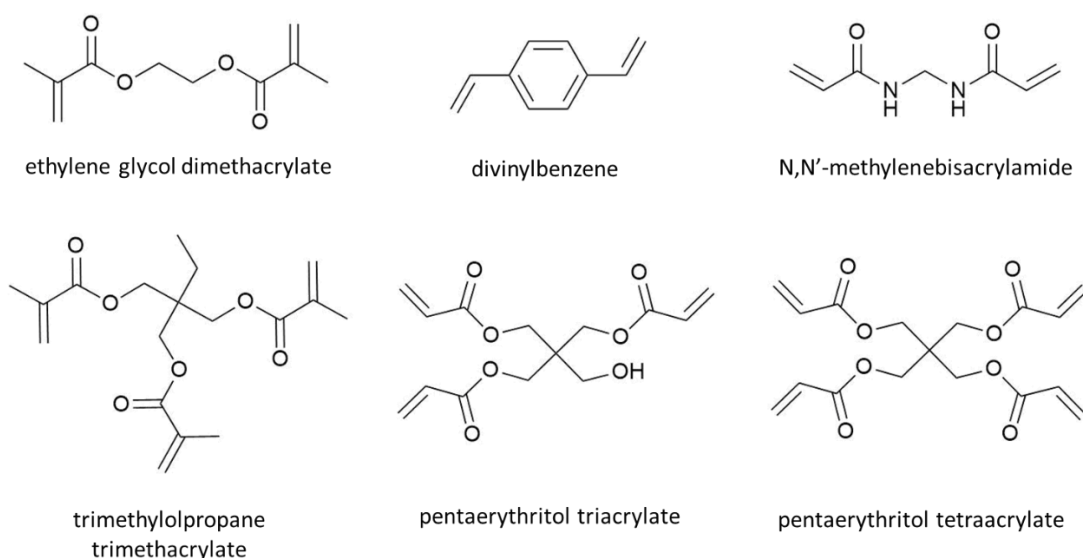


Figure 1.5. Chemical structures of some cross-linkers commonly used in the synthesis of MIPs.

Another important component of the pre-polymerization solution is the *initiator*. The initiator is a species that upon exposure to a suitable stimulus (e.g. heat, light, chemical/electrochemical reaction), generates other species capable of starting the polymerization reaction. Among the most common radical initiators for the synthesis of MIPs are 2,2'-azobisisobutyronitrile (AIBN), which can be either thermo- or photo-activated, and benzoyl peroxide, which is thermo-activated. The subject of initiators will be discussed more in depth in sections 2.6 and 3.

Finally, the *solvent* is in charge of (1) dissolving the components of the pre-polymerization solution (2) maximizing the interaction between template and functional monomer(s) and (3) helping driving the polymerization toward the aimed polymer format. Solubility permitting, aprotic and low-polarity organic solvents such as chloroform and toluene are preferred in order to favor hydrogen bond or strong polar interaction between the template and the functional monomers.<sup>59</sup> In that context, acetonitrile seems to be a good compromise, being a polar though aprotic solvent. In the case of problems of dissolving the template or other components, more polar solvent may be utilized such as dimethyl sulfoxide (DMSO) and dimethyl formamide (DMF).<sup>66</sup> Nevertheless, protic polar solvents and mixtures may also be used (e.g. acetonitrile/water, methanol/water), particularly when the template-monomer interactions are rather strong and/or involve hydrophobic forces.<sup>67</sup> In addition to solvating the constituents, the solvent also exerts influence on the morphology of the MIP especially on its specific surface area and pore diameter.<sup>61</sup> The solvent is also referred to as the “porogen” since it creates pores for macroporous MIPs. Pores are important to facilitate the diffusion of the template

molecules out of the MIP and the diffusion of the target into the inner recesses of the MIP during binding, as well as its exit when it is eluted. Without pores, the binding cavities found in the inner parts of the MIPs remain unavailable for molecular recognition, decreasing the MIP efficiency. Using a thermodynamically good solvent brings about the formation of high-surface area MIPs with well-defined pores. Conversely, a thermodynamically poor solvent produces low-surface area MIPs with poorly developed pores. An increase in the pore volume of the MIP can be achieved by an increase in the volume of the solvent in the pre-polymerization solution.<sup>63</sup> Large variations in the solvent volume, however, allow for the synthesis of MIPs in their various forms, which will be discussed in the following paragraphs. Lastly, the recognition performance of the MIPs is generally optimal when the binding is executed in the same solvent as the one used for imprinting.<sup>67</sup>

## 2.5. Conventional methods for preparing MIPs

There are several traditional methods available for synthesizing MIPs according to the desired physical form and the intended application. In general, the various ingredients are placed in contact with one another in a solvent, making sure that everything is dissolved. If free-radical polymerization is used to synthesize the MIPs, the solution is subjected to preliminary deoxygenation. The polymerization reaction is then induced by exposure to heat, light, a redox reaction or electric current. After the reaction, the MIP may undergo various post-polymerization treatment steps, depending on the technique used to prepare them. However, they all require the extraction of the template molecule from the MIP, usually *via* several washing steps. Once dried, the MIP is now available for recognizing the target molecule in a liquid or gaseous medium.

Traditionally, the simplest method for preparing MIPs is *bulk polymerization*, which produces MIPs in the form of monoliths. This is achieved by preparing a pre-polymerization solution that contains little to no solvent (typically 50%) and hence, is highly concentrated in terms of the template and the monomers. The cross-linked polymer forms a macroporous network if it is insoluble in the solvent and forms a microgel if it interacts sufficiently with it. The popularity of bulk polymerization stems from the simplicity of the setup as a one-pot reaction; however, the monoliths produced require several post-polymerization treatment steps that are tedious and time-consuming such as crushing, grinding and sieving of the particles with appropriate sizes. These particles often have irregular shapes and sizes, usually in the micrometer range. The treatment can also destroy some of the binding cavities of the MIP particles, which reduces their loading capacity.<sup>59,62,67</sup> Furthermore, this method encounters difficulties in upscaling for large-scale productions.

An alternative to bulk polymerization is the *precipitation polymerization*. The outstanding difference between the two methods is that a rather large volume of the solvent is used in precipitation polymerization. Under these conditions, polymer chains continue to grow in the solution during the reaction until they reach a certain critical mass and precipitate in the solvent if they are insoluble. Otherwise, they form a microgel (a fully solvated cross-linked network).<sup>59</sup> This allows for the formation of spherical MIP micro and nanoparticles with uniform size. The MIP particles are then recovered by centrifugation or filtration. Although it requires a higher amount of solvent and of template, precipitation polymerization is easier and favorable for controlling the size of the MIP particles. Because of the large volume of the solvent used, the solution is much less viscous and so the heat coming from the polymerization reaction is more dissipated, allowing for potential industrial upscaling of the method.<sup>68</sup> The reaction may take longer due to the dilute concentrations of the monomers; however, a significant amount of time is saved due to the absence of post-polymerization steps such as crushing, grinding and sieving.<sup>68</sup>

Another method of synthesizing MIPs is by *suspension polymerization*, which is a heterogeneous process. Here, the various components of the pre-polymerization mixture are first dissolved in a solvent and is then suspended (dispersed phase) in an immiscible continuous phase such as water, mineral oil or perfluorocarbon in the presence of a stabilizer. A stabilizer is responsible for increasing the viscosity of the continuous phase so that upon vigorous stirring of the system, droplets may form and remain suspended. The polymerization reaction is then induced.<sup>59</sup> This method produces spherical MIP particles, whose sizes can be modulated by changing the rate of stirring.<sup>69,70</sup> Moreover, it favors the formation of porous MIPs, efficiently dissipates the heat coming from polymerization and is scalable for commercial purposes. Nevertheless, the presence of water and the stabilizer can alter the noncovalent interactions between the template and the functional monomers. The stabilizer may also be seen as an impurity from the viewpoint of molecular imprinting.<sup>70</sup> This potentially weakens the specificity of the MIP for the target. However, it has also been shown with a polycarbonate-based spiral microflow reactor that using mineral oil as the continuous phase without any stabilizer yielded monodisperse MIP beads.<sup>71</sup>

*Emulsion polymerization* resembles suspension polymerization in that it also involves two initially immiscible phases: the template and monomers mixture (dispersed phase) and the continuous phase, which is commonly water. The rest, however, is different. For one, emulsion polymerization does not rely on vigorous stirring for the formation of droplets. Instead, the two phases are mixed with one another through the aid of an emulsifying agent, a surfactant. This leads to the formation of small micelles (diameters = 0.1 to 1  $\mu\text{m}$ ) that contain the template and the monomers. If the



continuous phase is water, a water-soluble initiator is then used to start the polymerization reaction. Polymerization occurs within the micelles, which prevents the viscosity of the reaction mixture from increasing. Emulsion polymerization permits the synthesis of MIPs with high homogeneity and uniformity in particle size in the nanometer range.<sup>68</sup> Inverse emulsion polymerization also exists and is used when a hydrophilic template and hydrophilic monomers are emulsified in a low polar continuous phase. Hydrophilic polymer particles with sizes as small as 50 nm are usually obtained.<sup>72</sup>

The polymerization reaction involved in the conventional methods for preparing MIPs listed above, as well as in various alternative techniques, may be triggered by electric current, redox reaction, heat or by light. The next section discusses the different ways of inducing the polymerization of MIPs. Special emphasis is given on photopolymerization. In fact, photopolymerization itself opened new routes for preparing MIPs. Some of these routes made it possible to construct arbitrary structural hierarchies of MIPs, which is central to the subject of this thesis.

## 2.6. Approaches for triggering the polymerization of MIPs

An important aspect to consider when synthesizing a MIP is the way of triggering its polymerization, as this choice affects the reaction conditions and thus the resulting MIP properties. Except for silica-based MIPs made by sol-gel chemistry (i.e. by hydrolysis-polycondensation), imprinted polymers are usually synthesized by electrochemically, thermally, photochemically or redox-initiated chain-reaction. *Electropolymerization* of electroactive monomers such as pyrrole, aniline or dopamine is a technique based on a redox process or a potential sweep<sup>73</sup> which is especially suited for depositing polymer films directly on electrodes for electrochemical sensors, since it allows controlling the rate of polymer growth, film thickness and film morphology. Unfortunately, this technique is limited to a restricted number of functional monomers, which in turn limits the functionalities available for molecular imprinting. *Redox-initiated* radical polymerization is also used for MIPs synthesis, and thanks to its ability to generate radicals under mild conditions, it is especially suited for the imprinting of proteins<sup>74</sup> or peptides<sup>75</sup> in aqueous *media*.

Conversely to electrochemical and redox polymerization, *thermal polymerizations* use thermal initiators to generate radicals and initiate the polymerization. Mostly based on azobis- or peroxy-derivatives,<sup>76,77</sup> such initiators cover a large range of temperatures thanks to the possibility of modulating their half-lives at a given temperature with changes in their chemical structure. Thermal

polymerization accounts for a great majority of (meth)acrylic and styrenic MIPs, with reaction temperatures usually spanning from room temperature to roughly 60°C.

*Photopolymerization* is another very common technique for MIPs, wherein radicals are generated upon photo-induced or photo-promoted dissociation of suitable initiating species. This approach has over the recent years gained much importance and is today often the method of choice. *So why photopolymerization?* There are two main reasons: *Firstly*, since light is directly responsible for radical generation, the temperature can be set to low values, which protects temperature-sensitive, noncovalent interactions between template and functional monomers, thus improving the imprinting efficiency and the MIP's affinity for its target.<sup>78</sup> Also, the use of low temperatures (e.g. 0°C to 20°C)<sup>79,80</sup> is preferred to avoid degradation of sensitive analytes such as proteins<sup>81</sup> and in some cases, to suppress undesired side reactions.<sup>82</sup>

*Secondly*, owing to their nature, photochemical processes allow spatiotemporal and intensity control over the polymerization reaction. By simply turning on or off the light source, the radical generation can instantaneously be “switched on” or “off” in a much more efficient way compared to the other approaches such as thermal polymerization. This is especially useful in photo-induced controlled radical polymerizations, officially referred to as reversible-deactivation radical polymerizations (RDRP), wherein the molecular weight of growing polymers directly relates to monomer conversion<sup>83</sup> and can thus be controlled by the irradiation time. RDRPs are well-established in the imprinting field thanks to their ability to easily chain-extend with consecutive blocks and to inherently boost the binding properties of MIPs compared to free radical polymerization (FRP).<sup>55,84–86</sup>

Light can also be confined into limited volumes to arbitrarily initiate localized polymerizations in restricted regions, as seen in various photolithographic and 3D printing techniques (i.e. spatial control). Adjusting the wavelength and the intensity of light sources allows the manipulation of the polymerization rate *via* controlling the number of generated radicals, similarly to varying the temperature in a thermal polymerization.<sup>83,87</sup> All these features, which also include relatively low costs and availability of a range of light sources (i.e. lamps, LED, lasers, UV plasma sources, sunlight),<sup>87,88</sup> make photopolymerization a convenient strategy for precise, hierarchical structuring and even automation in the design and fabrication of MIPs.

### 3. Photopolymerization of MIPs

#### 3.1. Introduction to photopolymerization

Photoinitiation is a process wherein a light-sensitive molecular system (called a photoinitiator) achieves, upon absorption of a suitable photon, an excited state that leads to a reactive species capable of initiating the polymerization of monomers (i.e. photopolymerization).<sup>89,90</sup> Depending on the nature of the photogenerated reactive species and on the chosen monomers, the polymerization can follow radical, cationic or anionic acid/base growing mechanism. If this variety provides the user with a wide choice of experimental setups, the reader should be aware that not all previously mentioned techniques are suited to the synthesis of MIPs. Indeed, in order to promote a strong interaction between the template and the functional monomers, the photoinitiating system should not interfere with them. If this can normally be controlled by formulating the photoinitiator in low molar amounts, this requirement can also be met by selecting initiating species that show poor reactivity toward common chemical functionalities in both their fundamental and excited state. Among the cited polymerization pathways (i.e. radical, cationic or anionic), the radical mechanism exhibits the best compatibility with the chemical functionalities borne by the different components of a MIP pre-polymerization mixture, which can be rather complex. Thus, over the years, radical polymerization has become the most viable solution for MIPs, due to its tolerance for many common functional groups as well as to the commercial availability of a wide range of (meth)acrylic and styrenic monomers.<sup>91,92</sup>

Radical polymerization reactions in general proceed in three main steps: (1) initiation, (2) propagation and (3) termination. In photopolymerization, initiation occurs when upon irradiation, a light-sensitive molecule known as the photoinitiator decomposes into reactive radicals. From the physico-chemical point of view, free radical photoinitiators are divided into two main categories: Type I and Type II photoinitiators. Type I photoinitiators undergo unimolecular homolytic bond cleavage upon excitation, to generate radicals (Figure 1.6A). They vary considerably in structure but prominent examples are aromatic carbonyl compounds such as acetophenone derivatives, benzoin derivatives, benzylketals, hydroxyalkylphenones and acyl (TPO) and diacyl (BAPO) phosphines.<sup>76,93</sup> Azoinitiators, notably AIBN, can also act as photoinitiators beyond being thermal initiators. From a general standpoint, ideal Type I photoinitiators should: (1) feature a high extinction coefficient at the selected (irradiation) wavelength to efficiently generate excited states (singlets), (2) provide a high internal conversion from singlets to (dissociative) triplet states, which in turn afford radicals by bond scission and (3) generate highly reactive radicals capable of triggering the polymerization of monomers.<sup>77,89,94</sup>

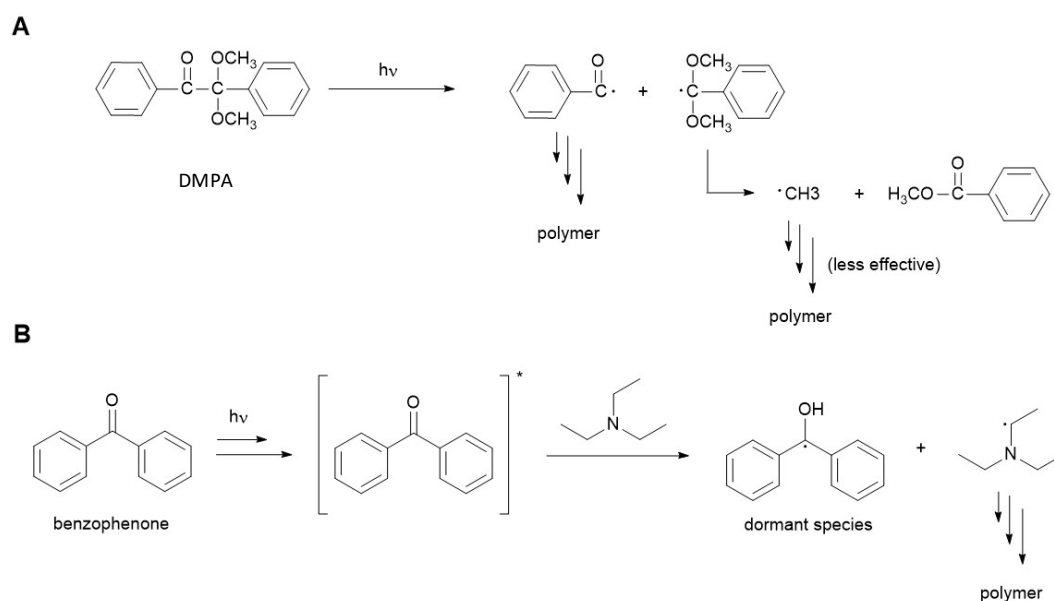


Figure 1.6. The initiating mechanism of a representative (A) Type I photoinitiator (dimethoxy-2-phenylacetophenone, DMPA) and (B) Type II photoinitiator. Figure 1.6(B) reprinted with permission from Wiley-VCH Verlag GmbH & Co. KGaA.<sup>95</sup>

Type II photoinitiators on the other hand, do not undergo bond cleavage; instead, they get excited to a triplet state and proceed to hydrogen abstraction from a donor (also known as a co-initiator, usually an alcohol or amine) thus generating an initiating radical (Figure 1.6B). Since this process involves a bimolecular reaction, Type II activation occurs more slowly than Type I activation and their efficiency is diffusion-controlled. Camphorquinones, benzophenones, thioxanthenes and many visible-light-activated initiators are representative examples of this second category.<sup>77,96,97</sup> One of the advantages of these systems is to allow extending the wavelength range by the choice of the suitable photosensitizer from the near UV up to the near infrared (NIR) (300 nm - 1064 nm).<sup>98-101</sup> On the other hand, the need for one, or more, coinitiators makes Type II photoinitiating systems less suitable than Type I for MIPs. Indeed, the increased number of chemicals required for a Type II photoinitiation, may interfere with the self-assembly process between template and functional monomer(s). A list of Type I and Type II photoinitiators widely used for radical polymerization, together with their excitation wavelengths, has recently been published by Lalevée and coworkers.<sup>88</sup>

After initiation, propagation happens by the addition of monomers to the radical center. Termination of the polymerization occurs when a macroradical reacts with a primary radical (radical formed directly from the initiator) which happens at high photoinitiator concentration or high light intensity conditions, or when a macroradical reacts with another macroradical which is the dominant mode of termination.<sup>102</sup> As a polymerization mechanism, however, FRP offers little control due to side

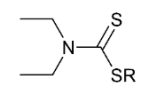
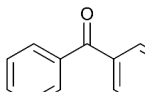
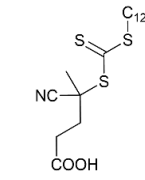
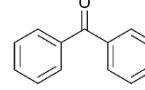
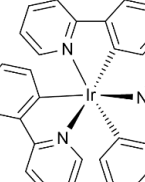
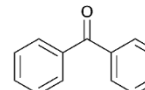
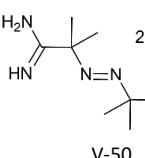
reactions such as undesired biradical terminations and chain transfers which compete with the propagation step. Unfortunately, this leads to dead polymer chains of largely varying molecular weights. It does not exactly reflect the temporal control that photopolymerization offers since propagation and termination are thermal reactions that continue to persist with or without light until the supply of radical centers become consumed or depleted.<sup>55,83</sup>

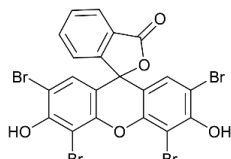
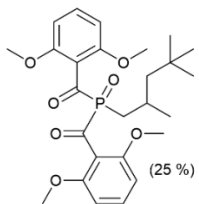
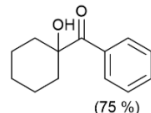
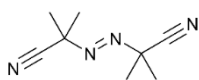
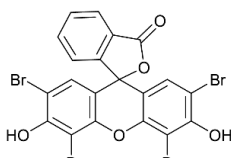
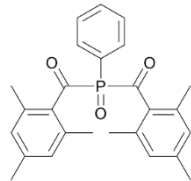
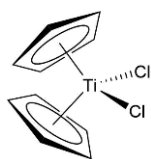
As previously mentioned, photopolymerization is an attractive technique for the synthesis of MIPs, and recent years have shown an increasing interest in exploring different controlled photopolymerization mechanisms (Table 1.1). Despite that, free-radical polymerization continues to be the most widely used polymerization approach to MIPs.<sup>91</sup> Its regular setup includes a light source, a photoinitiator and a solution of template and monomers. Light sources can be lamps, LEDs or lasers that emit at specific wavelengths in the UV or the visible range depending on the activation wavelength of the initiator.

While UV light remains a mainstay because many organic species generate radicals upon UV absorption, it also requires caution as absorption by the template and/or functional monomers may result in template degradation and/or monomer self-initiation.<sup>103,104</sup> For this reason, visible light has recently risen as an interesting alternative: applying initiators that specifically absorb in the visible spectrum allows to preserve sensitive molecules in solution by specifically triggering a single chemical species. This applies to conventional as well as to controlled radical polymerization, with the latter recently drawing great attention due to the possibility of easily tuning the polymer's features as detailed for instance by Johnson and co-workers.<sup>83</sup>

A promising alternative to FRP and its drawbacks is the controlled/living polymerization (CRP) whose mechanism leads to the synthesis of polymers possessing isotropic properties such as low polydispersity index, predictable molecular structure and homogeneous polymer networks, all of which have been shown to improve MIP target binding performance.<sup>91,104–107</sup> Furthermore, it allows the insertion of functional groups and structures within polymer chains and the extension of a polymeric chain thereby grants almost unlimited control of the composition, architecture and functionality of polymers.<sup>55,108</sup> In reality, CRP refers to a family of polymerization reactions that are characterized by a fast and reversible activation and deactivation of reactive species for better control of polymeric chain growth.<sup>86</sup> The most popular are the atom transfer radical polymerization (ATRP), the reversible addition-fragmentation chain-transfer (RAFT) polymerization and the stable free radical polymerization (SFRP) to which belongs the use of photoiniferters. ATRP involves the redox reaction between an initiator (or dormant species) in the form of an alkyl halide and a low-oxidation-state

Table 1.1. Non-exhaustive list of recent examples (from 2013 to 2018) of MIPs synthesized via photopolymerization.

Mechanism of Polymerization	Initiator	Initiator type	Light Source (nm)	Monomer Composition	Template	Solvent	Use	Ref
RDRP: SFRP	 grafted DEDTC (iniferter)	I	UV (365)	DEAEM, MBAAm	BSA	Ultrapure water	Surface film	106
FRP	 benzophenone (TEA as hydrogen donor)	II	NIR (980) upconverted to VIS (405)	MAA, EGDMA	Enrofloxacin	DCM	Core-shell nanoparticles	109
RDRP: RAFT	 CDTPA (iniferter)	I	VIS (435 or 525)	MAA, EGDMA	Testosterone	Acetonitrile	Microspheres	104
FRP	 benzophenone (ethanol as hydrogen donor)	II	UV (365)	Itaconic acid, EGDMA	Ciprofloxacin	EtOH/ deionized water	Surface film	110
RDRP: ATRP	 <i>fac</i> -[Ir(ppy) <sub>3</sub> ] (catalyst excited by UV to reduce the initiator ethyl $\alpha$ -bromophenylacetate)	II	UV (365)	MAA, EGDMA	(a) Testosterone, (b) S-propranolol	(a) Toluene, (b) acetonitrile	Monoliths, films, nanoparticles	107
FRP	 benzophenone (grafted DMA as hydrogen donor)	II	UV (365)	MMA, EGDMA	Melamine	DMSO	Surface film	111
FRP	(self-initiating monomers)	-	UV (312)	(a) AB, HEMA, EBAAm, (b) MAA or 4-VP, EGDMA or DVB	(a) Trypsin, (b) S-propranolol, 2,4-D, testosterone	(a) Sodium phosphate buffer, (b) acetonitrile or MeOH/ water	(a) Suspension, (b) bulk	112
FRP	 V-50	I	UV (365) via fluorescence microscope	Cyclodextrins, AAm, MBAA	Bisphenol-A	Deionized water	Microhydrogels for microvalves	113

Mechanism of Polymerization	Initiator	Initiator type	Light Source (nm)	Monomer Composition	Template	Solvent	Use	Ref
FRP	 Eosin Y (TEA as hydrogen donor)	II	NIR (980) upconverted to VIS (530)	HEMA, EbAAm, AB-HCl	Trypsin	DMSO/ toluene	Core-shell NP	95
FRP	 (25%)  (75%) Irgacure 1800	I	UV (<400)	MAA, EGDMA	Atrazine	DCM	SPE sorbent	114
RDRP	 AIBN, TED as chain transfer agent	I	UV (~320-400)	DEAEM, HEMA, PEG200DMA	Diclofenac sodium	-	Gel	91
FRP	 Eosin Y (MDEA as hydrogen donor)	II	VIS (532)	MAA	Rhodamine 123	ACN/DMSO	Sub-micron patterns	103
FRP	 Bis(2,4,6-trimethylbenzoyl)phenyl phosphine oxide	I	UV (375)	MAA, 4-VP, EGDMA, PETA	Z-L-Phe	Tetraglyme	Microstructure	115
FRP	 Bis(cyclopentadienyl)titanium dichloride	I	VIS (532 nm)	MAA, PETA	Testosterone	Triglyme	Hologram film	116

state transition metal-ligand complex (catalyst or activator) via halogen-atom transfer.<sup>117</sup> The reaction oxidizes the complex and forms an active radical species from the initiator. Monomer units add to the alkyl radical until the oxidized complex deactivates it to reform the dormant alkyl halide and the activator complex. A series of activation/deactivation steps results in the uniform growth of the polymer. ATRP in general is inherently incompatible with acidic monomers such as MAA and requires a high concentration of the metal complex to keep the polymerization rate and avoid unwanted biradical termination events,<sup>83,92,107</sup> which can sometimes be problematic for the synthesis of a MIP. The most suitable CRP reaction for molecular imprinting is RAFT polymerization, owing to the fact that it can be applied to a wide range of monomers. Another advantage is that its main transfer agents — the dithiocarbonyl compounds — and their dormant versions are inert to polar and ionic moieties.<sup>118</sup> RAFT polymerization features the use of chain transfer agents that are mainly dithioesters, dithiocarbamates, trithiocarbonates and xanthates. At the onset of the reaction, the radicals generated from the initiator rapidly react with the RAFT agent due to the latter's higher reactivity than a regular vinyl monomer. The weakest C-S bond of the resulting stabilized radical species is homolytically broken to yield a different radical which then reacts with monomers. This propagating radical remains in an equilibrium of degenerative chain transfer with the reacted RAFT agent. This equilibrium slows down the polymerization rate and grants "living" character to the technique although a small amount of dead polymers is produced since all radical species emanating directly from the initiator terminally react with one another.<sup>55,83,92</sup> When it comes to SFRPs, the use of photoiniferters is deemed the most suitable for the synthesis of MIPs due to its compatibility with most functional groups despite their slight tendency to dimerize and release CS<sub>2</sub> when decomposed. Photoiniferters are thio compounds (i.e. dithiocarbamates, thiocarbonylthio, trithiocarbonates and disulfides)<sup>119</sup> that act as *initiators*, *transfer* agent and *terminators* simultaneously, hence the name. Upon irradiation of the right wavelength, they decompose into an active radical and an inactive one. The active radical is responsible for the initiation of the polymerization while the inactive one serves as the capping agent for propagating radicals, producing dormant species. The polymerization is controlled and retains a "living" character by the equilibrium between the active and dormant species.<sup>55,83,84,120</sup>

The use of catalysts allowing for photo-electron transfer (PET) processes, as reported for instance by Hawker and co-workers,<sup>121–123</sup> and Boyer and co-workers,<sup>124–128</sup> has considerably helped the application of longer wavelengths in photo-controlled polymerization. During PET, light absorption causes a photo-redox catalyst to enter an excited state, which allows oxidizing or reducing a photoinitiator that in turn forms a radical able to start the polymerization.<sup>129,130</sup> The first successful attempt to control polymerization by means of activation/deactivation cycles mediated by blue light



was reported by Fors and Hawker who used *fac*-[Ir(ppy)<sub>3</sub>] as a catalyst for the atom transfer radical polymerization (ATRP) of methyl methacrylate (MMA), with ethyl- $\alpha$ -bromophenylacetate as an initiator.<sup>121</sup> Subsequently, Boyer and his team used *fac*-[Ir(ppy)<sub>3</sub>] as PET catalyst to thiocarbonyl compounds and thus to reversible addition-fragmentation chain-transfer (RAFT) polymerization.<sup>124,128</sup> Different kinds of catalysts have so far been applied to PET-RAFT polymerization, which have progressively allowed moving from blue to green<sup>131</sup> and red light (e.g. zinc porphyrins<sup>125</sup>) and up to the near-infrared (NIR) light thanks to the use of some pigments such as bacteriochlorophylls.<sup>126</sup>

NIR is particularly interesting for *in vivo* applications, as it is known to deeply penetrate biological tissues<sup>132,133</sup> thanks to the so called “biological window”,<sup>134</sup> which preserves cells from photodamage and holds great promise for *in vivo* polymerizations.<sup>96</sup> NIR photopolymers have been initially developed for graphic industry<sup>135</sup> and holography.<sup>136</sup> The recent interest for NIR photopolymer systems is due to the potential applications in the field of in-depth photocuring.<sup>137,138</sup> Indeed, as light penetration is higher in the NIR region than in the UV, NIR appears as a good solution to improve the penetration depth and polymerization of thick objects and composites. Other examples of photopolymerization and photostructuring using NIR lights have also been proposed.<sup>139–141</sup> Typical photoinitiator systems contain an NIR dye and a co-initiator. Carbocyanines (Indocyanine Green) associated to amines have shown their efficiency for polymerization in the 780-850 nm range. Indeed, due to its low energy content, NIR cannot excite a Type I photoinitiators upon a single absorption, conversely to UV or visible light.<sup>142</sup>

NIR can also trigger photopolymerization through two-photon absorption, where the simultaneous absorption of two photons allows matching the energy associated with a single UV or visible photon. This phenomenon, similar to photon “upconversion” in the field of fluorescence, thus allows triggering conventional UV or visible photoinitiators *via* NIR excitation. From the chemical point of view, multiple photon absorption can occur directly on suitable photoinitiators, such as Type I Lucirin TPO<sup>143</sup> and Type II 7-diethylamino-3-thenoylcoumarin,<sup>144</sup> or be mediated by exogenous species absorbing multiple NIR photons and returning this energy as UV or visible radiation, like upconverting phosphors.<sup>70</sup> A compelling example of photopolymerization mediated by NIR light was reported by Torgensen et al. who photopolymerized *via* two-photon polymerization a hydrogel which partially trapped the roundworm *Caenorhabditis elegans* as a model living organism.<sup>145</sup> *C. elegans* kept moving during the photopolymerization, while a short segment of its body was progressively immobilized into the growing hydrogel. This remarkable result proved that it was possible to drive a photopolymerization with NIR light in the presence of and through a living sample. The application of

two-photon polymerization to the synthesis and structuring of MIPs will be discussed later in this chapter.

### 3.2. UV mediated photopolymerization of MIPs

The majority of photopolymerized MIPs have been prepared by conventional UV-A photopolymerization (i.e. wavelength around 365 nm), as many photoinitiators are active in this region, while monomers such as acrylates absorb weakly and are therefore relatively stable.<sup>146</sup>

The recent years have seen the use of UV photopolymerization for the ingenious fabrication of MIPs that transcended microspheres and monoliths. For example, Shiraki and co-workers photopolymerized cylindrical MIP microhydrogels into microchannels by projecting 365-nm UV light through a fluorescence microscope into an aqueous solution of cyclodextrin and N,N'-methylenebisacrylamide (MBAAm) monomers with the initiator 2,2'-azobis(2-methylpropionamide) (V-50). Upon recognizing its target bisphenol-A (BPA), the MIP microhydrogel contracted and served as a self-regulating microvalve to allow automatic flow control as a function of the concentration of BPA.<sup>113</sup> There are also examples wherein common photoinitiators are synthesized as aryl diazonium salts for electrografting on gold electrodes. Using this approach, Khlifi et al.<sup>147</sup> and Gam-Derrouich et al.<sup>148</sup> were able to produce melamine and dopamine-imprinted MIP sensors via electrografting of the photoinitiator and subsequent surface-initiated polymerization. Upon immersing the electrode in a pre-polymerization mixture including the template, methacrylic acid (MAA) as a functional monomer, ethylene glycol dimethacrylate (EGDMA) as a cross-linker and a mixture of methanol-chloroform as solvent, they achieved a rapid and facile grafting of MIPs onto the gold surface by exposure to 365-nm UV light.

Another example was reported by Ton et al. who used a conventional telecommunication optical fiber to direct a 375-nm UV laser beam into a drop of a precursor solution suspended at the end of the fiber. This resulted in the formation of a MIP microtip directly interfaced with the optical fiber (Figure 1.7). This sensor allowed detecting the fluorescent target dansyl-phenylalanine based on a bifurcated setup allowing for separate excitation and detection, and also the non-fluorescent target 2,4-dichlorophenoxyacetic acid when a fluorescent reporter monomer was included into the MIP.<sup>115</sup> It should be mentioned here that UV light of shorter wavelengths (e.g. 312-nm) has been shown to self-initiate the polymerization of acrylic monomers,<sup>146</sup> which allows for the initiator-free synthesis of MIPs, as reported for instance by Panagiotopoulou et al. These monomers achieve a triplet state upon

UV absorption ( $\leq 312$  nm), which leads to either biradical formation or hydrogen abstraction.<sup>112,149</sup> Similar to thermal polymerization, UV photopolymerization has also been used for conventional MIP formats such as microparticles,<sup>150</sup> films<sup>110,111</sup> and membranes.<sup>151</sup>

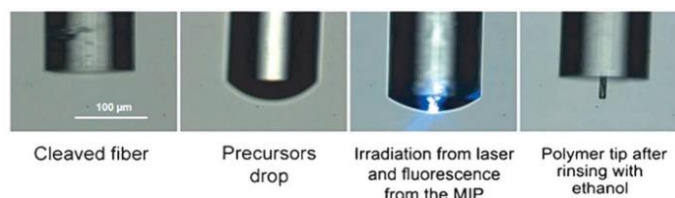


Figure 1.7. The fabrication process of an imprinted microtip by guiding UV through an optical fiber to the MIP precursor drop. Reprinted with permission from Wiley-VCH Verlag GmbH & Co.<sup>115</sup>

UV-A photopolymerization of MIPs can also proceed *via* controlled radical polymerization. As mentioned above, controlled radical polymerization allows controlling the molecular weight of growing species *via* the extent of monomer conversion, while simultaneously ensuring low polydispersity on polymer chains (i.e.  $< 1.3$ ). Another advantage of this technique is the easy access to block copolymers *via* chain-extension of polymers, which behave as macro-initiators. Controlled radical polymerization has also been applied to the synthesis of MIPs, often resulting in improved binding capacity and binding affinity compared to classical FRP. Nevertheless, its main advantage over FRP is the chain-extension capability, which allows tuning the chemistry and reactivity of the MIP surface.<sup>55</sup>

As mentioned above, a common example of controlled radical polymerization is iniferter polymerization. Photoiniferter was the first controlled polymerization technique applied to the synthesis of MIPs in 1997 by Wang et al.<sup>55</sup> A great majority of photoiniferters used for MIPs rely on benzyl-derived dithiocarbamates and require an excitation near 365 nm.<sup>120,152–155</sup> For instance, the iniferter diethyldithiocarbamate (DEDTC) was exploited by Kidakova et al. to control the thickness of MIP growth in combination with microcontact printing for the imprinting of bovine serum albumin (BSA). A chlorinated diazonium salt was electrochemically reduced onto a gold substrate for grafting DEDTC on the surface. Meanwhile, BSA was immobilized on a separate glass slide via an epoxy-silane linker. An aqueous precursor solution consisting of 2-(diethylamino)ethylmethacrylate (DEAEM) and MBAAm was sandwiched between the DEDTC-modified gold substrate and the BSA-modified glass slide before exposure to 365-nm UV light. After peeling off the glass slide bearing the BSA molecules,

the resulting thin MIP on the gold substrate allowed sensing the protein by surface plasmon resonance (SPR). The sensor displayed a rather narrow dynamic range between 2.5 nM and 25 nM and an adsorption capacity for BSA only twice that of similar proteins (i.e. human serum albumin and the Fc fragment of immunoglobulin G), indicating limited selectivity.<sup>106</sup>

ATRP is another widely used technique for controlled radical polymerization. This technique historically suffered the catalyst's incompatibility with acidic monomers such as MAA, which greatly limited its applicability to the molecular imprinting field. Indeed, most of the metal complexes based on chelating amino ligands failed to control the polymerization of methacrylic acid, which is arguably the most commonly used functional monomer for MIPs. However, a breakthrough was reported in 2012, when Fors and Hawker noticed that the photocatalyst fac-[Ir(ppy)<sub>3</sub>] could tolerate MAA much better than previous catalysts, making possible the synthesis of PMAA of around 30 000 kDa with a PDI as low as 1.61.<sup>121</sup> Taking advantage of the robustness of fac-[Ir(ppy)<sub>3</sub>], Adali-Kaya et al. thus reported on the synthesis of MIPs specific for S-propranolol and testosterone, both formulated using MAA as functional monomer. Two different formats were tested (i.e. bulk and nanoparticles) which in both cases afforded MIPs with affinities and selectivities comparable to those of similar MIPs obtained by FRP. In addition, the halide-capped chain-ends allowed for chain-extension and grafting of polyacrylamide p(AAm) brushes onto MIP nanoparticles.<sup>107</sup>

### 3.3. Visible and NIR light mediated photopolymerization

There is currently a growing interest in the use of visible light for photopolymerization (including in the MIP field) due to its considerable advantages over conventional UV polymerization. The lower energy of visible light allows for more specific light-induced processes. As opposed to UV radiation, visible light is safer to use for the operator and less likely to alter the ingredients of the MIP precursor mixture other than to initiate polymerization. Also, visible light is innocuous to living cells and therefore more suited to biological applications.<sup>96,104</sup> Incidentally, the now widely available LEDs as visible-light sources generate less heat and thus help avoiding thermal effects.

Various kinds of initiators exist for visible light photopolymerization such as some organic dyes and many organometallic compounds. Some initiators such as anthraquinone derivatives are actually Type II UV photoinitiators modified with auxochromes and extended  $\pi$ - $\pi$  bond conjugation to shift their absorption range from the UV to the visible region.<sup>98</sup> Urraca and co-workers exploited for instance a system composed of Eosin Y and methyldiethanolamine as a Type II initiator to synthesize

a MIP using a 532-nm green laser. To do that, they coated an aluminum film featuring nanoholes laid on top of a glass substrate with a precursor mixture containing the initiating system, the template rhodamine 123, MAA, the crosslinker EGDMA and acetonitrile (ACN). The laser beam was then directed onto the glass slide to synthesize sub-micron MIP dots for the fluorescent assay of rhodamine 123.<sup>103</sup> Wei's group chose a photo-redox couple sensitive to red light based on methylene blue/*p*-toluenesulfinate for the surface functionalization of SPR chips with theophylline-imprinted polymers. The aqueous pre-polymerization mixture composed of the template, MAA, MBAAM and the photo-redox initiator system was sandwiched between an SPR gold chip and a cover glass which was peeled off after polymerization. Irradiating with a red laser beam of 633-nm wavelength resulted in the formation of a MIP for theophylline.<sup>156</sup> There are only very few Type I visible-light photoinitiators with wavelengths above the blue region, one of them being the titanocene initiator at 532 nm (Table 1.1).<sup>116</sup>

Over the years, visible light has also been used to trigger controlled radical polymerizations, such as photoiniferter, NMP, RAFT and ATRP. The recent use of trithiocarbonates,<sup>157</sup> benzyl tellurides<sup>158</sup> and diselenide compounds<sup>159</sup> as visible-active photoiniferters has considerably expanded the use of this class of compounds.<sup>55,83,84,120</sup> In the molecular imprinting field, Garcia-Soto et al. reported for instance on the first use of 4-cyano-4-[(dodecylsulfanylthiocarbonyl)sulfanyl]pentanoic acid (CDTPA) as a photoiniferter under low-power visible light. CDTPA allowed polymerizing MIPs for testosterone by irradiating the prepolymerization mixture with either a blue (435-nm) or green (520-nm) LED. The resulting microspheres showed similar affinity for the template, albeit the size was smaller for the MIP synthesized at the shorter wavelength, which was related to the different extent of activation reached upon irradiation.<sup>104</sup>

Reversible addition-fragmentation chain-transfer (RAFT) polymerization is one of the most popular controlled radical polymerizations and operates with a chain transfer mechanism similar to that of iniferter. However, conversely to iniferter, RAFT polymerization requires an exogenous source of radicals and does not control the termination step. The tandem PET-RAFT has successfully been applied to the synthesis of MIPs, as showed by Cai et al. who grew a melamine-imprinted layer on gold nanoparticles (AuNPs) for electrochemiluminescence (ECL)-based sensing. The strategy involved the electrostatic adsorption of Ru(bpy)<sub>3</sub><sup>2+</sup>, a water-soluble PET catalyst and a typical ECL reagent, on negatively charged, citrate-stabilized AuNPs, and then the dispersion of such particles in a precursor mixture consisting of the template (melamine), MAA, EGDMA and the RAFT agent 4-cyano-4-ethyltrithiopentanoic acid (CETP) in an ethanol/water solution. Polymerization on the surface of the Au aggregates was achieved by triggering the PET process with 465-nm blue light. The hybrid MIP was further mixed with Nafion to form a composite that was later deposited on a highly ordered pyrolytic

graphite (HOPG) substrate. The resulting sensor could detect melamine over a wider concentration range compared, for instance, to silica and multiwalled carbon nanotubes, while showing similar LODs. This advantage was attributed to the properties of AuNPs such as good conductivity, large surface area available for ECL by  $\text{Ru}(\text{bpy})_3^{2+}$  and the LSPR phenomenon.<sup>160</sup>

Yet another interesting route for visible-light driven photopolymerization consists in using the emission of fluorescent nanoparticles such as quantum dots (QDs) upon excitation with shorter wavelengths. QDs are fluorescent semiconductor nanocrystals able to emit visible light of a certain wavelength upon excitation by UV light.<sup>161–163</sup> Panagiotopoulou et al. used two kinds of QDs to locally grow a MIP shell around them by excitation with UV in the presence of visible-light-active, Type II photoinitiators (Figure 1.8). Since the light intensity emitted by the QDs decreases with distance, polymerization only took place in close proximity to the QDs. In their experiment, they used InP/ZnS QDs (red and green emitting QDs) combined with two photo-initiating systems: respectively a methylene blue/trimethylamine (TEA) and an Eosin Y/TEA tandem. Thus, after growing a first hydrophilic shell based on poly[2-hydroxyethylmethacrylate-co-N,N'-ethylene bis(acrylamide)] by irradiating with 365-nm UV light, they then synthesized thin MIP shells imprinted with N-acetylneuraminic acid (NANA) on red emitting QDs and glucuronic acid (GlcA) on green emitting QDs as a second layer. Thanks to the embedded emission properties of the resulting imprinted composites, both red and green MIP-coated QDs were applied as biocompatible imaging agents for the multiplexed detection of glycosylations in cells.<sup>164</sup> The same principle was employed to synthesize thin MIP shells directly around carbon dots (CDs),<sup>165</sup> and very recently, around individual protein molecules. The latter was possible by using proteins (myoglobin, lactoferrin) surface-derivatized with Eosin, as macroinitiators. After removal of the template protein, the resulting nanogel particles contained on average one binding site and specifically recognized their target protein.<sup>166</sup>

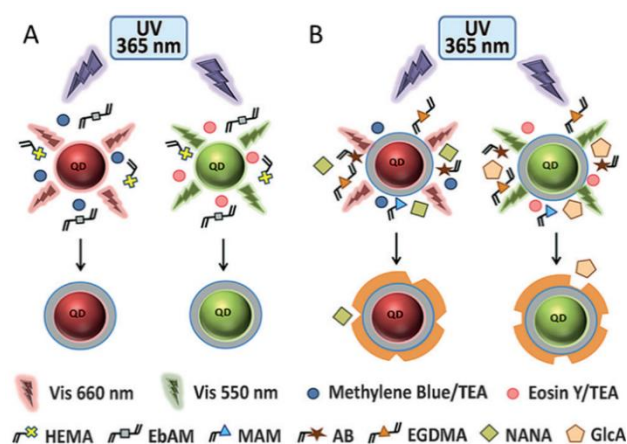


Figure 1.8. General scheme for the synthesis of a polymer shell around red and green InP/ZnS emitting QDs. Excitation with UV light allows sequentially polymerizing (A) a hydrophilic shell, and (B) the MIP layer. Reprinted with permission from Wiley-VCH Verlag GmbH & Co.<sup>164</sup>

By using the same rationale on stimulating a light emission using excitations from different spectral regions, visible light-driven photopolymerization can also be achieved upon upconversion. Upconverting particles (UCPs) are lanthanide- or actinide-based nanoparticles capable of converting low-energy radiation (such as infrared) into high-energy radiation (such as visible light or UV) through absorption of multiple photons or through energy transfer.<sup>167,168</sup> The first example of molecularly imprinted nanocomposites synthesized by upconversion of NIR light was reported by Beyazit et al. who demonstrated a general strategy for coating the  $\text{NaYF}_4:\text{Yb}^{3+},\text{Er}^{3+}$  UCPs with a polymer layer. Oleic acid-stabilized UCPs were immersed in a toluene/DMSO solution containing HEMA, EbAM, and N-acryloyl-*p*-aminobenzamidinium-HCl (AB) as monomers and Eosin Y/TEA as photoinitiator for growing a MIP. Upon exposure to 980-nm NIR, the UCPs emitted visible light between 520-540 nm, which allowed polymerizing first a hydrophilic polymeric shell around the particles. Similarly to the case of QDs, the light intensity emitted by UCPs decreases with distance, which confines the polymerization close to the surface, thus affording thin layers. The hydrophilic UCPs were subsequently dispersed in phosphate buffer containing new monomers, and a second (MIP) shell was synthesized using trypsin as a template. In this way, the AB monomer included in the first shell was used to anchor the template for the synthesis of a second, imprinted shell. Measurements with fluorescein isothiocyanate-labelled trypsin showed that the UCP-MIPs were selective for trypsin over other serine proteases such as kallikrein and thrombin.<sup>95</sup>

NIR can also be upconverted to UV light and used to locally trigger UV-mediated photopolymerization.<sup>95</sup> Tang et al. fabricated core-shell MIP nanoparticles based on the UCP  $\text{NaYF}_4:\text{Yb}^{3+},\text{Er}^{3+}$  that would serve as fluorescent probes for sensing quinolones in fish samples (Figure

1.9). The UCPs were first coated with an ultrathin silica shell doped with  $\text{Fe}_3\text{O}_4$  to render it magnetic for easy handling. They were then added to a MIP precursor composed of the template enrofloxacin (ENRO), MAA, EGDMA and benzophenone in dichloromethane (DCM)/TEA. The setup was exposed to a 980-nm infrared radiation, upon which the UCPs emitted light mainly at 405-nm, triggering the formation of the MIP layer on the surface. The resulting MIP UCPs were able to detect and measure ENRO together with other quinolones since these target molecules, through their hydrogen bond with the functional groups found in the binding sites, could quench the fluorescence of the MIP UCPs when exposed to 980-nm NIR. The MIP UCPs exhibited fast response, high selectivity and specificity towards five quinolones.<sup>109</sup>

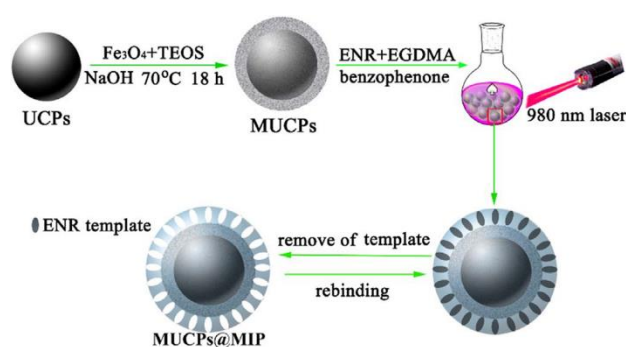


Figure 1.9. Schematic representation of the fabrication of the MIP magnetic upconverting particles (MUCP). Reprinted with permission from Elsevier B.V.<sup>109</sup>

### 3.4. Limitations of photopolymerization of MIPs

Despite the obvious advantages mentioned above, photopolymerization has also a number of limitations, both in general and from a MIP point of view. General limitations are more of the technical kind, such as the limited penetration depth of light into bulk solutions and suspensions (physical barrier). This is dependent on the wavelength (visible light usually penetrates better than UV), and may require special reactor designs to ensure homogeneous irradiation and high polymerization yields. As a result, photopolymerization has been more widely adopted to the synthesis of micro and nanostructures and to the patterning of polymers, than to the synthesis of bulk materials.

Specifically in the MIP field, there are a number of additional factors to be taken into account. Since most organic molecules absorb at least UV light, the template molecule used to generate the MIP may be sensitive to the irradiation during photopolymerization, in particular with UV initiators. On the other hand, photopolymerization at higher wavelengths of the visible spectrum mostly use Type II photoinitiators (a notable exception being the titanocene initiator at 532 nm,<sup>116</sup> see Table 1.1).



These require a co-initiator (often an amine), which renders the polymerization solution more complex and may even interfere with the template-monomer assembly.

#### 4. Photostructuring MIPs

The different means of tuning a photopolymerization (i.e. spatiotemporal, wavelength, intensity, pulsating) make this process a favorable strategy for the structuration of polymers and their intelligent design and engineering into arbitrary patterns. Adding photostructuring to molecular imprinting opens the possibility for non-contact high-resolution fabrication of micro- and nanostructures<sup>45,54</sup> exhibiting molecular recognition properties, with applications ranging from microelectromechanical systems (MEMS), to microfluidic channels, to transducers in sensors, etc. When MIPs are structured to have dimensions in the micro-/nano-range, their effective surface-to-volume ratio increases. This allows providing a high number of binding sites with only a limited mass of MIP, which in turn improves their sensitivity, binding kinetics and binding site regeneration.<sup>171-173</sup> Furthermore, since light can be projected onto a surface, it also allows for an easy *in situ* polymerization of structures on substrates.<sup>174</sup>

Thanks to these advantages, one of the obvious applications of photo-structured MIPs deals with chemical sensing. A chemical sensor, as defined by the IUPAC, is a *“device that transforms chemical information, ranging from the concentration of a specific sample component to total composition analysis, into an analytically useful signal. The chemical information, mentioned above, may originate from a chemical reaction of the analyte or from a physical property of the system investigated.”*<sup>175</sup> Chemical sensors are usually composed of two main functional units: a sensing element in charge of transforming the chemical information into a form of energy, and a transducer, which is responsible for translating this energy into an analytical signal. In the context of chemical sensing, it is desirable that the recognition element be optimally exposed to the sample while remaining well attached to the transducer, to effectively generate a signal upon interaction with its target. Assembling the recognition element into a structure, whether simple or hierarchical, thus needs to take into account the above requirements and is therefore a crucial step. Indeed, MIPs as synthetic polymers can be easily synthesized in a wide range of physical forms (e.g. bulk, micro-/nano-particles, membranes, films, complex 2.5D and 3D elements, etc.) and interfaced on a wide variety of substrates.

#### 4.1. Introduction to photolithography

Photolithography is a powerful technology for the fabrication of sophisticated 2D and 3D structures at the micro- and the nanoscale with the aid of light.<sup>176</sup> There exists a myriad of photolithographic techniques, which can be categorized into either “mask” or “maskless” techniques (Figure 1.10). Mask lithography relies on the use of masks, stamps or molds to transfer a pattern on a given surface. Mask photolithography (or optical lithography) and soft lithography (mechanical means involving stamps and molds) belong to this category. Conventional photolithography uses masks to transfer a pattern onto a given surface, by selectively allowing the transmission of light from a source onto a photosensitive material which is usually spread on top of a substrate. Depending on the nature of the material, the illuminated areas will either cross-link and harden, or become susceptible to removal. This is often followed by an etching step that eliminates the exceeding parts and reveals the actual pattern. These techniques are grouped according to the placement of the mask between the light source and the photoresist into: (i) contact photolithography, (ii) proximity lithography and (iii) projection lithography (Figure 1.11). Conventional photolithography is known as a “parallel” process, as it fully transfers the pattern of a mask onto a photoresist upon a single light exposure.<sup>177,178</sup> As such, it guarantees high throughput and high resolutions, which makes it the dominant fabrication method in microelectronics.<sup>177,179,180</sup> Unfortunately, photolithography can be costly as its setup often requires the use of clean rooms to prevent contamination from particulates and guarantee the quality of printed structures.<sup>181</sup>

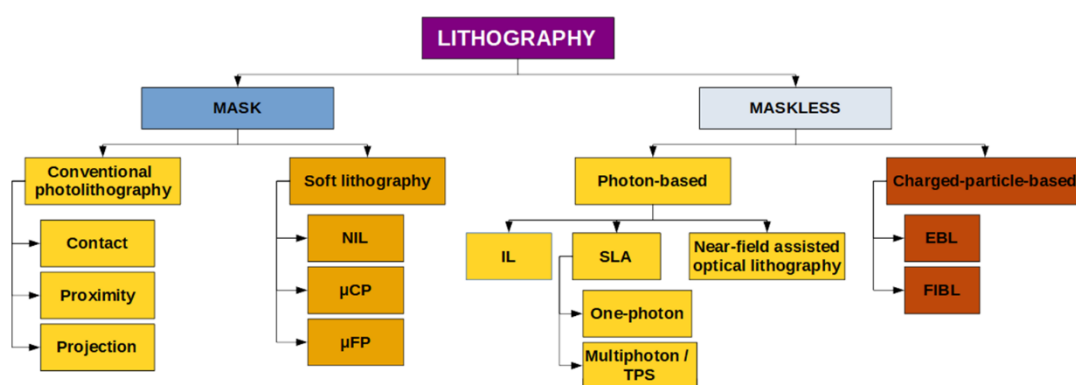


Figure 1.10. Classification of different lithographic techniques.

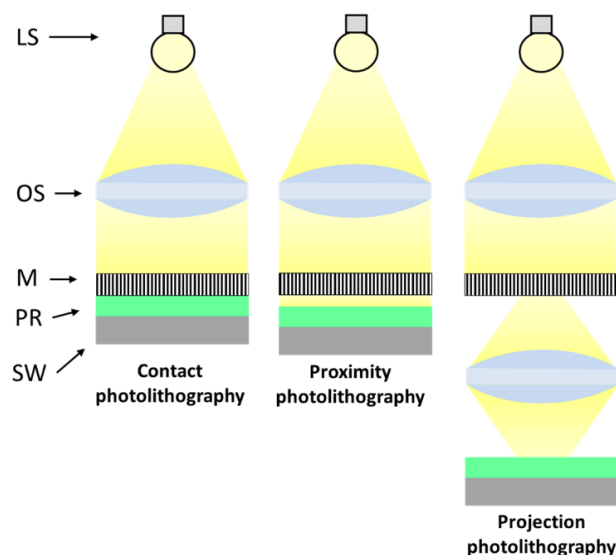


Figure 1.11. Comparison of different conventional photolithographic technique (LS=light source, OS=optical system, M=mask, PR=photoresist, SW=silicon wafer).

The main drawback of photolithography is its diffraction-limited resolution. For proximity lithography for instance, which is carried out within the near-field (Fresnel) diffraction regime, the achievable resolution ( $R$ ) is (Equation 1.1):

$$R \approx \sqrt{\lambda L} \quad (\text{Equation 1.1})$$

where  $\lambda$  is the wavelength of the source and  $L$  is the distance between the mask and the resist (usually 2-4  $\mu\text{m}$ ). This means that the lateral resolution for proximity lithography can be several times the used wavelength. In contact photolithography on the other hand, the mask directly touches the resist, thus bringing the resolution to the order of magnitude of the wavelength. The resolution ( $R$ ) of projection lithography (and of all other lens-based lithographies) is governed by far-field (Fraunhofer) diffraction and constrained by the Rayleigh equation (Equation 1.2):

$$R = k_1 \frac{k}{n \sin \theta} = k_1 \frac{\lambda}{NA} \quad (\text{Equation 1.2})$$

where " $k_1$ " is a process-dependent factor (with values typically between 0.25 and 0.8), " $n$ " is the refractive index of the medium, " $q$ " is the half-aperture angle of the lens or optical imaging system used and " $NA$ " corresponds to its numerical aperture. This places the resolution around half the wavelength of the source.<sup>182-184</sup> Many approaches have been developed by specifically targeting the different parameters of Equation 1.2 to improve lateral resolution, which afforded techniques such as deep and extreme UV lithography, phase-shift lithography or immersion lithography. As a result,

resolutions down to 10 nm can now be achieved.<sup>180,185</sup> Deep and extreme UV lithography utilize for instance short wavelengths (193 nm and 13.5 nm, respectively). Phase-shift lithography on the other hand relies on lowering the  $k_1$  parameter by using optically transparent masks which are micro-/nanostructured on their surface.<sup>183,185</sup> Such masks modify the light optical path *via* destructive interference, thus enhancing the sharpness of the replicated image. Immersing the mask projection system in a fluid with a refractive index higher than 1 (i.e. higher than air) also improves resolution as it occurs for immersion lithography.<sup>183,186</sup>

In contrast to the previous techniques, maskless lithography does not require any physical mask, as it relies on focusing a beam of photons or charged particles within a photoresist in order to construct patterns. Interference lithography, a photon-based technique, exploits the interference patterns of coherent optical beams incident at various angles within a photoresist. The resulting pattern may extend in 2D or 3D depending on the thickness of the reactive layer and it is generally further developed by thermal or chemical treatment in order to remove the unreacted photoresist. Also considered a “parallel” process, interference lithography represents a fast, straightforward and accurate approach for quasiperiodic structures with resolution below 10-nm, making it attractive for fabricating photonic crystals and metamaterials.<sup>187</sup> Another photon-based, maskless technique is stereolithography (SLA). In SLA, a computer-generated 3D design is “directly written” into a photoresist by focusing a laser beam of appropriate wavelength while following a sequence of stacked 2D layers which are thus photoprinted successively on top of each other by moving a “z” stage. SLA can operate via one-photon or multiphoton absorption. In one-photon stereolithography, a laser source (usually UV) is used to induce a cross-linking based on simple, one-photon absorption, as it occurs in ordinary photopolymerizations. On the other hand, multiphoton SLA (MSLA) involves the simultaneous absorption of multiple photons of low energy, which virtually matches a “single”, high-energy photon absorption. A prominent example of multiphoton SLA is the two-photon stereolithography (TPS) (Figure 1.12). In this technique, the use of a femtosecond laser (usually with wavelengths in the NIR around 800 nm) allows for a two-photon absorption, which corresponds to the mono-absorption of a 400-nm photon. Such two-photon absorption thus allows reaching the energy threshold required to trigger the dissociation of an ordinary, near UV-active photoinitiator such as TPO-L. Many works have been dedicated to develop specific photoinitiators exhibiting a high two-photon absorption cross-section. Unlike one-photon stereolithography, MSLA has the advantage of being exclusively confined within the (small) focal point of the beam (i.e. less than  $1 \mu\text{m}^3$ ) where high intensities promote a two-photon absorption process (Figure 1.12B). Thus, multiphoton SLA enables a highly localized polymerization of the photoresist, which is essential for the direct writing of elaborate 3D geometries (Figure 1.12D). However, multiphoton SLA only affords a resolution of a few

hundred nanometers and provides a low throughput as it belongs to “serial” processes, which operate with a multi-exposure to light for the voxel-to-voxel printing of the resist.<sup>177,178</sup> Nevertheless, MSLA is compatible with a wide variety of photoresists including (meth)acrylates, epoxides, organically modified silica and organically modified ceramics.<sup>187–189</sup>

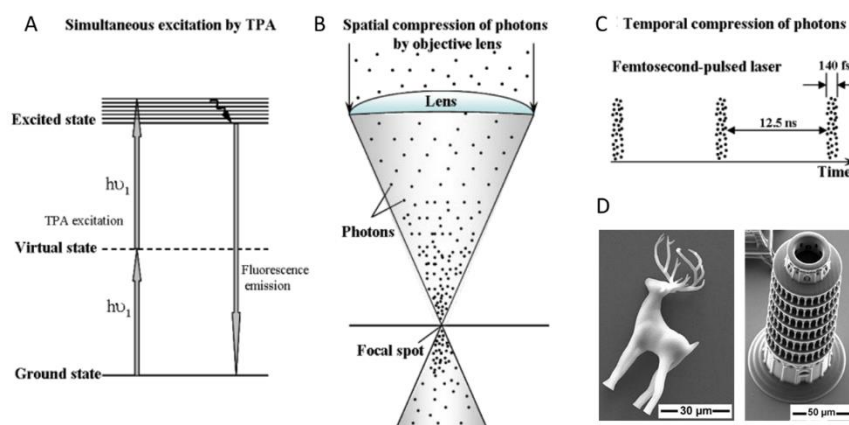


Figure 1.12. (A) Jablonski diagram showing electronic excitation via two-photon absorption. (B-C) Spatial and temporal compression of photons for increasing the probability of two-photon absorption. Reprinted with permission from IntechOpen.<sup>190</sup> (D) Representative SEM images of microstructures with complex geometries printed via TPS.

While the lateral resolution for traditional TPS can be as small as a few hundred nanometers, successful attempts have been made to reduce this value by modifying the experimental setup. For instance, Gan et al. relied on the use of a second laser beam around the focal point of the primary laser source for the activation of a photoinhibitor to limit the polymerization and reduce the lateral writing resolution to 52 nm and a record feature size of 9 nm.<sup>191</sup> Haske et al. reduced the resolution based on the Rayleigh equation (Equation 1.2) by using a 520-nm laser source whose dosage had been optimized against a resist containing the photoinitiator DABP.<sup>192</sup> Jiang et al. took advantage of polythiols to provide a photoresist with oxygen tolerance as well as to expand the writing range, while enabling the use of near-threshold laser dosages for the production of mechanically stable fine lines.<sup>193</sup>

A different approach was instead used by Liu and co-workers, who deliberately fabricated photonic woodpiles with an intralayer rod distance of 1.57  $\mu\text{m}$  which decreased to 350 nm by thermal-shrinking at 450°C, resulting in the appearance of a visible color due to the woodpiles.<sup>194</sup>

Defying the diffraction limit, near-field-assisted optical lithography may also be included among light-based lithography techniques, which can be used in different configurations, including mask and maskless approaches. This technique triggers a polymerization using the evanescent wave which can be generated in different configurations. By its nature, the optical near-field is not governed by the classical diffraction limit, which permits to reach high resolution (down to the lower nm scale using visible light). Total internal reflection of light at the interphase between two media with different refractive indices and which propagates into the medium of lower index can be used to generate near-field irradiation.<sup>195</sup> This technique allows for a highly confined polymerization (i.e. few tens of nm), as the energy of the evanescent wave which tails from the interphase decays exponentially.<sup>196,197</sup> Metal nanostructures excited in their resonance plasmonic bands are also very interesting to generate near-field excitation with nanoscale resolution, as described in several examples.<sup>198–200</sup> The near-field being generated at the surface of the metal structure, in hot-spots, this method is quite efficient to couple polymer materials with metal nanostructures, with a precise control of the polymer position in proximity of the nanostructure.<sup>201</sup>

Finally, maskless techniques can also rely on charged particles, such as electron-beam lithography (EBL) and focused-ion-beam lithography (FIBL). In EBL, a beam of accelerated electrons is scanned on the surface of a resist, such as polymethylmethacrylate (PMMA), in order to alter its solubility. Upon development, a pattern is created in the resist, which can in turn be transferred to a substrate upon further etching. FIBL is analogous to EBL but it applies an accelerated beam of ions, such as He<sup>+</sup> and Ga<sup>+</sup>. FIBL can also be used to deposit materials such as tungsten, platinum and carbon on a surface. This is typically achieved upon interaction between a focused ion beam and a gaseous precursor in proximity to a surface, wherein the precursor decomposes.<sup>202</sup> EBL and FIBL can achieve high resolutions, with features below 10 nm, but they remain costly and rather difficult to miniaturize. Similarly to SLAs, they also have low throughputs.<sup>180,183</sup> Representative examples of the above techniques triggered by light and applied to the synthesis or functionalization of MIPs will be discussed in the following paragraphs.

#### 4.2. Mask lithography of MIPs

**a. Contact and proximity photolithography.** A straightforward technique for photostructuring MIPs is contact lithography. Contact photolithography involves the use of a photomask touching the surface of a photoresist. Upon irradiation with a suitable wavelength, the exposed zones of the resist undergo polymerization, which results in transferring a pattern from the mask to the underlying polymer (i.e.

MIP). This approach involves the use of what is called a negative tone resist, which upon washing with a “developing” solution affords polymeric structure features as the inverse pattern of the mask. Similarly, positive tone resists also exist, which work in the opposite way, i.e. the exposed zones become soluble and can be removed with the developing solution. Despite being conceptually simple, contact photolithography requires a complete and direct contact between the resist and the photomask to avoid defects and contamination, but this can sometimes be particularly tricky. To avoid such mishaps, proximity printing can be used, which overcomes the above limitations by including a small gap between the resist and the mask during the photostructuring step (Figure 1.11). The gap must be as small as possible to preserve the resolution but big enough to prevent defects and contamination.

Ayela's group has pioneered contact photolithography of MIPs, at the wafer scale, fabricating consecutively multiplexed patterns of different MIPs on the same silicon wafer, with a  $\mu\text{m}$  resolution. This was done by UV photopolymerization of spin-coated monomer films under nitrogen atmosphere, using standard photolithography equipment with a mask aligner.<sup>203</sup> More recently, Hearn and co-workers applied contact lithography to the synthesis of a double-layered MIP thin film in the form of a grid-patterned surface, with the aim of developing a tool for the direct and visual comparison of different functional monomers toward the binding of the fluorescent target N-dansyl-L-phenylalanine (Figure 1.13A).<sup>204</sup> Their strategy relied on the spin-coating and curing of two consecutive prepolymerization mixtures based on different functional monomers: first, a formulation based on methacrylic acid (MAA, i.e. MIP1), then a second based on 4-vinyl pyridine (4-VP), with N-boc-L-phenylalanine as a non-fluorescent template analogue in both cases. The spin-coated formulations were both cured at 365 nm, but only for the second one a 300-mesh TEM gold grid was used as a mask, which resulted in a double layered MIP system consisting of a series of patterned squares (MIP2) on top of a continuous film (MIP1). Upon incubation with N-dansyl-L-phenylalanine, fluorescent microscopy images revealed that the squares had a much higher fluorescent intensity than the underlying film (Figure 1.13B), thus suggesting that 4-VP had a higher affinity for the target, as supported by molecular modelling and  $^1\text{H}$  NMR spectroscopy titrations.

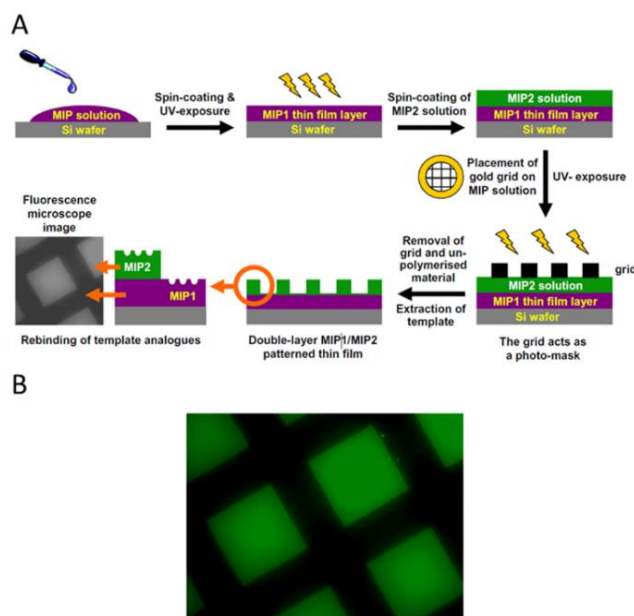


Figure 1.13. (A) Schematic representation for the preparation of a grid-patterned double-layered MIP2/MIP1 thin film by contact lithography. (B) Fluorescence microscope image of a grid-patterned double-layer MIP1/MIP2 thin film with the  $54\ \mu\text{m} \times 54\ \mu\text{m}$  raised MIP2 squares selectively binding the fluorescent target N-dansyl-L-phenylalanine. Reprinted with permission from Elsevier B.V.<sup>204</sup>

In another work, Liu's group fabricated thin-film arrays on a pre-treated glass slide or filter membrane by light-curing a pre-polymerization solution while covering it with a patterned photomask. The MIP was based on boronic acid as functional monomer, which is known to interact with cis-diols such as present in certain sugars via reversible covalent bonds. These imprinted arrays were used for the colorimetric detection and chemiluminescent assay of five glycoproteins, with the test exhibiting a limit of detection as low as  $1\ \text{ng mL}^{-1}$  for one of the glycoproteins.<sup>205</sup>

More recently, Nicu and his team integrated MIPs into arrays of nanocantilevers (Figure 1.14) for a label-free detection via functionalized resonators.<sup>206</sup> To achieve this, a 100-mm silicon-on-insulator (SOI) wafer was dry-etched to shape a cantilever and silanized with 3-(trimethoxysilyl)propyl methacrylate to anchor an organic MIP. The cantilever was then spin-coated with a monomer mixture and placed under an automatic mask aligner for photolithography. Upon photopolymerization and wet etching of the sacrificial oxide layer, a MIP coated cantilever was obtained which worked as a nanoelectromechanical system (NEMS) for sensing the fluorescent N-dansyl-L-phenylalanine. Preliminary results showed that while the mechanical sensing on cantilevers required further optimization due to the damping by the polymer, a direct fluorescence measurement of the target confirmed successful imprinting, with the MIP cantilever emitting about 3.5 times stronger fluorescence intensity than the corresponding NIP cantilever.



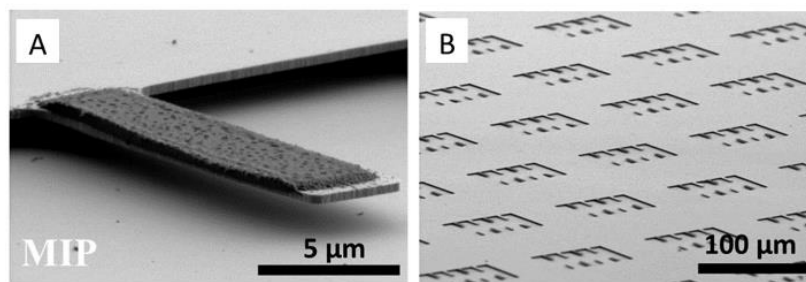


Figure 1.14. SEM images of (A) a MIP-coated silicon cantilever obtained by photolithography and (B) large-scale arrays of MIP cantilever. Reprinted with permission from IOP Publishing.<sup>206</sup>

**b. Projection photolithography.** In projection photolithography, the photomask is placed at a certain distance from the resist while an optical system is located in between to focus the pattern image from the mask onto the resist (Figure 1.11). In this way, it is possible to overcome the mechanical and diffraction issues encountered in contact and proximity photolithography, which improves the whole resolution. For instance, Haupt's group combined microscope projection photolithography with nanomolding to prepare arrays of MIP nanofilaments (Figure 1.15A-B) by inserting a photomask into the field-diagram plane of a microscope. In this way, UV light from the mercury lamp of the microscope could pass through the unmarked areas of the mask and polymerize 70 nm-dots from a methacrylate-based precursor solution. The light was also filtered with an IR mirror to prevent thermal polymerization. Since the precursor was deposited on a nanoporous alumina substrate, the polymerized spots were composed of upright MIP nanofilaments (Figure 1.15C-E) whose structure provided a large surface area and an easy diffusion of the targets fluorescein or myoglobin. This approach also allows decreasing the size of the projected pattern (i.e. the size of the dots) by simply using higher magnification objectives, as well as improving the whole resolution by using higher numerical apertures.<sup>207</sup>

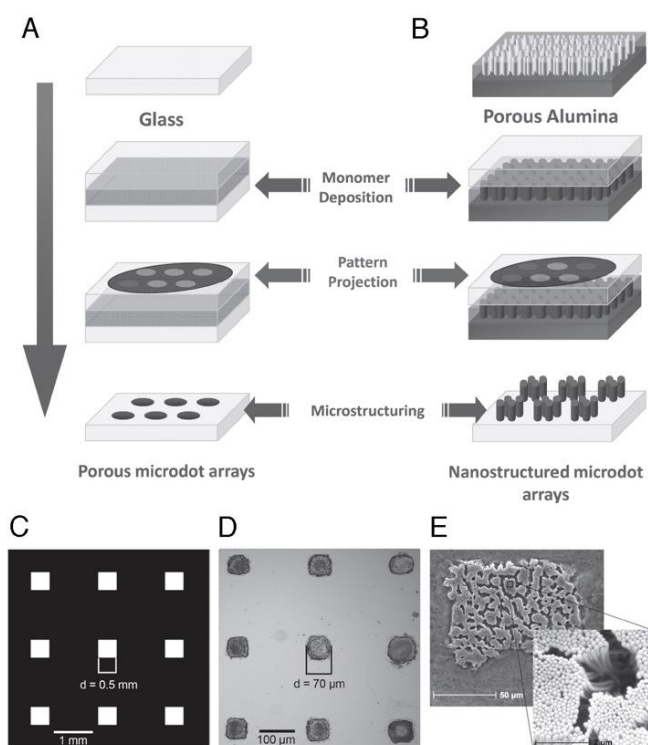


Figure 1.15. Schematic representation of the preparation of (A) porous microdot arrays and (B) nanofilament microdot arrays by microscope projection photolithography. (C) Transparent photomask. (D) Bright-field microscopy image of the polymer array obtained using the photomask by projection photolithography. (E) SEM image of a single nanofilament dot (magnification: 750 x, inset: 20000 x). Reprinted with permission from Wiley-VCH Verlag GmbH & Co. KGaA.<sup>207</sup>

### 4.3. Photon-based, maskless lithography

**a. Interference lithography.** Among the techniques that manipulate lasers for direct writing, holographic lithography or multibeam interference lithography (MBIL) consists of two or more non-parallel laser beams directed into a photoresist to trigger a polymerization according to their interference pattern.<sup>208</sup> An example of MBIL MIP writing was reported by Fuchs et al., who imprinted testosterone as template using MAA and pentaerythritol triacrylate (PETA) as monomers and bis(cyclopentadienyl)titanium dichloride as green light-sensitive radical initiator. Upon laminating this formulation between two microscope glass slides, one of which functionalized with double bonds for a better MIP adhesion, a coherent 532-nm laser beam was split into two components, which were later converged into the precursor mixture to polymerize a MIP. (Figure 1.16A). This resulted in well-defined diffraction gratings (Figure 1.16B-C), able to sense the presence of testosterone by varying their diffraction efficiency.<sup>116</sup>

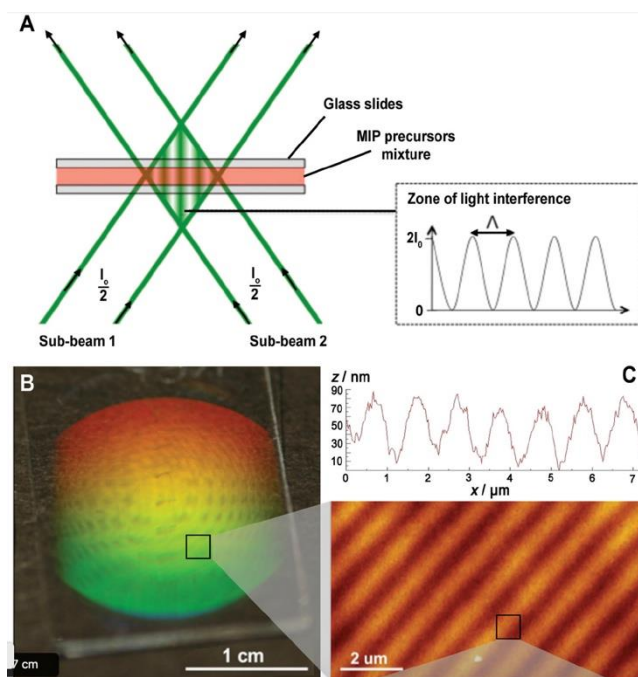


Figure 1.16. (A) Scheme showing the *in situ* MIP microstructuring process by interference lithography with two laser beams at 532 nm. (B) Holographic MIP film supported on a glass slide. (C) AFM image of the surface topography of a holographic MIP film (10  $\mu\text{m}$   $\times$  10  $\mu\text{m}$ ). Reprinted with permission from Wiley-VCH Verlag GmbH & Co. KGaA.<sup>116</sup>

**b. One-photon stereolithography.** Microstereolithography ( $\mu\text{SL}$ ) is another approach for fabricating 3D structures by localized photopolymerization using a sharply focused laser beam. A 3D model of the desired shape is initially sliced into consecutive 2D layers by a computer-aided design (CAD) program. A laser beam of the appropriate wavelength is then focused in a precursor solution a few micrometers above a microscope slide to write the first 2D layer. This allows minimizing light scattering, for an improved resolution, while also preventing a premature polymerization of the second 2D layer.<sup>189,209,210</sup> The motion of the substrate along the z-axis then allows the structure to grow to 3D. Shea and co-workers were the first to use this technique for MIPs, manufacturing 600  $\mu\text{m}$   $\times$  600  $\mu\text{m}$  2D and 3D (today considered 2.5D) grids (Figure 1.17) imprinted with 9-ethyladenine using a 364-nm Ar<sup>+</sup> laser and an x-y-z motorized stage to explore the possibilities of miniaturization, which is important in sensing and diagnostics as it limits both energy consumption and production costs. Recognition of the target 9-dansyladenine was evaluated through a fluorescence assay which showed that the MIP grids had affinity for the target comparable to bulk MIPs.<sup>174,211</sup>

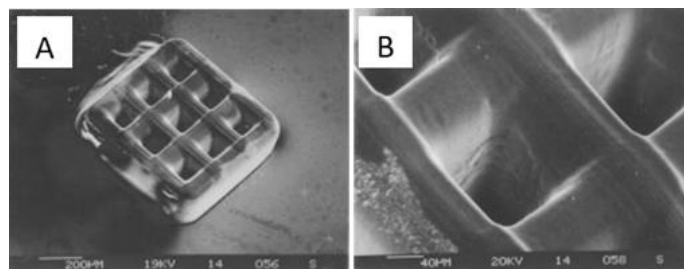


Figure 1.17. (A) SEM image of a 3D imprinted microstructure ( $600\ \mu\text{m} \times 600\ \mu\text{m} \times 100\ \mu\text{m}$ ) fabricated by microstereolithography. (B) Magnification of the structure showing a wall thickness of around  $10\ \mu\text{m}$ . Reprinted with permission from Wiley-VCH Verlag GmbH & Co. KGaA.<sup>211</sup>

**c. Multiphoton stereolithography.** The MIP photostructuring methods described so far were based on single-photon absorption. However, as outlined in section 3.1, fabrication of 3D structures by multiphoton stereolithography has recently gained great attention. Multiphoton stereolithography (MSLA) relies on a multiphoton absorption process highly confined within the focal volume of a laser beam passing through a microscope objective. It is therefore a true 3D fabrication approach since complex structures can be manufactured by moving the laser focus in three dimensions. The best-known example is two-photon stereolithography (TPS).<sup>190,208,212</sup> The use of TPS in molecular imprinting is relatively new, even though the technique has already been reported in several different applications such as scaffolding for cells,<sup>213,214</sup> shape-shifting of microstructures for proteins,<sup>215</sup> biocompatible hybrid materials,<sup>216</sup> tomography,<sup>217</sup> and optics.<sup>218,219</sup> This technique was first applied to the synthesis of MIPs by Chia Gomez et al., who showed its versatility by fabricating different structures such as grids, dot arrays and cantilevers smaller than  $60\ \mu\text{m}$  (Figure 1.18).<sup>143</sup> Lucirin TPO was used as a photoinitiator for a laser wavelength of 800 nm. An array of dots forming the words MIP (imprinted dots, with Z-L-Phe as template) and NIP (non-imprinted dots) were for instance printed, which upon incubation with a fluorescent template analogue (i.e. dansyl-L-Phe) only emitted green light in the case of the MIP (Figure 1.18B). Interestingly, MIP cantilevers, a format which normally requires time-consuming and multi-step processes to be made, were also conveniently fabricated by TPS and allowed the straightforward sensing of their target Z-L-Phe as shown by a frequency shift exquisitely limited to the MIP (Figure 1.18D).

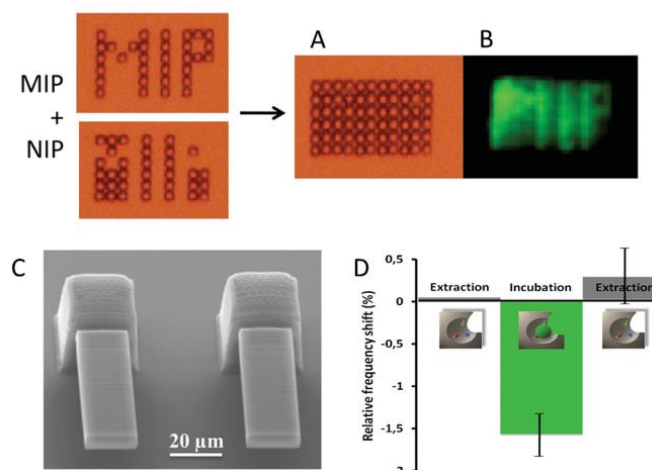


Figure 1.18. (A–B) Multiplexed NIP and MIP dots polymerized on the same sample by two-photon stereolithography (TPS): (A) Optical and (B) fluorescence microscopy images after binding of dansyl-L-Phe. (C) SEM images of MIP cantilevers fabricated by TPS. (D) Relative frequency shift of MIP microcantilevers after extraction, incubation in Z-L-Phe and second extraction. Reprinted with permission from Wiley-VCH Verlag GmbH & Co. KGaA.<sup>143</sup>

**d. Near-field assisted optical lithography.** Photolithographic techniques that rely on optical lenses are based on far-field optics, and as we previously mentioned, their resolution is limited by the Rayleigh resolution and the out-of-focus light. This means that current optical equipment allows resolution between  $\lambda/2$  to  $\lambda$ . Near-field optics, on the other hand, circumvent this problem by taking advantage of optical phenomena such as evanescent waves, which occur between the probe and the sample at sub-wavelength distance.<sup>220,221</sup> It should be stressed here that the evanescent wave features the same wavelength as the reflected radiation. Polymerization by evanescent wave (PEW) was first applied to MIPs by Fuchs et al. who fabricated ultrathin microdots imprinted against the template Z-L-Phe by using MAA, 4-VP and EGDMA as monomers in acetonitrile (ACN) and the initiator Irgacure819. The low-refractive index precursor solution was interfaced with a high-refractive index glass slab carrying a prism of the same index (Figure 1.19A). An actinic laser of 405 nm was internally reflected within the prism-slab system, allowing for the evanescent wave at the slab-precursor interface to initiate polymerization, leading to microdots of sub-100 nm thickness (Figure 1.19B-E). The MIP microdots showed selectivity and some degree of enantiospecificity toward their target, dansyl-D-phenylalanine. The method allowed for quick fabrication (within tens of seconds) of MIPs as thin as <100 nm.<sup>195</sup>

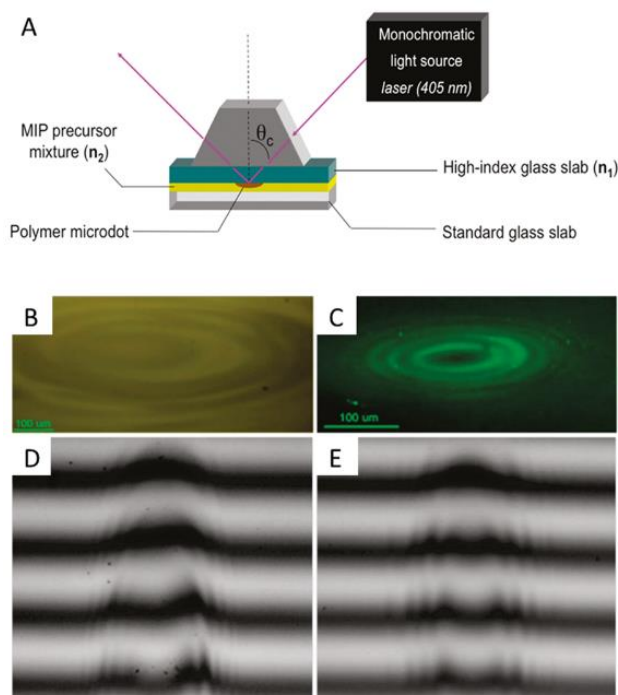


Figure 1.19. (A) Schematic representation of the setup for the polymerization of MIP microdots by evanescent wave. (B) Optical microscope image (20 x) of a MIP microdot. (C) Fluorescence microscope image (20 x) of a MIP microdot. Interferential microscopy images of (D) a MIP microdot and (E) a NIP microdot. Reprinted with permission from American Chemical Society.<sup>195</sup>

## 5. Conclusions

From the synthetic point of view, MIPs are compatible with a variety of structuring techniques, particularly with photon-based lithographic approaches as we presented in detail in this review. These techniques allow not only fabricating micro- and nano-structures with high capacity and sensitivity, due to favorable surface-to-volume ratios, but also shaping and patterning MIPs for generating a direct, analytical signal upon binding, which is essential for some applications such as sensing.

Each photon-based lithographic technique has its own strengths and weaknesses and this review is intended to help make an informed choice depending on the intended purpose. With its high-throughput and the different possibilities of improving resolution, conventional photopolymerization and photolithography are expected to continue flourishing in MIP fabrication. Focusing on the light sources associated with these techniques, a great majority of them use UV light to trigger the polymerization, but longer wavelengths such as visible and NIR are gaining attention in MIP synthesis, as they are more suited for processing mixtures containing sensitive templates such as bio(macro)molecules and are inherently safer.

Finally, stereolithographic techniques offer the most convenient solution to the direct writing of sophisticated architectures. Although limited by a low-throughput and rather expensive setups, stereolithography allows for direct, one-step prototyping of 2.5D and 3D structures. Among these techniques, TPS has risen as a “high-precision” technique which allows confining the polymerization to the focal point (voxel) of the used laser. Due to the multi-photon absorption process involved in TPS, NIR lasers can be used as sources to trigger near-UV or visible photoinitiators, which is advantageous when working with bio-based mixtures or even with living cells. More importantly, if strategies to improve the current TPS resolution can be standardized, it will be possible to shape materials with structural features able to rise optical properties falling directly in the visible spectrum, for a systematic tuning of molecularly imprinted optical sensors.

## 6. REFERENCES

- (1) Dong, J.; Davis, A. P. Molecular Recognition Mediated by Hydrogen Bonding in Aqueous Media. *Angew. Chem. Int. Ed.* **2021**, *60* (15), 8035–8048.  
<https://doi.org/10.1002/anie.202012315>.
- (2) Whitehead, T. A.; Baker, D.; Fleishman, S. J. Computational Design of Novel Protein Binders and Experimental Affinity Maturation. In *Methods in Enzymology*; Keating, A., Ed.; Elsevier Inc., 2013; Vol. 523, pp 1–19. <https://doi.org/10.1016/B978-0-12-394292-0.00001-1>.
- (3) Caminati, W.; Grabow, J. U. Microwave Spectroscopy: Molecular Systems. In *Frontiers of Molecular Spectroscopy*; Laane, J., Ed.; Elsevier B.V.: Hungary, 2009; pp 455–552.  
<https://doi.org/10.1016/B978-0-444-53175-9.00015-5>.
- (4) Tamura, M.; Nakagawa, Y.; Tomishige, K. Self-Assembled Materials for Catalysis. In *Comprehensive Supramolecular Chemistry II*; Raston, C., Ed.; Elsevier Ltd., 2017; Vol. 9, pp 329–349. <https://doi.org/10.1016/B978-0-12-409547-2.12652-6>.
- (5) Bharadwaj, P. K. Macrobicyclic Cryptands With Laterally Nonsymmetric Donors. In *Comprehensive Supramolecular Chemistry II*; Rissanen, K., Ed.; Elsevier Ltd., 2017; Vol. 3, pp 117–179. <https://doi.org/10.1016/b978-0-12-409547-2.12513-2>.
- (6) Gleitsman, K. R.; Sengupta, R. N.; Herschlag, D. Slow Molecular Recognition by RNA. *RNA* **2017**, *23*, 1745–1753. <https://doi.org/10.1261/rna.062026.117>.
- (7) Erdem, Ö.; Saylan, Y.; Andaç, M.; Denizli, A. Molecularly Imprinted Polymers for Removal of Metal Ions: An Alternative Treatment Method. *Biomimetics* **2018**, *3* (4), 1–15.  
<https://doi.org/10.3390/biomimetics3040038>.
- (8) Ardestani, F.; Hosseini, M. H.; Taghizadeh, M.; Rezaee, M. Synthesis and Characterization of Nanopore MoVI -Imprinted Polymer and Its Application as Solid Phase for Extraction, Separation and Preconcentration of Molybdenum Ions from Water Samples Fatemeh. *J. Brazilian Chem. Soc.* **2016**, *27* (7), 1279–1289. <https://doi.org/10.5935/0103-5053.20160026>.
- (9) Perera, R.; Ashraf, S.; Mueller, A. The Binding of Metal Ions to Molecularly-Imprinted Polymers. *Water Sci. Technol.* **2017**, *75* (7), 1643–1650.  
<https://doi.org/10.2166/wst.2017.036>.
- (10) Diliën, H.; Peeters, M.; Royackers, J.; Harings, J.; Cornelis, P.; Wagner, P.; Steen Redeker, E.; Banks, C. E.; Eersels, K.; Van Grinsven, B.; Cleij, T. J. Label-Free Detection of Small Organic Molecules by Molecularly Imprinted Polymer Functionalized Thermocouples: Toward in Vivo Applications. *ACS Sensors* **2017**, *2* (4), 583–589. <https://doi.org/10.1021/acssensors.7b00104>.



- (11) Lu, W.; Asher, S. A.; Meng, Z.; Yan, Z.; Xue, M.; Qiu, L.; Yi, D. Visual Detection of 2,4,6-Trinitrotoluene by Molecularly Imprinted Colloidal Array Photonic Crystal. *J. Hazard. Mater.* **2016**, *316*, 87–93. <https://doi.org/10.1016/j.jhazmat.2016.05.022>.
- (12) Anirudhan, T. S.; Christa, J.; Deepa, J. R. Extraction of Melamine from Milk Using a Magnetic Molecularly Imprinted Polymer. *Food Chem.* **2017**, *227*, 85–92. <https://doi.org/10.1016/j.foodchem.2016.12.090>.
- (13) Rossetti, C.; Ore, O. G.; Sellergren, B.; Halvorsen, T. G.; Reubsaet, L. Exploring the Peptide Retention Mechanism in Molecularly Imprinted Polymers. *Anal. Bioanal. Chem.* **2017**, *409* (24), 5631–5643. <https://doi.org/10.1007/s00216-017-0520-6>.
- (14) Nakamura, Y.; Masumoto, S.; Matsunaga, H.; Haginaka, J. Molecularly Imprinted Polymer for Glutathione by Modified Precipitation Polymerization and Its Application to Determination of Glutathione in Supplements. *J. Pharm. Biomed. Anal.* **2017**, *144*, 230–235. <https://doi.org/10.1016/j.jpba.2016.12.006>.
- (15) Sharma, P. S.; Iskierko, Z.; Noworyta, K.; Cieplak, M.; Borowicz, P.; Lisowski, W.; D'Souza, F.; Kutner, W. Synthesis and Application of a “Plastic Antibody” in Electrochemical Microfluidic Platform for Oxytocin Determination. *Biosens. Bioelectron.* **2018**, *100*, 251–258. <https://doi.org/10.1016/j.bios.2017.09.009>.
- (16) Saylan, Y.; Yilmaz, F.; Özgür, E.; Derazshamshir, A.; Yavuz, H.; Denizli, A. Molecular Imprinting of Macromolecules for Sensor Applications. *Sensors* **2017**, *17* (4), 1–30. <https://doi.org/10.3390/s17040898>.
- (17) Tchinda, R.; Tutsch, A.; Schmid, B.; Süßmuth, R. D.; Altintas, Z. Recognition of Protein Biomarkers Using Epitope-Mediated Molecularly Imprinted Films: Histidine or Cysteine Modified Epitopes? *Biosens. Bioelectron.* **2019**, *123*, 260–268. <https://doi.org/10.1016/j.bios.2018.09.010>.
- (18) Ying, X.; Zhu, X.; Li, D.; Li, X. Preparation and Specific Recognition of Protein Macromolecularly Imprinted Polyampholyte Hydrogel. *Talanta* **2019**, *192*, 14–23. <https://doi.org/10.1016/j.talanta.2018.08.084>.
- (19) Ait Lahcen, A.; Arduini, F.; Lista, F.; Amine, A. Label-Free Electrochemical Sensor Based on Spore-Imprinted Polymer for Bacillus Cereus Spore Detection. *Sensors Actuators B Chem.* **2018**, *276*, 114–120. <https://doi.org/10.1016/j.snb.2018.08.031>.
- (20) Idil, N.; Mattiasson, B. Imprinting of Microorganisms for Biosensor Applications. *Sensors* **2017**, *17* (4), 1–15. <https://doi.org/10.3390/s17040708>.

- (21) Xie, Z.; Zhang, L.; Chen, Y.; Hu, X. Magnetic Molecularly Imprinted Polymer Combined with High-Performance Liquid Chromatography for the Selective Separation and Determination of Glutathione in Various Wild Edible Boletes. *Food Anal. Methods* **2019**, *12*, 2908–2919. <https://doi.org/10.1007/s12161-019-01646-w>.
- (22) Hroboňová, K.; Lomenova, A. Molecularly Imprinted Polymer as Stationary Phase for HPLC Separation of Phenylalanine Enantiomers. *Monatsh. Chem.* **2018**, *149*, 939–946. <https://doi.org/10.1007/s00706-018-2155-5>.
- (23) Boysen, R. I. Advances in the Development of Molecularly Imprinted Polymers for the Separation and Analysis of Proteins with Liquid Chromatography. *J. Sep. Sci.* **2019**, *42*, 51–71. <https://doi.org/10.1002/jssc.201800945>.
- (24) Sánchez-González, J.; Odoardi, S.; Bermejo, A. M.; Bermejo-Barrera, P.; Romolo, F. S.; Moreda-Piñeiro, A.; Strano-Rossi, S. Development of a Micro-Solid-Phase Extraction Molecularly Imprinted Polymer Technique for Synthetic Cannabinoids Assessment in Urine Followed by Liquid Chromatography–Tandem Mass Spectrometry. *J. Chromatogr. A* **2018**, *1550*, 8–20. <https://doi.org/10.1016/j.chroma.2018.03.049>.
- (25) Kurczewska, J.; Cegłowski, M.; Pecyna, P.; Ratajczak, M.; Gajęcka, M.; Schroeder, G. Molecularly Imprinted Polymer as Drug Delivery Carrier in Alginate Dressing. *Mater. Lett.* **2017**, *201*, 46–49. <https://doi.org/10.1016/j.matlet.2017.05.008>.
- (26) Luliński, P. Molecularly Imprinted Polymers Based Drug Delivery Devices: A Way to Application in Modern Pharmacotherapy. A Review. *Mater. Sci. Eng. C* **2017**, *76*, 1344–1353. <https://doi.org/10.1016/j.msec.2017.02.138>.
- (27) Bodoki, A. E.; Iacob, B.-C.; Bodoki, E. Perspectives of Molecularly Imprinted Polymer-Based Drug Delivery Systems in Cancer Therapy. *Polymers*. **2019**, *11* (12), 2085. <https://doi.org/10.3390/polym11122085>.
- (28) Medina Rangel, P. X.; Laclef, S.; Xu, J.; Panagiotopoulou, M.; Kovensky, J.; Tse Sum Bui, B.; Haupt, K. Solid-Phase Synthesis of Molecularly Imprinted Polymer Nanolabels: Affinity Tools for Cellular Bioimaging of Glycans. *Sci. Rep.* **2019**, *9*, 3923. <https://doi.org/10.1038/s41598-019-40348-5>.
- (29) Wang, H.-Y.; Cao, P.-P.; He, Z.-Y.; He, X.-W.; Li, W.-Y.; Li, Y.-H.; Zhang, Y.-K. Targeted Imaging and Targeted Therapy of Breast Cancer Cells: Via Fluorescent Double Template-Imprinted Polymer Coated Silicon Nanoparticles by an Epitope Approach. *Nanoscale* **2019**, *11* (36), 17018–17030. <https://doi.org/10.1039/c9nr04655k>.

- (30) Panagiotopoulou, M.; Kunath, S.; Medina-Rangel, P. X.; Haupt, K.; Tse Sum Bui, B. Fluorescent Molecularly Imprinted Polymers as Plastic Antibodies for Selective Labeling and Imaging of Hyaluronan and Sialic Acid on Fixed and Living Cells. *Biosens. Bioelectron.* **2017**, *88*, 85–93. <https://doi.org/10.1016/j.bios.2016.07.080>.
- (31) Nestora, S.; Merlier, F.; Beyazit, S.; Prost, E.; Duma, L.; Baril, B.; Greaves, A.; Haupt, K.; Tse Sum Bui, B. Plastic Antibodies for Cosmetics: Molecularly Imprinted Polymers Scavenge Precursors of Malodors. *Angew. Chemie Int. Ed.* **2016**, *55* (21), 6252–6256. <https://doi.org/10.1002/anie.201602076>.
- (32) Wang, R.; Pan, J.; Qin, M.; Guo, T. Molecularly Imprinted Nanocapsule Mimicking Phosphotriesterase for the Catalytic Hydrolysis of Organophosphorus Pesticides. *Eur. Polym. J.* **2019**, *110*, 1–8. <https://doi.org/10.1016/j.eurpolymj.2018.10.045>.
- (33) Mohamed, S.; Balieu, S.; Petit, E.; Galas, L.; Schapman, D.; Hardouin, J.; Baati, R.; Estour, F. A Versatile and Recyclable Molecularly Imprinted Polymer as an Oxidative Catalyst of Sulfur Derivatives: A New Possible Method for Mustard Gas and V Nerve Agent Decontamination. *Chem. Commun.* **2019**, *55* (88), 13243–13246. <https://doi.org/10.1039/c9cc04928b>.
- (34) Mathew, D.; Thomas, B.; Devaky, K. S. Design, Synthesis and Characterization of Enzyme-Analogue-Built Polymer Catalysts as Artificial Hydrolases. *Artif. Cells Nanomed. Biotechnol.* **2019**, *47* (1), 1149–1172. <https://doi.org/10.1080/21691401.2019.1576703>.
- (35) Rico-Yuste, A.; Carrasco, S. Molecularly Imprinted Polymer-Based Hybrid Materials for the Development of Optical Sensors. *Polymers* **2019**, *11* (7), 1173. <https://doi.org/10.3390/polym11071173>.
- (36) Saylan, Y.; Akgönüllü, S.; Yavuz, H.; Ünal, S.; Denizli, A. Molecularly Imprinted Polymer Based Sensors for Medical Applications. *Sensors* **2019**, *19* (6), 1279. <https://doi.org/10.3390/s19061279>.
- (37) Uzun, L.; Turner, A. P. F. Molecularly-Imprinted Polymer Sensors: Realising Their Potential. *Biosens. Bioelectron.* **2016**, *76*, 131–144. <https://doi.org/10.1016/j.bios.2015.07.013>.
- (38) Polyakov, M. V. Adsorption Properties and Structure of Silica Gel. *Zhurnal Fizieskoj Khimii/Akademiya SSSR* **1931**, *2*, 799–805.
- (39) Alexander, C.; Andersson, H. S.; Andersson, L. I.; Ansell, R. J.; Kirsch, N.; Nicholls, I. A.; O'Mahony, J.; Whitcombe, M. J. Molecular Imprinting Science and Technology: A Survey of the Literature for the Years up to and Including 2003. *J. Mol. Recognit.* **2006**, *19* (2), 106–180. <https://doi.org/10.1002/jmr.760>.

- (40) Andersson, H. S.; Nicholls, I. A. A Historical Perspective of the Development of Molecular Imprinting. In *Molecularly imprinted polymers: Man-made mimics of antibodies and their applications in analytical chemistry*; Sellergren, B., Ed.; Elsevier Science B.V.: Amsterdam, 2001; pp 1–2.
- (41) Pauling, L. A Theory of the Structure and Process of Formation of Antibodies. *J. Am. Chem. Soc.* **1940**, *62* (10), 2643–2657. <https://doi.org/10.1021/ja01867a018>.
- (42) Dickey, F. The Preparation of Specific Adsorbents. *Proc. Natl. Acad. Sci.* **1949**, *35* (5), 227–229.
- (43) Haldeman, R. G.; Emmett, P. H. Specific Adsorption of Alkyl Orange Dyes on Silica Gel. *J. Phys. Chem.* **1955**, *59* (10), 1039–1043.
- (44) Curti, R.; Colombo, U. Chromatography of Stereoisomers with “Tailor Made” Compounds. *J. Am. Chem. Soc.* **1952**, *74* (15), 3961.
- (45) Beckett, A. H.; Anderson, P. The Determination of the Relative Configuration of Morphine, Levorphanol and Laevo-Phenazocine by Stereoselective Adsorbents. *J. Pharm. Pharmacol.* **1960**, *12*, 228T-236T.
- (46) Wulff, G.; Sarhan, A. The Use of Polymers with Enzyme-Analogous Structures for the Resolution of Racemates. *Angew. Chem. Int. Ed.* **1972**, *11* (4), 341. <https://doi.org/10.1002/anie.197203341>.
- (47) Nishide, H.; Deguchi, J.; Tsuchida, E. Selective Adsorption of Metal Ions on Crosslinked Poly(Vinylpyridine) Resin Prepared With a Metal Ion As a Template. *Chem. Lett.* **1976**, *5* (2), 169–174. <https://doi.org/10.1246/cl.1976.169>.
- (48) Arshady, R.; Mosbach, K. Synthesis of Substrate-Selective Polymers by Host-Guest Polymerization. *Macromol. Chem. Phys.* **1981**, *187*, 687–692.
- (49) Glad, M.; Norrlöw, O.; Sellergren, B.; Siegbahn, N.; Mosbach, K. Use of Silane Monomers for Molecular Imprinting and Enzyme Entrapment in Polysiloxane-Coated Porous Silica. *J. Chromatogr. A* **1985**, *347* (C), 11–23. [https://doi.org/10.1016/S0021-9673\(01\)95465-2](https://doi.org/10.1016/S0021-9673(01)95465-2).
- (50) Sellergren, B.; Ekberg, B.; Mosbach, K. Molecular Imprinting of Amino Acid Derivatives in Macroporous Polymers. Demonstration of Substrate- and Enantio-Selectivity by Chromatographic Resolution of Racemic Mixtures of Amino Acid Derivatives. *J. Chromatogr. A* **1985**, *347* (C), 1–10. [https://doi.org/10.1016/S0021-9673\(01\)95464-0](https://doi.org/10.1016/S0021-9673(01)95464-0).
- (51) Wulff, G.; Heide, B.; Helfmeier, G. Enzyme-Analogue Built Polymers, 24 On the Distance Accuracy of Functional Groups in Polymers and Silicas Introduced by a Template Approach. *React. Polym. Ion Exch. Sorbents* **1987**, *6* (2–3), 299–310. <https://doi.org/10.1016/0167->

- 6989(87)90101-2.
- (52) Shea, K. J.; Sasaki, D. Y.; Stoddard, G. J. Fluorescence Probes for Evaluating Chain Solvation in Network Polymers. An Analysis of the Solvatochromic Shift of the Dansyl Probe in Macroporous Styrene-Divinylbenzene and Styrene-Diisopropenylbenzene Copolymers. *Macromolecules* **1989**, *22* (4), 1722–1730. <https://doi.org/10.1021/ma00194a037>.
- (53) Shea, K. J.; Thompson, E. A.; Pandey, S. D.; Beauchamp, P. S. Template Synthesis of Macromolecules. Synthesis and Chemistry of Functionalized Macroporous Polydivinylbenzene. *J. Am. Chem. Soc.* **1980**, *102* (9), 3149–3155. <https://doi.org/10.1021/ja00529a044>.
- (54) Wulff, G.; Schulze, I. Enzyme–Analogue Built Polymers. IX. Polymers with Mercapto Groups of Definite Cooperativity. *Isr. J. Chem.* **1978**, *17* (4), 291–297. <https://doi.org/10.1002/ijch.197800053>.
- (55) Beyazit, S.; Tse Sum Bui, B.; Haupt, K.; Gonzato, C. Molecularly Imprinted Polymer Nanomaterials and Nanocomposites by Controlled/Living Radical Polymerization. *Prog. Polym. Sci.* **2016**, *62*, 1–21. <https://doi.org/10.1016/j.progpolymsci.2016.04.001>.
- (56) Włoch, M.; Datta, J. Synthesis and Polymerisation Techniques of Molecularly Imprinted Polymers. In *Comprehensive Analytical Chemistry*; Marć, M., Ed.; Elsevier B.V., 2019; Vol. 86, pp 17–40. <https://doi.org/10.1016/bs.coac.2019.05.011>.
- (57) Sellergren, B.; Andersson, L. Molecular Recognition in Macroporous Polymers Prepared by a Substrate Analogue Imprinting Strategy. *J. Org. Chem.* **1990**, *55* (10), 3381–3383. <https://doi.org/10.1021/jo00297a074>.
- (58) Whitcombe, M. J.; Rodriguez, M. E.; Villar, P.; Vulfson, E. N. A New Method for the Introduction of Recognition Site Functionality into Polymers Prepared by Molecular Imprinting: Synthesis and Characterization of Polymeric Receptors for Cholesterol. *J. Am. Chem. Soc.* **1995**, *117* (27), 7105–7111. <https://doi.org/10.1021/ja00132a010>.
- (59) Parisi, O. I.; Ruffo, M.; Puoci, F. Molecularly Imprinted Polymers for Selective Recognition in Regenerative Medicine. In *Nanostructured Biomaterials for Regenerative Medicine*; Guarino, V., Iafisco, M., Spriano, S., Eds.; Elsevier Ltd., 2020; pp 141–163. <https://doi.org/10.1016/B978-0-08-102594-9.00005-X>.
- (60) Li, S.; Cao, S.; Whitcombe, M. J.; Piletsky, S. A. Size Matters: Challenges in Imprinting Macromolecules. *Prog. Polym. Sci.* **2014**, *39* (1), 145–163. <https://doi.org/10.1016/j.progpolymsci.2013.10.002>.

- (61) Turiel, E.; Esteban, A. M. Molecularly Imprinted Polymers. In *Solid-Phase Extraction*; Poole, C., Ed.; Elsevier Inc., 2020; pp 215–233. <https://doi.org/10.1016/B978-0-12-816906-3.00008-X>.
- (62) Li, J.; Wei, G.; Zhang, Y. Molecularly Imprinted Polymers as Recognition Elements in Sensors. In *Molecularly Imprinted Sensors*; Li, S., Ge, Y., Piletsky, S., Lunec, J., Eds.; Elsevier B.V.: Oxford, 2012; pp 35–55. <https://doi.org/10.1016/B978-0-444-56331-6.00002-5>.
- (63) Cormack, P. A. G.; Elorza, A. Z. Molecularly Imprinted Polymers: Synthesis and Characterisation. *J. Chromatogr. B* **2004**, *804* (1), 173–182. <https://doi.org/10.1016/j.jchromb.2004.02.013>.
- (64) Golker, K.; Nicholls, I. A. The Effect of Crosslinking Density on Molecularly Imprinted Polymer Morphology and Recognition. *Eur. Polym. J.* **2016**, *75*, 423–430. <https://doi.org/10.1016/j.eurpolymj.2016.01.008>.
- (65) Sellergren, B. Molecular Imprinting by Noncovalent Interactions: Enantioselectivity and Binding Capacity of Polymers Prepared under Conditions Favoring the Formation of Template Complexes. *Makromol. Chem.* **1989**, *190* (11), 2703–2711. <https://doi.org/10.1002/macp.1989.021901104>.
- (66) Haupt, K.; Linares, A. V.; Bompert, M.; Tse Sum Bui, B. Molecularly Imprinted Polymers. In *Topics in Current Chemistry*; Haupt, K., Ed.; Springer-Verlag: Berlin Heidelberg, 2012; Vol. 325, pp 1–26. <https://doi.org/10.1007/978-3-642-28421-2>.
- (67) Vasapollo, G.; Sole, R. Del; Mergola, L.; Lazoi, M. R.; Scardino, A.; Scorrano, S.; Mele, G. Molecularly Imprinted Polymers: Present and Future Prospective. *Int. J. Mol. Sci.* **2011**, *12* (9), 5908–5945. <https://doi.org/10.3390/ijms12095908>.
- (68) Shakerian, F.; Kim, K. H.; Kwon, E.; Szulejko, J. E.; Kumar, P.; Dadfarnia, S.; Haji Shabani, A. M. Advanced Polymeric Materials: Synthesis and Analytical Application of Ion Imprinted Polymers as Selective Sorbents for Solid Phase Extraction of Metal Ions. *Trends Anal. Chem.* **2016**, *83*, 55–69. <https://doi.org/10.1016/j.trac.2016.08.001>.
- (69) Adumitrăchioaie, A.; Tertiş, M.; Cernat, A.; Săndulescu, R.; Cristea, C. Electrochemical Methods Based on Molecularly Imprinted Polymers for Drug Detection. A Review. *Int. J. Electrochem. Sci.* **2018**, *13* (3), 2556–2576. <https://doi.org/10.20964/2018.03.75>.
- (70) Nabavi, S. A.; Vladisavljević, G. T.; Zhu, Y.; Manović, V. Synthesis of Size-Tunable CO<sub>2</sub>-Philic Imprinted Polymeric Particles (MIPs) for Low-Pressure CO<sub>2</sub> Capture Using Oil-in-Oil Suspension Polymerization. *Environ. Sci. Technol.* **2017**, *51* (19), 11476–11483. <https://doi.org/10.1021/acs.est.7b03259>.

- (71) Zourob, M.; Mohr, S.; Mayes, A. G.; Macaskill, A.; Pérez-Moral, N.; Fielden, P. R.; Goddard, N. J. A Micro-Reactor for Preparing Uniform Molecularly Imprinted Polymer Beads. *Lab Chip* **2006**, *6* (2), 296–301. <https://doi.org/10.1039/b513195b>.
- (72) Haupt, K.; Medina Rangel, P. X.; Tse Sum Bui, B. Molecularly Imprinted Polymers: Antibody Mimics for Bioimaging and Therapy. *Chem. Rev.* **2020**, *120* (17), 9554–9582. <https://doi.org/10.1021/acs.chemrev.0c00428>.
- (73) Sharma, P. S.; Pietrzyk-Le, A.; D'Souza, F.; Kutner, W. Electrochemically Synthesized Polymers in Molecular Imprinting for Chemical Sensing. *Anal. Bioanal. Chem.* **2012**, *402*, 3177–3204. <https://doi.org/10.1007/s00216-011-5696-6>.
- (74) Ambrosini, S.; Beyazit, S.; Haupt, K.; Tse Sum Bui, B. Solid-Phase Synthesis of Molecularly Imprinted Nanoparticles for Protein Recognition. *Chem. Commun.* **2013**, *49* (60), 6746–6748. <https://doi.org/10.1039/c3cc41701h>.
- (75) Hoshino, Y.; Kodama, T.; Okahata, Y.; Shea, K. J. Peptide Imprinted Polymer Nanoparticles: A Plastic Antibody. *J. Am. Chem. Soc.* **2008**, *130* (46), 15242–15243. <https://doi.org/10.1021/ja8062875>.
- (76) Székely, A.; Klussmann, M. Molecular Radical Chain Initiators for Ambient- to Low-Temperature Applications. *Chem. Asian J.* **2019**, *14* (1), 105–115. <https://doi.org/10.1002/asia.201801636>.
- (77) Ehlers, F.; Barth, J.; Vana, P. Kinetics and Thermodynamics of Radical Polymerization. In *Fundamentals of Controlled/Living Radical Polymerization*; Tsarevsky, N., Sumerlin, B., Eds.; The Royal Society of Chemistry, 2013; pp 1–59. <https://doi.org/10.1039/9781849737425-00001>.
- (78) O'Shannessy, D. J.; Ekberg, B.; Mosbach, K. Molecular Imprinting of Amino Acid Derivatives at Low Temperature (0°C) Using Photolytic Homolysis of Azobisnitriles. *Anal. Biochem.* **1989**, *177* (1), 144–149. [https://doi.org/10.1016/0003-2697\(89\)90029-8](https://doi.org/10.1016/0003-2697(89)90029-8).
- (79) Söylemez, M. A.; Güven, O. Preparation and Detailed Structural Characterization of Penicillin G Imprinted Polymers by PALS and XPS. *Radiat. Phys. Chem.* **2019**, *159*, 174–180. <https://doi.org/10.1016/j.radphyschem.2019.02.050>.
- (80) Lu, Y.; Li, C.; Wang, X.; Sun, P.; Xing, X. Influence of Polymerization Temperature on the Molecular Recognition of Imprinted Polymers. *J. Chromatogr. B* **2004**, *804* (1), 53–59. <https://doi.org/10.1016/j.jchromb.2003.10.013>.
- (81) Piletsky, S. A.; Piletska, E. V.; Karim, K.; Freebairn, K. W.; Legge, C. H.; Turner, A. P. F. Polymer

- Cookery: Influence of Polymerization Conditions on the Performance of Molecularly Imprinted Polymers. *Macromolecules* **2002**, *35* (19), 7499–7504.  
<https://doi.org/10.1021/ma0205562>.
- (82) Quinn, J. F.; Davis, T. P.; Barner, L.; Barner-Kowollik, C. The Application of Ionizing Radiation in Reversible Addition-Fragmentation Chain Transfer (RAFT) Polymerization: Renaissance of a Key Synthetic and Kinetic Tool. *Polymer*. **2007**, *48* (22), 6467–6480.  
<https://doi.org/10.1016/j.polymer.2007.08.043>.
- (83) Chen, M.; Zhong, M.; Johnson, J. A. Light-Controlled Radical Polymerization: Mechanisms, Methods, and Applications. *Chem. Rev.* **2016**, *116* (17), 10167–10211.  
<https://doi.org/10.1021/acs.chemrev.5b00671>.
- (84) Zhang, H. Recent Advances in Macromolecularly Imprinted Polymers by Controlled Radical Polymerization Techniques. *Mol. Imprinting* **2015**, *3* (1), 35–46.  
<https://doi.org/10.1515/molim-2015-0005>.
- (85) Zhang, H. Controlled/"living" Radical Precipitation Polymerization: A Versatile Polymerization Technique for Advanced Functional Polymers. *Eur. Polym. J.* **2013**, *49* (3), 579–600.  
<https://doi.org/10.1016/j.eurpolymj.2012.12.016>.
- (86) Salián, V. D.; Vaughan, A. D.; Byrne, M. E. The Role of Living/Controlled Radical Polymerization in the Formation of Improved Imprinted Polymers. *J. Mol. Recognit.* **2012**, *25* (6), 361–369. <https://doi.org/10.1002/jmr.2168>.
- (87) Corrigan, N.; Yeow, J.; Judzewitsch, P.; Xu, J.; Boyer, C. Seeing the Light: Advancing Materials Chemistry through Photopolymerization. *Angew. Chem. Int. Ed.* **2019**, *58* (16), 5170–5189.  
<https://doi.org/10.1002/anie.201805473>.
- (88) Dietlin, C.; Schweizer, S.; Xiao, P.; Zhang, J.; Morlet-Savary, F.; Graff, B.; Fouassier, J. P.; Lalevée, J. Photopolymerization upon LEDs: New Photoinitiating Systems and Strategies. *Polym. Chem.* **2015**, *6* (21), 3895–3912. <https://doi.org/10.1039/c5py00258c>.
- (89) Frick, E.; Schweigert, C.; Noble, B. B.; Ernst, H. A.; Lauer, A.; Liang, Y.; Voll, D.; Coote, M. L.; Unterreiner, A. N.; Barner-Kowollik, C. Toward a Quantitative Description of Radical Photoinitiator Structure-Reactivity Correlations. *Macromolecules* **2016**, *49* (1), 80–89.  
<https://doi.org/10.1021/acs.macromol.5b02336>.
- (90) Michaudel, Q.; Kottisch, V.; Fors, B. P. Cationic Polymerization: From Photoinitiation to Photocontrol. *Angew. Chem. Int. Ed.* **2017**, *56* (33), 9670–9679.  
<https://doi.org/10.1002/anie.201701425>.



- (91) Salian, V. D.; White, C. J.; Byrne, M. E. Molecularly Imprinted Polymers via Living Radical Polymerization: Relating Increased Structural Homogeneity to Improved Template Binding Parameters. *React. Funct. Polym.* **2014**, *78*, 38–46.  
<https://doi.org/10.1016/j.reactfunctpolym.2014.02.003>.
- (92) Bompart, M.; Haupt, K. Molecularly Imprinted Polymers and Controlled/Living Radical Polymerization. *Aust. J. Chem.* **2009**, *62* (8), 751–761. <https://doi.org/10.1071/CH09124>.
- (93) Karaca, N.; Temel, G.; Karaca Balta, D.; Aydin, M.; Arsu, N. Preparation of Hydrogels by Photopolymerization of Acrylates in the Presence of Type I and One-Component Type II Photoinitiators. *J. Photochem. Photobiol. A* **2010**, *209* (1), 1–6.  
<https://doi.org/10.1016/j.jphotochem.2009.09.017>.
- (94) Barner-Kowollik, C.; Vana, P.; Davis, T. P. The Kinetics of Free-Radical Polymerization. In *Handbook of Radical Polymerization*; Matyjaszewski, K., Davis, T. P., Eds.; John Wiley & Sons, Inc.: Hoboken, 2002; pp 187–261. <https://doi.org/10.1002/0471220450.ch4>.
- (95) Beyazit, S.; Ambrosini, S.; Marchyk, N.; Palo, E.; Kale, V.; Soukka, T.; Tse Sum Bui, B.; Haupt, K. Versatile Synthetic Strategy for Coating Upconverting Nanoparticles with Polymer Shells through Localized Photopolymerization by Using the Particles as Internal Light Sources. *Angew. Chem. Int. Ed.* **2014**, *53* (34), 8919–8923. <https://doi.org/10.1002/anie.201403576>.
- (96) Bagheri, A.; Jin, J. Photopolymerization in 3D Printing. *ACS Appl. Polym. Mater.* **2019**, *1* (4), 593–611. <https://doi.org/10.1021/acscapm.8b00165>.
- (97) Esen, D. S.; Temel, G.; Balta, D. K.; Allonas, X.; Arsu, N. One-Component Thioxanthone Acetic Acid Derivative Photoinitiator for Free Radical Polymerization. *Photochem. Photobiol.* **2014**, *90* (2), 463–469. <https://doi.org/10.1111/php.12218>.
- (98) Shao, J.; Huang, Y.; Fan, Q. Polymer Chemistry Photopolymerization : Status , Development And Challenges. *Polym. Chem.* **2014**, *5*, 4195–4210. <https://doi.org/10.1039/c4py00072b>.
- (99) Tar, H.; Sevinc Esen, D.; Aydin, M.; Ley, C.; Arsu, N.; Allonas, X. Panchromatic Type II Photoinitiator for Free Radical Polymerization Based on Thioxanthone Derivative. *Macromolecules* **2013**, *46* (9), 3266–3272. <https://doi.org/10.1021/ma302641d>.
- (100) Allushi, A.; Kutahya, C.; Aydogan, C.; Kreutzer, J.; Yilmaz, G.; Yagci, Y. Conventional Type II Photoinitiators as Activators for Photoinduced Metal-Free Atom Transfer Radical Polymerization. *Polym. Chem.* **2017**, *8* (12), 1972–1977. <https://doi.org/10.1039/c7py00114b>.
- (101) Mokbel, H.; Graff, B.; Dumur, F.; Lalevée, J. NIR Sensitizer Operating under Long Wavelength (1064 Nm) for Free Radical Photopolymerization Processes. *Macromol. Rapid Commun.* **2020**,

- 41 (15), 1–5. <https://doi.org/10.1002/marc.202000289>.
- (102) Andrzejewska, E. Free Radical Photopolymerization of Multifunctional Monomers. In *Three-Dimensional Microfabrication Using Two-photon Polymerization*; Baldacchini, T., Ed.; Elsevier Inc.: Oxford, 2016; pp 62–81. <https://doi.org/10.1016/B978-0-323-35321-2.00004-2>.
- (103) Urraca, J. L.; Barrios, C. A.; Canalejas-Tejero, V.; Orellana, G.; Moreno-Bondi, M. C. Molecular Recognition with Nanostructures Fabricated by Photopolymerization within Metallic Subwavelength Apertures. *Nanoscale* **2014**, *6* (15), 8656–8663. <https://doi.org/10.1039/c4nr01129e>.
- (104) Garcia-Soto, M. J.; Haupt, K.; Gonzato, C. Synthesis of Molecularly Imprinted Polymers by Photo-Iniferter Polymerization under Visible Light. *Polym. Chem.* **2017**, *8* (33), 4830–4834. <https://doi.org/10.1039/C7PY01113J>.
- (105) Abdollahi, E.; Abdouss, M.; Salami-Kalajahi, M.; Mohammadi, A. Molecular Recognition Ability of Molecularly Imprinted Polymer Nano- and Micro-Particles by Reversible Addition-Fragmentation Chain Transfer Polymerization. *Polym. Rev.* **2016**, *56* (4), 557–583. <https://doi.org/10.1080/15583724.2015.1119162>.
- (106) Kidakova, A.; Reut, J.; Rappich, J.; Öpik, A.; Syritski, V. Preparation of a Surface-Grafted Protein-Selective Polymer Film by Combined Use of Controlled/Living Radical Photopolymerization and Microcontact Imprinting. *React. Funct. Polym.* **2018**, *125*, 47–56. <https://doi.org/10.1016/j.reactfunctpolym.2018.02.004>.
- (107) Adali-Kaya, Z.; Tse Sum Bui, B.; Falcimaigne-Cordin, A.; Haupt, K. Molecularly Imprinted Polymer Nanomaterials and Nanocomposites: Atom-Transfer Radical Polymerization with Acidic Monomers. *Angew. Chem. Int. Ed.* **2015**, *54* (17), 5192–5195. <https://doi.org/10.1002/anie.201412494>.
- (108) Atilla Tasdelen, M.; Yagci, Y. Controlled/Living Radical Polymerization in the Presence of Iniferters. In *Fundamentals of Controlled/Living Radical Polymerization*; Tsarevsky, N., Sumerlin, B., Eds.; The Royal Society of Chemistry: Cambridge, 2013; pp 78–111. <https://doi.org/10.1039/9781849737425-00078>.
- (109) Tang, Y.; Liu, H.; Gao, J.; Liu, X.; Gao, X.; Lu, X.; Fang, G.; Wang, J.; Li, J. Upconversion Particle@Fe<sub>3</sub>O<sub>4</sub>@molecularly Imprinted Polymer with Controllable Shell Thickness as High-Performance Fluorescent Probe for Sensing Quinolones. *Talanta* **2018**, *181*, 95–103. <https://doi.org/10.1016/j.talanta.2018.01.006>.

- (110) Luo, Q.; Yu, N.; Shi, C.; Wang, X.; Wu, J. Surface Plasmon Resonance Sensor for Antibiotics Detection Based on Photo-Initiated Polymerization Molecularly Imprinted Array. *Talanta* **2016**, *161*, 797–803. <https://doi.org/10.1016/j.talanta.2016.09.049>.
- (111) Bakas, I.; Salmi, Z.; Jouini, M.; Geneste, F.; Mazerie, I.; Floner, D.; Carbonnier, B.; Yagci, Y.; Chehimi, M. M. Picomolar Detection of Melamine Using Molecularly Imprinted Polymer-Based Electrochemical Sensors Prepared by UV-Graft Photopolymerization. *Electroanalysis* **2015**, *27* (2), 429–439. <https://doi.org/10.1002/elan.201400382>.
- (112) Panagiotopoulou, M.; Beyazit, S.; Nestora, S.; Haupt, K.; Tse Sum Bui, B. Initiator-Free Synthesis of Molecularly Imprinted Polymers by Polymerization of Self-Initiated Monomers. *Polymer* **2015**, *66*, 43–51. <https://doi.org/10.1016/j.polymer.2015.04.012>.
- (113) Shiraki, Y.; Tsuruta, K.; Morimoto, J.; Ohba, C.; Kawamura, A.; Yoshida, R.; Kawano, R.; Uragami, T.; Miyata, T. Preparation of Molecule-Responsive Microsized Hydrogels via Photopolymerization for Smart Microchannel Microvalves. *Macromol. Rapid Commun.* **2015**, *36* (6), 515–519. <https://doi.org/10.1002/marc.201400676>.
- (114) Chen, J.; Bai, L. Y.; Liu, K. F.; Liu, R. Q.; Zhang, Y. P. Atrazine Molecular Imprinted Polymers: Comparative Analysis by Far-Infrared and Ultraviolet Induced Polymerization. *Int. J. Mol. Sci.* **2014**, *15* (1), 574–587. <https://doi.org/10.3390/ijms15010574>.
- (115) Ton, X. A.; Tse Sum Bui, B.; Resmini, M.; Bonomi, P.; Dika, I.; Soppera, O.; Haupt, K. A Versatile Fiber-Optic Fluorescence Sensor Based on Molecularly Imprinted Microstructures Polymerized in Situ. *Angew. Chem. Int. Ed.* **2013**, *52* (32), 8317–8321. <https://doi.org/10.1002/anie.201301045>.
- (116) Fuchs, Y.; Soppera, O.; Mayes, A. G.; Haupt, K. Holographic Molecularly Imprinted Polymers for Label-Free Chemical Sensing. *Adv. Mater.* **2013**, *25* (4), 566–570. <https://doi.org/10.1002/adma.201203204>.
- (117) Matyjaszewski, K. Atom Transfer Radical Polymerization (ATRP): Current Status and Future Perspectives. *Macromolecules* **2012**, *45* (10), 4015–4039. <https://doi.org/10.1021/ma3001719>.
- (118) Salian, V. D.; Byrne, M. E. Living Radical Polymerization and Molecular Imprinting: Improving Polymer Morphology in Imprinted Polymers. *Macromol. Mater. Eng.* **2013**, *298* (4), 379–390. <https://doi.org/10.1002/mame.201200191>.
- (119) Otsu, T. Iniferter Concept and Living Radical Polymerization. *J. Polym. Sci. A Polym. Chem.* **2000**, *38* (12), 2121–2136. [https://doi.org/10.1002/\(SICI\)1099-](https://doi.org/10.1002/(SICI)1099-)

- 0518(20000615)38:12<2121::AID-POLA10>3.0.CO;2-X.
- (120) Bonomi, P.; Attieh, M. D.; Gonzato, C.; Haupt, K. A New Versatile Water-Soluble Iniferter Platform for the Preparation of Molecularly Imprinted Nanoparticles by Photopolymerisation in Aqueous Media. *Chem. Eur. J.* **2016**, *22* (29), 10150–10154. <https://doi.org/10.1002/chem.201600750>.
- (121) Fors, B. P.; Hawker, C. J. Control of a Living Radical Polymerization of Methacrylates by Light. *Angew. Chem. Int. Ed.* **2012**, *51* (35), 8850–8853. <https://doi.org/10.1002/anie.201203639>.
- (122) Lee, I. H.; Discekici, E. H.; Anastasaki, A.; De Alaniz, J. R.; Hawker, C. J. Controlled Radical Polymerization of Vinyl Ketones Using Visible Light. *Polym. Chem.* **2017**, *8* (21), 3351–3356. <https://doi.org/10.1039/c7py00617a>.
- (123) Seo, S. E.; Discekici, E. H.; Zhang, Y.; Bates, C. M.; Hawker, C. J. Surface-Initiated PET-RAFT Polymerization under Metal-Free and Ambient Conditions Using Enzyme Degassing. *J. Polym. Sci. A Polym. Chem.* **2019**, 70–76. <https://doi.org/10.1002/pola.29438>.
- (124) Xu, J.; Jung, K.; Atme, A.; Shanmugam, S.; Boyer, C. A Robust and Versatile Photoinduced Living Polymerization of Conjugated and Unconjugated Monomers and Its Oxygen Tolerance. *J. Am. Chem. Soc.* **2014**, *136* (14), 5508–5519. <https://doi.org/10.1021/ja501745g>.
- (125) Shanmugam, S.; Xu, J.; Boyer, C. Exploiting Metalloporphyrins for Selective Living Radical Polymerization Tunable over Visible Wavelengths. *J. Am. Chem. Soc.* **2015**, *137* (28), 9174–9185. <https://doi.org/10.1021/jacs.5b05274>.
- (126) Shanmugam, S.; Xu, J.; Boyer, C. Light-Regulated Polymerization under near-Infrared/Far-Red Irradiation Catalyzed by Bacteriochlorophyll A. *Angew. Chem. Int. Ed.* **2016**, *55* (3), 1036–1040. <https://doi.org/10.1002/anie.201510037>.
- (127) Zhang, Z.; Corrigan, N.; Bagheri, A.; Jin, J.; Boyer, C. A Versatile 3D and 4D Printing System through Photocontrolled RAFT Polymerization Research Articles. *Angew. Chem. Int. Ed.* **2019**, *58* (50), 17954–17963. <https://doi.org/10.1002/anie.201912608>.
- (128) Shanmugam, S.; Xu, J.; Boyer, C. Photoinduced Electron Transfer-Reversible Addition-Fragmentation Chain Transfer (PET-RAFT) Polymerization of Vinyl Acetate and N-Vinylpyrrolidinone: Kinetic and Oxygen Tolerance Study. *Macromolecules* **2014**, *47* (15), 4930–4942. <https://doi.org/10.1021/ma500842u>.
- (129) Dadashi-Silab, S.; Doran, S.; Yagci, Y. Photoinduced Electron Transfer Reactions for Macromolecular Syntheses. *Chem. Rev.* **2016**, *116* (17), 10212–10275. <https://doi.org/10.1021/acs.chemrev.5b00586>.

- (130) Escudero, D. Revising Intramolecular Photoinduced Electron Transfer (PET) from First-Principles. *Acc. Chem. Res.* **2016**, *49* (9), 1816–1824.  
<https://doi.org/10.1021/acs.accounts.6b00299>.
- (131) Kameche, F.; Heni, W.; Telitel, S.; Ge, D.; Vidal, L.; Dumur, F.; Gigmes, D.; Lalevée, J.; Marguet, S.; Douillard, L.; Fiorini-Debuisschert, C.; Bachelot, R.; Soppera, O. Plasmon-Triggered Living Photopolymerization for Elaboration of Hybrid Polymer/Metal Nanoparticles. *Mater. Today* **2020**, *40*, 38–47. <https://doi.org/10.1016/j.mattod.2020.03.023>.
- (132) Zhang, H.; Salo, D.; Kim, D. M.; Komarov, S.; Tai, Y.-C.; Berezin, M. Y. Penetration Depth of Photons in Biological Tissues from Hyperspectral Imaging in Shortwave Infrared in Transmission and Reflection Geometries. *J. Biomed. Opt.* **2016**, *21* (12), 126006.  
<https://doi.org/10.1117/1.jbo.21.12.126006>.
- (133) Henderson, T. A.; Morris, L. D. Near-Infrared Photonic Energy Penetration: Can Infrared Phototherapy Effectively Reach the Human Brain? *Neuropsychiatr. Dis. Treat.* **2015**, *11*, 2191–2208. <https://doi.org/10.2147/NDT.S78182>.
- (134) Cao, J.; Zhu, B.; Zheng, K.; He, S.; Meng, L.; Song, J.; Yang, H. Recent Progress in NIR-II Contrast Agent for Biological Imaging. *Front. Bioeng. Biotechnol.* **2020**, *7*, 487.  
<https://doi.org/10.3389/fbioe.2019.00487>.
- (135) Strehmel, B.; Brömme, T.; Schmitz, C.; Reiner, K.; Ernst, S.; Keil, D. NIR-Dyes for Photopolymers and Laser Drying in the Graphic Industry. In *Dyes and Chromophores in Polymer Science*; Lalevée, J., Fouassier, J.-P., Eds.; John Wiley & Sons, Inc.: Hoboken, 2015; pp 213–249. <https://doi.org/10.1002/9781119006671.ch7>.
- (136) Nagtegale, P.; Galstian, T. V. Holographic Characterization of near Infra Red Photopolymerizable Materials. *Synth. Met.* **2002**, *127* (1–3), 85–87.  
[https://doi.org/10.1016/S0379-6779\(01\)00601-4](https://doi.org/10.1016/S0379-6779(01)00601-4).
- (137) Schmitz, C.; Halbhuber, A.; Keil, D.; Strehmel, B. NIR-Sensitized Photoinitiated Radical Polymerization and Proton Generation with Cyanines and LED Arrays. *Prog. Org. Coatings* **2016**, *100*, 32–46. <https://doi.org/10.1016/j.porgcoat.2016.02.022>.
- (138) Bonardi, A. H.; Bonardi, F.; Morlet-Savary, F.; Dietlin, C.; Noirbent, G.; Grant, T. M.; Fouassier, J. P.; Dumur, F.; Lessard, B. H.; Gigmes, D.; Lalevée, J. Photoinduced Thermal Polymerization Reactions. *Macromolecules* **2018**, *51* (21), 8808–8820.  
<https://doi.org/10.1021/acs.macromol.8b01741>.
- (139) Soppera, O.; Turck, C.; Lougnot, D. J. Fabrication of Micro-Optical Devices by Self-Guiding

- Photopolymerization in the near IR. *Opt. Lett.* **2009**, *34* (4), 461–463.  
<https://doi.org/10.1364/ol.34.000461>.
- (140) Dika, I.; Malval, J. P.; Soppera, O.; Bardinal, V.; Barat, D.; Turck, C.; Spangenberg, A.; Bruyant, A. Near-Infrared Photopolymerization: Initiation Process Assisted by Self-Quenching and Triplet-Triplet Annihilation of Excited Cyanine Dyes. *Chem. Phys. Lett.* **2011**, *515* (1–3), 91–95.  
<https://doi.org/10.1016/j.cplett.2011.08.091>.
- (141) Dika, I.; Diot, F.; Bardinal, V.; Malval, J.-P.; Ecoffet, C.; Bruyant, A.; Barat, D.; Reig, B.; Doucet, J.-B.; Camps, T.; Soppera, O. Near Infrared Photopolymer for Micro-Optics Applications. *J. Polym. Sci.* **2020**, *58* (13), 1–14. <https://doi.org/10.1002/pol.20200106>.
- (142) Bonardi, A.; Bonardi, F.; Noirbent, G.; Dumur, F.; Gigmes, D.; Dietlin, C.; Lalevée, J. Free-radical Polymerization upon Near-infrared Light Irradiation, Merging Photochemical and Photothermal Initiating Methods. *J. Polym. Sci.* **2020**, *58* (2), 300–308.  
<https://doi.org/10.1002/pol.20190079>.
- (143) Gomez, L. P. C.; Spangenberg, A.; Ton, X.-A.; Fuchs, Y.; Bokeloh, F.; Malval, J.-P.; Tse Sum Bui, B.; Thuau, D.; Ayela, C.; Haupt, K.; Soppera, O. Rapid Prototyping of Chemical Microsensors Based on Molecularly Imprinted Polymers Synthesized by Two-Photon Stereolithography. *Adv. Mater.* **2016**, *28*, 5931–5937. <https://doi.org/10.1002/adma.201600218>.
- (144) Fischer, J.; Mueller, J. B.; Kaschke, J.; Wolf, T. J. A.; Unterreiner, A.-N.; Wegener, M. Three-Dimensional Multi-Photon Direct Laser Writing with Variable Repetition Rate. *Opt. Express* **2013**, *21* (22), 26244. <https://doi.org/10.1364/oe.21.026244>.
- (145) Torgersen, J.; Mironov, A. O. V.; Pucher, N.; Qin, X.; Li, Z.; Cicha, K.; Machacek, T.; Liska, R.; Jantsch, V.; Stampfl, J. Photo-Sensitive Hydrogels for Three- Dimensional Laser Microfabrication in the Presence of Whole Organisms. *J. Biomed. Opt.* **2012**, *17* (10), 15–18.  
<https://doi.org/https://doi.org/10.1117/1.JBO.17.10.105008>.
- (146) Scherzer, T. Photopolymerization of Acrylates without Photoinitiators with Short-Wavelength UV Radiation: A Study with Real-Time Fourier Transform Infrared Spectroscopy. *J. Polym. Sci. A Polym. Chem.* **2004**, *42* (4), 894–901. <https://doi.org/10.1002/pola.11039>.
- (147) Khlifi, A.; Gam-Derouich, S.; Jouini, M.; Chehimi, M. M. Melamine-Imprinted Polymer Grafts through Surface Photopolymerization Initiated by Aryl Layers from Diazonium Salts. *Food Control* **2013**, *31* (2), 379–386. <https://doi.org/10.1016/j.foodcont.2012.10.013>.
- (148) Gam-Derouich, S.; Jouini, M.; Hassen-chehimi, D. Ben; Chehimi, M. M. Electrochimica Acta Aryl Diazonium Salt Surface Chemistry and Graft Photopolymerization for the Preparation of

- Molecularly Imprinted Polymer Biomimetic Sensor Layers. *Electrochim. Acta* **2012**, *73*, 45–52. <https://doi.org/10.1016/j.electacta.2011.11.022>.
- (149) Scherzer, T.; Knolle, W.; Naumov, S.; Mehnert, R. Direct Initiation of the Photopolymerization of Acrylates by Short-Wavelength Excimer UV Radiation. *Nucl. Instruments Methods Phys. Res. B* **2003**, *208*, 271–276. [https://doi.org/10.1016/S0168-583X\(03\)00620-7](https://doi.org/10.1016/S0168-583X(03)00620-7).
- (150) Paruli, E.; Griesser, T.; Merlier, F.; Gonzato, C.; Haupt, K. Molecularly Imprinted Polymers by Thiol–Yne Chemistry: Making Imprinting Even Easier. *Polym. Chem.* **2019**, *10* (34), 4732–4739. <https://doi.org/10.1039/c9py00403c>.
- (151) Tavares, L. S.; Carvalho, T. C.; Romão, W.; Vaz, B. G.; Chaves, A. R. Paper Spray Tandem Mass Spectrometry Based on Molecularly Imprinted Polymer Substrate for Cocaine Analysis in Oral Fluid. *J. Am. Soc. Mass Spectrom.* **2018**, *29* (3), 566–572. <https://doi.org/10.1007/s13361-017-1853-2>.
- (152) Luo, N.; Brian Hutchison, J.; Anseth, K. S.; Bowman, C. N. Synthesis of a Novel Methacrylic Monomer Iniferter and Its Application in Surface Photografting on Crosslinked Polymer Substrates. *J. Polym. Sci. A Polym. Chem.* **2002**, *40* (11), 1885–1891. <https://doi.org/10.1002/pola.10272>.
- (153) Çakir, P.; Cutivet, A.; Resmini, M.; Bui, B. T. S.; Haupt, K. Protein-Size Molecularly Imprinted Polymer Nanogels as Synthetic Antibodies, by Localized Polymerization with Multi-Initiators. *Adv. Mater.* **2013**, *25* (7), 1048–1051. <https://doi.org/10.1002/adma.201203400>.
- (154) Marchyk, N.; Maximilien, J.; Beyazit, S.; Haupt, K.; Sum Bui, B. T. One-Pot Synthesis of Iniferter-Bound Polystyrene Core Nanoparticles for the Controlled Grafting of Multilayer Shells. *Nanoscale* **2014**, *6* (5), 2872–2878. <https://doi.org/10.1039/c3nr05295h>.
- (155) Tom, J. C.; Brilmayer, R.; Schmidt, J.; Andrieu-Brunsen, A. Optimisation of Surface-Initiated Photoiniferter-Mediated Polymerisation under Confinement, and the Formation of Block Copolymers in Mesoporous Films. *Polymers.* **2017**, *9* (10), 4–8. <https://doi.org/10.3390/polym9100539>.
- (156) Jing, L.; Zhang, Q.; Wang, Y.; Liu, X.; Wei, T. Surface Plasmon Resonance Sensor for Theophylline Using a Water-Compatible Molecularly Imprinted Film. *Anal. Methods* **2016**, *8* (11), 2349–2356. <https://doi.org/10.1039/C6AY00028B>.
- (157) Rubens, M.; Latsrisaeng, P.; Junkers, T. Visible Light-Induced Iniferter Polymerization of Methacrylates Enhanced by Continuous Flow. *Polym. Chem.* **2017**, *8* (42), 6496–6505. <https://doi.org/10.1039/c7py01157a>.

- (158) Benedikt, S.; Moszner, N.; Liska, R. Benzoyl Phenyltelluride as Highly Reactive Visible-Light TERP- Reagent for Controlled Radical Polymerization. *Macromolecules* **2014**, *47* (16), 5526–5531.
- (159) Ding, C.; Fan, C.; Jiang, G.; Zhang, J.; Li, X.; Li, N.; Pan, X.; Zhang, Z.; Zhang, W.; Zhu, J.; Zhu, X. Diselenide Mediated Controlled Radical Polymerization under Visible Light Irradiation: Mechanism Investigation and  $\alpha,\omega$ -Ditelechellic Polymers. *Polym. Chem.* **2015**, *6* (35), 6416–6423. <https://doi.org/10.1039/c5py00803d>.
- (160) Cai, J.; Chen, T.; Xu, Y.; Wei, S.; Huang, W.; Liu, R.; Liu, J. A Versatile Signal-Enhanced ECL Sensing Platform Based on Molecular Imprinting Technique via PET-RAFT Cross-Linking Polymerization Using Bifunctional Ruthenium Complex as Both Catalyst and Sensing Probes. *Biosens. Bioelectron.* **2019**, *124–125*, 15–24. <https://doi.org/10.1016/j.bios.2018.09.083>.
- (161) Pandey, S.; Bodas, D. High-Quality Quantum Dots for Multiplexed Bioimaging: A Critical Review. *Adv. Colloid Interface Sci.* **2020**, *278*, 102137. <https://doi.org/10.1016/j.cis.2020.102137>.
- (162) Sumanth Kumar, D.; Jai Kumar, B.; Mahesh, H. M. Quantum Nanostructures (QDs): An Overview. In *Synthesis of Inorganic Nanomaterials*; Bhagyaraj, S. M., Oluwafemi, O. S., Kalarikkal, N., Thomas, S., Eds.; Woodhead Publishing, 2018; pp 59–88. <https://doi.org/10.1016/b978-0-08-101975-7.00003-8>.
- (163) Berry, C. C. Applications of Inorganic Nanoparticles for Biotechnology. In *Frontiers of Nanoscience*; de la Fuente, J. M., Grazu, V., Eds.; Elsevier LTD., 2012; Vol. 4, pp 159–180. <https://doi.org/10.1016/B978-0-12-415769-9.00006-6>.
- (164) Panagiotopoulou, M.; Salinas, Y.; Beyazit, S.; Kunath, S.; Duma, L.; Prost, E.; Mayes, A. G.; Resmini, M.; Tse, B.; Bui, S.; Haupt, K. Molecularly Imprinted Polymer Coated Quantum Dots for Multiplexed Cell Targeting and Imaging. *Angew. Chemie - Int. Ed.* **2016**, *55*, 8244–8248. <https://doi.org/10.1002/anie.201601122>.
- (165) Demir, B.; Lemberger, M. M.; Panagiotopoulou, M.; Medina Rangel, P. X.; Timur, S.; Hirsch, T.; Tse Sum Bui, B.; Wegener, J.; Haupt, K. Tracking Hyaluronan: Molecularly Imprinted Polymer Coated Carbon Dots for Cancer Cell Targeting and Imaging. *ACS Appl. Mater. Interfaces* **2018**, *10* (4), 3305–3313. <https://doi.org/10.1021/acsami.7b16225>.
- (166) Bossi, A. M.; Haupt, K. Tailoring a Dress to Single Protein Molecules: Proteins Can Do It Themselves through Localized Photo-Polymerization and Molecular Imprinting. *Chem. Eur. J.* **2020**, *26* (64), 14556–14559. <https://doi.org/10.1002/chem.202002787>.



- (167) Zhu, X.; Zhang, J.; Liu, J.; Zhang, Y. Recent Progress of Rare-Earth Doped Upconversion Nanoparticles: Synthesis, Optimization, and Applications. *Adv. Sci.* **2019**, *6* (22), 1901358. <https://doi.org/10.1002/advs.201901358>.
- (168) Wen, S.; Zhou, J.; Zheng, K.; Bednarkiewicz, A.; Liu, X.; Jin, D. Advances in Highly Doped Upconversion Nanoparticles. *Nat. Commun.* **2018**, *9*, 2415. <https://doi.org/10.1038/s41467-018-04813-5>.
- (169) Rocheva, V. V.; Koroleva, A. V.; Savelyev, A. G.; Khaydukov, K. V.; Generalova, A. N.; Nechaev, A. V.; Guller, A. E.; Semchishen, V. A.; Chichkov, B. N.; Khaydukov, E. V. High-Resolution 3D Photopolymerization Assisted by Upconversion Nanoparticles for Rapid Prototyping Applications. *Sci. Rep.* **2018**, *8*, 3663. <https://doi.org/10.1038/s41598-018-21793-0>.
- (170) Chiappini, A.; Pasquardini, L.; Bossi, A. M. Molecular Imprinted Polymers Coupled to Photonic Structures in Biosensors: The State of Art. *Sensors* **2020**, *20* (18), 5069. <https://doi.org/10.3390/s20185069>.
- (171) Yang, J. C.; Shin, H. K.; Hong, S. W.; Park, J. Y. Lithographically Patterned Molecularly Imprinted Polymer for Gravimetric Detection of Trace Atrazine. *Sens. Actuators, B Chem.* **2015**, *216*, 476–481. <https://doi.org/10.1016/j.snb.2015.04.079>.
- (172) Ertürk, G.; Mattiasson, B. Molecular Imprinting Techniques Used for the Preparation of Biosensors. *Sensors* **2017**, *17* (2), 288. <https://doi.org/10.3390/s17020288>.
- (173) Trotta, F.; Biasizzo, M.; Caldera, F. Molecularly Imprinted Membranes. *Membranes*. **2012**, *2* (3), 440–477. <https://doi.org/10.3390/membranes2030440>.
- (174) Fuchs, Y.; Soppera, O.; Haupt, K. Photopolymerization and Photostructuring of Molecularly Imprinted Polymers for Sensor Applications-A Review. *Anal. Chim. Acta* **2012**, *717*, 7–20. <https://doi.org/10.1016/j.aca.2011.12.026>.
- (175) Hulanicki, A.; Glab, S.; Ingman, F. Chemical Sensors Definitions and Classification. *Pure Appl. Chem.* **1991**, *63* (9), 1247–1250. <https://doi.org/10.1351/pac199163091247>.
- (176) Tran, K. T. M.; Nguyen, T. D. Lithography-Based Methods to Manufacture Biomaterials at Small Scales. *J. Sci. Adv. Mater. Devices* **2017**, *2* (1), 1–14. <https://doi.org/10.1016/j.jsamd.2016.12.001>.
- (177) Aasime, A.; Hamouda, F. Conventional and Un-Conventional Lithography for Fabricating Thin Film Functional Devices. In *Modern technologies for creating the thin-film systems and coatings*; Nikitenkov, N., Ed.; IntechOpen, 2017; pp 43–58. <https://doi.org/http://dx.doi.org/10.5772/57353>.

- (178) Higuera, G. A.; Truckenmüller, R. K.; Zhang, R.; Pernagallo, S.; Guillemot, F.; Moroni, L. Upscaling of High-Throughput Material Platforms in Two and Three Dimensions. In *Materiomics: High-Throughput Screening of Biomaterial Properties*; de Boer, J., van Blitterswijk, C., Eds.; Cambridge University Press: Cambridge, 2013; pp 133–154. <https://doi.org/10.1017/CBO9781139061414.009>.
- (179) Traub, M. C.; Longsine, W.; Truskett, V. N. Advances in Nanoimprint Lithography. *Annu. Rev. Chem. Biomol. Eng.* **2016**, *7* (1), 583–604. <https://doi.org/10.1146/annurev-chembioeng-080615-034635>.
- (180) Hasan, R. M. M.; Luo, X. Promising Lithography Techniques for Next-Generation Logic Devices. *Nanomanufacturing Metrol.* **2018**, *1*, 67–81. <https://doi.org/10.1007/s41871-018-0016-9>.
- (181) Madou, M. J. *Manufacturing Techniques for Microfabrication and Nanotechnology*, 1st ed.; CRC Press: Boca Raton, 2011. <https://doi.org/https://doi.org/10.1201/9781439895306>.
- (182) Lawson, R. A.; Robinson, A. P. G. Overview of Materials and Processes for Lithography. In *Frontiers of Nanoscience*; Robinson, A. P. G., Lawson, R. A., Eds.; Elsevier Ltd., 2016; Vol. 11, pp 1–90. <https://doi.org/10.1016/B978-0-08-100354-1.00001-6>.
- (183) Papadopoulos, C. *Nanofabrication: Principles and Applications*; Springer Nature: Victoria, 2016. <https://doi.org/10.4324/9780203489680-7>.
- (184) Sakai, K. High-Index Immersion Lithography. In *Recent Advances in Nanofabrication Techniques and Applications*; Cui, B., Ed.; IntechOpen, 2011; pp 397–416. <https://doi.org/10.5772/23630>.
- (185) Kwak, M. K.; Guo, L. J. Phase-Shift Lithography. In *Encyclopedia of Microfluidics and Nanofluidics*; Springer Science+Business Media, 2014; pp 1–10. <https://doi.org/10.1007/978-3-642-27758-0>.
- (186) Sanders, D. P. Advances in Patterning Materials for 193 Nm Immersion Lithography. *Chem. Rev.* **2010**, *110* (1), 321–360. <https://doi.org/10.1021/cr900244n>.
- (187) Martinez-Chapa, S. O.; Salazar, A.; Madou, M. J. Two-Photon Polymerization as a Component of Desktop Integrated Manufacturing Platforms. In *Three-Dimensional Microfabrication Using Two-Photon Polymerization: Fundamentals, Technology, and Applications*; Baldacchini, T., Ed.; Elsevier Inc., 2016; pp 374–416. <https://doi.org/10.1016/B978-0-323-35321-2.00019-4>.
- (188) Fourkas, J. T. Fundamentals of Two-Photon Fabrication. In *Three-Dimensional Microfabrication Using Two-Photon Polymerization*; Baldacchini, T., Ed.; Elsevier Inc., 2016;

- pp 45–61. <https://doi.org/10.1016/B978-0-323-35321-2/00003-0>.
- (189) Bertsch, A.; Renaud, P. Microstereolithography. In *Three-Dimensional Microfabrication Using Two-Photon Polymerization*; Baldacchini, T., Ed.; Elsevier Inc., 2016; pp 20–44. <https://doi.org/10.1016/B978-0-323-35321-2/00002-9>.
- (190) Spangenberg, A.; Hobeika, N.; Stehlin, F.; Malval, J.-P.; Wieder, F.; Prabhakaran, P.; Baldeck, P.; Soppera, O. Recent Advances in Two-Photon Stereolithography. In *Updates in advanced lithography*; Hosaka, S., Ed.; IntechOpen, 2013; pp 35–63. <https://doi.org/10.5772/56165>.
- (191) Gan, Z.; Cao, Y.; Evans, R. A.; Gu, M. Three-Dimensional Deep Sub-Diffraction Optical Beam Lithography with 9 Nm Feature Size. *Nat. Commun.* **2013**, *4*, 2061. <https://doi.org/10.1038/ncomms3061>.
- (192) Haske, W.; Chen, V. W.; Hales, J. M.; Dong, W.; Barlow, S.; Marder, S. R.; Perry, J. W. 65 nm Feature Sizes Using Visible Wavelength 3-D Multiphoton Lithography. *Opt. Express* **2007**, *15* (6), 3426. <https://doi.org/10.1364/oe.15.003426>.
- (193) Jiang, L.; Xiong, W.; Zhou, Y.; Liu, Y.; Huang, X.; Li, D.; Baldacchini, T.; Jiang, L.; Lu, Y. Performance Comparison of Acrylic and Thiol-Acrylic Resins in Two-Photon Polymerization. *Opt. Express* **2016**, *24* (12), 13687. <https://doi.org/10.1364/oe.24.013687>.
- (194) Liu, Y.; Wang, H.; Ho, J.; Ng, R. C.; Ng, R. J. H.; Hall-Chen, V. H.; Koay, E. H. H.; Dong, Z.; Liu, H.; Qiu, C.-W.; Greer, J. R.; Yang, J. K. W. Structural Color Three-Dimensional Printing by Shrinking Photonic Crystals. *Nat. Commun.* **2019**, *10*, 4340. <https://doi.org/10.1038/s41467-019-12360-w>.
- (195) Fuchs, Y.; Linares, A. V.; Mayes, A. G.; Haupt, K.; Soppera, O. Ultrathin Selective Molecularly Imprinted Polymer Microdots Obtained by Evanescent Wave Photopolymerization. *Chem. Mater.* **2011**, *23* (16), 3645–3651. <https://doi.org/10.1021/cm2009829>.
- (196) Milosevic, M. On the Nature of the Evanescent Wave. *Appl. Spectrosc.* **2013**, *67* (2), 126–131. <https://doi.org/10.1366/12-06707>.
- (197) Taitt, C. R.; Anderson, G. P.; Ligler, F. S. Evanescent Wave Fluorescence Biosensors: Advances of the Last Decade. *Biosens. Bioelectron.* **2016**, *76*, 103–112. <https://doi.org/10.1016/j.bios.2015.07.040>.
- (198) Zhou, X.; Soppera, O.; Plain, J.; Jradi, S.; Wei Sun, X.; Volkan Demir, H.; Yang, X.; Deeb, C.; Gray, S. K.; Wiederrecht, G. P.; Bachelot, R. Plasmon-Based Photopolymerization: Near-Field Probing, Advanced Photonic Nanostructures and Nanophotochemistry. *J. Opt.* **2014**, *16* (11), 114002. <https://doi.org/10.1088/2040-8978/16/11/114002>.

- (199) Deeb, C.; Ecoffet, C.; Bachelot, R.; Plain, J.; Bouhelier, A.; Soppera, O. Plasmon-Based Free-Radical Photopolymerization: Effect of Diffusion on Nanolithography Processes. *J. Am. Chem. Soc.* **2011**, *133* (27), 10535–10542. <https://doi.org/10.1021/ja201636y>.
- (200) Ibn El Ahrach, H.; Bachelot, R.; Vial, A.; Léron del, G.; Plain, J.; Royer, P.; Soppera, O. Spectral Degeneracy Breaking of the Plasmon Resonance of Single Metal Nanoparticles by Nanoscale Near-Field Photopolymerization. *Phys. Rev. Lett.* **2007**, *98* (10), 1–4. <https://doi.org/10.1103/PhysRevLett.98.107402>.
- (201) Ge, D.; Marguet, S.; Issa, A.; Jradi, S.; Nguyen, T. H.; Nahra, M.; Béal, J.; Deturche, R.; Chen, H.; Blaize, S.; Plain, J.; Fiorini, C.; Douillard, L.; Soppera, O.; Dinh, X. Q.; Dang, C.; Yang, X.; Xu, T.; Wei, B.; Sun, X. W.; Couteau, C.; Bachelot, R. Hybrid Plasmonic Nano-Emitters with Controlled Single Quantum Emitter Positioning on the Local Excitation Field. *Nat. Commun.* **2020**, *11*, 3414. <https://doi.org/10.1038/s41467-020-17248-8>.
- (202) Ali, M. Y.; Hung, W. N. P. Micromachining. In *Comprehensive Materials Finishing*; Hashmi, M. S. J., Ed.; Elsevier Inc., 2017; Vol. 1, pp 322–343. <https://doi.org/10.1016/B978-0-12-803581-8.09156-6>.
- (203) Guillon, S.; Lemaire, R.; Linares, A. V.; Haupt, K.; Ayela, C. Single Step Patterning of Molecularly Imprinted Polymers for Large Scale Fabrication of Microbiochips. *Lab Chip* **2009**, *9* (20), 2987–2991. <https://doi.org/10.1039/b905608d>.
- (204) Boysen, R. I.; Li, S.; Chowdhury, J.; Schwarz, L. J.; Hearn, M. T. W. Selectivity Optimisation of Biomimetic Molecularly Imprinted Polymer Thin Film. *Microelectron. Eng.* **2012**, *97*, 81–84. <https://doi.org/10.1016/j.mee.2012.03.026>.
- (205) Li, L.; Lu, Y.; Bie, Z.; Chen, H. Y.; Liu, Z. Photolithographic Boronate Affinity Molecular Imprinting: A General and Facile Approach for Glycoprotein Imprinting. *Angew. Chem. Int. Ed.* **2013**, *52* (29), 7451–7454. <https://doi.org/10.1002/anie.201207950>.
- (206) Dezest, D.; Leïchlé, T.; Teerapanich, P.; Matthieu, F.; Tse Sum Bui, B.; Haupt, K.; Nicu, L. Multiplexed Functionalization of Nanoelectromechanical Systems with Photopatterned Molecularly Imprinted Polymers. *J. Micromech. Microeng.* **2019**, *29* (2), 025013. <https://doi.org/https://doi.org/10.1088/1361-6439/aaf84e>.
- (207) Linares, A. V.; Falcimaigne-Cordin, A.; Gheber, L. A.; Haupt, K. Patterning Nanostructured, Synthetic, Polymeric Receptors by Simultaneous Projection Photolithography, Nanomolding, and Molecular Imprinting. *Small* **2011**, *7* (16), 2318–2325. <https://doi.org/10.1002/smll.201100248>.

- (208) LaFratta, C. N.; Fourkas, J. T.; Baldacchini, T.; Farrer, R. A. Multiphoton Fabrication. *Angew. Chem. Int. Ed.* **2007**, *46* (33), 6238–6258. <https://doi.org/10.1002/anie.200603995>.
- (209) Wu, Y.; Chen, R.; Zhao, G.; Chen, X.; Qu, X.; Liu, Y. Effect of Graphite Particles as Additive on the Curing Behaviour of  $\beta$ -Tricalcium Phosphate Suspensions and Scaffold Fabrication by Digital Light Processing. *J. Eur. Ceram. Soc.* **2020**, *40* (12), 4323–4331. <https://doi.org/10.1016/j.jeurceramsoc.2020.05.013>.
- (210) Sun, C.; Zhang, X. Experimental and Numerical Investigations on Microstereolithography of Ceramics. *J. Appl. Phys.* **2002**, *92* (8), 4796–4802. <https://doi.org/10.1063/1.1503410>.
- (211) Conrad, P. G.; Nishimura, P. T.; Aherne, D.; Schwartz, B. J.; Wu, D.; Fang, N.; Zhang, X.; Roberts, M. J.; Shea, K. J. Functional Molecularly Imprinted Polymer Microstructures Fabricated Using Microstereolithography. *Adv. Mater.* **2003**, *15* (18), 1541–1544. <https://doi.org/10.1002/adma.200304602>.
- (212) Ovsianikov, A.; Chichkov, B. N. Two-Photon Polymerization - High Resolution 3D Laser Technology and Its Applications. In *Nanoelectronics and Photonics: From Atoms to Materials, Devices and Architectures*; Korkin, A., Rosei, F., Eds.; Springer Science+Business Media, LLC: New York, 2008; pp 427–446.
- (213) Crowe, J. A.; El-Tamer, A.; Nagel, D.; Koroleva, A. V.; Madrid-Wolff, J.; Olarte, O. E.; Sokolovsky, S.; Estevez-Priego, E.; Ludl, A.-A.; Soriano, J.; Loza-Alvarez, P.; Chichkov, B. N.; Hill, E. J.; Parri, H. R.; Rafailov, E. U. Development of Two-Photon Polymerised Scaffolds for Optical Interrogation and Neurite Guidance of Human iPSC-Derived Cortical Neuronal Networks. *Lab Chip* **2020**, *20* (10), 1792–1806. <https://doi.org/10.1039/c9lc01209e>.
- (214) Trautmann, A.; R uth, M.; Lemke, H.-D.; Walther, T.; Hellmann, R. Two-Photon Polymerization Based Large Scaffolds for Adhesion and Proliferation Studies of Human Primary Fibroblasts. *Opt. Laser Technol.* **2018**, *106*, 474–480. <https://doi.org/10.1016/j.optlastec.2018.05.008>.
- (215) Lee, M. R.; Phang, I. Y.; Cui, Y.; Lee, Y. H.; Ling, X. Y. Shape-Shifting 3D Protein Microstructures with Programmable Directionality via Quantitative Nanoscale Stiffness Modulation. *Small* **2015**, *11* (6), 740–748. <https://doi.org/10.1002/smll.201401343>.
- (216) Parkatzidis, K.; Chatzinikolaidou, M.; Koufakis, E.; Kaliva, M.; Farsari, M.; Vamvakaki, M. Multi-Photon Polymerization of Bio-Inspired, Thymol-Functionalized Hybrid Materials with Biocompatible and Antimicrobial Activity. *Polym. Chem.* **2020**, *11* (25), 4078–4083. <https://doi.org/10.1039/d0py00281j>.
- (217) Saha, S. K.; Oakdale, J. S.; Cuadra, J. A.; Divin, C.; Ye, J.; Forien, J. B.; Bayu Aji, L. B.; Biener, J.;

- Smith, W. L. Radiopaque Resists for Two-Photon Lithography to Enable Submicron 3D Imaging of Polymer Parts via X-Ray Computed Tomography. *ACS Appl. Mater. Interfaces* **2018**, *10* (1), 1164–1172. <https://doi.org/10.1021/acsami.7b12654>.
- (218) Thiele, S.; Pruss, C.; Herkommer, A. M.; Giessen, H. 3D Printed Stacked Diffractive Microlenses. *Opt. Express* **2019**, *27* (24), 35621–35630. <https://doi.org/10.1364/oe.27.035621>.
- (219) Wang, H.; Liu, Y.; Ruan, Q.; Liu, H.; Ng, R. J. H.; Tan, Y. S.; Wang, H.; Li, Y.; Qiu, C.-W.; Yang, J. K. W. Off-Axis Holography with Uniform Illumination via 3D Printed Diffractive Optical Elements. *Adv. Opt. Mater.* **2019**, *7* (12), 1900068. <https://doi.org/10.1002/adom.201900068>.
- (220) Lewis, A.; Taha, H.; Strinkovski, A.; Manevitch, A.; Khatchatourians, A.; Dekhter, R.; Ammann, E. Near-Field Optics: From Subwavelength Illumination to Nanometric Shadowing. *Nat. Biotechnol.* **2003**, *21* (11), 1378–1386. <https://doi.org/10.1038/nbt898>.
- (221) Greffet, J. J.; Carminati, R. Image Formation in Near-Field Optics. *Prog. Surf. Sci.* **1997**, *56* (3), 133–237. [https://doi.org/10.1016/S0079-6816\(98\)00004-5](https://doi.org/10.1016/S0079-6816(98)00004-5).

## Chapter 2

# THIOL-YNE CHEMISTRY FOR MOLECULAR IMPRINTING

## Chapter 2: THIOL-YNE CHEMISTRY FOR MOLECULAR IMPRINTING

---

---

### 1. Introduction

As outlined in Chapter 1, light is a powerful tool for the photostructuring of polymers in general, and in particular of molecularly imprinted polymers (MIPs), for different applications such as chemical sensors. Among the photostructuring techniques, two-photon stereolithography (TPS) stands out as a particularly attractive one due to its mask-less, direct and precise fabrication of 3D structures with a resolution in the range of a few hundred nanometers. In fact, Chia Gomez et al. demonstrated for the first time the use of TPS for the synthesis of MIPs, in the form of microcantilevers.<sup>1</sup> Inspired by this innovation, we aspired to explore limits of TPS and in particular, to fabricate MIPs of submicron dimensions, which their group did not explore although this could unlock interesting optical properties that can be useful in molecular sensing as will be explained further in Chapter 3.

In this context, it appeared that a possible limitation of the combination of MIP synthesis with their micro or nanostructuring is the low oxygen tolerance of the free radical polymerization (FRP) reaction. Oxygen molecules react with the active radicals in a FRP to form peroxy radicals which tend to terminate the polymerization prematurely. Indeed, from a synthetic point of view, a great majority of MIPs is nowadays obtained *via* free-radical polymerization (FRP) of (meth)acrylates. This polymerization technique represents a convenient way to MIPs, thanks to its tolerance to reagent purity, flexibility in terms of experimental setups and to the wide range of commercially available functional monomers.<sup>2</sup> Nonetheless, its main drawback lies in oxygen inhibition, which requires the reaction to take place under oxygen-free conditions. However, it may be difficult to operate the specialized equipment that is often used for micro and nanofabrication under inert atmosphere. One of the possible solutions to this problem would be to use an alternative polymerization approach that is not, or less, sensitive to oxygen but that is still easy and straightforward to perform and allows to adopt as many of the common MIP precursors as possible. Thereby, a promising option appeared to be the thiol-yne reaction. The chemistry of this reaction allows it to be tolerant to oxygen, making it possible to perform radical polymerization in an open-air setup. Moreover, it has additional advantages including the possibility of a high degree of crosslinking through the use of multi-functional monomers and low shrinkage stress.

In this chapter, we demonstrate how the use of radical-mediated thiol-yne chemistry perfectly matches the above requirements. To test this method with MIPs, their synthesis via precipitation



polymerization at open air while taking advantage of its resistance to oxygen was hence performed for the first time.

To the best of our knowledge, only one manuscript has been published on thiol-yne MIPs: in their attempt to imprint hypericin *via* “click-type” approaches, Pei and coworkers observed that thiol-yne is far more effective than azide-alkyne.<sup>3</sup> However, the authors ran their polymerization under nitrogen atmosphere, and did not consider the use of conventional vinyl monomers, which would have been of great interest to the imprinting community.

Thiol-yne, similarly to the more popular thiol-ene, is an oxygen-tolerant reaction, based on the hydrothiolation of an unsaturated bond.<sup>4-6</sup> However, while peroxy radicals, which are formed upon addition of radical to molecular oxygen, are relatively unreactive in the polymerization of vinyls,<sup>7</sup> they are reactive enough to abstract a hydrogen from a thiol,<sup>8</sup> thus continuing the main propagation step in thiol-yne/ene mechanisms. Overall, a thiol-yne reaction consists of the addition of a thiol to an alkyne, as depicted in Figure 2.1. Nevertheless, the resulting vinyl sulfide can ideally undergo, depending on steric hindrance and experimental conditions, a second thiol addition, so that thiol-yne could be considered a step beyond thiol-ene. Therefore, it is not surprising that (meth)acrylates can successfully be incorporated into thiol-yne scaffolds too.<sup>9</sup> This represents a great advantage for the imprinting community, since the whole, well-established library of template-functional monomer(s) pairs developed over the years by the imprinters would then be amenable to this technique. Thereby, thiol-yne chemistry is expected to afford MIPs with more rigid structures compared to thiol-ene, as suggested by the superior mechanical properties and higher glass transition temperatures shown by these matrices.<sup>10,11</sup>

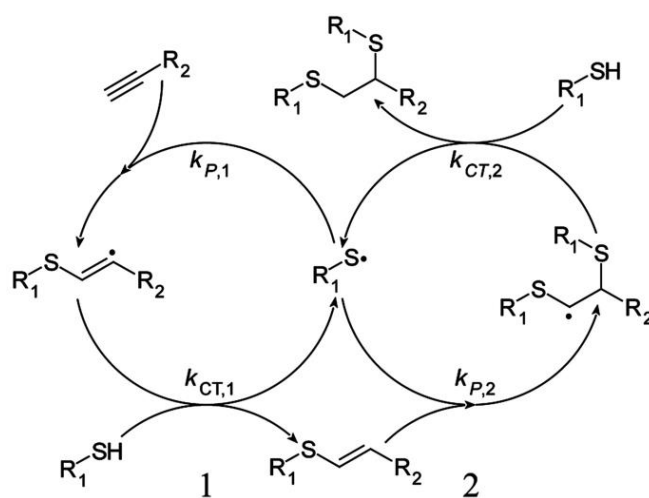


Figure 2.1. Schematic representation of the thiol-yne mechanism. Reprinted with permission from the American Chemical Society.<sup>11</sup>

The  $\beta$ -antagonist drug propranolol is a common model template in the MIP field, as its imprinting using (meth)acrylic acid in either acetonitrile or toluene is well established (e.g. ref. <sup>12</sup>). For this reason, it has often been used as a model template during the development of new synthetic approaches,<sup>13–15</sup> or in comparative studies on MIPs.<sup>16</sup> Additionally, it does not contain any reactive double bond which may be incompatible with imprinting *via* thiol-yne chemistry. Indeed, thiols add to low reactive bonds too, such as unsubstituted alkenes, which are normally less prone to radical polymerization than (meth)acrylates<sup>17</sup> (i.e. the thiol-ene reaction). Thus, templates bearing double bonds which do not normally participate to the radical polymerization of (meth)acrylates, may react and covalently attach to the MIP, which might limit, or even prevent, the formation of suitable binding cavities.

While the use of a thiol (such as mercapto-propionic acid) or an alkyne (such as propargylacetic acid) would have been an obvious choice for a functional monomer involved in a thiol-yne reaction,<sup>3</sup> we thought that acrylates (such as acrylic acid) would be much more interesting, considering the large amount of knowledge accumulated over the years by the imprinting community with this class of monomers. These monomers have been reported to react with thiols, and oxygen tolerance is expected to rise for relatively low thiol amounts<sup>9</sup> (i.e. ranging from 1 – 10 % wt.).

Nevertheless, thiol-yne differs from free-radical polymerization in terms of reaction mechanism, as it mainly proceeds by step-growth, rather than chain-growth mechanism. Thus, we were also interested in testing a recipe formulating high amounts of thiol, in order to highlight possible differences with the conventional, free-radical approach arising from the different reaction mechanisms. Thiol-yne-(meth)acrylate ternary systems were reported to afford mixed “step/chain-growth” mechanisms involving homopolymerization of (meth)acrylates and chain-transfer to the thiol. Therefore, this hybrid mechanism (Figure 2. 2) is different from that occurring in pure thiol-ene/yne formulations. Nonetheless, Bowman and co-workers showed that formulating “thiol-yne-vinyl” ternary mixtures with acrylates rather than methacrylates, makes chain transfer to the thiol more competitive with homopolymerization, thus increasing the overall hybrid step/chain-growth character, leading to fuller conversions of the thiols and alkyne bonds and to more homogeneous polymer networks.<sup>18</sup>

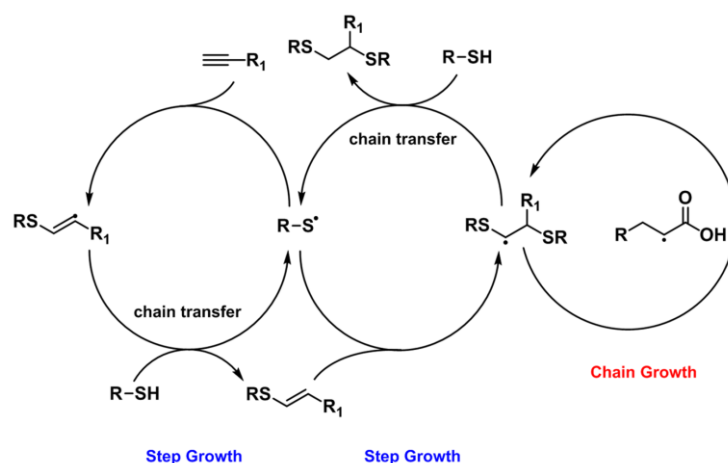


Figure 2. 2. Proposed mechanism for polymerization via the thiol-yne reaction showing its chain growth and step growth cycles.

Herein, we report on the synthesis of imprinted microspheres *via* radical-mediated, thiol-yne polymerization, using propranolol as model template<sup>13,19</sup> and acrylic acid as functional monomer. The cross-linker was based on a stoichiometric mixture of two different polythiols, pentaerythritol tetra(3-mercaptopropionate) (PETMP) and dipentaerythritol hexa(3-mercaptopropionate) (diPETMP) and a dialkyne, di(but-1-yne-4-yl)carbonate (DBC), as shown in Figure 2. 3. The polymerization was run with low power, near-visible UV light in open vials in the presence of oxygen.

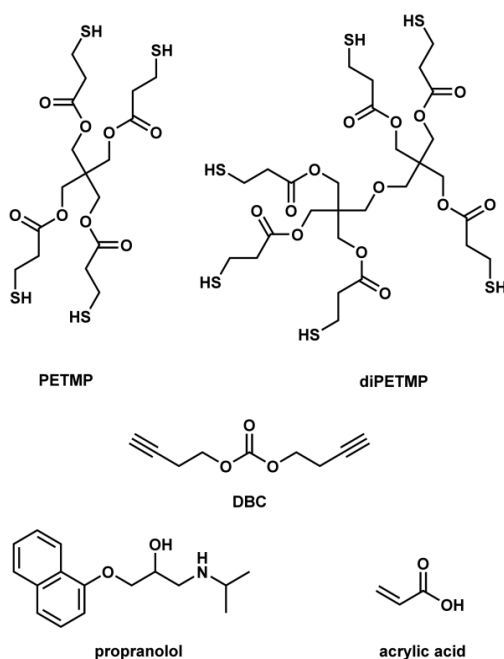


Figure 2. 3. Structures of the template propranolol and the monomers used.

## 2. Experimental

### 2.1. Chemicals

(±)-Propranolol hydrochloride ( $\geq 99\%$ ), anhydrous acetonitrile (99.8%), methacrylic acid (MAA) (99%), pentaerythritol triacrylate (PETA) and ethylene glycol dimethacrylate (EGDMA) (98%) were purchased from Sigma-Aldrich. Di(but-1-yne-4-yl)carbonate (DBC) was synthesized as previously reported.<sup>10</sup> THIOCURE<sup>®</sup> pentaerythritol tetra(3-mercaptopropionate) (PETMP) and THIOCURE<sup>®</sup> dipentaerythritol hexa(3-mercaptopropionate) (diPETMP) were from Bruno Bock Chemische Fabrik GmbH & Co. KG. Methanol and glacial acetic acid were from VWR Chemicals. Acrylic acid (AA) (99.5%) was from Acros Organics. Omnirad ethyl (2,4,6-trimethylbenzoyl) phenylphosphinate (Omnirad TPO-L) was from IGM Resins. Acetone (AR grade) was obtained from Biosolve. 2,2'-azobis(2,4-dimethylvaleronitrile) (ABDV) was from DuPont Chemicals. Tetrahydrofuran-*d*<sub>8</sub> (d8-THF) was from Euriso-top. Propranolol hydrochloride was converted into free base by extracting from a sodium carbonate solution at pH 9 into chloroform.

### 2.2. Synthesis of thiol-yne polymers

Propranolol-imprinted microspheres (MIP) were prepared by thiol-yne precipitation polymerization as follows: in a 20 mL glass vial, propranolol (25.93 mg, 100  $\mu\text{mol}$ ), acrylic acid (58.23 mg, 800  $\mu\text{mol}$ ), DBC (174.50 mg, 1050  $\mu\text{mol}$ ) and PETMP (642.97 mg, 1250  $\mu\text{mol}$ ) or diPETMP (652.54 mg, 833  $\mu\text{mol}$ ) were dissolved in acetonitrile (9.2 mL). Upon addition of Omnirad TPO-L (15.98 mg, 50  $\mu\text{mol}$ ) as an initiator, photo-polymerization was induced by exposing the open vial to 365-nm UV light (1.6 mW/cm<sup>2</sup>) for 5 minutes at room temperature. The resulting polymer particles were then homogenized on a Precellys<sup>®</sup>24 homogenizer (Bertin Instruments, Montigny-le-Bretonneux, France) and washed with three rounds each of methanol:acetic acid (3:1 v/v), methanol, and acetone, until no residual template could be detected in the supernatant. The polymer was finally dried overnight at reduced pressure (i.e. 8 mbar).

Non-imprinted, reference microspheres (NIP) were synthesized based on the same protocol except that propranolol was omitted.

### 2.3. Synthesis of reference (meth)acrylic scaffolds

Poly(acrylic acid-co-pentaerythritol triacrylate) p(AA-co-PETA) nanoparticles were synthesized by precipitation polymerization as follows: in a 20 mL glass vial, acrylic acid (29.12 mg, 400  $\mu\text{mol}$ ), PETA (402.69 mg, 1350  $\mu\text{mol}$ ) and TPO-L (14.22 mg, 45  $\mu\text{mol}$ ) were dissolved in 17.8 mL acetonitrile. The vial

was then closed with an air-tight silicon cap and the mixture was purged with nitrogen for 15 min. Polymerization was induced by exposing the sealed vial to 365-nm UV light ( $1.6 \text{ mW/cm}^2$ ) for 15 hours at room temperature. The resulting polymer was washed with three rounds each of methanol:acetic acid (3:1 v/v), methanol, and acetone. The polymer was dried overnight at reduced pressure (i.e. 8 mbar).

Poly(methacrylic acid-co-ethyleneglycol dimethacrylate) p(MAA-co-EGDMA) nanoparticles were obtained by precipitation polymerization as follows: in a 20 mL glass vial, methacrylic acid (27.82 mg, 320  $\mu\text{mol}$ ), EGDMA (317.15 mg, 1600  $\mu\text{mol}$ ) and azobis(2,4-dimethyl)valeronitrile ABDV (8.74 mg, 35.2  $\mu\text{mol}$ ) were dissolved in acetonitrile (4.4 mL). The vial was then sealed with an air-tight silicon cap and the mixture was purged with nitrogen for 15 min. The pre-polymerization mixture was immersed overnight in a pre-heated oil bath at  $60^\circ\text{C}$ . The polymerization was stopped upon exposure to air and the resulting polymer was washed with three rounds each of methanol:acetic acid (3:1 v/v), methanol, and acetone. The polymer was dried at reduced pressure (i.e. 8 mbar).

#### 2.4. Characterization of the thiol-yne MIPs

FTIR spectra were recorded in attenuated total reflection (ATR) mode on a Nicolet iS5 FTIR spectrometer (Thermo Fisher Scientific, USA) from  $4000 \text{ cm}^{-1}$  to  $400 \text{ cm}^{-1}$  with a resolution of  $4 \text{ cm}^{-1}$  over 16 scans.

$^1\text{H-NMR}$  spectra of the products of alkaline hydrolysis in  $d_8\text{-THF}$  were recorded on a 400MHz Bruker spectrometer at  $25^\circ\text{C}$ .

Scanning electron microscopy (SEM) images were recorded on a QUANTA FEG 250 on gold sputter coated samples.

BET surface area measurements were performed using a 3Flex surface characterization analyzer (Micromeritics, France) with dinitrogen as an adsorbate at 77 K. Samples were degassed under vacuum at room temperature for at least 15 h prior to analysis.

Size-exclusion chromatography/high-resolution mass spectrometry (SEC/HRMS) analyses were performed with 3 columns Aquagel-50, Aquagel-40 (300 x 7.5 mm id, 8  $\mu\text{m}$ ) (Agilent technologies, France) and Polysep-GFC-P 2000 (300 x 7.8 mm id) (Phenomenex, Le Pecq, France). The eluent consisted of 0.1% (v/v) TFA in water at a flow rate of 0.8 mL/min. The sample was slowly acidified to  $\text{pH} = 5$  using hydrochloric acid before injecting 20  $\mu\text{L}$  for measurement.

Positive and negative ion electrospray mass spectra were acquired by scan mode, scanning from  $m/z$  100 to 3200 at electrospray voltage -3800 V and +3800 V respectively. Fragmentor voltage was 100 V. Nitrogen was nebulized at 12.0 L/min under  $2.068 \cdot 10^5$  Pa and heated at 300 °C.

### 2.5. Equilibrium binding assays

Imprinted (MIP) and non-imprinted (NIP) microspheres were suspended in acetonitrile in polypropylene Eppendorf tubes to concentrations ranging from 0.05 to 1 mg/mL in 1  $\mu$ M solutions of either propranolol or atenolol. The dispersions were incubated for 12 hours on a Stuart tube rotator at room temperature. After centrifugation, the fluorescence of the supernatant was measured on a HORIBA fluorolog spectrofluorometer to determine the free unbound template ( $n = 3$ ). Two different settings were used, respectively, for propranolol ( $\lambda_{\text{ex}} = 300$  nm, slit = 2 nm,  $\lambda_{\text{em}} = 380$  nm, slit = 3 nm) and atenolol ( $\lambda_{\text{ex}} = 289$  nm, slit = 2 nm,  $\lambda_{\text{em}} = 305$  nm, slit = 3 nm). The amount of bound molecule was then calculated by subtracting the amount of unbound molecule from that initially added.

### 2.6. Hydrolytic degradation of the thiol-yne MIPs

The MIP stability was determined by incubation in NaOH and HCl aqueous solutions at a polymer concentration of 5 mg/mL. Turbidity measurements were performed by monitoring the % transmittance over the time at 500 nm with an Agilent Cary 60 UV-Vis spectrophotometer (Agilent Technologies).

Hydrolysis products were analyzed by FTIR as follows: the pH of the basic solutions was slowly adjusted to 4 - 5 with hydrochloric acid. The aqueous solutions were then extracted thrice by diethyl ether. The organic phase was dried over  $\text{Na}_2\text{SO}_4$  and the solvent was removed by rotary evaporation. The crude extract was then transferred onto the ATR crystal for recording the spectra.

## 3. Results and discussion

The synthetic conditions that we applied for the synthesis of p(AA-co-PETMP-co-DBC) and p(AA-co-diPETMP-co-DBC) propranolol imprinted microspheres were very convenient: the pre-polymerization mixture was prepared by omitting the de-oxygenation step commonly required for (meth)acrylic MIPs, and irradiated with low power, near visible UV-light. A schematic representation of the synthesis of the thiol-yne MIPs is shown in Figure 2. 4.

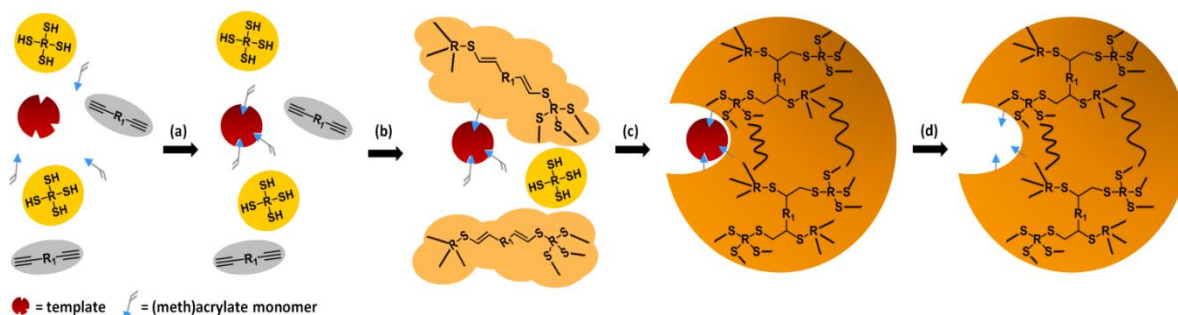


Figure 2. 4. Schematic representation of MIP formation via thiol-yne chemistry in the presence of (meth)acrylic functional monomers: (a) formation of the pre-polymerization complex through coordination of functional monomers (blue) around the template (red), (b) addition of thiols (yellow) to alkynes (grey), (c) addition of thiol to vinyl sulfides, (d) template removal.

As expected for “click” reactions, the synthesis was fast, with almost quantitative conversion of both thiol and alkyne reached just within minutes, as judged by FTIR analysis. Figure 2. 5 shows how both the terminal alkyne and the thiol signatures respectively at  $3300\text{ cm}^{-1}$  and  $2569\text{ cm}^{-1}$ , which are typical of the monomers, have almost disappeared upon polymerization, in both recipes. It is noteworthy here that conversions by FTIR were estimated according to the peak variation before and after polymerization (Table A1, Appendix A). Percent conversion was calculated using Equation 2.1:

$$\text{conversion (\%)} = \frac{r_p}{r_m} \times 100 \quad (\text{Equation 2.1})$$

where:

$$r_p = \frac{\text{peak height of active bond in the polymer}}{\text{peak height of C=O bond in the polymer}} \quad (\text{Equation 2.2})$$

$$r_m = \frac{\text{peak height of active bond in the monomer}}{\text{peak height of C=O bond in the monomer}} \quad (\text{Equation 2.3})$$

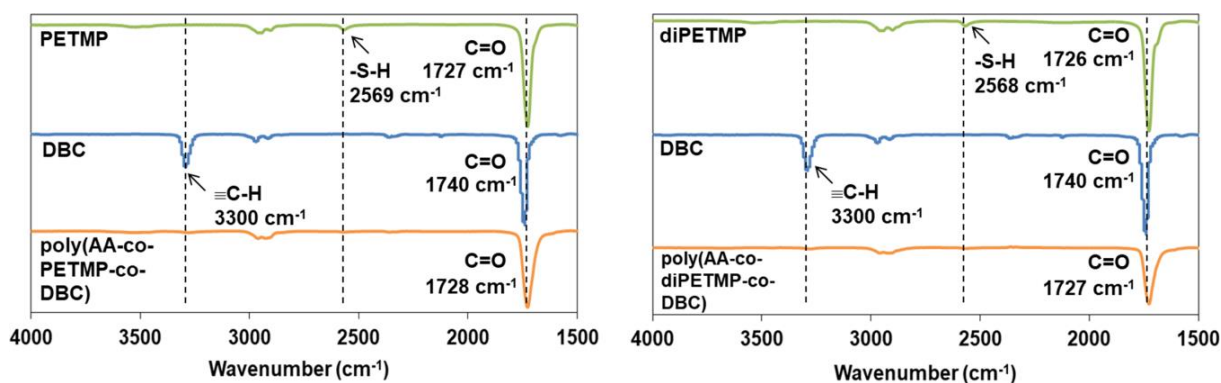


Figure 2. 5. FTIR spectra of the thiol-yne polymers (orange), polythiols (green) and the dialkyne DBC (blue).

Since the stretching of the thiol groups is usually weak, the calculated conversions on both polymers are probably underestimated for thiols (Table A1, Appendix A). Nevertheless, these results represent a substantial advantage compared to ordinary (meth)acrylic MIPs, wherein the average double bond conversion usually sets below 70%.<sup>16,20</sup>

Thiol-yne polymerization also yielded an almost full gravimetric conversion (Table 2. 1). SEM images for the different samples (Figure 2. 6) revealed the presence of a fine micro-particular texture, with spherical particles of a size of about 2  $\mu\text{m}$ . Particles synthesized in absence of template (i.e. non-imprinted particles or NIPs), were smaller than particles synthesized in presence of the template (MIPs) for both recipes (1  $\mu\text{m}$  versus 2  $\mu\text{m}$ ). Such a difference is quite common for poly(meth)acrylate MIPs, and has also been reported for sol-gel MIPs.<sup>21</sup> This phenomenon probably relates to some template effect leading to the formation of bigger nuclei, or facilitating the oligomers' capture by preformed particles. The use of diPETMP in the cross-linking formulation allowed reducing particle sizes over the analogous PETMP. This is probably due to the slightly higher cross-linking density achieved with diPETMP, which is a hexa-thiol rather than a tetra-thiol. The cross-linker also affected the surface areas as measured by BET: the smaller particles obtained with diPETMP showed slightly higher values (Table 2. 2). Interestingly, all the measured formulations provided very low values, suggesting the absence of a dry-state porosity on these matrices.

Table 2. 1. Gravimetric conversions for p(AA-co-PETMP-co-DBC) and p(AA-co-diPETMP-co-DBC).

	MIP	NIP
p(AA-co-PETMP-co-DBC)	92 %	94 %
p(AA-co-diPETMP-co-DBC)	>99 %	95 %



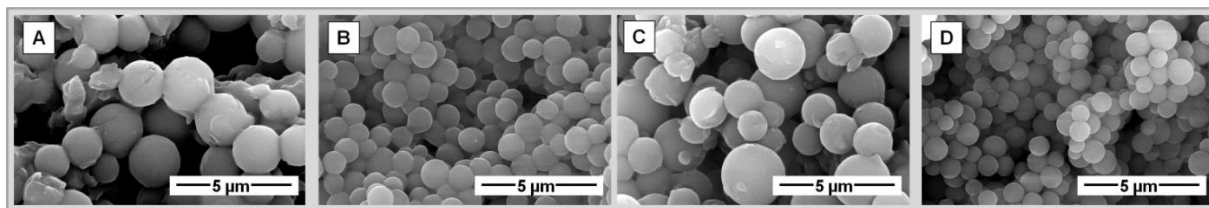


Figure 2. 6. Representative SEM images of poly(AA-co-PETMP-co-DBC) MIP (A) and NIP (B) and poly(AA-co-diPETMP-co-DBC) MIP (C) and NIP (D).

Table 2. 2. Surface area (in  $\text{m}^2/\text{g}$ ) for p(AA-co-PETMP-co-DBC) and p(AA-co-diPETMP-co-DBC).

	<b>MIP</b>	<b>NIP</b>
<b>p(AA-co-PETMP-co-DBC)</b>	1.7197	1.9699
<b>p(AA-co-diPETMP-co-DBC)</b>	2.1016	2.5275

### 3.1. Affinity and selectivity of thiol-yne MIPs

The main feature of MIPs is their ability to discriminate and recognize their target among other, similar molecules. Upon an overnight incubation with respectively propranolol and atenolol, we proved that both MIPs had a high affinity and were selective for the former. Figure 2. 7 shows that the polymer synthesized in presence of the template binds more propranolol than the reference polymer synthesized without and can be fitted with a mono-site Langmuir isotherm. Compared to NIPs, which bind much less, this means that the template promoted the creation of high affinity binding regions, which are missing in NIPs.

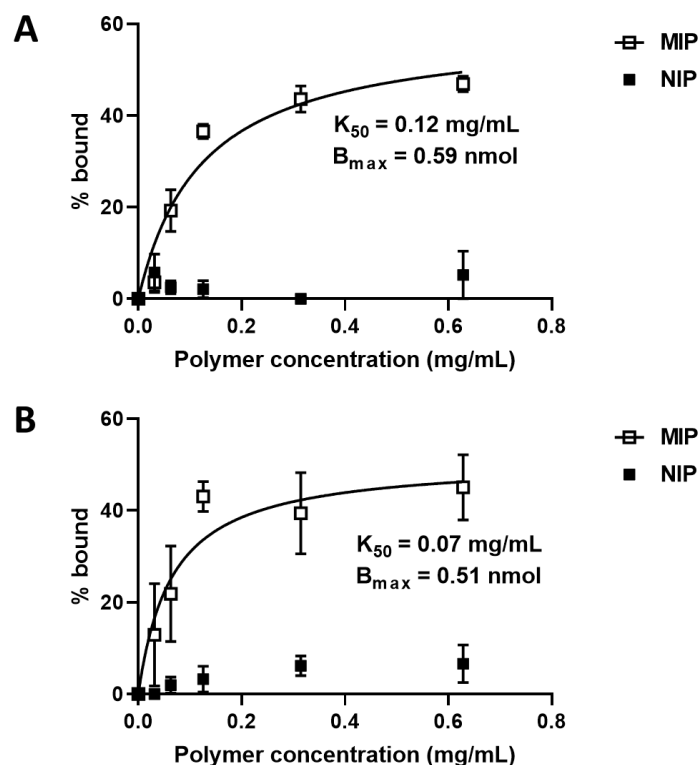


Figure 2. 7. Equilibrium binding for thiol-yne MIPs (empty squares) and NIPs (filled squares) incubated with 1  $\mu\text{M}$  of propranolol. (A) poly(AA-co-PETMP-co-DBC). (B) poly(AA-co-diPETMP-co-DBC) ( $n = 3$ ).

The binding parameters  $K_{50}$  and  $B_{\text{max}}$  were calculated by fitting with a Langmuir model (Equation 2.4):

$$\theta = \frac{B_{\text{max}}[\text{MIP}]}{K_{50} + [\text{MIP}]} \quad (\text{Equation 2.4})$$

where  $\theta$  = fraction of bound template,  $B_{\text{max}}$  = maximum binding capacity,  $[\text{MIP}]$  = MIP concentration and  $K_{50}$  = apparent binding affinity.

The estimated maximum binding (i.e.  $B_{\text{max}}$ ) are similar for both MIPs, even though the template affinity measured with the same model appears to be slightly higher for the MIP formulated with diPETMP. The apparent binding affinities (i.e.  $K_{50}$ ), which correspond to the polymer concentrations affording 50% of the total binding, are respectively 0.20 mg/mL and 0.10 mg/mL for PETMP- and diPETMP-based MIPs, and are consistent with previous data reported for propranolol MIPs by free-radical polymerization.<sup>15</sup> This possibly reflects the higher rigidity of the imprinted cavities, related to the higher cross-linking density induced by the hexa-thiol<sup>10</sup> (diPETMP, Figure 2. 7) over PETMP. MIPs

also showed to be reusable, as upon washing and re-incubation with propranolol, their maximum binding was preserved within 15 % derivation from the original value.

As an additional important parameter, the selectivity was determined by replacing the actual template with a molecule having a closely related structure: atenolol. Atenolol has a similar basic structure as propranolol, but it possesses a benzeneacetamide moiety rather than a naftyl group. Hence, it may also interact with the functional monomer *via* hydrogen bonding. Nevertheless, incubation with an equimolar solution of atenolol afforded no or negligible binding (Figure 2. 8). This proved that the molecular cavities were carefully tailored to propranolol and the imprinting was effective.

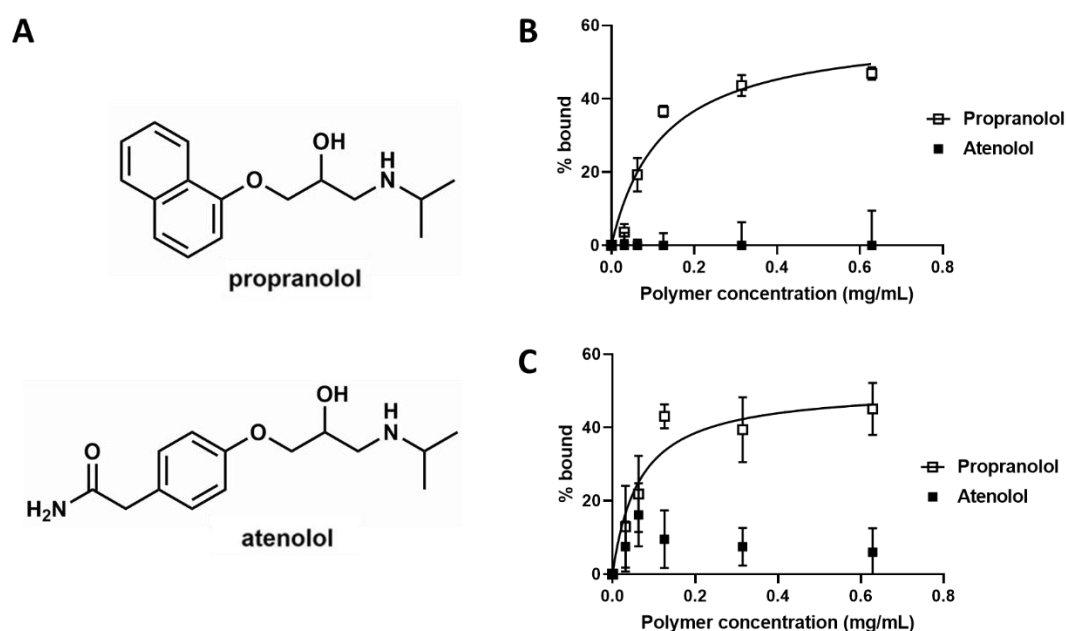


Figure 2. 8. (A) The chemical structures of propranolol and atenolol. (B-C) Equilibrium binding of thiol-yne MIPs incubated with 1  $\mu$ M of propranolol (empty squares) or atenolol (filled squares). (B) poly(AA-co-PETMP-co-DBC). (C) poly(AA-co-diPETMP-DBC) ( $n = 3$ ).

### 3.2. Hydrolytic degradation of ester-based, thiol-yne MIPs

As mentioned in the introduction, the superior physical and chemical stability is one of the benefits that MIPs can claim over their natural counterparts. However, this is at the same time a drawback, since it makes them poorly degradable and thus persistent in the environment. This is primarily the consequence of the main polymer backbone of (meth)acrylic MIPs consisting exclusively

of carbon atoms. Although the pendant ester moieties can be hydrolyzed, this reaction is generally very slow and affords high molecular weight poly(meth)acrylic acid, which have been reported to induce tissue necrosis.<sup>22</sup> On the other hand, addressing degradability has become extremely important, especially with respect to the recent concerns for micro-plastics polluting the environment.<sup>23</sup> In this perspective, the formulation of ester-based thiols in thiol-yne MIPs allows inserting the ester moiety directly into the main polymer back-bone, thus affording more easily hydrolysable polymers.

Hydrolysis tests in 1.0 M NaOH revealed that our thiol-yne matrices dissolved within minutes, conversely to reference poly(acrylic acid- co-pentaerythritol triacrylate) p(AA-co-PETA) and poly(methacrylic acid-co-ethyleneglycol dimethacrylate) p(MAA-co-EGDMA) synthesized by free-radical polymerization. The dispersions of our thiol-yne MIPs turned into solutions in less than 15 minutes (Figure 2. 9), while those of analogous polymers by free-radical polymerization lasted for much longer, especially for p(MAA-co-EGDMA) (Figure 2. 10).

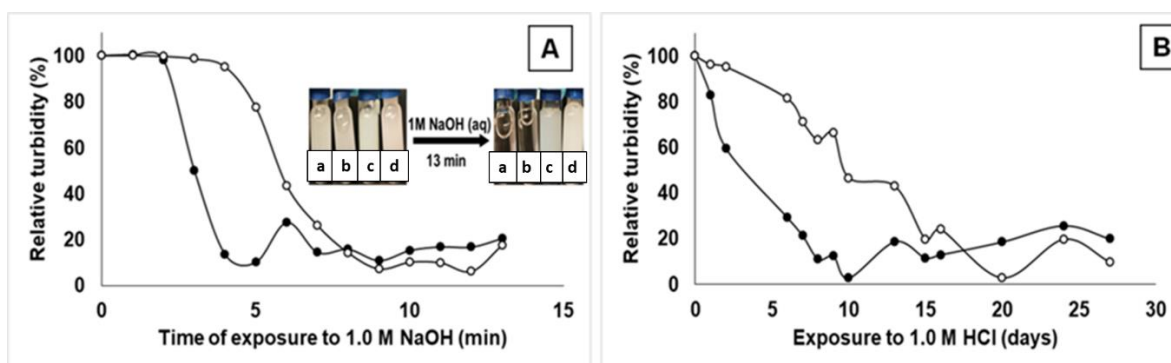


Figure 2. 9. Hydrolytic degradation of p(AA-co-PETMP-co-DBC) (filled circles) and p(AA-co-diPETMP-co-DBC) (empty circles) over the time in (A) 1.0 M NaOH at room temperature, and (B) in 1.0 M HCl at 60 °C. Inset: aqueous dispersions of p(AA-co-PETMP-co-DBC) (a), p(AA-co-diPETMP-co-DBC) (b), p(AA-co-PETA) (c) and p(MAA-co-EGDMA) (d) before and after 13 minutes of exposure to 1 molar aqueous NaOH.

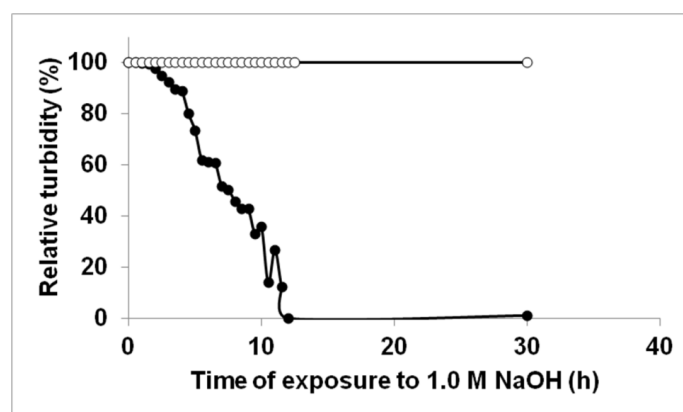


Figure 2. 10. Turbidity measurements over the time for the alkaline hydrolysis of p(AA-co-PETA) (filled circles) and p(MAA-co-EGDMA) (empty circles) in 1.0 M aqueous NaOH.

Upon decreasing NaOH concentration, the alkaline hydrolysis markedly decreased its rate, with only a partial dissolution achieved over 2 days for p(AA-co-PETMP-co-DBC) and over 9 days for p(AA-co-diPETMP-co-DBC) for a 0.1 M NaOH solution, and virtually no effect for a 0.01 M NaOH solution over 33 days (Figure A1, Appendix A). This means that our ester-based, thiol-yne matrices can be easily hydrolyzed at room temperature under strong alkaline conditions, while keeping a convenient stability at lower pH, similarly to conventional MIPs. Also, diPETMP-based matrices showed to be less prone to hydrolysis than PETMP-based scaffolds, which is probably once again due to the higher cross-linking density achieved with the higher polythiol. It is important to note that this increased stability does not arise from different sizes: diPETMP and PETMP-based particles have similar diameters, and hence, similar surface areas. Thus, a quicker hydrolysis compared to traditional vinyl matrices arises from polymeric, intrinsic features rather than geometric limitations affecting the contact area between polymer and the alkaline solution. This becomes evident if we look at the size of reference p(AA-co-PETA) and p(MAA-co-EGDMA):  $46.72 \pm 11.63$  nm and  $329.7 \pm 39.1$  nm respectively (Table A2 and Figure A2, Appendix A). Smaller sizes imply, for a same mass, a much higher surface area, which is expected to afford higher rates of hydrolysis compared to big particles. Instead, we observed for thiol-yne matrices a much faster hydrolysis, meaning that their polymeric backbones were more prone to hydrolysis than vinyl ones. It is important to stress here that despite thiol-yne polymers containing a hydrolysable carbonate group, the ester moiety is the one undergoing preferentially the hydrolysis as previously demonstrated.<sup>24</sup> Interestingly, the reference scaffold p(AA-co-PETA) also showed an appreciable hydrolysis under these conditions (Figure 2. 10).

As expected, acid hydrolysis proved to be much slower.<sup>25</sup> Dispersions incubated in 1.0 M HCl did not show any decrease in turbidity at room temperature over two weeks. Only by raising the temperature to 60 °C in an accelerating aging, the dispersions started to turn into solutions, although this took 6 days. Once again, diPETMP-based particles showed to be much more stable.

Besides the “visual” inspection by turbidity measurements, aqueous size-exclusion chromatography coupled to mass spectrometry (SEC/HRMS) was also used to analyze the products of hydrolysis (Table A3-A5, Figures A3-A5, Appendix A). The alkaline treatment on p(AA-co-PETA) afforded low molecular weight species and oligomers up to 2600 g/mol (Table A3, Figure A3, see Appendix A). Similar results were also obtained with diPETMP-based microparticles (i.e. low molecular weight species and oligomers up to 2300 g/mol), whereas the PETMP-based formulation allowed for shorter oligomers (1700 g/mol). This result achieved on PETMP-based formulations was quite remarkable, and shorter oligomers might arise from the lower cross-linking density achieved with PETMP over diPETMP.

To get more insights about the cleaved bonds, we also inspected the product of the alkaline hydrolysis by FTIR and by <sup>1</sup>H-NMR. The FTIR spectra (Figures A6-A7, Appendix A) showed that the main peak of C=O stretching shifted from 1730 cm<sup>-1</sup> to 1700 cm<sup>-1</sup>, with a shoulder still visible at 1730 cm<sup>-1</sup>, and a broad peak raised at around 3400 cm<sup>-1</sup>: this suggested that ester moieties were converted into carboxylic groups, as previously reported.<sup>24</sup> On the other hand, the hydrolysis of thioethers and (possible) formation of thiol was more difficult to judge *via* FTIR: the thiol signal at 2570 cm<sup>-1</sup> is already very weak on (di)PETMP and the products of hydrolysis only showed a tiny, very broad signal at 2450 - 2700 cm<sup>-1</sup> which cannot unequivocally be attributed to thiols. Similarly, the C-S signal at 600 – 700 cm<sup>-1</sup>, which is visible for the polymers, can still be seen for the products of hydrolysis.

To assess the presence of thiols, we then turn to <sup>1</sup>H-NMR. Figure A8 (Appendix A) reveals the presence of some thiols for the products of hydrolysis, due to the presence of a very weak signal at 1.96 ppm. Nevertheless, this small signal is most probably due to residual, unreacted thiols from the polymer, rather than to thiols generated upon thioether hydrolysis. Thus, this analysis further supports the conclusion that esters are the hydrolysable moieties responsible for the overall hydrolysable character of such matrices.

#### 4. Conclusions

In conclusion, we synthesized selective MIPs for propranolol *via* radical-mediated, thiol-yne chemistry. Acrylic acid as a functional monomer was formulated together with two different ester-based polythiols (PETMP and di-PETMP) and a dialkyne (DBC) to afford discrete micro-particles upon near-UV photo-polymerization. Both recipes afforded MIPs with affinity and selectivity for propranolol, with di-PETMP providing a higher affinity probably due to a higher cross-linking density. As expected for a “click reaction”, the polymerization was quick, had a high yield and was oxygen tolerant, which represents an important advantage over the conventional free-radical polymerization of (meth)acrylates. This latter feature is particularly convenient for micro and nanofabrication of MIPs, as it usually requires an equipment which is difficult to place in an oxygen-free atmosphere. Also, thiol-yne polymerization showed to be compatible with (meth)acrylates, which offers the possibility of building on the huge library of functional monomer reported by the imprinting community over the years.

The incorporation of ester-based polythiols into the pre-polymerization mixture resulted in MIPs which could be easily degraded within minutes in 1.0 M NaOH, conversely to reference scaffolds based on poly(acrylic acid-co-pentaerythritol triacrylate) or poly(methacrylic acid-co-ethyleneglycol dimethacrylate). An acid hydrolysis was also possible in 1.0 M HCl at 60 °C. Size-exclusion chromatography coupled to mass-spectrometry revealed that alkaline hydrolysis afforded low molecular weight species and short oligomers, especially for polymers based on PETMP which also were hydrolyzed, at their ester moieties, quicker than polymers based on diPETMP. This latter feature represents a remarkable improvement for MIPs as it offers a viable way to improve their hydrolytic degradation.

After demonstrating that the thiol-yne chemistry is an effective route for the synthesis of MIPs, we are now ready to incorporate the use of thiol-yne formulations into the TPS fabrication of MIP structures with submicron features, potentially granting these polymers with interesting optical properties.

**5. REFERENCES**

- (1) Gomez, L. P. C.; Spangenberg, A.; Ton, X. A.; Fuchs, Y.; Bokeloh, F.; Malval, J.-P.; Tse Sum Bui, B.; Thuau, D.; Ayela, C.; Haupt, K.; Soppera, O. Rapid Prototyping of Chemical Microsensors Based on Molecularly Imprinted Polymers Synthesized by Two-Photon Stereolithography. *Adv. Mater.* **2016**, *28*, 5931–5937. <https://doi.org/10.1002/adma.201600218>.
- (2) Bompert, M.; Haupt, K. Molecularly Imprinted Polymers and Controlled/Living Radical Polymerization. *Aust. J. Chem.* **2009**, *62* (8), 751–761. <https://doi.org/10.1071/CH09124>.
- (3) Pei, Y.; Fan, F.; Wang, X.; Feng, W.; Hou, Y.; Pei, Z. Fabrication of Hypericin Imprinted Polymer Nanospheres via Thiol-Yne Click Reaction. *Polymers*. **2017**, *9* (10). <https://doi.org/10.3390/polym9100469>.
- (4) Hoyle, C. E.; Lowe, A. B.; Bowman, C. N. Thiol-Click Chemistry: A Multifaceted Toolbox for Small Molecule and Polymer Synthesis. *Chem. Soc. Rev.* **2010**, *39* (4), 1355–1387. <https://doi.org/10.1039/b901979k>.
- (5) Fairbanks, B. D.; Sims, E. A.; Anseth, K. S.; Bowman, C. N. Reaction Rates and Mechanisms for Radical, Photoinitiated Addition of Thiols to Alkynes, and Implications for Thiol-Yne Photopolymerizations and Click Reactions. *Macromolecules* **2010**, *43* (9), 4113–4119. <https://doi.org/10.1021/ma1002968>.
- (6) Chan, J. W.; Shin, J.; Hoyle, C. E.; Bowman, C. N.; Lowe, A. B. Synthesis, Thiol-Yne “Click” Photopolymerization, and Physical Properties of Networks Derived from Novel Multifunctional Alkynes. *Macromolecules* **2010**, *43* (11), 4937–4942. <https://doi.org/10.1021/ma1004452>.
- (7) Bhanu, V. A.; Kishore, K. Role of Oxygen in Polymerization Reactions. *Chem. Rev.* **2005**, *91* (2), 99–117. <https://doi.org/10.1021/cr00002a001>.
- (8) Hoyle, C. E.; Lee, T. Y.; Roper, T. Thiol-Enes: Chemistry of the Past with Promise for the Future. *J. Polym. Sci. A Polym. Chem.* **2004**, *42* (21), 5301–5338. <https://doi.org/10.1002/pola.20366>.
- (9) Hoyle, C. E.; Bowman, C. N. Thiol-Ene Click Chemistry. *Angew. Chem. Int. Ed.* **2010**, *49* (9), 1540–1573. <https://doi.org/10.1002/anie.200903924>.
- (10) Oesterreicher, A.; Gorsche, C.; Ayalur-Karunakaran, S.; Moser, A.; Edler, M.; Pinter, G.; Schlögl, S.; Liska, R.; Griesser, T. Exploring Network Formation of Tough and Biocompatible Thiol-Yne Based Photopolymers. *Macromol. Rapid Commun.* **2016**, *37* (20), 1701–1706. <https://doi.org/10.1002/marc.201600369>.



- (11) Fairbanks, B. D.; Scott, T. F.; Kloxin, C. J.; Anseth, K. S.; Bowman, C. N. Thiol-Yne Photopolymerizations: Novel Mechanism, Kinetics, and Step-Growth Formation of Highly Cross-Linked Networks. *Macromolecules* **2009**, *42* (1), 211–217. <https://doi.org/10.1021/ma801903w>.
- (12) Andersson, L. I. Application of Molecular Imprinting to the Development of Aqueous Buffer and Organic Solvent Based Radioligand Binding Assays for (S)-Propranolol. *Anal. Chem.* **1996**, *68* (1), 111–117. <https://doi.org/10.1021/ac950668+>.
- (13) Bompert, M.; Goto, A.; Waittraint, O.; Sarazin, C.; Tsujii, Y.; Gonzato, C.; Haupt, K. Molecularly Imprinted Polymers by Reversible Chain Transfer Catalysed Polymerization. *Polymer*. **2015**, *78*, 31–36. <https://doi.org/10.1016/j.polymer.2015.09.060>.
- (14) Adali-Kaya, Z.; Tse Sum Bui, B.; Falcimaigne-Cordin, A.; Haupt, K. Molecularly Imprinted Polymer Nanomaterials and Nanocomposites: Atom-Transfer Radical Polymerization with Acidic Monomers. *Angew. Chemie - Int. Ed.* **2015**, *54* (17), 5192–5195. <https://doi.org/10.1002/anie.201412494>.
- (15) Panagiotopoulou, M.; Beyazit, S.; Nestora, S.; Haupt, K.; Tse Sum Bui, B. Initiator-Free Synthesis of Molecularly Imprinted Polymers by Polymerization of Self-Initiated Monomers. *Polymer*. **2015**, *66*, 43–51. <https://doi.org/10.1016/j.polymer.2015.04.012>.
- (16) Gonzato, C.; Pasetto, P.; Bedoui, F.; Mazeran, P. E.; Haupt, K. On the Effect of Using RAFT and FRP for the Bulk Synthesis of Acrylic and Methacrylic Molecularly Imprinted Polymers. *Polym. Chem.* **2014**, *5* (4), 1313–1322. <https://doi.org/10.1039/c3py01246h>.
- (17) Matsumoto, A.; Asai, S.; Shimizu, S.; Aota, H. Free-Radical Cross-Linking Polymerization of Unsymmetrical Divinyl Compounds 2. Steric Effect on Gelation in the Copolymerizations of Allyl Methacrylate with Several Alkyl Methacrylates. *Eur. Polym. J.* **2002**, *38* (5), 863–868. [https://doi.org/10.1016/S0014-3057\(01\)00269-5](https://doi.org/10.1016/S0014-3057(01)00269-5).
- (18) Ye, S.; Cramer, N. B.; Smith, I. R.; Voigt, K. R.; Bowman, C. N. Reaction Kinetics and Reduced Shrinkage Stress of Thiol–Yne–Methacrylate and Thiol–Yne–Acrylate Ternary Systems. *Macromolecules* **2011**, *44* (23), 9084–9090. <https://doi.org/10.1021/ma2018809>.
- (19) Gonzato, C.; Pasetto, P.; Bedoui, F.; Mazeran, P. E.; Haupt, K. On the Effect of Using RAFT and FRP for the Bulk Synthesis of Acrylic and Methacrylic Molecularly Imprinted Polymers. *Polym. Chem.* **2014**, *5* (4), 1313–1322. <https://doi.org/10.1039/c3py01246h>.
- (20) Bompert, M.; Goto, A.; Waittraint, O.; Sarazin, C.; Tsujii, Y.; Gonzato, C.; Haupt, K. Molecularly Imprinted Polymers by Reversible Chain Transfer Catalysed Polymerization. *Polymer*. **2015**, *78*,

- 31–36. <https://doi.org/10.1016/j.polymer.2015.09.060>.
- (21) Li, B.; Xu, J.; Hall, A. J.; Haupt, K.; Tse Sum Bui, B. Water-Compatible Silica Sol-Gel Molecularly Imprinted Polymer as a Potential Delivery System for the Controlled Release of Salicylic Acid. *J. Mol. Recognit.* **2014**, *27* (9), 559–565. <https://doi.org/10.1002/jmr.2383>.
- (22) Husár, B.; Heller, C.; Schwentenwein, M.; Mautner, A.; Varga, F.; Koch, T.; Stampfl, J.; Liska, R. Biomaterials Based on Low Cytotoxic Vinyl Esters for Bone Replacement Application. *J. Polym. Sci. A Polym. Chem.* **2011**, *49* (23), 4927–4934. <https://doi.org/10.1002/pola.24933>.
- (23) Ivar Do Sul, J. A.; Costa, M. F. The Present and Future of Microplastic Pollution in the Marine Environment. *Environ. Pollut.* **2014**, *185*, 352–364. <https://doi.org/10.1016/j.envpol.2013.10.036>.
- (24) Oesterreicher, A.; Wiener, J.; Roth, M.; Moser, A.; Gmeiner, R.; Edler, M.; Pinter, G.; Griesser, T. Tough and Degradable Photopolymers Derived from Alkyne Monomers for 3D Printing of Biomedical Materials. *Polym. Chem* **2016**, *7*, 5169. <https://doi.org/10.1039/c6py01132b>.
- (25) Ginde, R. M.; Gupta, R. K. In Vitro Chemical Degradation of Poly(Glycolic Acid) Pellets and Fibers. *J. Appl. Polym. Sci.* **2018**, *33* (7), 2411–2429. <https://doi.org/10.1002/app.1987.070330712>.

## Chapter 3

# TWO-PHOTON STEREOLITHOGRAPHY AND PHOTOSTRUCTURATION FOR MOLECULAR RECOGNITION

# Chapter 3: TWO-PHOTON STEREOLITHOGRAPHY AND PHOTOSTRUCTURATION FOR MOLECULAR RECOGNITION

---

---

The present chapter is dedicated to the use of the two-photon stereolithography (TPS) as a novel technique for the structuring of molecularly imprinted polymers (MIPs) into photonic crystals (PhC) with the aim to recognize a molecular target. It begins with an introduction to rapid prototyping, stereolithography and TPS followed by a discussion on the theoretical background and the applications of PhCs in molecular imprinting. It then proceeds to the strategies employed in our experiments to fabricate MIP PhCs via TPS and the discussion of the results obtained.

## 1. Introduction

### 1.1. Rapid Prototyping

Rapid prototyping (RP) is an umbrella term that encompasses technologies that fabricate three-dimensional physical objects through a layer-by-layer additive approach.<sup>1</sup> Its commercial roots can be traced back to the 1980s when its principal function, as its name suggests, was to construct prototypes within a time-efficient product development taking usually a few hours to a few days. This was and still is possible because most RP technologies rely on the use of computer-aided design (CAD) for the layout of the structures, which is then translated electronically into the RP systems for the fast fabrication of 3D objects. Over time, RP transcended the step of prototypes and assumed a niche in various sectors such as manufacturing,<sup>2,3</sup> aerospace,<sup>4</sup> automobile,<sup>5,6</sup> biomedical,<sup>7,8</sup> ceramics<sup>9,10</sup> and optics.<sup>11,12</sup>

The term “rapid prototyping” tends to highlight the application of the technique rather than describe its underlying mechanism, i.e. the layer-by-layer additive fabrication, which is a “bottom-up” approach consisting in depositing multiple constituent layers using digitally controlled systems in order to build and shape an object.<sup>13</sup> Indeed, “additive manufacturing” (AM) has become the standardized terminology for all additive processes as stated in the Standard Terminology for Additive Manufacturing Technologies (ASTM 2972).<sup>1</sup> This is in contrast to “subtractive manufacturing” in which objects are casted or formed by removing materials via forging, etching or machining, the so-called “top-down” approaches.<sup>13</sup> In the sense of the term, AM does not only produce prototypes but more

importantly, yields finished products or provides repair parts.<sup>14,15</sup> Throughout this manuscript, however, RP and AM are used as synonyms.

There exist various examples of RP and they can be categorized into three different types according to the state of the initial material used for fabrication: (1) bulk solid-based, (2) powder-based, and (3) liquid-based (Figure 3.1).<sup>16</sup> Bulk solid-based RP systems rely on transforming solid starting materials into wires, rolls, laminates or pellets by a suitable technique such as cutting or extrusion and processing them through fusion or melting to finally assemble the components into the desired shape. Laminated object manufacturing and fused deposition modelling (FDM), which is the second most commonly used RP technology, belong to this category.<sup>17,18</sup> Powder-based AM technologies include selective laser sintering (SLS), in which a powdered form of a material is spread on a build platform to be locally sintered by a laser for the formation of layers that will be sintered together at a later step to build the desired object,<sup>15</sup> and inkjet 3D printing, wherein an inkjet head prints a liquid binder on thin layers of powder.<sup>19</sup> Lastly, liquid-based RP systems consist in the careful exposures of a photo-curable liquid resin to a suitable radiation, usually ultraviolet (UV) light, to form thin hardened layers, one on top of another, until the envisaged 3D object is complete.<sup>17</sup> Stereolithography (SLA) is a prominent example of this and is also the most popular RP system. SLA will be discussed further in the following section.

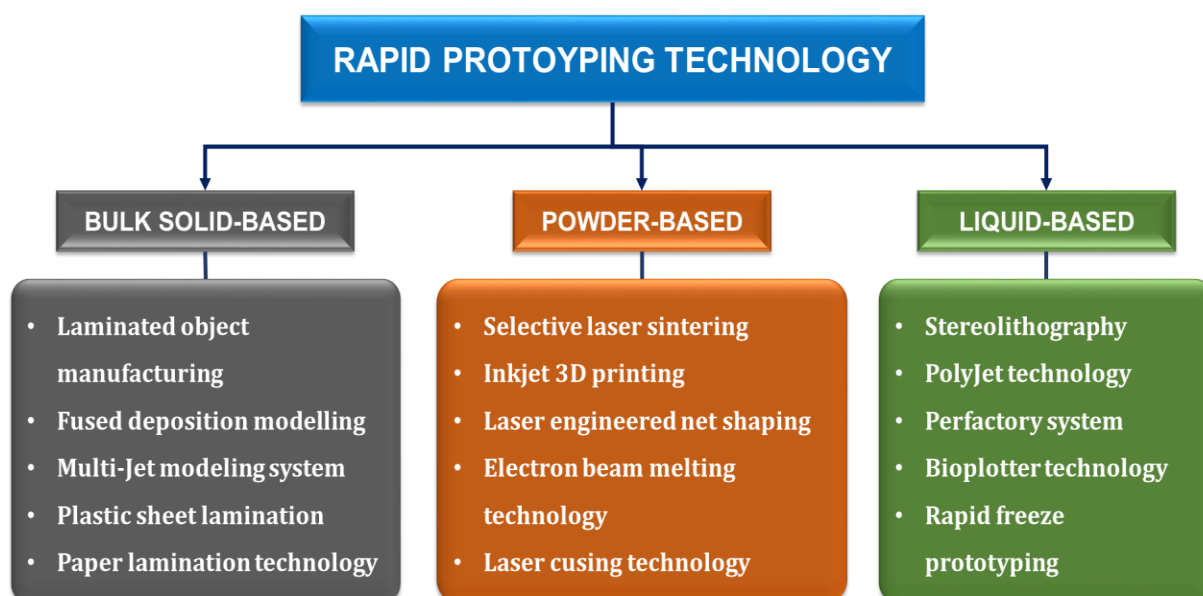


Figure 3.1. The three categories of rapid prototyping technology and their examples.

## 1.2. Stereolithography

Developed in the 1980s by Charles Hull, stereolithography (SLA) became the first available form of additive manufacturing (AM) technology (Figure 3.2). It effectively emerged as the first known form of 3D printing.<sup>15</sup> SLA combines the use of computer-aided design (CAD) and laser technology to fabricate 3D solid objects. A 3D model of the envisaged object is initially designed and rendered through a CAD software on a computer. The CAD model is then converted to a “standard tessellation language” (STL) file format, the *de facto* standard data transmission format of RP systems, although other file formats also exist such as “stereolithography contour” (SLC), computerized tomography (CT) scan data, initial graphics exchange specification (IGES) and Hewlett-Packard graphics language (HP/GL).<sup>1,20</sup> The STL file is an approximation of 3D surfaces using oriented triangles or facets for a smooth representation of the CAD model.<sup>21</sup> Here, the model is also virtually divided into two-dimensional (2D) thin layers, the thickness of which is employed in the layer-by-layer fabrication process later on.<sup>22</sup> The data are then uploaded to the SLA apparatus, which is composed of four main parts: 1) a photo-curable resin reservoir or a vat, 2) a laser source (usually UV light), 3) controlling system for the XY-movement of the light beam, and 4) vertical plane fabrication or building platform.<sup>17</sup> The apparatus is controlled by the computer so that a laser beam is used to project the first layer of the model on the surface of the resin. The light induces the crosslinking of the monomers of the resin within the irradiated zone, resulting in the fabrication of the first layer of the object. The resin is polymerized to a certain depth, which allows the layer to adhere to the building platform. The platform then moves vertically and away from the laser source so that the “printed” layer is submerged in a fresh supply of the resin inside the vat. The process is reenacted to fabricate the succeeding layers until the top layer is reached and the 3D object completed. The depth of curing must be greater than the platform step height to guarantee interlayer adherence. The unreacted resin is finally drained and washed off, revealing the printed structure. A post-curing step by exposure to UV light may be necessary especially when the monomer conversion is usually incomplete in order to render the structure mechanically more stable.<sup>22</sup>

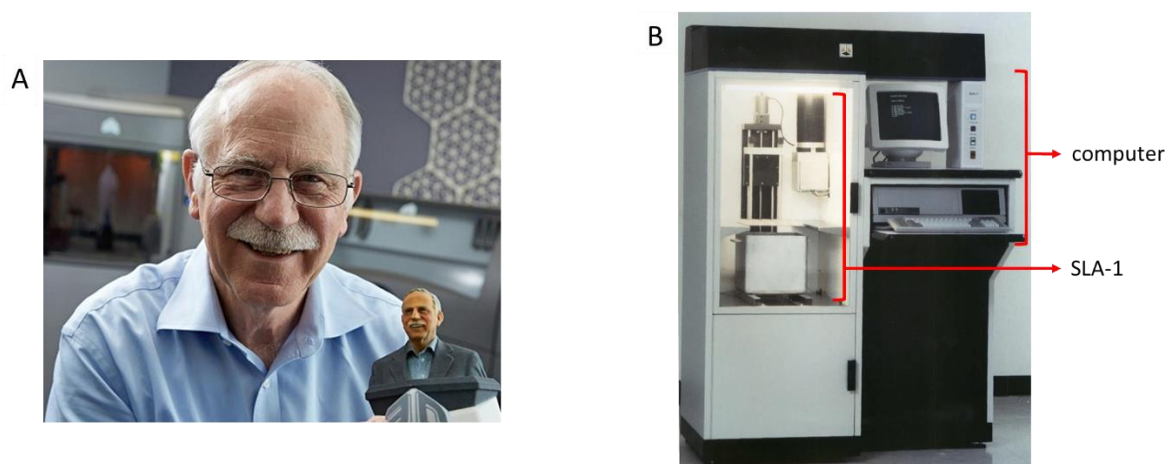


Figure 3.2. (A) Charles Hull, inventor of the first commercial 3D printer, holding a small 3D printed bust of himself. (B) SLA-1, the first commercial 3D printer produced in 1987. Reprinted from Ref. <sup>23,24</sup>.

More than thirty years after its invention, SLA currently stands out as the most commonly used AM technology. This fact is attributed to its various advantages that include higher accuracy and resolution, surface smoothness, processing speed and bonding between layers. It also provides an alternative to thermal-based AM technologies when degradation of material due to heat becomes an issue.<sup>16</sup> As such, SLA has been used in different fields such as biomedical engineering,<sup>22,25</sup> microfluidics,<sup>26,27</sup> ceramics,<sup>28–30</sup> and optics (Figure 3.3).<sup>31</sup>

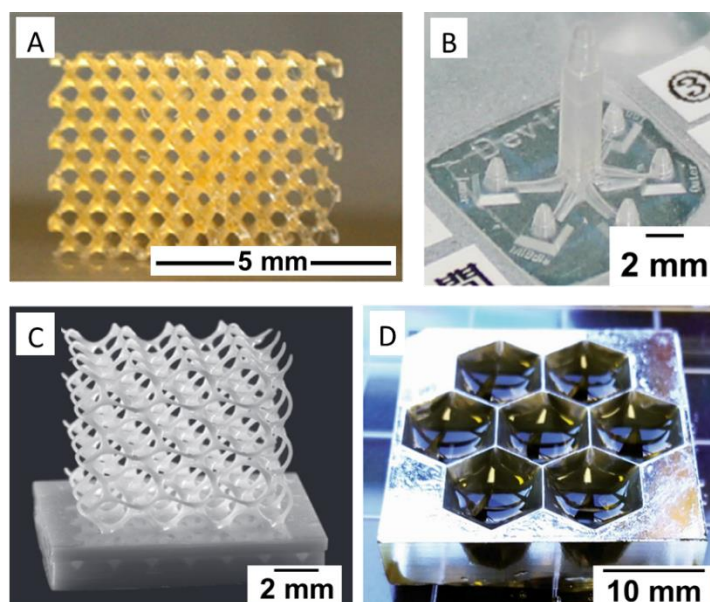


Figure 3.3. Several examples of 3D objects manufactured by stereolithographic techniques: (A) a poly( $\epsilon$ -caprolactone)-based tissue engineering scaffold,<sup>25</sup> (B) a microfluidic device with 3D flow channels,<sup>26</sup> (C) a cellular cube based on alumina ceramic,<sup>28</sup> and (D) a tiled solar concentrator lens array.<sup>31</sup> Reprinted with permissions from Elsevier Ltd, the American Chemical Society and Springer Nature.

Stereolithography, in its core, is photopolymerization; more specifically, the careful application of it in space and time that results in the fabrication of solid objects. As in any photopolymerization process, it needs a suitable match between applied wavelength and initiator in the monomer mixture, to make the latter to initiate the polymerisation. Because of this, conventional stereolithography is also known as one-photon stereolithography since one photon is expected to excite and activate an initiator molecule. However, this is not to say that other forms of SLA do not exist. In fact, SLA systems based on multiple-photon processes are gaining recognition in the recent years. One prominent example of such is the two-photon stereolithography (TPS), as mentioned in Chapter 1.

### 1.3. Two-photon stereolithography

Two-photon stereolithography (TPS) sets itself apart from conventional stereolithography by harnessing two photons to induce the formation of active radicals normally furnished by an energetically equivalent single photon, as explained already in Chapter 1. This provides the principal advantage of TPS over conventional stereolithography: true 3D structures can be written within the photoresist volume since the required photon intensity for two-photon processes setting off the initiator is only given in the voxel, and only for a very short time, so that submicron features are typically achieved and the remaining volume of the photoresist remains unchanged.<sup>32,33</sup>

A typical TPS setup consists in three main parts: 1) an excitation source, 2) the CAD system and 3) the scan method (Figure 3.4).<sup>32</sup> As mentioned earlier, a Ti:Sapphire femtosecond laser often acts as the excitation source, although alternatives such as an inexpensive Nd-YAG microlaser operating at 532 nm have also been used in the past.<sup>34</sup> The CAD system is housed in a computer where it should be converted to a STL file or an equivalent as in other RP technologies. Lastly, the choice of the scan method presents a crucial influence on the throughput of the process. On one hand, galvo mirrors can be used for horizontal scanning coupled to a piezoelectric stage for vertical scanning. This configuration is advantageous since it provides high scan speeds. However, the total horizontal range accessible is only a few tens of micrometers because of spherical aberrations arising from the use of high-NA objectives. The other configuration is the use of a piezoelectric stage to scan in the x, y and z directions. This allows scan ranges up to few hundreds of micrometers although the scan suffers low speeds.<sup>32</sup>



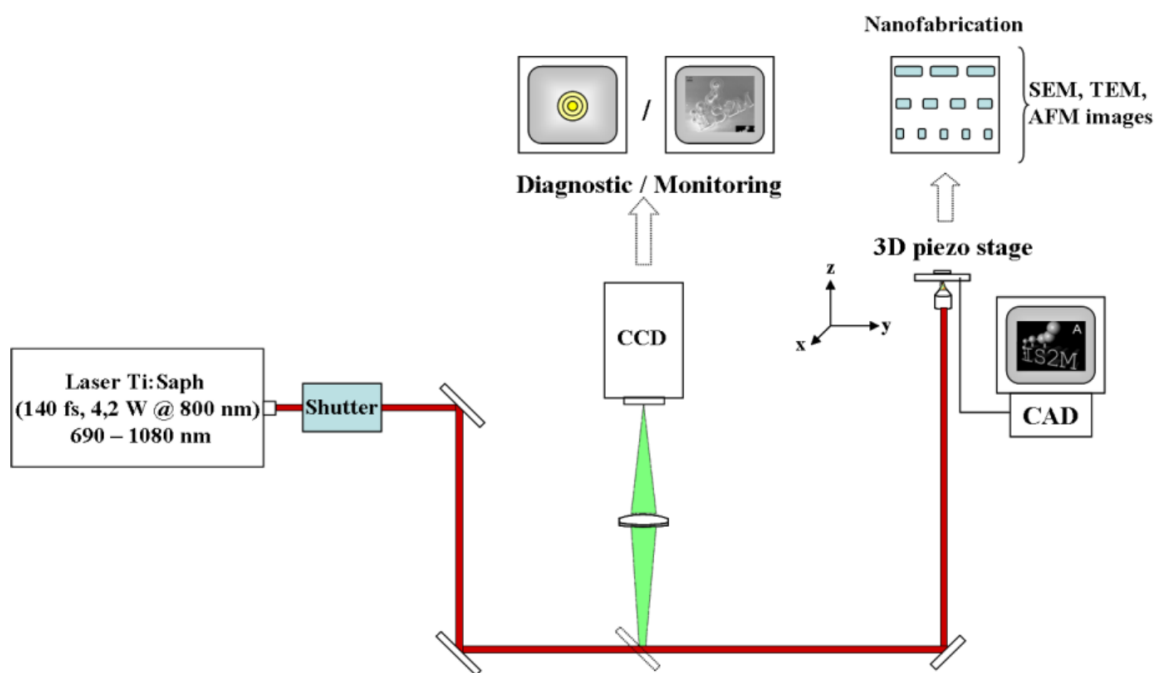


Figure 3.4. Schematic representation of a typical TPS experimental setup. Reprinted with permission from IntechOpen.<sup>32</sup>

An important concept and physical reality in TPS is the voxel. A voxel is the smallest unit volume of cured photoresist produced after performing TPS. It is analogous to a pixel in a 2D image. A voxel, therefore, is the volume within which photopolymerization took place after a laser beam has been concentrated within the focal point of an objective in a TPS system. Due to the oval shape of the focal spot of the objective in a TPS setup, voxels are also naturally oval in shape, the axial size being greater than the lateral size (Figure 3.5). The ratio of the axial size to the lateral size is known as the aspect ratio. Understanding the dimensions of the voxel is essential to understand the resolution of a given TPS setup.

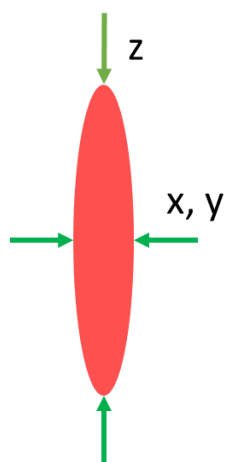


Figure 3.5. A representation of a voxel projected from an objective of a TPS system.

Due to the microfabrication and even sub-micron fabrication capabilities of TPS, it has found diverse applications such as scaffolds for 3D cell culture,<sup>35,36</sup> shape-shifting 3D protein microstructures,<sup>37</sup> biocompatible hybrid materials,<sup>38</sup> tomography,<sup>39</sup> microelectromechanical systems (MEMS),<sup>40-42</sup> microsensors,<sup>33</sup> and optical materials (e.g. microlenses, waveguides).<sup>43,44</sup> Notably, it has also been exploited in the construction of photonic crystals, whose internal structure allow them to interfere with electromagnetic radiation. Photonic crystals will be discussed more in detail in the next section.

#### 1.4. Photonic crystals

Photonic crystals (PhCs) are known for their intense and selective reflective properties for which they are largely applied in various fields such as optics,<sup>45-47</sup> display technology,<sup>48,49</sup> telecommunications<sup>50</sup> and chemical sensing.<sup>51-53</sup> PhCs are materials whose refractive index varies periodically in space throughout their structures.<sup>54</sup> This periodicity in the refractive index gives rise to a “photonic band gap” (PBG), which forbids the propagation through the crystal of certain frequencies (energies) of electromagnetic radiation (usually in the visible or infrared region). In this manner, the PBG becomes analogous to the electronic band gap found in semiconductors, where electrons cannot freely travel from one atom to another throughout the lattice of a material unless they possess sufficient energy for the level found in the conduction band. Since these light frequencies are not allowed to be transmitted, they instead become reflected off the PhC. But the mechanism involves more than just a simple reflection. To understand it, it is important to know that PhC can be classified as either one- (1D), two- (2D) or three-dimensional (3D) PhCs, depending on the orientation of the periodicity of its refractive index (Figure 3.6). A PhC is classified as 1D when its refractive index varies only in one direction (e.g. Bragg stacks<sup>55</sup>), 2D when it varies in two directions (e.g. pillar arrays<sup>56</sup>) and 3D when it varies in the x, y and z directions (e.g. opaline crystals,<sup>57</sup> photonic woodpiles<sup>58</sup>). A 1D PhC can therefore be described as a series of layers (films) of alternating refractive indices,  $n_1$  and  $n_2$ . Thus, when polychromatic light strikes and enters through a 1D PhC, a fraction of the wavelength(s) corresponding to the PBG is diffracted at the interface between the first and the second layer (Figure 3.7). As light continues to propagate throughout the PhC, other fractions will repeatedly be diffracted.<sup>59</sup> If the waves diffracted are in-phase, they will enter into a constructive interference, and the resulting amplitude gain will rise as an intense reflection corresponding to forbidden wavelength(s).

$$m\lambda_B = 2d_{hkl} \sin \theta$$

(Equation 3.1)

Equation 3.1 also known as the “Bragg’s Law” accounts for this phenomenon:  $m$  is the order of diffraction,  $\lambda_B$  is the Bragg wavelength (i.e. the reflectance maximum),  $d_{hkl}$  is the interplanar spacing, and  $\theta$  is the angle of incidence of light with respect to the normal.

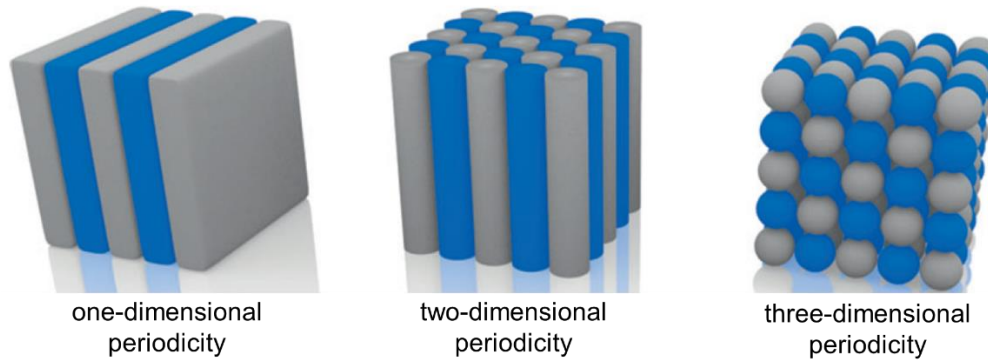


Figure 3.6. Schematic representation of the three classifications of photonic crystals according to the periodicity of their refractive indices (RI). The different colors represent materials of different RI. Reprinted with permission from Wiley-VCH Verlag GmbH & Co. KGaA.<sup>60</sup>

As the spatial period of the change in refractive index in PhC is in the range of several hundred nanometers to a few micrometers, the diffracted wavelengths belong to the visible or the infrared range. In order to take into account the refractive index, Bragg’s law of diffraction (Equation 3.1) is combined with Snell’s law of refraction (Equation 3.2) to obtain the Bragg-Snell law (Equation 3.3), which predicts the reflection maximum or the Bragg wavelength of a given PhC.<sup>61</sup>

$$n_1 \sin \theta = n_2 \sin \varphi \quad (\text{Equation 3.2})$$

where  $n_1$  and  $n_2$  are the refractive indices of the interstitial medium and of the microstructure, respectively, and  $\varphi$  is the angle of the refracted ray in the crystal with respect to the normal.

$$m\lambda_B = 2d_{hkl} \sqrt{n_{eff}^2 - \sin^2 \theta} \quad (\text{Equation 3.3})$$

where  $n_{eff}$  is the effective refractive index defined as:

$$n_{eff}^2 = f_1 n_1^2 + f_2 n_2^2 \quad (\text{Equation 3.4})$$

where  $f$  is the filling fraction of the component (i.e. the interstitial medium or the microstructure).

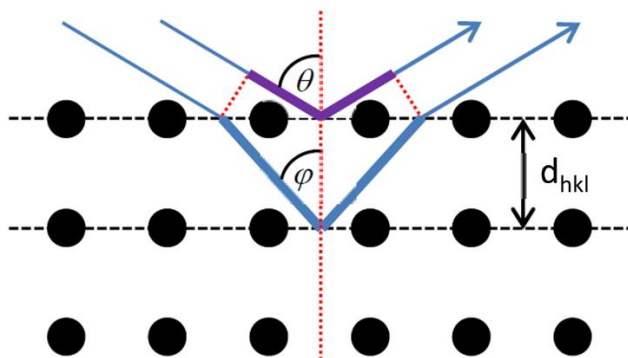


Figure 3.7. The Bragg diffraction of an electromagnetic radiation as it interacts with the particles of a crystal whose lattice constant is of the same magnitude as its wavelength. Adapted from Ref.<sup>62</sup>

The Bragg-Snell law (Equation 3.3) may also be extended to 2D and 3D photonic crystals to determine the reflection maximum as multiple works have already attested, though several numerical analysis techniques such as the finite difference time domain (FDTD) method, the finite element method (FEM), the transfer matrix method (TMM) and the plane wave expansion (PWE) method are used to be more accurate as to the position and extent of the PBG.<sup>63</sup> If the Bragg wavelength falls within the visible light spectrum then the PhC will appear intensely colored. Colors observed on these PhCs are called “structural colors” since they do not arise from molecular dyes but rather from the interaction of light with a periodic structure.<sup>64</sup> In nature, for example, photonic structures are responsible for the iridescent color of natural opals,<sup>65</sup> peacock feathers<sup>66</sup> and the scales of some butterflies<sup>67,68</sup> and beetles.<sup>69,70</sup>

Among the classifications of PhCs, the 3D PhC distinguishes itself by providing favorable conditions for a complete bandgap, i.e. refractive index periodicity found in all three directions.<sup>71</sup> A complete PBG has very particular requirements: the refractive index contrast must be high (>2.85) which occurs usually between silicon and air. Another requirement is that the crystal structure must be inverse opal with face-centered (fcc) or diamond crystal symmetry.<sup>59,61,72,73</sup> However, a PBG can also be incomplete (we will refer hereon to it as *pseudo* PBG), where the band of forbidden wavelengths changes depends on the angle of propagation of light in the PhC.<sup>73,74</sup> Examples of PhCs featuring pseudo PBG are the natural PhCs mentioned in the previous paragraph and the PhCs composed of alternating polymer (or silica) and air used for the detection of analytes, etc.

At laboratory and industrial scale, PhCs are fabricated by using either a bottom-up or a top-down approach. Bottom-up approaches rely on the spontaneous self-assembly of building blocks such as silica, latex or polystyrene microspheres into ordered periodic structures, usually the “colloidal

crystal arrays" (CCAs), also known as the "opal structure".<sup>75-77</sup> When closely packed, CCAs assume a fcc symmetry. While some approaches use an opal structure for their intended applications, others proceed with infiltrating the CCA gaps with the desired material and removing the spheres either thermally or chemically to obtain a negative replica of the CCA assembly, an opal structure of "air spheres" better known as "inverse opal".<sup>78</sup> Inverse opals are particularly attractive over conventional opals as they exhibit wider photonic bandgaps under the same parameters in accordance to the Bragg-Snell Law (Equation 3.3) and hence, are more favorable to exhibit a complete PBG, i.e. an omnidirectional complete prohibition of a band of wavelengths regardless of polarization, as long as the refractive index contrast exceeds 2.85.<sup>49,75,79</sup> While bottom-up approaches are generally quicker, less expensive and easier to scale-up, top-down approaches feature on the other hand higher control and precision on the final structure. Top-down approaches include various lithographic techniques that use either photons or charged particles or that rely on embossing or scanning tips followed by an etching step. Although the equipment involved can be rather expensive and the fabrication speed reduced, especially for larger structures, top-down approaches are known for their high precision and resolution.<sup>79</sup>

### 1.5. Photonic crystals based on molecularly imprinted polymers

Since the reflected wavelength depends on the PhC's refractive index contrast and on its structural lattice, changes in these parameters will affect the reflected wavelength. Therefore, if an event, such as molecular recognition, will cause a change in any of these parameters, a concomitant change in the reflected wavelength will be produced, which allows the PhC to serve as a sensor to detect the presence and possibly quantify the amount of the species generating the change. This is exactly what has been reported in several papers on PhCs coupled to MIPs. In general, MIP PhCs works in one or both of the following mechanisms. The first mechanism goes with a change in the refractive index contrast if a template with a different refractive index binds to the MIP. The second mechanism relies on a change in the lattice constant. This happens when the binding triggers a swelling or a shrinking of the PhC. Lu et al. reported for instance on the fabrication of PhCs consisting of MIP in the form of colloidal particles (MICs) for the colorimetric detection of 2,4,6-trinitrotoluene (TNT).<sup>53</sup> The MICs were synthesized by dissolving the template TNT and the functional monomer acrylamide in methyl methacrylate prior to dilution in water. The polymerization was initiated by adding potassium persulfate while stirring the mixture for 45 minutes at 80°C. In this way, monodisperse MICs with a diameter of 210 nm were formed, which were then separated from the mixture by centrifugation

followed by washing. Afterwards, the MICs were assembled into an opal structure by dispersing them in deionized water inside square glass containers. Glass slides activated in piranha solution and rinsed after were immersed vertically and left inside the glass containers for two days at 30°C in 50% relative humidity. The MIC array films that deposited on both sides of the glass slides were peeled off using an adhesive tape. The MIC array on the adhesive tape in its dry state displayed a base wavelength of 533 nm. An increasing red shift was visually observed on the dry MIC array after it was incubated in increasing concentration of TNT 3:2 v/v methanol/water from 0 mM to 20 mM, exhibiting successively green, yellow, orange and red colors as seen in Figure 3. 8. In contrast, the non-imprinted colloidal array red-shifted rather restrictively from green to yellow-green despite a 20-mM change in the TNT concentration. The change in the color of the MIC array, i.e. the Bragg wavelength, was attributed to the swelling of the MIC particles and the increase in their refractive index upon binding the TNT molecules.

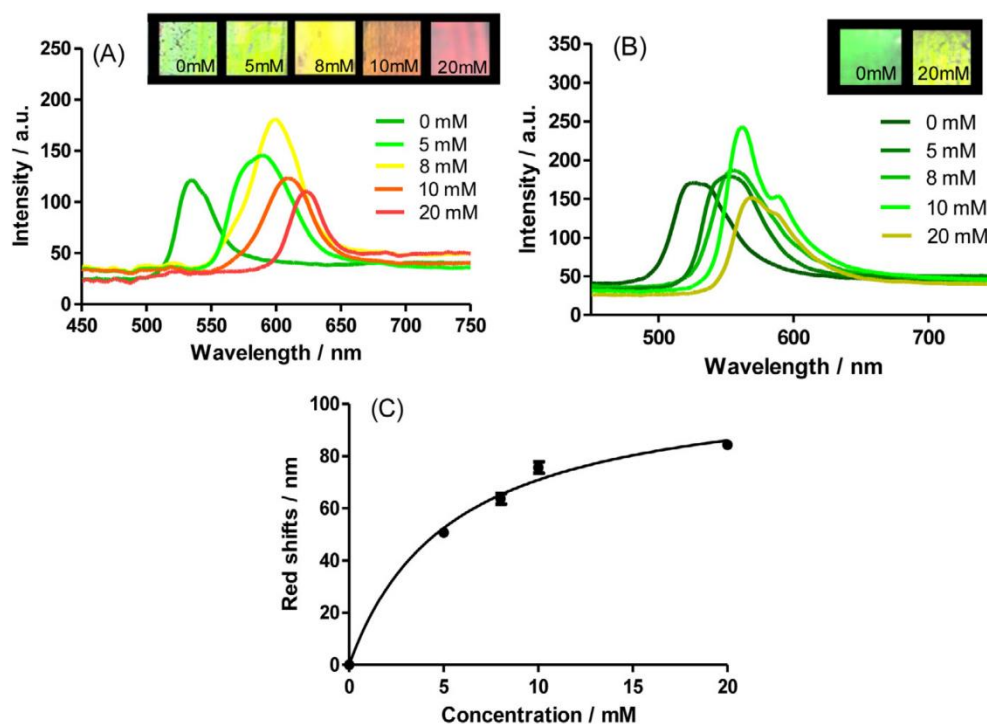


Figure 3. 8. The colors exhibited by (A) the MIC array and (B) the NIC array after incubation in increasing concentrations of TNT in 3:2 v/v methanol/water. (C) The red shift in the Bragg wavelength of the MIP as a function of the TNT concentration. Reprinted with permission from Elsevier B.V.<sup>53</sup>

Another example of molecularly imprinted photonic crystal is the inverse opal constructed by Song and co-workers for the colorimetric detection of tetracycline (TC).<sup>80</sup> They prepared an aqueous MIP precursor solution consisting of the template TC, the functional monomers acrylamide and acrylic acid, the crosslinker N,N'-methylene bisacrylamide and the initiator 2,2-diethoxyacetophenone and

immersed in it a latex-based opal mold dots that were coated on a hydrophobic polydimethylsiloxane (PDMS) substrate. After pulling the substrate out of the solution, it was exposed to UV light to induce polymerization. The substrate was immersed in toluene to remove the opal molds, leaving behind a molecularly imprinted inverse opal dots of 1.35- $\mu\text{m}$  diameter, which were washed thereafter. When dried after incubation in increasing aqueous concentrations of TC from 0 to 60 nM, these inverse opals displayed increasing red shift from cyan to dark red wavelengths as shown in Figure 3. 9.

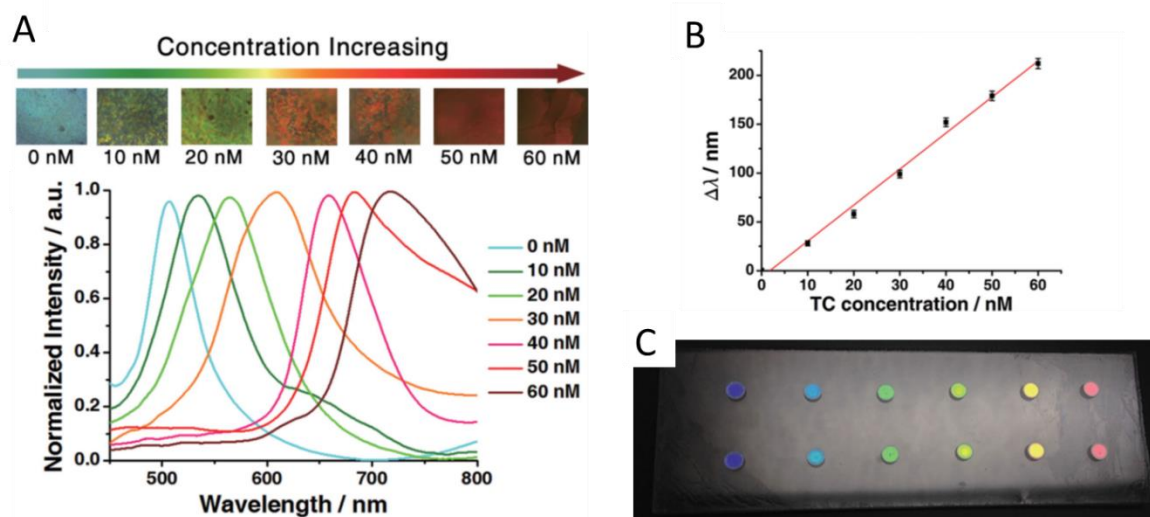


Figure 3. 9. (A) The colors exhibited by the molecularly imprinted inverse opal dots in response to increasing aqueous concentrations of tetracycline (TC). (B) The red shift in the Bragg wavelength of the molecularly imprinted inverse opal as a function of the TC concentration. (C) The molecularly imprinted inverse opal dots coated on the hydrophobic PDMS substrate. Reprinted with permission from Wiley-VCH Verlag GmbH & Co. KGaA.<sup>80</sup>

Yet another example of atrazine-imprinted PhC was reported by Li and co-workers by polymerizing a MIP precursor solution on silica CCA with an individual sphere diameter of 186 nm.<sup>52</sup> The MIP precursor was composed of atrazine, acrylic acid, EGDMA and AIBN as photoinitiator. After infiltrating the silica CCA, the precursor solution was sandwiched between the glass slide containing on its surface the CCA and a PMMA slide and was exposed to 365-nm UV light to induce polymerization. The sandwich was then immersed in 1% hydrofluoric acid to fully etch the silica particles, allowing the molecularly imprinted inverse opal hydrogel to stick onto the PMMA slide. As in the previous examples, the inverse opal showed a red shift in its Bragg wavelength, due to the swelling of the hydrogel when exposed to increasing concentrations of atrazine in phosphate buffer (Figure 3.10).

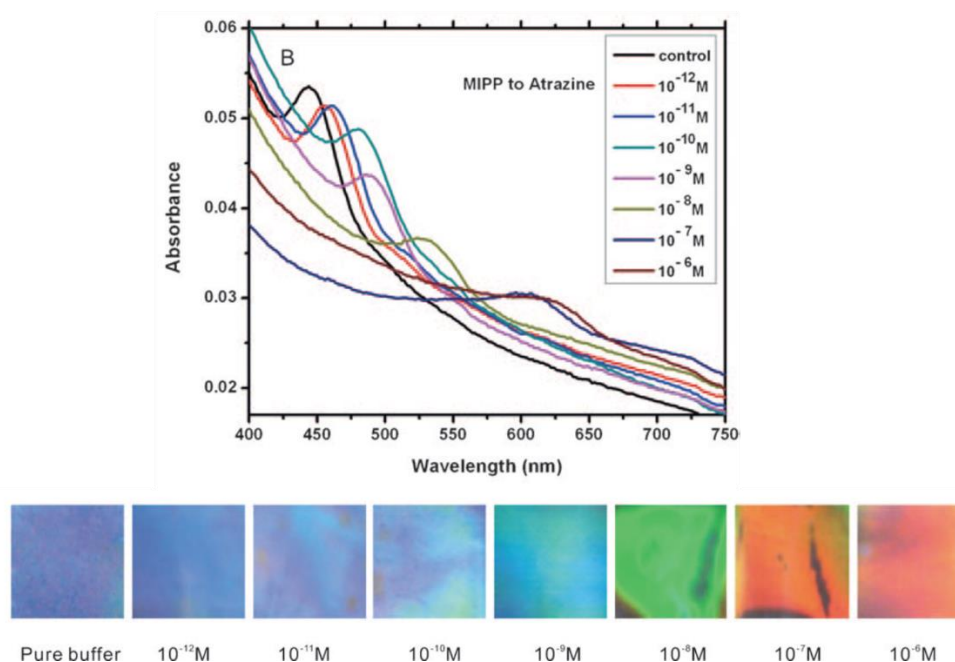


Figure 3.10. The colors exhibited by the molecularly imprinted inverse opal hydrogel upon rebinding atrazine in increasing concentrations. Reprinted with permission from Wiley-VCH Verlag GmbH & Co. KGaA.<sup>52</sup>

The majority of the synthetic 3D PhCs used for the detection of molecules of interest has undergone one form or another of the conventional bottom-up approaches. In spite of its precision and its flexibility to fabricate arbitrary structures, TPS has been used very limitedly in this regard. Most applications of TPS to fabricate photonic crystals resulted in photonic crystals that function in the infrared region of the spectrum.<sup>50,81,82</sup> This means that in spite of the straightforward approach of using TPS, the photonic crystals cannot be readily used for colorimetric detection of molecules of interest. For this reason, TPS would be exploited for the fabrication of PhCs with a pseudo PBG in the visible spectrum for the colorimetric detection of analytes. The following sections will show the use of TPS for the fabrication of opal- as well as woodpile-based photonic crystals.

## 2. Experimental

### 2.1. Materials

The photoresist IP-Dip and the fused silica substrates (3D SF DiLL) of dimensions 25 mm x 25 mm x 7 mm were from Nanoscribe GmbH, Germany. IP-Dip is the standard proprietary negative-tone photoresist of Nanoscribe for high-resolution TPS printing. 3-(trimethoxysilyl)propyl methacrylate (TMPPM) ( $\geq 98\%$ ), propylene glycol methyl ether acetate (PGMEA) ( $\geq 99.5\%$ ), 2-propanol (99.9%), ( $\pm$ )-propranolol hydrochloride ( $\geq 99\%$ ) and anhydrous acetonitrile (99.8%) were from Sigma-Aldrich.



Methanol, glacial acetic acid and absolute ethanol were from VWR Chemicals. Propranolol hydrochloride was converted into free base by extracting from a sodium carbonate solution at pH 9 into chloroform. THIOCURE® pentaerythritol tetra(3-mercaptopropionate) (PETMP) and THIOCURE® dipentaerythritol hexa(3-mercaptopropionate) (diPETMP) were from Bruno Bock Chemische Fabrik GmbH & Co. KG. Di(but-1-yn-4-yl) carbonate (DBC) was synthesized as previously reported.<sup>83</sup> Omnirad ethyl (2,4,6-trimethylbenzoyl) phenylphosphinate (Omnirad TPO-L) was from IGM resins.

## 2.2. Equipment and software

The TPS system used for the entire study was a unit of Nanoscribe Photonic Professional GT 3D printer (Nanoscribe GmbH, Germany). It is equipped with a pulsed femtosecond laser source at a center wavelength of 780 nm. It also includes a Carl Zeiss Axio observer microscope, which focuses the laser beam via an objective into the photoresist and together with the live camera, allows the monitoring of the printing process. It has motorized stages for the coarse movement of the photoresist sample and piezoelectric stages for finer but slower movements. The scan modes for printing available are the galvo and the piezo scan modes, the former of which was used throughout the study for its straightforward and rapid approach.

Two important software are associated with the Nanoscribe Photonic Professional GT. The first one is DeScribe which is an editor for General Writing Language (GWL) files. GWL is a script language developed by Nanoscribe that describes the trajectories to be followed by the laser focus and configures all the system parameters to be used during the writing process. DeScribe is used to design structures (in addition to third-party CAD software), to check syntax errors in the commands and to convert STL files to GWL files. The other software is called NanoWrite which presents a user interface to manipulate the Nanoscribe Photonic Professional GT. Through NanoWrite, the autofocus system is used to locate the interface between the photoresist and the substrate, and the printing process may be viewed online via a live camera.

## 2.3. Methods

### 2.3.1. TPS for the fabrication of opal photonic crystals

*Functionalization of fused silica substrates with TMPM.* All fused silica substrates used for TPS were functionalized with TMPM as follows: four fused silica substrates were placed inside a ceramic box

covered with a ceramic lid and immersed in 10 v/v%  $\text{NH}_3$  (aq), before being heated at  $80^\circ\text{C}$  for 15 minutes. The  $\text{NH}_3$  (aq) was then removed and replaced with a freshly prepared aqueous solution of 10 v/v%  $\text{H}_2\text{O}_2$  and 10 v/v% HCl to be heated once more at  $80^\circ\text{C}$  for 15 minutes. Afterwards, the solution was removed and the fused silica substrates were rinsed inside the box three times with milliQ water, thrice with acetone and dried under a stream of dinitrogen. The substrates were then immersed and left overnight in a 2 m/v% TMPM in toluene solution. After rinsing three times with acetone, they were dried again with dinitrogen and stored in a watertight container at  $4^\circ\text{C}$  until use.

*Direct writing of opal crystals via TPS.* A 3D opal crystal structure was initially designed using the computer-aided-design software (CAD) Fusion 360. The lattice was made up of spheres arranged in a face-centered cubic (fcc) unit cell that repeat 4.5 times in the x, y and z directions (Figure 3.11). The diameter of the spheres was varied for each writing of a crystal lattice: 2400, 800, 500, 240 nm. The design was saved as a STL file and translated to a GWL file for TPS in the following step.

The fabrication of opal crystal structures was performed using a Nanoscribe Photonic Professional GT printer as the TPS system. A drop of IP-Dip was placed on a TMPM-functionalized fused silica substrate mounted on a designated sample holder. The sample holder was then loaded into the Nanoscribe printer in DiLL configuration. The objective used was 63X NA1.4. The scan speed was set to  $10000 \mu\text{m/s}$  while the nominal laser power was at 20 mW.

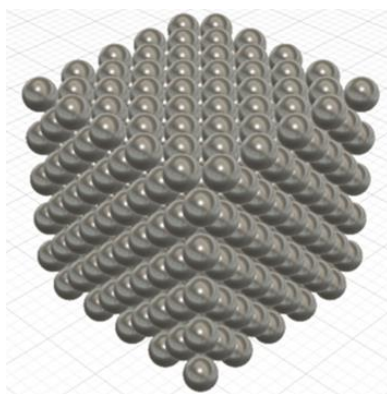


Figure 3.11. 3D model of an opal crystal with a fcc unit cell that repeats 4.5 times along the x, y and z axes.

After TPS, the opal crystal structures were developed by immersion in PGMEA for 20 minutes followed by 2 minutes in 2-propanol. The structures were then dried gently by air through a rubber blower.

*Characterization of the opal crystals.* Microscopy images of the opal crystals written via TPS were obtained using the brightfield mode of a Leica DMI6000 B fluorescence microscope (Leica Microsystems, Germany). The scanning electron microscopy (SEM) images were recorded on a QUANTA FEG 250 on gold sputter-coated samples.

### 2.3.2. Woodpiles based on functionalized IP-Dip

*Preparation of formulations for MIP and NIP woodpiles.* The formulation for MIP woodpiles was prepared by weighing 2.36 mg propranolol in a 2-mL glass vial followed by the addition of 5.30 mg acrylic acid and 2.5  $\mu$ L acetonitrile. The propranolol was allowed to dissolve spontaneously. Then, 53.00 mg IP-Dip photoresist was added. The relationship between the constituents is as follows: the molar ratio of propranolol to acrylic acid was 1:8; the mass ratio of acrylic acid to IP-Dip was 1:10.

The formulation for NIP woodpiles was prepared in the same manner while excluding propranolol.

*Direct writing of woodpiles via TPS.* The printing of the 3D structures was set to Dip-in Laser Lithography (DiLL) configuration (Figure 3.12). The DiLL configuration means that the objective of the TPS system is in direct contact with the photoresist, which keeps the spherical aberrations to a minimum constant for the full printing range. The objective used was 63X NA 1.4. Either the unaltered commercial formulation IP-Dip photoresist, the MIP photoresist or the NIP photoresist was dropped on the center of a fused silica slide previously functionalized with TMPM. The GWL files were loaded into Nanowrite and printing was executed.

Development of the structures was performed by dipping the slides in propylene glycol methyl ether acetate (PGMEA) for 20 minutes and then in 2-propranolol for 2 minutes. The structures were then allowed to dry. The 3D microstructures were visualized using the transmitted-light polarization-mode (TP-POL) of a Leica DMI6000 B fluorescence microscope (Leica Microsystems, Germany). The scanning electron microscopy (SEM) images were recorded on a QUANTA FEG 250 on gold sputter-coated samples.

*Washing of MIP and NIP woodpiles and preliminary binding test.* The woodpiles were washed by carefully placing its substrate in a 150-mL beaker containing 50-mL washing solvent. They were washed twice with 3:1 (v/v) methanol:acetic acid and then once with methanol while in an orbital

shaker set at  $50 \text{ min}^{-1}$ , each wash lasting an hour. They were then dried with  $\text{N}_2$  gas for TP-POL microscopy.

Consequently, the woodpiles were incubated with 10 mL 1.0 mM propranolol for two hours. The woodpiles were then washed with 100 to 200  $\mu\text{L}$  methanol and dried with  $\text{N}_2$  gas.

The woodpiles were then visualized using the transmitted-light polarization-mode (TP-POL) of a Leica DMI6000 B fluorescence microscope (Leica Microsystems, Germany).

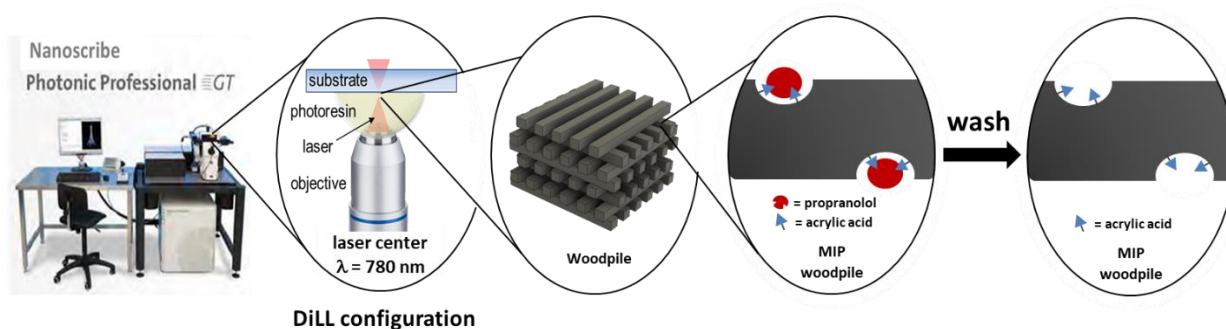


Figure 3.12. Scheme of the fabrication of MIP woodpiles via TPS.

### 2.3.3. Woodpiles based on thiol-containing formulations

*Preparation of thiol-yne formulations for the fabrication of microstructures.*

(a) *Snowflake microstructures.* The thiol-yne formulations prepared was grouped into two: 1) The PETMP/DBC formulations; and 2) the diPETMP/DBC formulations. The first group consisted of acrylic acid (110  $\mu\text{L}$ ), PETMP (1285.95 mg) and DBC (349.00 mg) in a 1 : 1.6 : 1.3 molar ratio. The second group consisted of acrylic acid (110  $\mu\text{L}$ ), diPETMP (1305.08 mg) and DBC (349.00 mg) in a 1 : 1 : 1.3 molar ratio. The photoinitiator TPO-L was added to both groups to a final concentration of 0.1, 1, 3, 5 or 10 % of the total number of moles of thiol groups in the mixture. No solvent was added. The formulations were mixed thoroughly in the dark with a stir bar.

(b) *Woodpiles.* The thiol-yne formulations prepared was grouped into two: 1) The PETMP/DBC formulations; and 2) the diPETMP/DBC formulations. Both these groups followed the same stoichiometric relationships of their constituents as presented in Chapter 1. However, no propranolol was added and the concentration of the photoinitiator TPO-L was raised to 10 % of the total number of moles of thiol groups in the mixture. A small amount of acetonitrile was added so that the final

concentration of the thiol bonds in the solution was 1.75 M. The formulations were mixed thoroughly in the dark with a stir bar.

*Preparation of thiol-acrylate formulations for the fabrication of microstructures.* Four acrylate-thiol resists were prepared based on the formulations adapted and modified from the work of Jiang et al.<sup>84</sup> The tetraacrylate used was pentaerythritol tetraacrylate, the polythiol was pentaerythritol tetrakis(3-mercaptopropionate) (PETMP) and the photoinitiator was ethyl (2,4,6-trimethylbenzoyl) phenylphosphinate (TPO-L). The tetrathiol was measured according to its percent weight in the final resist on Jiang's paper and its stoichiometric relationship to the tetraacrylate and to the photoinitiator was preserved in our experiment. The mole ratio of PETMP to pentaerythritol tetraacrylate and TPO-L for each formulation were as follows: AcryS1 (1 : 9.32 : 0.13), AcryS2 (1 : 4.14 : 0.07), AcryS3 (1 : 2.41 : 0.04) and AcryS4 (1 : 1.55 : 0.03).

*Direct writing of microstructures via TPS.* After the STL files were converted to GWL files, the fabrication of the microstructures was performed using Nanoscribe Photonic Professional GT printer as the TPS system. A drop of a thiol-containing formulation was placed on a TMPM-functionalized fused silica substrate mounted on a designated sample holder. The sample holder was then loaded into the Nanoscribe printer in DiLL configuration. The objective used was 63X NA1.4. The scan speed and the laser power were set accordingly.

Development of the structures was performed by dipping the slides in propylene glycol methyl ether acetate (PGMEA) for 20 minutes and then in 2-propanol for 2 minutes. The structures were then allowed to dry. The 3D microstructures were visualized using the transmitted-light polarization-mode (TP-POL) of a Leica DMI6000 B fluorescence microscope (Leica Microsystems, Germany). The scanning electron microscopy (SEM) images were recorded on a QUANTA FEG 250 on gold sputter-coated samples.

### 3. Results and Discussion

#### 3.1. TPS for the fabrication of opal photonic crystals

The first step in fabricating an opal photonic crystal via TPS is the design of an opal structure, or more specifically, of a closely packed opal structure with a fcc unit cell of spheres. If the aimed reflectance peak maximum ( $\lambda_{\max}$ ) is 560 nm when  $\Theta = 0^\circ$ , the diameter of the spheres of the opal

crystal can be calculated using the Bragg-Snell equation (Equation 3.3). For the first order Bragg diffraction from fcc (111) planes,  $d_{hkl} = 0.8165D$ .<sup>57</sup> The equation is therefore transformed into the following:

$$\lambda_B = 1.633D \sqrt{n_{eff}^2 - \sin^2 \theta} \quad (\text{Equation 3.5})$$

where  $D$  = average center-to-center distance between spheres on the (111) planes, i.e. the theoretical sphere diameter. Taking into consideration that TPS would be performed on a photoresist for the fabrication of polymeric opal structures, it was important to know the refractive index of the polymerized photoresist. The photoresist to be used was IP-Dip, whose polymer has a RI of 1.552 according to its specifications.<sup>85</sup> In a fcc lattice, the filling factor of the polymer spheres was 0.74 while that of the air matrix was 0.26. Solving the modified Bragg-Snell equation, the theoretical diameter of each sphere should be 240 nm.

The result of the calculation agrees with the fact that a photonic crystal diffracts radiation whose wavelength is comparable (around twice<sup>61</sup>) to the magnitude of the crystal's lattice constant. This was also in agreement with the several works that reveal that lattice constants between 200 nm and 350 nm often give rise to visible-light-range photonic crystals.<sup>57,58,61,86</sup>

The aim therefore was then to fabricate via TPS a 3D PhC of opal structure with a band gap located in the visible range consisting of spheres of 240 nm in diameter. These structures were intended to be used for the optical detection of analytes, which to the best of our knowledge, has never been done before on MIP-based PhCs made by TPS.

### 3.1.1. Fabrication of opal crystals via TPS

Opal crystal structures were fabricated via TPS such that their fcc unit cell repeated 4.5 times in the x, y and z direction. The diameter of the spheres was initially set to 2400 nm, in order to start with a feature size within the conventional printing range for the Nanoscribe Photonic Professional GT printer. At this diameter, the Nanoscribe printer easily achieved the structure considering that its typical smallest feature size in the xy plane is 200 nm while in the z direction is 700 nm (under the following conditions: DiLL configuration, IP-Dip as photoresist, fused silica as substrate, use of 63X NA 1.4 objective). As such, the resulting crystal featured well defined and distinct spheres, whose periodic

arrangement appeared in the brightfield of a microscope as alternating dots of shade and light (Figure 3.13).

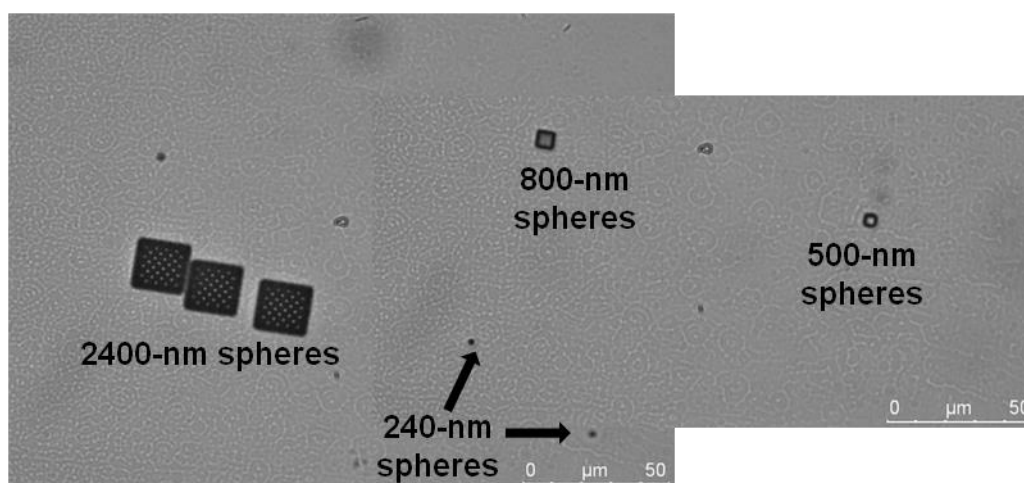


Figure 3.1312. Optical microscopy image of TPS-fabricated opal crystals based on spheres of different size (as indicated by the arrows).

The diameter of the spheres was then progressively reduced, in order to investigate the feasibility of writing opals with lattice constants in the range 200 - 350 nm. Such constants would indeed provide the crystals with visible colors. The following diameters were tested: 800 nm, 500 nm and 240 nm. At a diameter of 800 nm, the contours of the spheres appeared less defined than at a diameter of 2400 nm as shown by the SEM images (Figure 3.14). In fact, the spheres looked more like rectangles. This was because the height of the spheres at 800 nm was just 100 nm away from the typical vertical limit of resolution of Nanoscribe, i.e. 700 nm. The resolution at 500-nm diameter was even worse, as the programmed height of the spheres was already below the vertical limit. This led to spheres extending beyond their intended height, occupying the space intended for air holes and could even be overlapping with one another. This gave the impression that the spheres were being melded to each other, so that that the crystal structure was melting. Eventually, the 240-nm spheres were no longer found by SEM.

However, according to the results on the crystal based on 500-nm spheres, TPS using Nanoscribe is not suited to write “colored” opals with lattice constants in the range of 200 to 350 nm. Indeed, when visible (white) light was shone through an optical fiber onto the structure, no reflection could be distinguished even under an optical microscope.

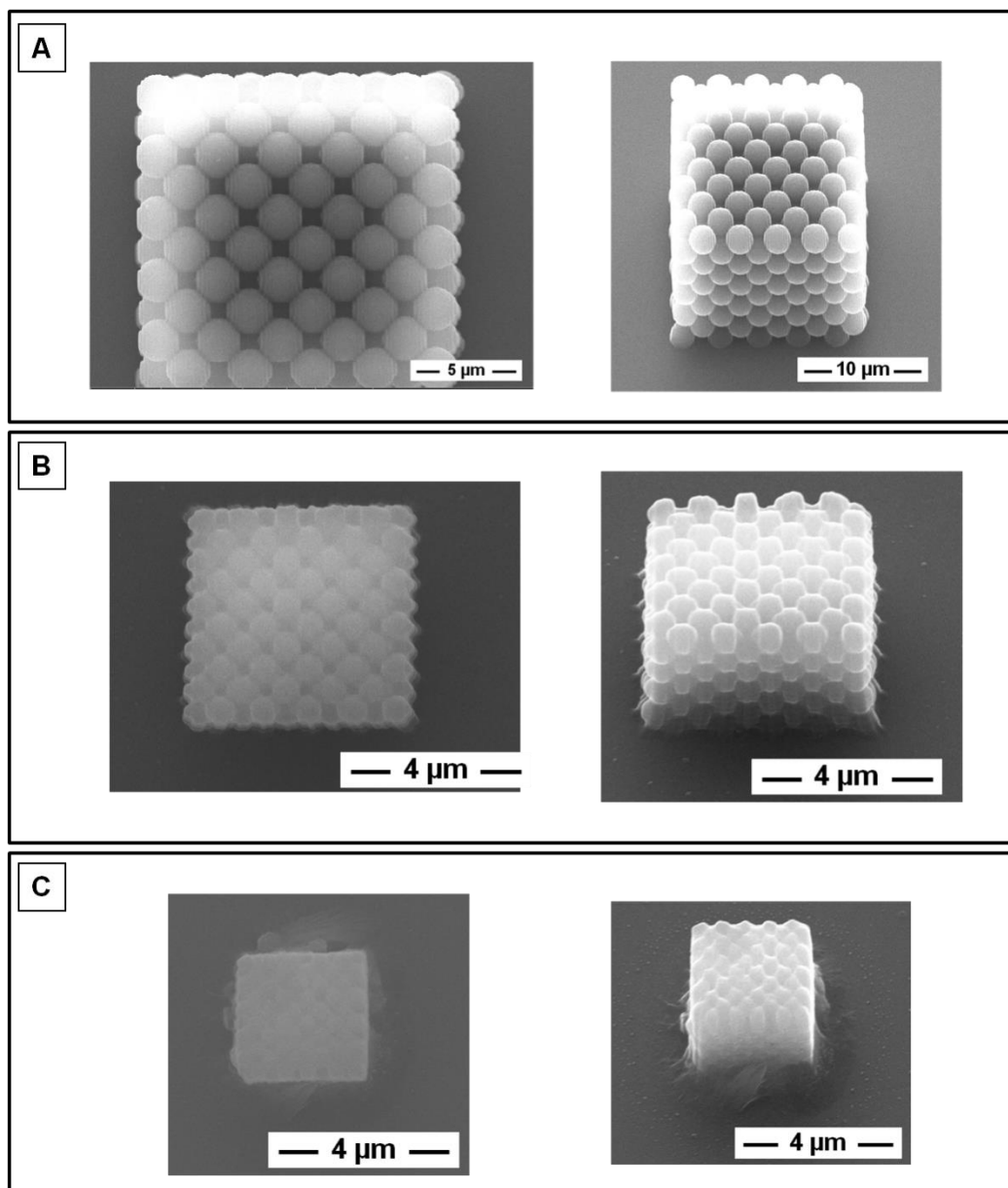


Figure 3.14. Top-view and angled-view (left and right, respectively) of opal crystals consisting of (A) 2400-nm, (B) 800-nm and (C) 500-nm spheres.

When running these tests, we also noticed that extra voxels were mechanically added by the software during the CAD-STL conversion, in order to better approximate the spherical geometry, albeit this resulted in loss in the fidelity to the original design. It must be remembered here that, according to the data sheet, the smallest voxel has an upright oval shape with a lateral size of 200 nm and a height of 700 nm, values which are very close to the diameter of the spheres. Therefore, to achieve a length of 500 nm at the equator of a sphere, voxels must be added; however, this would severely affect and diminish the curvature of the sphere along the Z axis. This would in turn also reduce the



inter-sphere distances, which could make active radicals to preferentially diffuse in certain direction, thus causing “excessive printing” or unwanted polymerization within the local vicinity of the voxel.

Therefore, the strategy to write photonic crystals using TPS was modified as follows: (1) the 3D model would be encoded directly on the Describe software to ensure faithful writing of the design. (2) spheres would be replaced by rods assembled into woodpile structures (i.e. another example of 3D photonic crystals) in order to avoid any problem of anisotropic curvature.

### 3.2. TPS for the fabrication of woodpile photonic crystals

Along with ordinary and inverse opals, woodpile lattices stand as one of the prominent 3D structures in the field of photonics. In contrast to other structures, woodpiles are known to generate high quality PBGs from a wider range of filling ratios, i.e. ratio of the space occupied by the constituting material of the woodpile to that of the interstitial medium (e.g. air), at a set refractive index ratio.<sup>87,88</sup> These structures are also more straightforward to fabricate especially using stereolithography. Woodpiles are comprised of layers of one-dimensional rods stacked on top of each another with a repeating sequence every four layers (Figure 3.15). The axes of intra-layer rods are parallel to each other and separated by a certain distance,  $a$ . Meanwhile, the adjacent layers are rotated  $90^\circ$ , which makes the axes of the rods within the second and the fourth layers perpendicular to those of the first and the third layers. The axes of the rods are laterally shifted by  $a/2$  every second layer (i.e. first and third layers, second and fourth, etc.).<sup>89</sup> If the periodicity in the  $z$  direction,  $c$ , is equal to  $a\sqrt{2}$ , then the woodpile is described as having a fcc lattice. Otherwise, the woodpile adopts a face-centered tetragonal (fct) lattice symmetry.<sup>87</sup>

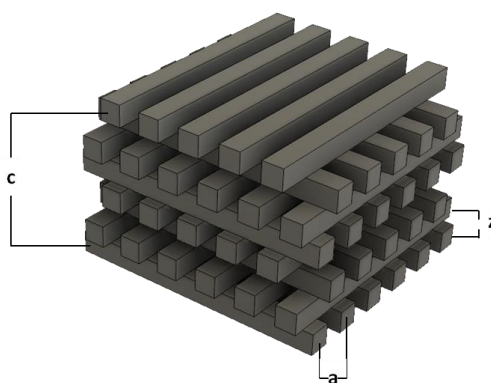


Figure 3.15. 3D model of a woodpile structure.

While there exist many theoretical blueprints as well as actual woodpile structures in literature, most of them worked in the infrared or the microwave range. A few notable exceptions affording visible colors include woodpiles by Wegener et al.<sup>90</sup> and by Yang et al.<sup>58</sup> The firsts achieved such result by coupling stimulated-emission-depletion microscopy (STEM) with direct laser writing (DLW), which allowed projection of a secondary laser that would deplete excited molecules on the edges of the writing laser voxel, thereby reducing its effective exposure volume and resulting in lattice constants between 250 nm to 450 nm. On the other hand, Yang and his team applied a post-printing thermal annealing, at 450°C (and in an inert environment) which allowed shrinking the lattice constant down to 475 nm. Both approaches thus resulted in woodpiles generating colors in the visible spectrum. It should be noted, however, that no color-generating woodpile has ever been used for molecular recognition.

The aim therefore was to try to fabricate via TPS woodpiles that have PBG in the visible light range for the facile colorimetric detection of analytes. Herein, various combinations of scan speeds and laser powers were investigated to bring out the smallest possible lattice constants. The woodpiles were expected to furnish a pseudo PBG instead of a complete PBG, given the low RI contrast (<2.85) between MIP and air. Several formulations would then also be tested. Fabrication of the woodpiles was performed first by using a “functionalized” formulation of the IP-Dip. With “functionalized photoresist” we then mean that a functional monomer would be added, in order to raise binding sites for the template molecule, propranolol in this case. Woodpiles were also fabricated using thiol-containing formulations, more specifically, thiol-yne and thiol-acrylate formulations. Their chemistries eliminate the inhibition effects of oxygen on radical polymerization, which is useful especially in setups such as TPS wherein the photoresist is in contact with air. Furthermore, the thiol-yne reaction yields polymers with higher modulus than the corresponding and more popular thiol-ene, due to the higher functionality of the alkyne groups, leading to higher crosslinking.<sup>91,92</sup> Durable polymers are important especially when structures as thin as a few hundred nanometers are sought. Finally, thiol-acrylate formulations have been reported to produce structures with dimensions as low as 180 nm via TPS,<sup>84</sup> which is interesting for the fabrication of color-generating woodpiles.

### **3.2.1. Fabrication of woodpiles via TPS**

The design of the woodpiles was mainly adapted from the work of Fischer and Wegener<sup>90</sup> wherein they fabricated multiple woodpiles under different laser powers and scan speeds. In their work, rods that were spaced laterally from one another of 450 nm yielded the best results in terms of color.

Therefore, the same distance was adapted herein. As for the distance between adjacent sets of four layers, they used  $c = a\sqrt{2}$ , which fulfills the condition for a woodpile lattice to have a fcc symmetry. In addition, they increased  $c$  by 28% to compensate for shrinking after the development of the structures. This led to an axial distance between adjacent layers equal to 204 nm which is below the vertical resolution of the Nanoscribe whose typical finest vertical resolution is 700 nm. Hence, we directly used the value of  $c$  for axial separation between layers,  $z$ , which is 815 nm. It should be noted that their photoresist was based on the monomer pentaerythritol tetraacrylate and the initiator 7-diethylamino-3-thenoylcoumarin. Through mass spectrometry and the literature,<sup>93</sup> IP-Dip was confirmed to contain pentaerythritol triacrylate (60% - 80 %).

Woodpiles are attractive structures to be fabricated using direct laser writing techniques such as TPS because of the simplicity of writing layers of rods on top of each other. To this end, we utilized codes directly on DeScribe since rods can be generated to have the width and height of a voxel (and hence the smallest dimensions possible) as opposed to creating a 3D model on Fusion360 which we observed can assign several voxels to one point.

#### **3.2.1.1. Woodpiles based on commercial formulation**

Woodpiles were initially fabricated using the commercial formulation IP-Dip on a functionalized fused silica substrate. The laser power (LP) and the scan speed (SS) were varied. Figure 3.16 shows that writing at SS = 8000  $\mu\text{m/s}$  and LP = 15, 20 and 25 mW generated visible-colored woodpiles. This was also true at SS = 1000  $\mu\text{m/s}$  and LP = 10 and 15 mW. At higher laser power, rods became thicker, exceeding the necessary dimensions for a PBG in the visible range. On the other hand, a very low laser power posed the risk of weak structural integrity. While the colored woodpiles exhibited even slight changes in color when the substrate was laterally moved under the objective, the change was most pronounced for the woodpile written at SS = 1000 and LP = 15 mW as seen in the outset of Figure 3.15.

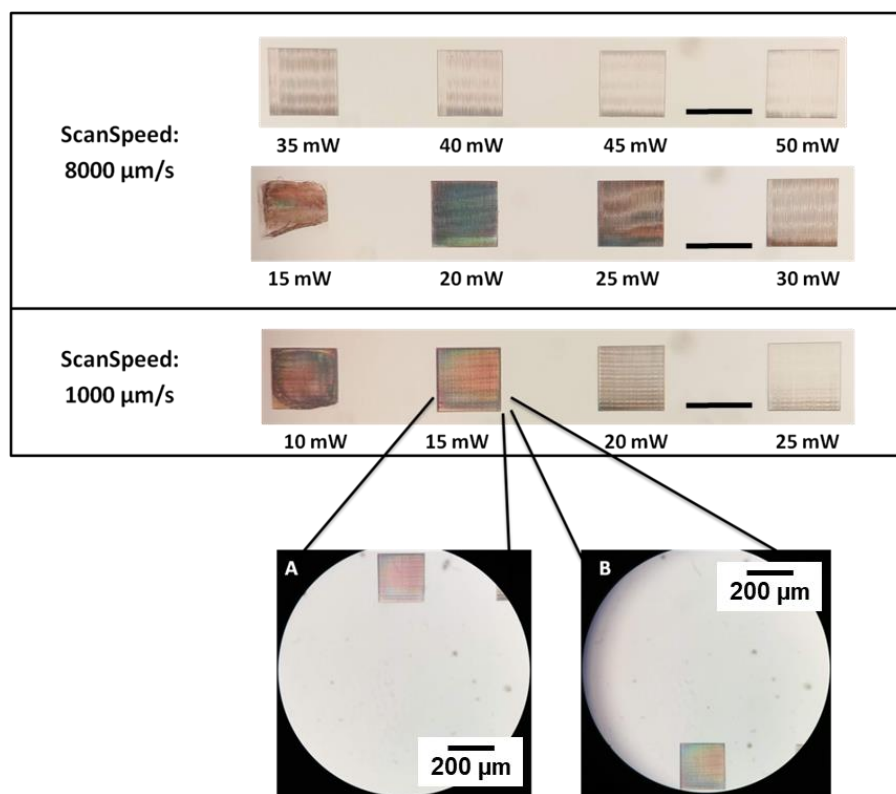


Figure 3.16. Optical microscopy images (TL-POL) of  $200 \times 200 \mu\text{m}^2$  woodpiles at the center of the field of view (FOV) of a 20x objective (scale bar =  $200 \mu\text{m}$ ). Laser power values expressed in mW. (Outset) Woodpile written at SS =  $1000 \mu\text{m/s}$  and LP = 15 mW moved across the FOV.

**Functionalized woodpiles for molecular imprinting: preliminary results.** The direct writing of molecularly imprinted woodpiles required the modification of the photoresist IP-Dip. Acrylic acid was added as the functional monomer at an arbitrary level of 10% of the weight of the IP-Dip used. This is based on the observation that acrylic acid was usually around 7% of the weight of the cross-linker in our past pre-polymerization mixtures (thiol-yne- and (meth)acrylate-based). Propranolol was used as the imprinting template in a 1:8 molar ratio with acrylic acid, a common ratio in literature.<sup>94–96</sup> Acetonitrile of half the volume of acrylic acid was added to help dissolve propranolol. The formulation for NIP woodpiles was prepared in the same way but without propranolol.

Figure 3.17 shows the representative SEM images of the MIP and the NIP woodpiles written at SS = 8000 and LP = 40 mW. The NIP woodpile conformed to the intended spacing between the rods, i.e. 450 nm and the width of the rods were around 200 nm which is the expected x-y width of a voxel using the 63x NA 1.4 objective of Nanoscribe. In contrast, the MIP woodpile had thicker rods and wider gaps.

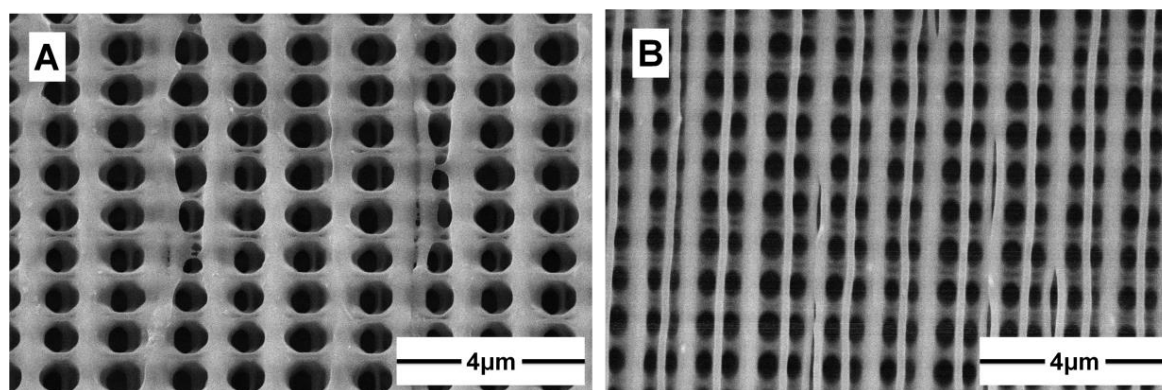


Figure 3.17. Representative SEM images of (A) the MIP woodpile and (B) the NIP woodpile.

A preliminary binding test was performed to investigate the optical response of the MIP and NIP woodpiles. When immersed in methanol (RI = 1.3312) or acetonitrile (RI = 1.3421), the woodpiles lost their colors. This may be attributed to the resulting low RI contrast between the polymeric rods and each solvent, considering that RI of the polymer was 1.552. Nevertheless, they regained their color upon complete drying (RI of air = 1). For the binding test, incubation with a relatively high concentration of propranolol in acetonitrile at 1.0 mM was performed to easily observe any optical response. After incubation, a small volume of methanol was used to flush away any unbound propranolol.

Figure 3.18 presents the MIP woodpile before washing, after washing and after incubation with propranolol. All the images were taken after drying the woodpiles. Here, the MIP woodpile changed its color after incubation from pinkish-blue to dark blue. This can be attributed to the shift in the transmitted wavelength due to the change in the average refractive index of the molecularly imprinted polymer upon template uptake.

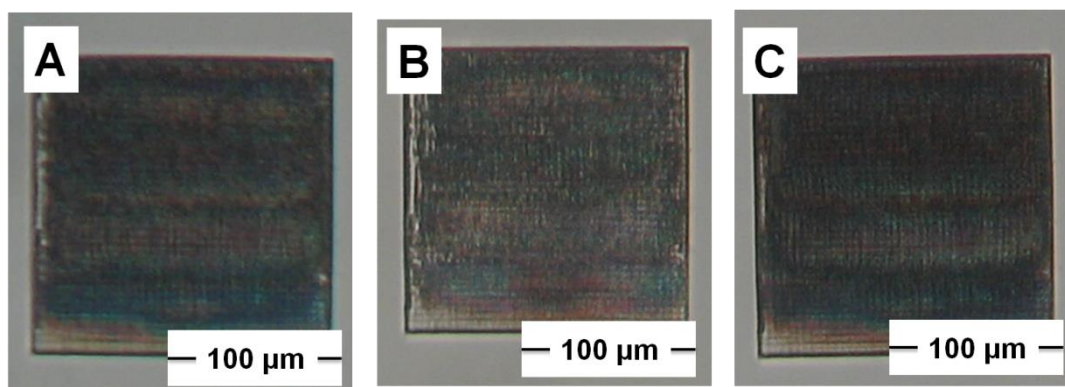


Figure 3.18. Microscopy images (TP-POL) of the MIP woodpile (A) before washing, (B) after washing and (C) after incubation with 1.0 mM propranolol in acetonitrile.

On the other hand, the NIP woodpiles did not display a significant color change after incubation with the propranolol solution due to lack of binding sites (Figure 3.19).

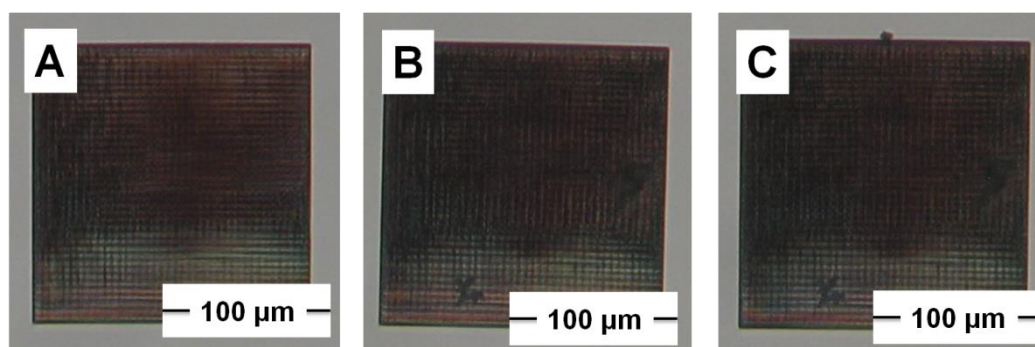


Figure 3.19. Microscopy images (TP-POL) of the NIP woodpile (A) before washing, (B) after washing and (C) after incubation with 1.0 mM propranolol in acetonitrile.

There exist two sensing schemes in photonic sensing: 1) measuring the shift in the resonant wavelength of the PhC, and (2) measuring the change in its intensity.<sup>63</sup> In order to quantitatively express the optical response of the PhCs so far presented, the difference in the dimness of the woodpiles, which is taken as a change in intensity, after washing and after incubation with propranolol was compared through the software ImageJ as presented in Figure 3.20.

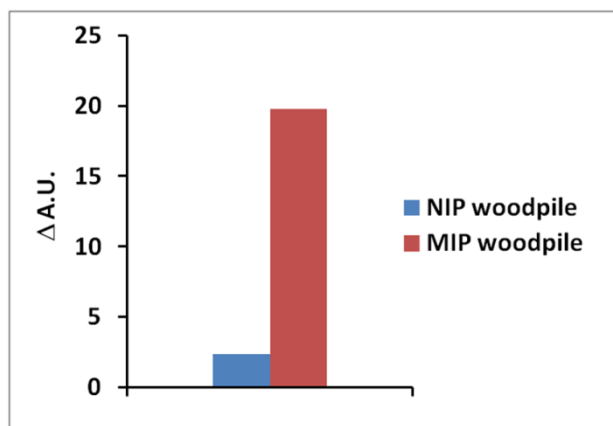


Figure 3.20. Darkness increase for the woodpiles incubated with 1.0 mM propranolol in acetonitrile.



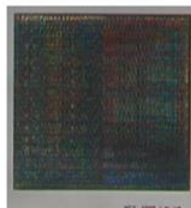

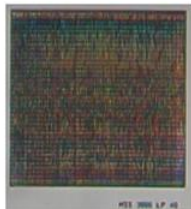
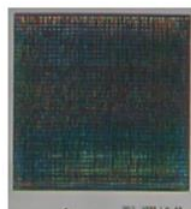



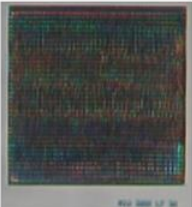
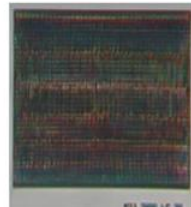
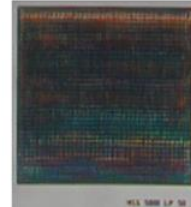
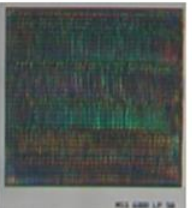
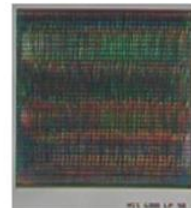
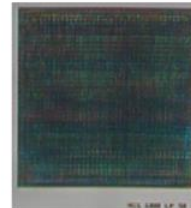
The preliminary results shown so far were promising in terms of using TPS to directly write molecularly imprinted woodpile photonic crystals. This paves the way for the optimization of the writing parameters, i.e. the power and the scan speed of the laser used in TPS.

**Functionalized woodpiles for molecular imprinting: optimization.** The MIP and NIP IP-Dip precursor formulations were investigated for their suitability for the construction of woodpiles under different scan speeds and laser power values to determine the optimized conditions for molecular recognition. Initially, lines of one-voxel width and a half-voxel height were written in triplicates at varying parameters to determine those which yielded the smallest features. Smaller features would mean smaller lattice constants, which would favor color-generating woodpiles. The scan speeds used were from 1000  $\mu\text{m/s}$  to 10000  $\mu\text{m/s}$  with 1000- $\mu\text{m/s}$  interval while the laser power values used were from 5 mW to 50 mW with 5-mW interval. The results showed that in general, higher scan speeds and lower laser powers gave smaller written voxel features (Appendix B, Figures B1 and B2). A higher scan speed denoted shorter time of exposure of the photoresist to the laser while a lower laser power implied less number of photons for inducing polymerization. Both of these conditions contributed therefore to the generation of a minimum number of photoinitiator radicals enough to initiate polymerization and yield thin and short lines strong enough to withstand the development step after TPS. With the MIP IP-Dip precursor formulation, the mean smallest voxel width achievable was 277.0 nm  $\pm$  156.7 and was obtained using a scan speed of 10000  $\mu\text{m/s}$  and a laser power of 50 mW. The mean smallest voxel height was 618.0 nm, which was attained at a scan speed of 4000  $\mu\text{m/s}$  and a laser power of 40 mW (Appendix B, Figure B1). On the other hand, the mean smallest voxel width attained using the NIP

IP-Dip precursor was  $304.7 \text{ nm} \pm 39.2$  ( $SS = 4000 \text{ } \mu\text{m/s}$ ,  $LP = 35 \text{ mW}$ ) while the mean smallest voxel height was  $575.2 \text{ nm} \pm 88.0$  ( $SS = 3000 \text{ } \mu\text{m/s}$ ,  $LP = 30 \text{ mW}$ ) (Appendix B, Figure B2).

The next step was the fabrication of MIP and NIP woodpiles at different scan speeds and laser powers just as with the lines in the previous paragraph. Figure 3.21 and Figure 3.22 show MIP and NIP woodpiles, respectively, for each “color-generating” parameters (in triplicate). Curiously, these parameters did not correspond to the values that had yielded the smallest widths for the MIP and NIP lines described earlier. Indeed, the “color-generating” parameters for woodpiles were found 10 to 25 mW lower in laser power for the same scan speed, and a few woodpiles even appeared at parameters where no lines had been previously written with success. One explanation could be that when the rods were written very close to each other laterally (i.e. voxel boundaries separated only by less than 200 nm, unlike the lines in the previous paragraph separated by about 2  $\mu\text{m}$ ), the same number of initiator radicals as before was generated, only this time, they were concentrated in a much smaller volume and thus, were present in high density. This high density is not homogeneous, however, throughout the space spanning the laterally neighboring rods, with higher densities remaining within the inner regions of the lines and lower densities in the space between them. The high density of the active radicals allowed for the polymerization of the rods even at lower laser powers than with the lines before. On the other hand, the heterogeneity of the density permitted distinction of boundaries between the rods.



<b>MIP<sub>T1</sub></b>	<b>MIP<sub>T2</sub></b>	<b>MIP<sub>T3</sub></b>
 <p>SS1000 LP15</p>		
 <p>SS3000 LP20</p>		
 <p>SS4000 LP20</p>		
 <p>SS5000 LP25</p>		
 <p>SS6000 LP25</p>		

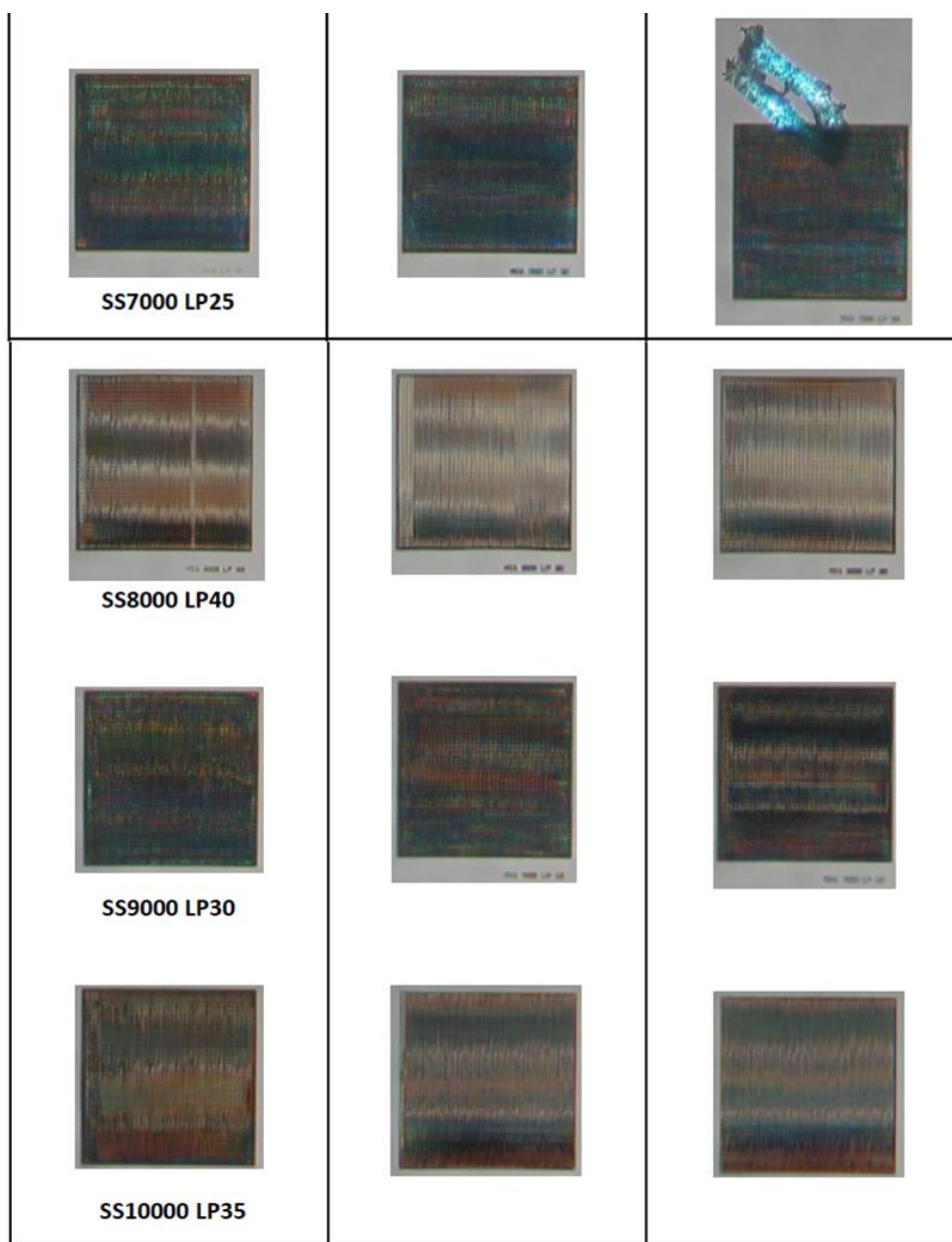





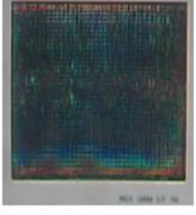



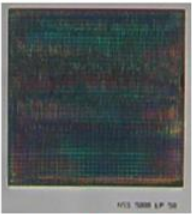
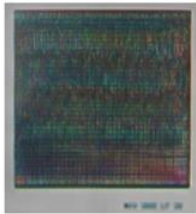

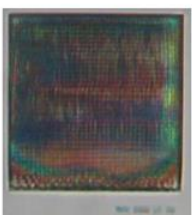
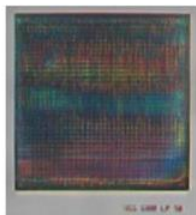



Figure 3.21. TP-POL microscopy images of IP-Dip MIP woodpile triplicates 3D printed using the experimentally determined “color-generating” parameters. The fiber-like figure on the third replicate at SS7000 LP25 is a contamination.

<b>NIP<sub>T1</sub></b>	<b>NIP<sub>T2</sub></b>	<b>NIP<sub>T3</sub></b>
 <p>SS1000 LP15</p>		
 <p>SS3000 LP20</p>		
 <p>SS4000 LP20</p>		
 <p>SS5000 LP25</p>		
 <p>SS6000 LP25</p>		

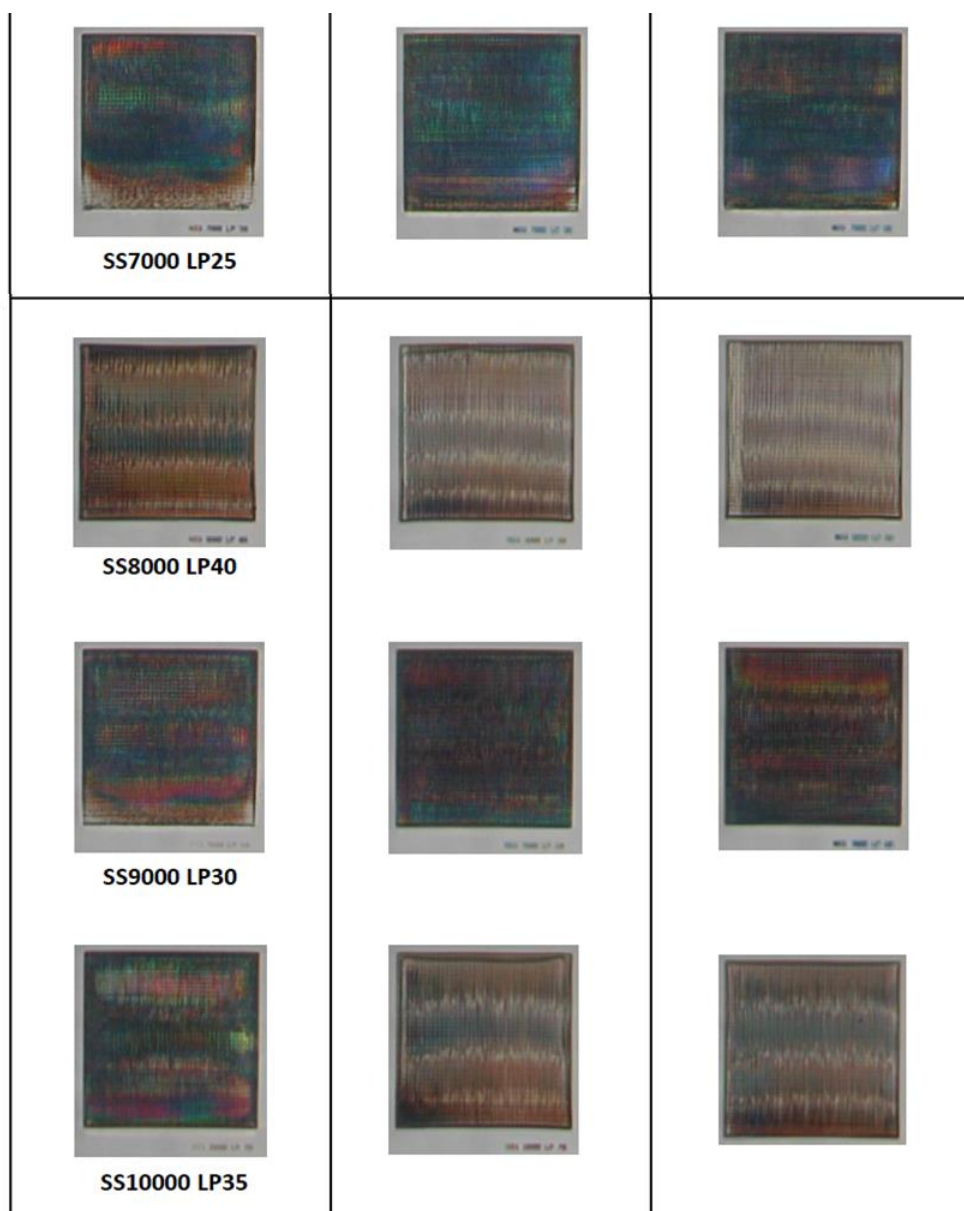
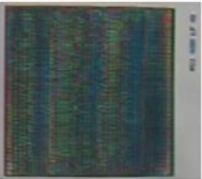
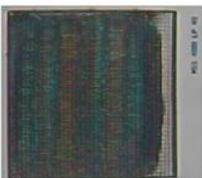
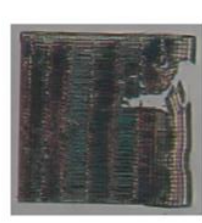




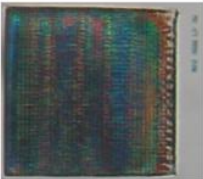
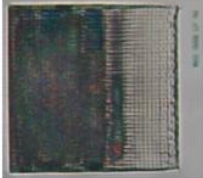
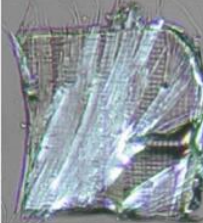
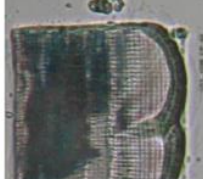
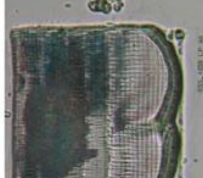
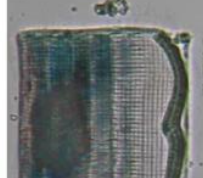
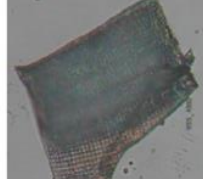
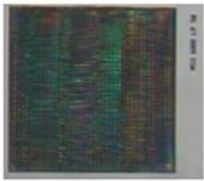
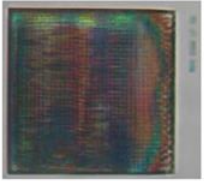
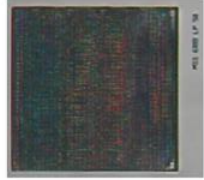
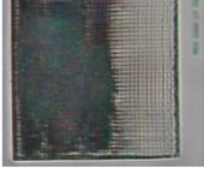
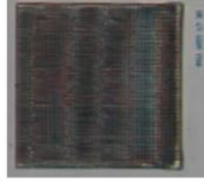
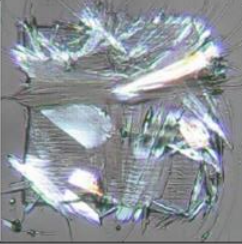
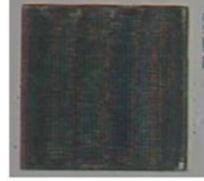
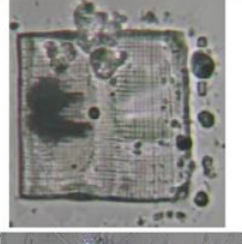
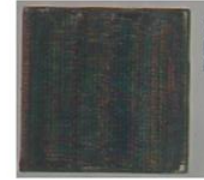
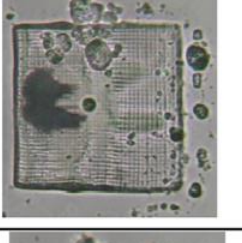
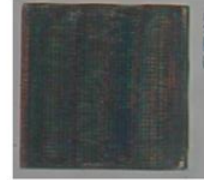
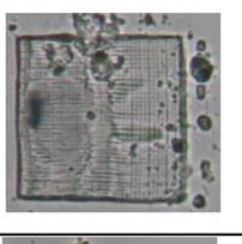
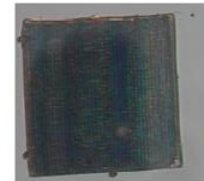
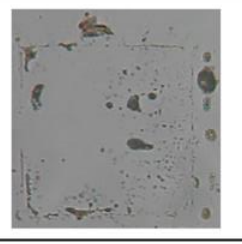


Figure 3.22. TP-POL microscopy images of IP-Dip MIP woodpile triplicates 3D printed using the experimentally determined “color-generating” parameters.

The woodpiles in Figure 3.21 and Figure 3.22 were washed with 3:1 methanol/acetic acid and then incubated in 1.0 mM propranolol in acetonitrile to see if they would change in color as a response to the target molecule due to the local change in the refractive index contrast. In general, the woodpiles showed a slight change in color after washing and drying. After incubation in the propranolol solution and drying, some changed their colors while others retained propranolol crystals on their surfaces. Methanol was then used to wash away any propranolol crystals and unbound propranolol molecules from the woodpiles, which were then allowed to dry. Surprisingly, we noticed

that upon washing several times, the woodpiles were unable to return to their color just before incubation. We speculate that an extensive washing destroyed and/or prevented the return to their color before incubation. It could be that woodpiles based on the functionalized IP-Dip were not durable enough to sustain several and prolonged exposure to liquid medium. Figure 3.23 shows the progress of representative MIP and NIP woodpiles as they underwent the various stages of the experiment.

<p>After printing</p>  <p>MT1 SS4000 LP20</p>	<p>After washing</p> 	<p>After PRO incubation</p> 	<p>After 100 <math>\mu</math>L wash</p> 	<p>After 200 <math>\mu</math>L wash</p> 	<p>After 500 <math>\mu</math>L wash</p> 	<p>After washing for reuse</p> 
<p>After printing</p>  <p>NT1 SS4000 LP20</p>	<p>After washing</p> 	<p>After PRO incubation</p> 	<p>After 100 <math>\mu</math>L wash</p> 	<p>After 200 <math>\mu</math>L wash</p> 	<p>After 500 <math>\mu</math>L wash</p> 	<p>After washing for reuse</p> 

After printing	 MT1 SS6000 LP25	 NT1 SS6000 LP25
After washing		
After PRO incubation		
After 100 $\mu$ L wash		
After 200 $\mu$ L wash		
After 500 $\mu$ L wash		
After washing for reuse		

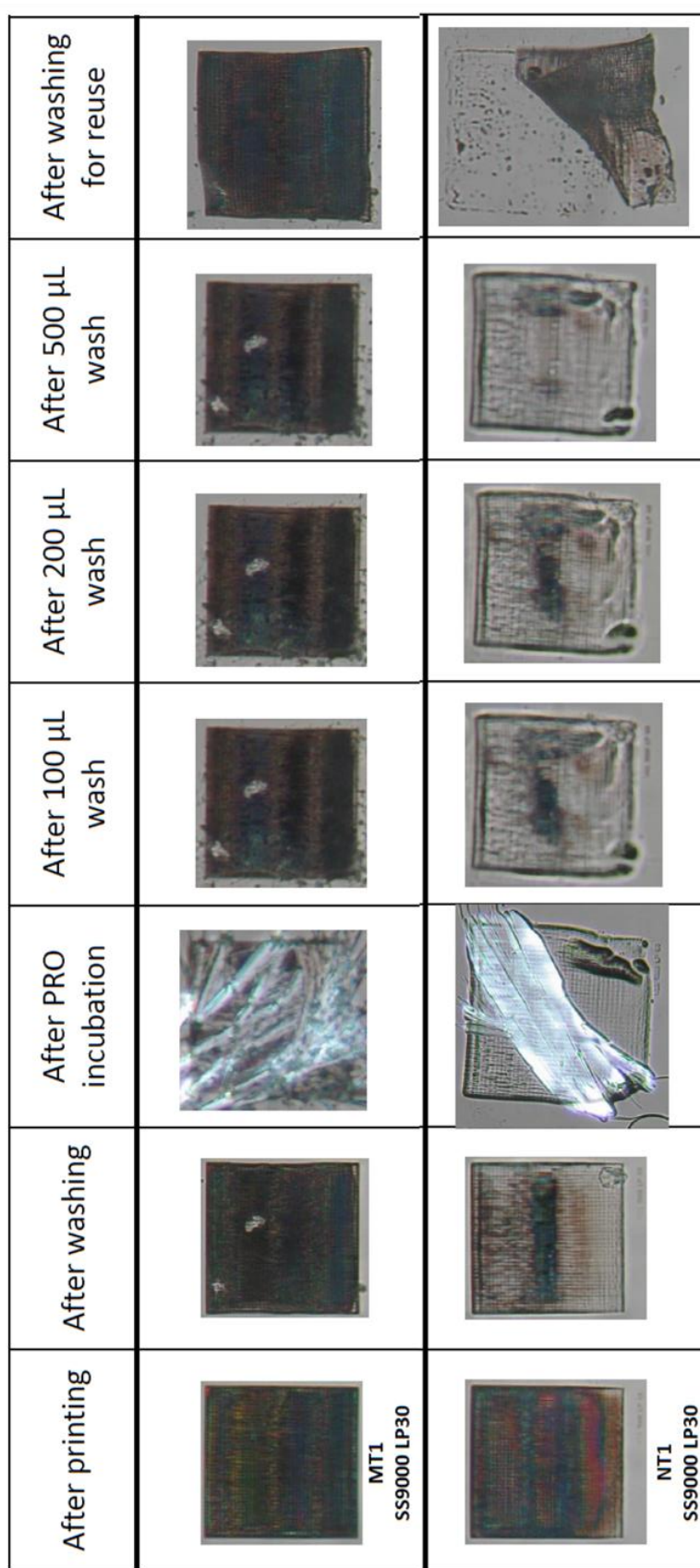


Figure 3.23. TP-POL microscopy images of three representative IP-Dip MIP-NIP pairs as they underwent changes through the various steps of processing and incubation experiments.



### 3.2.1.2. Woodpiles based on thiol-containing formulations

Fabrication of woodpiles was also attempted on home-made thiol-containing formulations. The first set of these formulation involved thiol-yne formulations while the second set was composed of the thiol-acrylate formulations. Due to their oxygen-tolerant chemistries, it was envisioned that they would be useful in bringing about well-defined polymer structures in open-air setups such as TPS. Following a step-growth mechanism, they also experience delayed gelation during polymerization and therefore, less shrinkage of the polymers.<sup>97</sup> The thiol-yne chemistry also offers polymers with higher crosslinking and thus, higher modulus compared to the corresponding and better known thiol-ene reaction because of the higher functionality of the alkyne group.<sup>91,92</sup> High modulus becomes important especially when thin, durable rods for woodpiles are pursued to avoid the damage observed in the previous subsection. Moreover, the thiol-yne chemistry was demonstrated to effectively recognize the template propranolol in Chapter 2. On the other hand, thiol-acrylate were reported to with dimensions as low as 180 nm via TPS,<sup>84</sup> which is interesting for the fabrication of color-generating woodpiles.

Pre-polymerization mixtures were prepared using the thiol-yne formulation for propranolol already described in Chapter 2.

Viscosity is an important parameter for the printing setup we adopted: indeed, the DiLL configuration that is compatible for high-resolution printing requires that the resin be viscous enough to stick to the substrate without dropping onto the objective. The thiol-yne formulation used to synthesize micro-particles included a high amount of solvent acetonitrile. Thus, in order to raise the viscosity, acetonitrile was removed, leaving only AA, DBC and the viscous PETMP or diPETMP. When applied on the fused silica substrate and positioned upside-down in the DiLL configuration, it remained stuck to the substrate throughout the experiment (and remained stuck even overnight on a glass substrate).

***Fabrication via TPS of woodpile structures based on thiol-yne formulations.*** Prior to the fabrication of woodpiles using the thiol-yne formulations, microstructures with features in the microscale range were constructed under varying laser powers, photoinitiator (TPO-L) concentration and identity of the polythiol (i.e. PETMP or diPETMP). This was done since the thiol-yne formulations would be used for the first time with the Nanoscribe printer so it was important to investigate their behavior under various parameters. A snowflake microstructure was chosen due to its complex geometry with the

following dimensions:  $80 \times 105.24 \times 6.264 \mu\text{m}^3$  (Appendix B, Figure B3). The SEM images of the fabricated snowflake microstructures revealed some important trends: At constant scan speed, (1) there is a minimum laser power at which the structures printed becomes defined and tough, (2) too excessive laser power leads to bubble formation and “excessive printing” (i.e. dimensions become larger than they are supposed to), (3) higher photoinitiator concentrations lead to defined structures even at lower laser power, and (4) lower photoinitiator concentrations allow for fabrication of defined structures at very high laser power while avoiding bubble formation to a certain degree, (5) PETMP-based formulations required higher laser power for the fabrication of defined structures, and (6) using diPETMP formulations, structures were more defined and tougher even at lower TPO-L concentrations and lower laser power (Appendix B, Figures B4 and B5).

After the study on the effects of the laser power and the TPO-L concentration on the structures obtained via TPS, the thiol-yne formulations were used for the fabrication of woodpile structures. The TPO-L concentration, the scan speed and the laser power were systematically varied. Various TPO-L concentrations such that the number of moles of TPO-L was 1%, 3%, 5% and 10% of the number of moles of thiol groups ( $n_{\text{SH}}$ ) in the photoresist. However, only at 10%  $n_{\text{SH}}$  the formulation did afford written woodpiles. Therefore, this was the TPO-L concentration used for the rest of the experiment. The scan speed was varied from 2000 to 10000  $\mu\text{m/s}$  at an interval of 2000  $\mu\text{m/s}$ . On the other hand, the laser power was changed from 10 to 50 mW at an interval of 10 mW. As seen in Figure 3.24, no parameter set produced a color-generating woodpile. Such result may once again be attributed to the reactivity and oxygen-tolerance of the thiol-yne chemistry. It could be that a minimum number of generated initiating radical was enough to maintain the propagation of the polymerization reaction in the local vicinity of the focal laser point for some time. As a consequence, the distance between the rods of the woodpiles was occupied by polymer material from this undesired propagation, eliminating the necessary RI contrast for a color-generating woodpile.

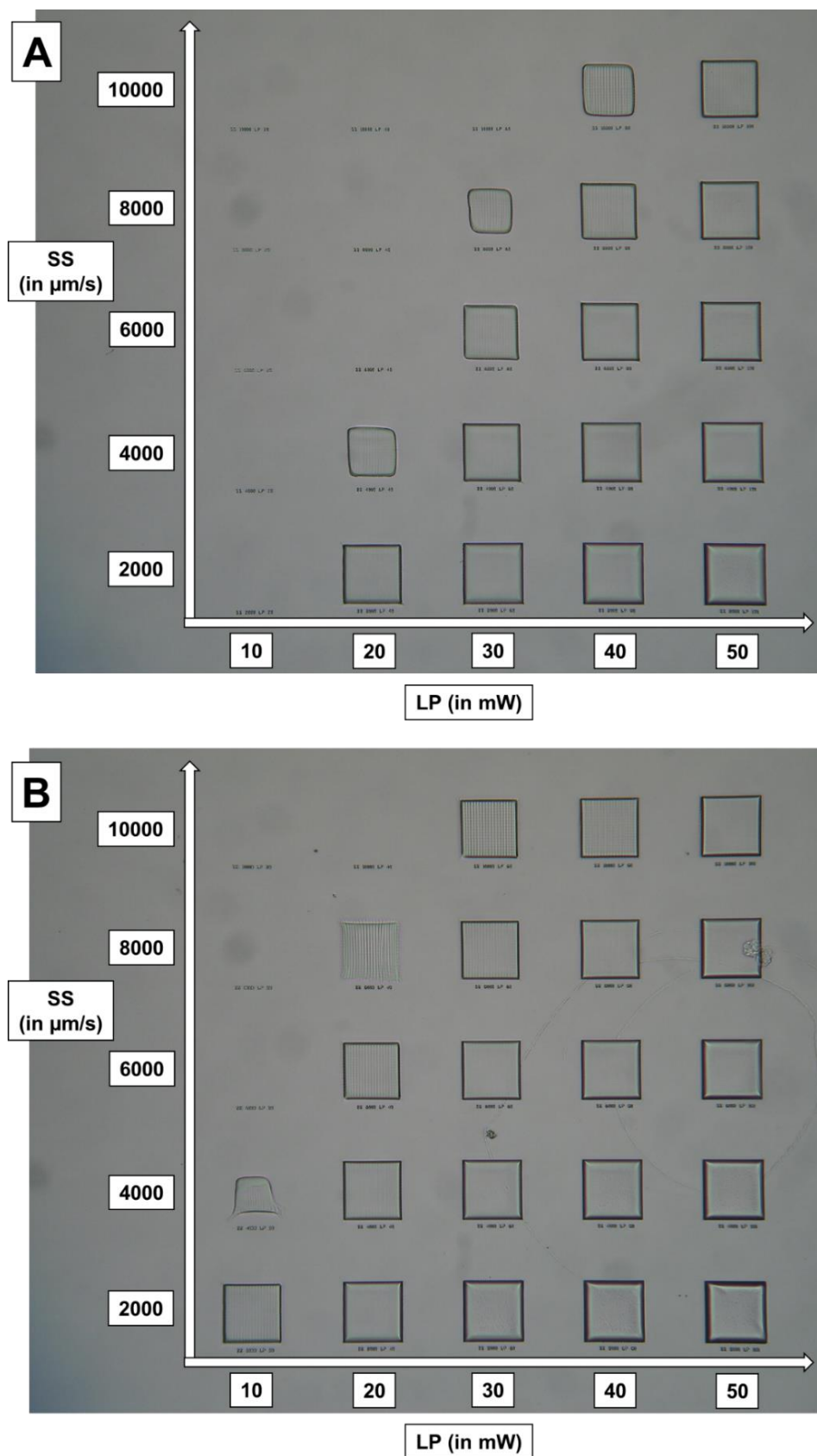


Figure 3.24. Optical microscopy images (TP-POL) of woodpile structures based on the (A) PETMP/DBC, and the (B) diPETMP/DBC thiol-yne formulations fabricated via TPS under various laser power and scan speed values.

***Fabrication via TPS of woodpile structures based on thiol-acrylate formulations.*** Since the thiol-yne formulations did not yield color-generating woodpiles, we decided to use a hybrid thiol-acrylate formulations, similarly to what Jiang et al. reported.<sup>84</sup> In their paper, these formulations attained linewidths as thin as 180 nm. In addition, their polymers were mechanically stable due to the high crosslinking brought about by the use of the polythiol PETMP and the polyacrylate di(trimethylolpropane) tetraacrylate. Following a step-growth mechanism, they experienced delayed gelation during polymerization and therefore, less shrinking of the polymers.

The use of acrylates and thiols as components of a photoresist means that polymerization can be initiated even at higher scan speeds and lower laser power values than required for the corresponding acrylate-based-only photoresist due to the oxygen-tolerant nature of thiol-acrylate chemistry. We therefore tested this in our experiments. We used PETMP as the polythiol, pentaerythritol tetraacrylate as the acrylate, and TPO-L as the photoinitiator. We also tested the effect of raising the percent weight of PETMP: AcryS1 (13%), AcryS2 (25%), AcryS3 (36%) and AcryS4 (47%). Similarly to Jiang and coworkers, we wrote suspended lines spaced from one another by 5  $\mu\text{m}$  between two blocks using various laser power values between 1 to 10 mW. The lines between each pair of blocks represented the same scan speed (5 to 40  $\mu\text{m}/\text{s}$ ). When printed, the AcryS1 matrix was too cloudy and it was impossible to locate its interface with the silanized substrate to start printing so it was cancelled. On the other hand, the writing of suspended lines and blocks was enough to polymerize the entire drop of AcryS4 on the substrate, making it impossible and useless to evaluate the lines. AcryS3 yielded lines with widths over 1000 nm which do not concern our purpose. AcryS2 gave results consistent with the general tendencies of laser dose-lateral feature size relationship as shown in (Appendix B, Figures B6 and B7). The smallest minimum lateral feature size achieved was 578.8 nm either by SS = 40, LP = 4 mW or SS = 30, LP = 4 mW. This is much higher than the one in Jiang's paper which was 272 nm for 20 w/w % PETMP formulation. The difference could be explained by the different photoinitiator and the different tetraacrylate used.

The fabrication of woodpiles under different scan speeds and laser powers was also performed using the AcryS2 formulation (25 w/w % PETMP). The first set of woodpiles were constructed using very high scan speeds (i.e. 50000, 40000, 30000, 20000 and 10000  $\mu\text{m}/\text{s}$ ) in an attempt to minimize the quantity of initiating radicals to obtain thin rods. The laser power values used were as follows: 15, 30, 45, 60 and 75 mW. The second set of woodpiles were generated using the "usual" scan speeds (i.e. 5000, 6000, 7000, 8000, 9000  $\mu\text{m}/\text{s}$ ) and select lower ones based on the suspended lines experiment in Section III B (i.e. 30 and 40  $\mu\text{m}/\text{s}$ ). The laser power values used were as follows: 3, 4, 5, 15, 25, 35 and 45 mW. As seen in Figure 3.25, none of the parameters resulted in colored woodpiles. This may

once again be attributed to the oxygen-tolerant nature of the thiol-acrylate polymerization reaction which even at low laser doses, managed to proceed vigorously from a low quantity of initiating radicals.

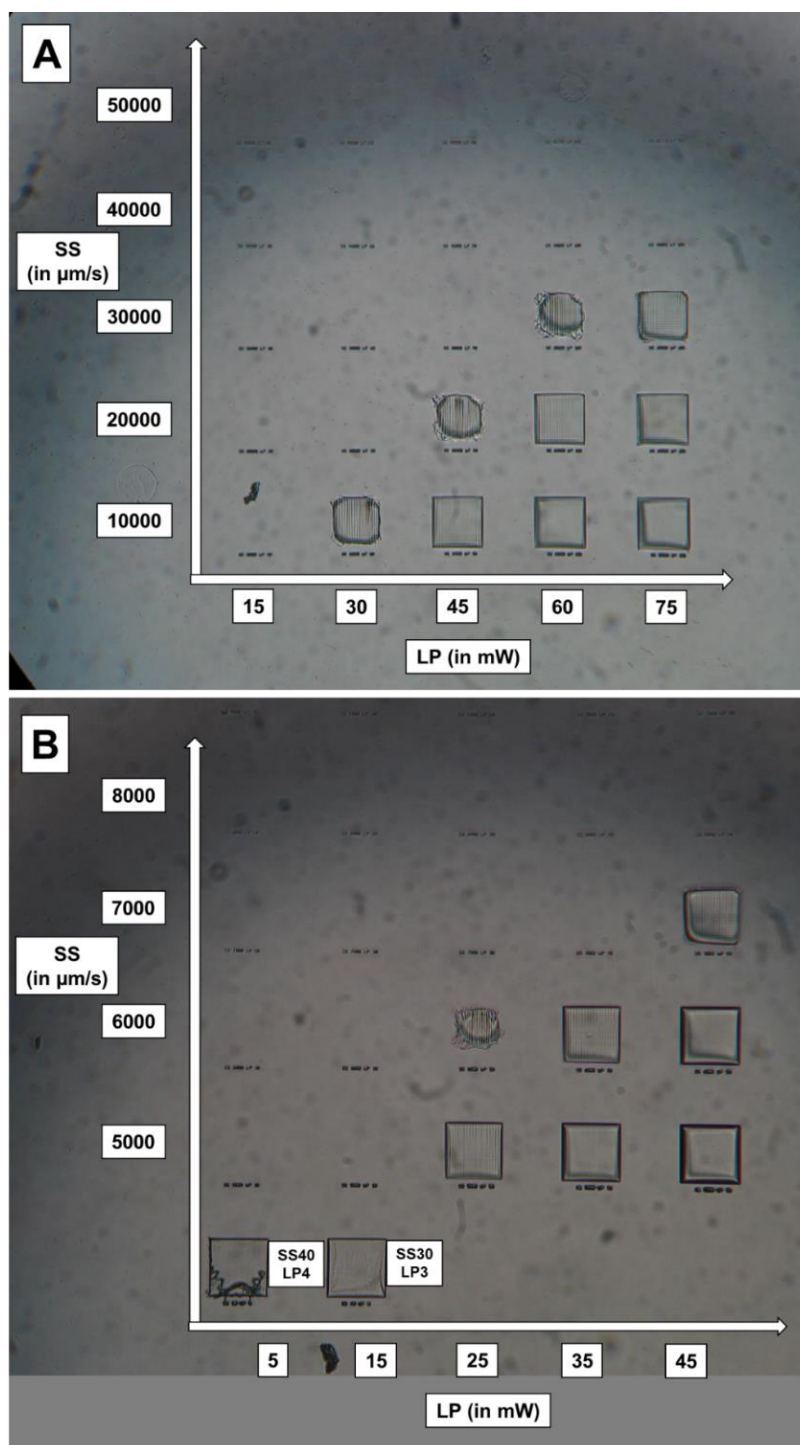


Figure 3.25. Optical microscopy images (TP-POL) of the AcryS2-based woodpiles generated at various laser power values and at (A) “higher” scan speeds and (B) “usual” and very low scan speeds.

#### 4. Conclusions

Several attempts were performed to fabricate MIP PhCs whose Bragg wavelength would be in the visible light spectrum for colorimetric detection of analytes. Three-dimensional PhCs in the form of opal crystals were first constructed using the commercial photoresist IP-Dip; however, the resolution of the Nanoscribe printer was not sufficiently high to allow well-defined spheres to be written adjacent to one another at diameters equal to or below 500 nm for visible-light PhCs. In addition, the CAD-STL file translation automatically brought additional voxels to the structure, which further diminished the clarity of the spherical boundaries of the structure. Another 3D PhC structure was therefore adapted for TPS, the woodpile lattice, whose simpler geometry makes fabrication more straightforward. The photoresist IP-Dip was “functionalized” for the template propranolol to obtain a MIP IP-Dip precursor photoresist. Colored MIP and NIP woodpiles were obtained, which displayed optical changes when incubated with the target propranolol, with MIP exhibiting a greater response. However, the fabrication was shown not to be reproducible from one batch to another since the woodpiles constructed under the same parameters did not yield the same color and intensity. The issues with the reproducibility were attributed to the batch-to-batch deviations in the quantity of the components of the MIP IP-Dip precursor photoresists, which gave rise to the fluctuations in the optical behavior of the MIP and NIP woodpiles. Furthermore, the woodpiles were not durable enough to withstand the experimental conditions in re-binding and washing of the target, as shown by the structural damage that they sustained.

Thiol-containing formulations were also utilized as photoresists for the fabrication of woodpiles using TPS due to the chemistry’s oxygen tolerance and the low shrinkage experienced by their polymers, as well as the durability of the highly crosslinked polymers. However, the thiol-yne woodpiles fabricated at various scan speeds and laser powers did not generate colors, lacking the striations of a woodpile when observed under a microscope. The thiol-yne formulations were too reactive due to their oxygen-resistance to allow the formation of a periodic polymer-air interface, resulting to non-color-generating woodpiles. Hence, a set of thiol-acrylate formulations, which was previously shown in literature to attain sub-200 nm linewidths, were adapted with changes in the identity of the polyacrylate and the photoinitiator. Only one of the formulations yielded sub-micron rods spaced from one another significantly. Nevertheless, when TPS was performed on this formulation, the resulting woodpiles did not generate colors and most of them appeared like solid blocks too. Again, this was attributed to the high reactivity of the thiol-acrylate chemistry owing to its oxygen-tolerance. As such, “excessive printing” closed the gaps between the rods, as with the thiol-yne woodpiles.

The results of the experiments done so far presented several issues regarding the fabrication of PhCs via TPS, more importantly, the fabrication of structures with feature dimensions around 200 to 350 nm. A main problem is the inconsistency of optical properties and the mechanical instability of the fabricated woodpiles when the commercial photoresist IP-Dip was modified for molecular imprinting. Another challenge was the resolution of the Nanoscribe printer, particularly its vertically resolution, which did not allow defined structures below around 700 nm. The thiol-containing formulations also proved too reactive to produce sufficiently thin structural features.

In view of these challenges, a new strategy was to be adapted. Instead of modifying the commercial photoresist, it would be used unaltered for TPS in order to achieve consistent optical properties and mechanical stability. A post-TPS step would be performed, in the form photoiniferter coupling, in order to grant molecular recognition capabilities to the resulting polymer structure. Also, a 2D structure would be fabricated, in place of a 3D one, to eliminate the issue on the limits of the vertical resolution. The new structure would not be a photonic crystal per se, but would resemble a 2D inverse opal lattice. This is expected to lead to the construction of sub-500 nm polymeric structures with geometrical intricacies for the molecular recognition of analytes, as will be discussed in the next chapter.

## 5. REFERENCES

- (1) Chua, C. K.; Leong, K. F.; An, J. Introduction to Rapid Prototyping of Biomaterials. In *Rapid Prototyping of Biomaterials: Principles and Applications*; Narayan, R., Ed.; Woodhead Publishing Limited: Cambridge, 2014; pp 1–15. <https://doi.org/10.1533/9780857097217.1>.
- (2) Stampfl, J.; Liu, H. C.; Nam, S. W.; Sakamoto, K.; Tsuru, H.; Kang, S.; Cooper, A. G.; Nickel, A.; Prinz, F. B. Rapid Prototyping and Manufacturing by Gelcasting of Metallic and Ceramic Slurries. *Mater. Sci. Eng. A* **2002**, *334* (1–2), 187–192. [https://doi.org/10.1016/S0921-5093\(01\)01800-7](https://doi.org/10.1016/S0921-5093(01)01800-7).
- (3) Rieger, T.; Schubert, T.; Schurr, J.; Butschle, M.; Schwenkel, M.; Bernthaler, T.; Schneider, G. Slurry Development for Lithography-Based Additive Manufacturing of Cemented Carbide Components. *Powder Technol.* **2021**, *383*, 498–508. <https://doi.org/10.1016/j.powtec.2021.01.049>.
- (4) Najmon, J. C.; Raeisi, S.; Tovar, A. Review of Additive Manufacturing Technologies and Applications in the Aerospace Industry. In *Additive Manufacturing for the Aerospace Industry*; Froes, F., Boyer, R., Eds.; Elsevier Inc.: Amsterdam, 2019; pp 7–31. <https://doi.org/10.1016/B978-0-12-814062-8.00002-9>.
- (5) Duc-Toan, N.; Seung-Han, Y.; Dong-Won, J.; Tae-Hoon, C.; Young-Suk, K. Incremental Sheet Metal Forming: Numerical Simulation and Rapid Prototyping Process to Make an Automobile White-Body. *Steel Res. Int.* **2011**, *82* (7), 795–805. <https://doi.org/10.1002/srin.201000284>.
- (6) Song, Y.; Yan, Y.; Zhang, R.; Xu, D.; Wang, F. Manufacture of the Die of an Automobile Deck Part Based on Rapid Prototyping and Rapid Tooling Technology. *J. Mater. Process. Technol.* **2002**, *120* (1–3), 237–242. [https://doi.org/10.1016/S0924-0136\(01\)01165-7](https://doi.org/10.1016/S0924-0136(01)01165-7).
- (7) Kryou, C.; Leva, V.; Chatzipetrou, M.; Zergioti, I. Bioprinting for Liver Transplantation. *Bioengineering* **2019**, *6* (4), 95. <https://doi.org/10.3390/bioengineering6040095>.
- (8) Bedir, T.; Ulag, S.; Ustundag, C. B.; Gunduz, O. 3D Bioprinting Applications in Neural Tissue Engineering for Spinal Cord Injury Repair. *Mater. Sci. Eng. C* **2020**, *110*, 110741. <https://doi.org/10.1016/j.msec.2020.110741>.
- (9) Ortona, A.; D’Angelo, C.; Gianella, S.; Gaia, D. Cellular Ceramics Produced by Rapid Prototyping and Replication. *Mater. Lett.* **2012**, *80*, 95–98. <https://doi.org/10.1016/j.matlet.2012.04.050>.
- (10) Louh, R. F.; Ku, Y.; Tsai, I. Rapid Prototyping Technique for Ceramic Mini-Devices Containing Internal Channels with Asymmetrical Contour. *J. Eur. Ceram. Soc.* **2010**, *30* (14), 2841–2847.



- <https://doi.org/10.1016/j.jeurceramsoc.2010.02.018>.
- (11) Gissibl, T.; Thiele, S.; Herkommer, A.; Giessen, H. Sub-Micrometre Accurate Free-Form Optics by Three-Dimensional Printing on Single-Mode Fibres. *Nat. Commun.* **2016**, *7*, 11763. <https://doi.org/10.1038/ncomms11763>.
- (12) Headland, D.; Withayachumnankul, W.; Webb, M.; Ebendorff-Heidepriem, H.; Luiten, A.; Abbott, D. Analysis of 3D-Printed Metal for Rapid-Prototyped Reflective Terahertz Optics. *Opt. Express* **2016**, *24* (15), 17384–17396. <https://doi.org/10.1364/oe.24.017384>.
- (13) Tofail, S. A. M.; Koumoulos, E. P.; Bandyopadhyay, A.; Bose, S.; O'Donoghue, L.; Charitidis, C. Additive Manufacturing: Scientific and Technological Challenges, Market Uptake and Opportunities. *Mater. Today* **2018**, *21* (1), 22–37. <https://doi.org/10.1016/j.mattod.2017.07.001>.
- (14) Anant Pidge, P.; Kumar, H. Additive Manufacturing: A Review on 3 D Printing of Metals and Study of Residual Stress, Buckling Load Capacity of Strut Members. *Mater. Today Proc.* **2020**, *21*, 1689–1694. <https://doi.org/10.1016/j.matpr.2019.12.012>.
- (15) Bandyopadhyay, A.; Gualtieri, T.; Bose, S. Global Engineering and Additive Manufacturing. In *Additive Manufacturing*; CRC, 2015; pp 1–18. <https://doi.org/10.1201/b18893-2>.
- (16) Robles Martinez, P.; Basit, A. W.; Gaisford, S. The History, Developments and Opportunities of Stereolithography. In *AAPS Advances in the Pharmaceutical Sciences Series*; Basit, A. W., Gaisford, S., Eds.; Springer: Cham, 2018; Vol. 31, pp 55–79. [https://doi.org/10.1007/978-3-319-90755-0\\_4](https://doi.org/10.1007/978-3-319-90755-0_4).
- (17) Touri, M.; Kabirian, F.; Saadati, M.; Ramakrishna, S.; Mozafari, M. Additive Manufacturing of Biomaterials – The Evolution of Rapid Prototyping. *Adv. Eng. Mater.* **2019**, *21* (2), 1800511. <https://doi.org/10.1002/adem.201800511>.
- (18) Chandra, U.; Porwal, R. K. A Comprehensive Study of the Dynamics of Density in 3d Printed Ceramic Structures. *Mater. Today Proc.* **2020**, *44*, 336–340. <https://doi.org/10.1016/j.matpr.2020.09.740>.
- (19) Shirazi, S. F. S.; Gharekhani, S.; Mehrali, M.; Yarmand, H.; Metselaar, H. S. C.; Adib Kadri, N.; Osman, N. A. A. A Review on Powder-Based Additive Manufacturing for Tissue Engineering: Selective Laser Sintering and Inkjet 3D Printing. *Sci. Technol. Adv. Mater.* **2015**, *16* (3), 033502. <https://doi.org/10.1088/1468-6996/16/3/033502>.
- (20) Gupta, S.; Bit, A. Rapid Prototyping for Polymeric Gels. In *Polymeric Gels*; Pal, K., Ed.; Woodhead Publishing: Rourkela, 2018; pp 397–439. <https://doi.org/10.1016/b978-0-08->

- 102179-8.00016-8.
- (21) Rypl, D.; Bittnar, Z. Generation of Computational Surface Meshes of STL Models. *J. Comput. Appl. Math.* **2006**, *192* (1), 148–151. <https://doi.org/10.1016/j.cam.2005.04.054>.
- (22) Melchels, F. P. W.; Feijen, J.; Grijpma, D. W. A Review on Stereolithography and Its Applications in Biomedical Engineering. *Biomaterials* **2010**, *31* (24), 6121–6130. <https://doi.org/10.1016/j.biomaterials.2010.04.050>.
- (23) Mike. Histoire de l'impression 3D et son évolution au cours du temps <https://www.geekonline.fr/2016/01/28/histoire-limpression-3d/> (accessed Jun 30, 2021).
- (24) Kerns, J. 3D printing: The machine that started it all [https://www.machinedesign.com/3d-printing-cad/article/21835865/3d-printing-the-machine-that-started-it-all?utm\\_campaign=WeeklyNewsletters&utm\\_source=hs\\_email&utm\\_medium=email&\\_hsenc=p2ANqtz-8Uo8I4RBNHqeVusHML\\_\\_tTABTc2ZzIINBbsjQsMb37FyAdiTbcRExY1D0znDaz1v](https://www.machinedesign.com/3d-printing-cad/article/21835865/3d-printing-the-machine-that-started-it-all?utm_campaign=WeeklyNewsletters&utm_source=hs_email&utm_medium=email&_hsenc=p2ANqtz-8Uo8I4RBNHqeVusHML__tTABTc2ZzIINBbsjQsMb37FyAdiTbcRExY1D0znDaz1v) (accessed Jun 30, 2021).
- (25) Elomaa, L.; Teixeira, S.; Hakala, R.; Korhonen, H.; Grijpma, D. W.; Seppälä, J. V. Preparation of Poly( $\epsilon$ -Caprolactone)-Based Tissue Engineering Scaffolds by Stereolithography. *Acta Biomater.* **2011**, *7* (11), 3850–3856. <https://doi.org/10.1016/j.actbio.2011.06.039>.
- (26) Kanai, T.; Tsuchiya, M. Microfluidic Devices Fabricated Using Stereolithography for Preparation of Monodisperse Double Emulsions. *Chem. Eng. J.* **2016**, *290*, 400–404. <https://doi.org/10.1016/j.cej.2016.01.064>.
- (27) Fuad, N. M.; Zhu, F.; Kaslin, J.; Wlodkowic, D. Applications of Stereolithography for Rapid Prototyping of Biologically Compatible Chip-Based Physiometers. *Proc. SPIE BioPhotonics Australas.* **2016**, *10013*, 1001326. <https://doi.org/10.1117/12.2242824>.
- (28) Schwentenwein, M.; Homa, J. Additive Manufacturing of Dense Alumina Ceramics. *Int. J. Appl. Ceram. Technol.* **2015**, *12* (1), 1–7. <https://doi.org/10.1111/ijac.12319>.
- (29) Zanchetta, E.; Cattaldo, M.; Franchin, G.; Schwentenwein, M.; Homa, J.; Brusatin, G.; Colombo, P. Stereolithography of SiOC Ceramic Microcomponents. *Adv. Mater.* **2016**, *28* (2), 370–376. <https://doi.org/10.1002/adma.201503470>.
- (30) Halloran, J. W. Ceramic Stereolithography: Additive Manufacturing for Ceramics by Photopolymerization. *Annu. Rev. Mater. Res.* **2016**, *46*, 19–40. <https://doi.org/10.1146/annurev-matsci-070115-031841>.
- (31) Vaidya, N.; Solgaard, O. 3D Printed Optics with Nanometer Scale Surface Roughness.

- Microsystems Nanoeng.* **2018**, *4*, 18. <https://doi.org/10.1038/s41378-018-0015-4>.
- (32) Spangenberg, A.; Hobeika, N.; Stehlin, F.; Malval, J.; Wieder, F.; Prabhakaran, P.; Baldeck, P.; Soppera, O. Recent Advances in Two-Photon Stereolithography. In *Updates in advanced lithography*; Hosaka, S., Ed.; IntechOpen, 2013; pp 35–63. <https://doi.org/10.5772/56165>.
- (33) Gomez, L. P. C.; Spangenberg, A.; Ton, X. A.; Fuchs, Y.; Bokeloh, F.; Malval, J. P.; Tse Sum Bui, B.; Thuau, D.; Ayela, C.; Haupt, K.; Soppera, O. Rapid Prototyping of Chemical Microsensors Based on Molecularly Imprinted Polymers Synthesized by Two-Photon Stereolithography. *Adv. Mater.* **2016**, *28*, 5931–5937. <https://doi.org/10.1002/adma.201600218>.
- (34) Wang, I.; Bouriau, M.; Baldeck, P. L.; Martineau, C.; Andraud, C. Three-Dimensional Microfabrication by Two-Photon-Initiated Polymerization with a Low-Cost Microlaser. *Opt. Lett.* **2002**, *27* (15), 1348–1350. <https://doi.org/10.1364/ol.27.001348>.
- (35) Crowe, J. A.; El-Tamer, A.; Nagel, D.; Koroleva, A. V.; Madrid-Wolff, J.; Olarte, O. E.; Sokolovsky, S.; Estevez-Priego, E.; Ludl, A.-A.; Soriano, J.; Loza-Alvarez, P.; Chichkov, B. N.; Hill, E. J.; Parri, H. R.; Rafailov, E. U. Development of Two-Photon Polymerised Scaffolds for Optical Interrogation and Neurite Guidance of Human iPSC-Derived Cortical Neuronal Networks. *Lab Chip* **2020**, *20*, 1792–1806. <https://doi.org/10.1039/c9lc01209e>.
- (36) Trautmann, A.; R uth, M.; Lemke, H. D.; Walther, T.; Hellmann, R. Two-Photon Polymerization Based Large Scaffolds for Adhesion and Proliferation Studies of Human Primary Fibroblasts. *Opt. Laser Technol.* **2018**, *106*, 474–480. <https://doi.org/10.1016/j.optlastec.2018.05.008>.
- (37) Lee, M. R.; Phang, I. Y.; Cui, Y.; Lee, Y. H.; Ling, X. Y. Shape-Shifting 3D Protein Microstructures with Programmable Directionality via Quantitative Nanoscale Stiffness Modulation. *Small* **2015**, *11* (6), 740–748. <https://doi.org/10.1002/smll.201401343>.
- (38) Parkatzidis, K.; Chatzinikolaidou, M.; Koufakis, E.; Kaliva, M.; Farsari, M.; Vamvakaki, M. Multi-Photon Polymerization of Bio-Inspired, Thymol-Functionalized Hybrid Materials with Biocompatible and Antimicrobial Activity. *Polym. Chem.* **2020**, *11*, 4078–4083. <https://doi.org/10.1039/d0py00281j>.
- (39) Saha, S. K.; Oakdale, J. S.; Cuadra, J. A.; Divin, C.; Ye, J.; Forien, J. B.; Bayu Aji, L. B.; Biener, J.; Smith, W. L. Radiopaque Resists for Two-Photon Lithography to Enable Submicron 3D Imaging of Polymer Parts via X-Ray Computed Tomography. *ACS Appl. Mater. Interfaces* **2018**, *10* (1), 1164–1172. <https://doi.org/10.1021/acsami.7b12654>.
- (40) Zheng, C.; Jin, F.; Zhao, Y.; Zheng, M.; Liu, J.; Dong, X.; Xiong, Z.; Xia, Y.; Duan, X. Light-Driven Micron-Scale 3D Hydrogel Actuator Produced by Two-Photon Polymerization

- Microfabrication. *Sens. Actuators B Chem.* **2020**, *304*, 127345.  
<https://doi.org/10.1016/j.snb.2019.127345>.
- (41) Huang, T. Y.; Sakar, M. S.; Mao, A.; Petruska, A. J.; Qiu, F.; Chen, X. B.; Kennedy, S.; Mooney, D.; Nelson, B. J. 3D Printed Microtransporters: Compound Micromachines for Spatiotemporally Controlled Delivery of Therapeutic Agents. *Adv. Mater.* **2015**, *27* (42), 6644–6650. <https://doi.org/10.1002/adma.201503095>.
- (42) Maruo, S.; Ikuta, K.; Korogi, H. Submicron Manipulation Tools Driven by Light in a Liquid. *Appl. Phys. Lett.* **2003**, *82* (1), 133–135. <https://doi.org/10.1063/1.1533853>.
- (43) Thiele, S.; Pruss, C.; Herkommer, A. M.; Giessen, H. 3D Printed Stacked Diffractive Microlenses. *Opt. Express* **2019**, *27* (24), 35621. <https://doi.org/10.1364/oe.27.035621>.
- (44) Wang, H.; Liu, Y.; Ruan, Q.; Liu, H.; Ng, R. J. H.; Tan, Y. S.; Wang, H.; Li, Y.; Qiu, C. W.; Yang, J. K. W. Off-Axis Holography with Uniform Illumination via 3D Printed Diffractive Optical Elements. *Adv. Opt. Mater.* **2019**, *7* (12), 1–9. <https://doi.org/10.1002/adom.201900068>.
- (45) Parimi, P. V.; Lu, W. T.; Vodo, P.; Sridhar, S. Imaging by Flat Lens Using Negative Refraction. *Nature* **2003**, *426*, 404. <https://doi.org/10.1038/426404a>.
- (46) Kim, J.-Y.; Kim, M.-K.; Seo, M.-K.; Kwon, S.-H.; Shin, J.-H.; Lee, Y.-H. Two-Dimensionally Relocatable Microfiber-Coupled Photonic Crystal Resonator. *Opt. Express* **2009**, *17* (15), 13009–13016. <https://doi.org/10.1364/oe.17.013009>.
- (47) Reimer, C.; Nedeljkovic, M.; Stothard, D.; Esnault, M.; Reardon, C.; O’Faolain, L.; Dunn, M.; Mashanovich, G.; Krauss, T. Mid-Infrared Photonic Crystal Waveguides in Silicon. *Opt. Express* **2012**, *20* (28), 29361–29368. <https://doi.org/10.3791/50216>.
- (48) Kim, S.-U.; Lee, S.-H.; Lee, I.-H.; Lee, B.-Y.; Na, J.-H.; Lee, S.-D. Generation of Intensity-Tunable Structural Color from Helical Photonic Crystals for Full Color Reflective-Type Display. *Opt. Express* **2018**, *26* (10), 13561–13572. <https://doi.org/10.1364/oe.26.013561>.
- (49) Liu, W.; Liu, X.; Yang, B. Photonic Materials for Sensing, Biosensing and Display Devices. In *Photonic materials for sensing, biosensing and display devices*; Serpe, M. J., Kang, Y., Zhang, Q. M., Eds.; Springer, 2016; pp 101–158.
- (50) Deubel, M.; Von Freymann, G.; Wegener, M.; Pereira, S.; Busch, K.; Soukoulis, C. M. Direct Laser Writing of Three-Dimensional Photonic-Crystal Templates for Telecommunications. *Nat. Mater.* **2004**, *3*, 444–447. <https://doi.org/10.1038/nmat1155>.
- (51) Zhang, J. T.; Cai, Z.; Kwak, D. H.; Liu, X.; Asher, S. A. Two-Dimensional Photonic Crystal Sensors for Visual Detection of Lectin Concanavalin A. *Anal. Chem.* **2014**, *86* (18), 9036–9041.

- <https://doi.org/10.1021/ac5015854>.
- (52) Wu, Z.; Tao, C. A.; Lin, C.; Shen, D.; Li, G. Label-Free Colorimetric Detection of Trace Atrazine in Aqueous Solution by Using Molecularly Imprinted Photonic Polymers. *Chem. Eur. J.* **2008**, *14* (36), 11358–11368. <https://doi.org/10.1002/chem.200801250>.
- (53) Lu, W.; Asher, S. A.; Meng, Z.; Yan, Z.; Xue, M.; Qiu, L.; Yi, D. Visual Detection of 2,4,6-Trinitrotoluene by Molecularly Imprinted Colloidal Array Photonic Crystal. *J. Hazard. Mater.* **2016**, *316*, 87–93. <https://doi.org/10.1016/j.jhazmat.2016.05.022>.
- (54) Yablonovitch, E. Photonic Crystals. *J. Mod. Opt.* **1994**, *41* (2), 173–194. <https://doi.org/10.1080/09500349414550261>.
- (55) Lee, T. K.; Bristow, A. D.; Hübner, J.; van Driel, H. M. Linear and Nonlinear Optical Properties of Au-Polymer Metallodielectric Bragg Stacks. *J. Opt. Soc. Am. B* **2006**, *23* (10), 2142–2147. <https://doi.org/10.1364/josab.23.002142>.
- (56) Xu, T.; Zhu, N.; Xu, M. Y. C.; Wosinski, L.; Aitchison, J. S.; Ruda, H. E. A Pillar-Array Based Two-Dimensional Photonic Crystal Microcavity. *Appl. Phys. Lett.* **2009**, *94*, 241110. <https://doi.org/10.1063/1.3152245>.
- (57) Waterhouse, G. I. N.; Waterland, M. R. Opal and Inverse Opal Photonic Crystals: Fabrication and Characterization. *Polyhedron* **2007**, *26* (2), 356–368. <https://doi.org/10.1016/j.poly.2006.06.024>.
- (58) Liu, Y.; Wang, H.; Ho, J.; Ng, R. C.; Ng, R. J. H.; Hall-Chen, V. H.; Koay, E. H. H.; Dong, Z.; Liu, H.; Qiu, C.-W.; Greer, J. R.; Yang, J. K. W. Structural Color Three-Dimensional Printing by Shrinking Photonic Crystals. *Nat. Commun.* **2019**, *10*, 4340. <https://doi.org/10.1038/s41467-019-12360-w>.
- (59) Ovsianikov, A.; Chichkov, B. Two-Photon Polymerization - High Resolution 3D Laser Technology and Its Applications. In *Nanoelectronics and Photonics: From Atoms to Materials, Devices and Architectures*; Korkin, A., Rosei, F., Eds.; Springer Science+Business Media, LLC: New York, 2008; pp 430–433.
- (60) Fenzl, C.; Hirsch, T.; Wolfbeis, O. S. Photonic Crystals for Chemical Sensing and Biosensing. *Angew. Chem. Int. Ed.* **2014**, *53* (13), 3318–3335. <https://doi.org/10.1002/anie.201307828>.
- (61) Maka, T.; Chigrin, D. N.; Romanov, S. G.; Sotomayor Torres, C. M. Three Dimensional Photonic Crystals in the Visible Regime. *Prog. Electromagn. Res.* **2003**, *41*, 307–335. <https://doi.org/10.2528/PIER02010894>.
- (62) Mayonado, G.; Mian, S. M.; Robbiano, V.; Cacialli, F. Investigation Of The Bragg-Snell Law In

- Photonic Crystals. In *2015 BFY Conference*; 2015; pp 60–63.  
<https://doi.org/10.1119/bfy.2015.pr.015>.
- (63) Arunkumar, R.; Suaganya, T.; Robinson, S. Design and Analysis of 2D Photonic Crystal Based Biosensor to Detect Different Blood Components. *Photonic Sensors* **2019**, *9* (1), 69–77.  
<https://doi.org/10.1007/s13320-018-0479-8>.
- (64) Fudouzi, H.; Xia, Y. Colloidal Crystals with Tunable Colors and Their Use as Photonic Papers. *Langmuir* **2003**, *19* (23), 9653–9660. <https://doi.org/10.1021/la034918q>.
- (65) Marlow, F.; Muldarisnur; Sharifi, P.; Brinkmann, R.; Mendive, C. Opals: Status and Prospects. *Angew. Chem. Int. Ed.* **2009**, *48* (34), 6212–6233. <https://doi.org/10.1002/anie.200900210>.
- (66) Zi, J.; Yu, X.; Li, Y.; Hu, X.; Xu, C.; Wang, X.; Liu, X.; Fu, R. Coloration Strategies in Peacock Feathers. *Proc. Natl. Acad. Sci. U. S. A.* **2003**, *100* (22), 12576–12578.  
<https://doi.org/10.1073/pnas.2133313100>.
- (67) Biró, L. P.; Kertész, K.; Vértesy, Z.; Márk, G. I.; Bálint, Z.; Lousse, V.; Vigneron, J. P. Living Photonic Crystals: Butterfly Scales - Nanostructure and Optical Properties. *Mater. Sci. Eng. C* **2007**, *27* (5-8 SPEC ISS), 941–946. <https://doi.org/10.1016/j.msec.2006.09.043>.
- (68) MatĚjková-Plsková, J.; Shiojiri, S.; Shiojiri, M. Fine Structures of Wing Scales in *Sasakia Charonda* Butterflies as Photonic Crystals. *J. Microsc.* **2009**, *236* (2), 88–93.  
<https://doi.org/10.1111/j.1365-2818.2009.03233.x>.
- (69) Wilts, B. D.; Sheng, X.; Holler, M.; Diaz, A.; Guizar-Sicairos, M.; Raabe, J.; Hoppe, R.; Liu, S. H.; Langford, R.; Onelli, O. D.; Chen, D.; Torquato, S.; Steiner, U.; Schroer, C. G.; Vignolini, S.; Sepe, A. Evolutionary-Optimized Photonic Network Structure in White Beetle Wing Scales. *Adv. Mater.* **2018**, *30* (19), 1702057. <https://doi.org/10.1002/adma.201702057>.
- (70) Bartl, M. H.; Galusha, J. W.; Richey, L. R.; Gardner, J. S.; Cha, J. N. Discovery of a Diamond-Based Photonic Crystal Structure in Beetle Scales. *Phys. Rev. E* **2008**, *77* (5), 050904.  
<https://doi.org/10.1103/PhysRevE.77.050904>.
- (71) Berger, V. Photonic Crystals and Photonic Structures. *Curr. Opin. Solid State Mater. Sci.* **1999**, *4* (2), 209–216. [https://doi.org/10.1016/S1359-0286\(99\)00004-2](https://doi.org/10.1016/S1359-0286(99)00004-2).
- (72) Nair, R. V.; Vijaya, R. Photonic Crystal Sensors: An Overview. *Prog. Quantum Electron.* **2010**, *34* (3), 89–134. <https://doi.org/10.1016/j.pquantelec.2010.01.001>.
- (73) Armstrong, E.; O'Dwyer, C. Artificial Opal Photonic Crystals and Inverse Opal Structures - Fundamentals and Applications from Optics to Energy Storage. *J. Mater. Chem. C* **2015**, *3* (24), 6109–6143. <https://doi.org/10.1039/c5tc01083g>.

- (74) Sai, N.; Ning, B.; Huang, G.; Wu, Y.; Zhou, Z.; Peng, Y.; Bai, J.; Yu, G.; Gao, Z. An Imprinted Crystalline Colloidal Array Chemical-Sensing Material for Detection of Trace Diethylstilbestrol. *Analyst* **2013**, *138* (9), 2720–2728. <https://doi.org/10.1039/c3an36829g>.
- (75) Takeoka, Y. Stimuli-Responsive Opals: Colloidal Crystals and Colloidal Amorphous Arrays for Use in Functional Structurally Colored Materials. *J. Mater. Chem. C* **2013**, *1* (38), 6059–6074. <https://doi.org/10.1039/c3tc30885e>.
- (76) Asher, S. A.; Weissman, J. M.; Tikhonov, A.; Coalson, R. D.; Kesavamoorthy, R. Diffraction in Crystalline Colloidal-Array Photonic Crystals. *Phys. Rev. E* **2004**, *69* (6), 14. <https://doi.org/10.1103/PhysRevE.69.066619>.
- (77) Gu, Z. Z.; Chen, H.; Zhang, S.; Sun, L.; Xie, Z.; Ge, Y. Rapid Synthesis of Monodisperse Polymer Spheres for Self-Assembled Photonic Crystals. *Colloids Surf. A* **2007**, *302* (1–3), 312–319. <https://doi.org/10.1016/j.colsurfa.2007.02.064>.
- (78) Dawes, J. M. Synthesis, Characterization, and Applications of Opals. In *Nano-Optics: Fundamentals, Experimental Methods, and Applications*; Thomas, S., Grohens, Y., Vignaud, G., Kalarikkal, Na., James, J., Eds.; Elsevier Inc.: Amsterdam, 2020; pp 305–325. <https://doi.org/10.1016/b978-0-12-818392-2.00012-3>.
- (79) Zheng, H.; Ravaine, S. Bottom-up Assembly and Applications of Photonic Materials. *Crystals* **2016**, *6* (5). <https://doi.org/10.3390/cryst6050054>.
- (80) Hou, J.; Zhang, H.; Yang, Q.; Li, M.; Jiang, L.; Song, Y. Hydrophilic-Hydrophobic Patterned Molecularly Imprinted Photonic Crystal Sensors for High-Sensitive Colorimetric Detection of Tetracycline. *Small* **2015**, *11* (23), 2738–2742. <https://doi.org/10.1002/smll.201403640>.
- (81) Ovsianikov, A.; Viertl, J.; Chichkov, B.; Oubaha, M.; MacCraith, B.; Sakellari, I.; Giakoumaki, A.; Gray, D.; Vamvakaki, M.; Farsari, M.; Fotakis, C. Ultra-Low Shrinkage Hybrid Photosensitive Material for Two-Photon Polymerization Microfabrication. *ACS Nano* **2008**, *2* (11), 2257–2262. <https://doi.org/10.1021/nn800451w>.
- (82) Serbin, J.; Gu, M. Experimental Evidence for Superprism Effects in Three-Dimensional Polymer Photonic Crystals. *Adv. Mater.* **2006**, *18* (2), 221–224. <https://doi.org/10.1002/adma.200501665>.
- (83) Oesterreicher, A.; Gorsche, C.; Ayalur-Karunakaran, S.; Moser, A.; Edler, M.; Pinter, G.; Schlögl, S.; Liska, R.; Griesser, T. Exploring Network Formation of Tough and Biocompatible Thiol-Yne Based Photopolymers. *Macromol. Rapid Commun.* **2016**, *37* (20), 1701–1706. <https://doi.org/10.1002/marc.201600369>.

- (84) Jiang, L.; Xiong, W.; Zhou, Y.; Liu, Y.; Huang, X.; Li, D.; Baldacchini, T.; Jiang, L.; Lu, Y. Performance Comparison of Acrylic and Thiol-Acrylic Resins in Two-Photon Polymerization. *Opt. Express* **2016**, *24* (12), 13687. <https://doi.org/10.1364/oe.24.013687>.
- (85) Nanoscribe GmbH. Resins for Printing: IP-Dip <https://support.nanoscribe.com/hc/en-gb/articles/360001748953-IP-Dip> (accessed Jul 5, 2021).
- (86) Sakellari, I.; Kabouraki, E.; Gray, D.; Purlys, V.; Fotakis, C.; Pikulin, A.; Bityurin, N.; Vamvakaki, M.; Farsari, M. Diffusion-Assisted High-Resolution Direct Femtosecond Laser Writing. *ACS Nano* **2012**, *6* (3), 2302–2311. <https://doi.org/10.1021/nn204454c> C2012.
- (87) Liu, H.; Yao, J.; Xu, D.; Wang, P. Characteristics of Photonic Band Gaps in Woodpile Three-Dimensional Terahertz Photonic Crystals. *Opt. Express* **2007**, *15* (2), 695–703. <https://doi.org/10.1364/oe.15.000695>.
- (88) Kopperschmidt, P. Tetragonal Photonic Woodpile Structures. *Appl. Phys. B* **2003**, *76*, 729–734. <https://doi.org/10.1007/s00340-003-1169-8>.
- (89) Serbin, J.; Ovsianikov, A.; Chichkov, B. Fabrication of Woodpile Structures by Two-Photon Polymerization and Investigation of Their Optical Properties. *Opt. Express* **2004**, *12* (21), 5221. <https://doi.org/10.1364/opex.12.005221>.
- (90) Fischer, J.; Wegener, M. Three-Dimensional Direct Laser Writing Inspired by Stimulated-Emission-Depletion Microscopy. *Opt. Mater. Express* **2011**, *1* (4), 614–624.
- (91) Oesterreicher, A.; Wiener, J.; Roth, M.; Moser, A.; Gmeiner, R.; Edler, M.; Pinter, G.; Griesser, T. Tough and Degradable Photopolymers Derived from Alkyne Monomers for 3D Printing of Biomedical Materials. *Polym. Chem.* **2016**, *7*, 5169. <https://doi.org/10.1039/c6py01132b>.
- (92) Bagheri, A.; Jin, J. Photopolymerization in 3D Printing. *ACS Appl. Polym. Mater.* **2019**, *1* (4), 593–611. <https://doi.org/10.1021/acsapm.8b00165>.
- (93) Seniutinas, G.; Weber, A.; Padeste, C.; Sakellari, I.; Farsari, M.; David, C. Beyond 100 nm Resolution in 3D Laser Lithography — Post Processing Solutions. *Microelectron. Eng.* **2018**, *191*, 25–31. <https://doi.org/10.1016/j.mee.2018.01.018>.
- (94) Gonzato, C.; Pasetto, P.; Bedoui, F.; Mazeran, P. E.; Haupt, K. On the Effect of Using RAFT and FRP for the Bulk Synthesis of Acrylic and Methacrylic Molecularly Imprinted Polymers. *Polym. Chem.* **2014**, *5* (4), 1313–1322. <https://doi.org/10.1039/c3py01246h>.
- (95) Tse Sum Bui, B.; Haupt, K. Preparation and Evaluation of a Molecularly Imprinted Polymer for the Selective Recognition of Testosterone—Application to Molecularly Imprinted Sorbent Assays. *J. Mol. Recognit.* **2011**, *24* (6), 1123–1129. <https://doi.org/10.1002/jmr.1162>.



- (96) Paruli, E.; Griesser, T.; Merlier, F.; Gonzato, C.; Haupt, K. Molecularly Imprinted Polymers by Thiol–Yne Chemistry: Making Imprinting Even Easier. *Polym. Chem.* **2019**, *10* (34), 4732–4739. <https://doi.org/10.1039/c9py00403c>.
- (97) Cramer, N. B.; Bowman, C. N. Chapter 1 - Thiol-Ene and Thiol-Yne Chemistry in Ideal Network Synthesis. In Lowe, A. Bowman, C., eds.) *Thiol-X Chemistries in Polymer and Materials Science*. RSC **2015**, pp. 1-27. <https://doi.org/10.1039/9781849736961-00001>.

## **Chapter 4**

# **TPS OF MICROSTRUCTURES AND THEIR FUNCTIONALIZATION WITH MIP**

## Chapter 4: TPS OF MICROSTRUCTURES AND THEIR FUNCTIONALIZATION WITH MIP

---

---

### 1. Introduction

Molecularly imprinted polymers (MIPs) are synthetic materials often dubbed “plastic antibodies” because of their remarkable affinity and selectivity for their target molecules,<sup>1</sup> making them useful in different applications.<sup>2-7</sup> MIPs can be synthesized by a redox-initiated reaction,<sup>8</sup> electropolymerization,<sup>9</sup> thermal polymerization<sup>75</sup> or photopolymerization.<sup>10</sup> Photopolymerization in particular attracts interest because it uses light as an accessible tool to enable spatial and temporal control of the polymerization reaction<sup>11,12</sup> and therefore, the structuration of MIPs.<sup>13,14</sup> Two-photon stereolithography (TPS), a technique based on photopolymerization, has emerged as a rapid prototyping (RP) technology that allows for the direct and precise fabrication of microstructures, as explained in Chapter 3. With all its capabilities, TPS appears as an attractive means for the direct micro-/nano-structuration of MIPs<sup>15</sup> while insuring, when needed, large surface area-to-volume ratios.<sup>16</sup>

If printing a MIP precursor formulated directly based on a commercial photoresist may seem straightforward, our previous experiments (see Chapter 3, Section 3.2.1.1) have shown that this is a rather tedious process requiring time-consuming optimization which necessarily varies depending on the specific monomer composition (i.e. from MIP to MIP) and photoresist. Thus, in order to overcome this problem, we propose here to use a rather different approach, consisting in writing a polymeric microstructure **as a backbone** and later growing a thin MIP layer on top of it. This strategy should indeed allow: (1) an easier and more generic synthetic approach, since “TPS-printing” and “molecular imprinting” are split, and (2) to avoid compromises between printing resolution and molecular recognition, as the thin MIP layer would only barely affect the geometrical features of the printed structure.

In this context, we decided to grow a MIP through an innovative **photoiniferter-coupling and polymerization** strategy, consisting in anchoring a photoiniferter to the backbone microstructure through the ubiquitous unreacted C=C bonds remaining on the (meth)acrylic cross-linked networks made by free radical polymerization (FRP)-based TPS (Figure 4. 1). Iniferter polymerization belongs to the family of reverse deactivation radical polymerization (RDRP) reactions along with atom transfer radical polymerization (ATRP), nitroxide mediated polymerization (NMP) and reverse addition fragmentation transfer polymerization (RAFT), which make chain extension possible by granting a

“living” character to polymer ends. Unlike other RDRP reactions, however, iniferter polymerization does not require any exogenous radical source nor a catalyst to initiate the reaction, occurs in mild conditions and is compatible with many monomers, including (meth)acrylate groups, which are the active groups of the photoresists that we used for MIPs.<sup>17,18</sup> These characteristics make it the simplest and the most straightforward choice. This strategy borrows from previous work in our group wherein the presence of unreacted C=C bonds on the surface of MIP nanoparticles (MIP NPs) by FRP served as anchoring points for a RAFT agent which thus allowed for chain-extension as for RDRPs methods.<sup>19</sup> After imprinting nanoparticles based on methacrylic acid and 1,1,1-trimethylolpropane trimethacrylate (TRIM) with the template propranolol via FRP, either the RAFT agent 4-(((2-carboxyethyl)thio)thioxomethyl)thio)-4-cyanopentanoic acid (CETPA) or 4-cyano-4-(phenylcarbonothioylthio) pentanoic acid (CPADB) was coupled to the C=C bonds on the surface of the NPs in the presence of the radical source ABDV. The coupled RAFT agent did not affect the MIP binding properties in terms of affinity and selectivity for the target, while it allowed for chain extension with hydrophilic poly(N-isopropylacrylamide) (p(NIPAm)) brushes which granted water compatible binding.

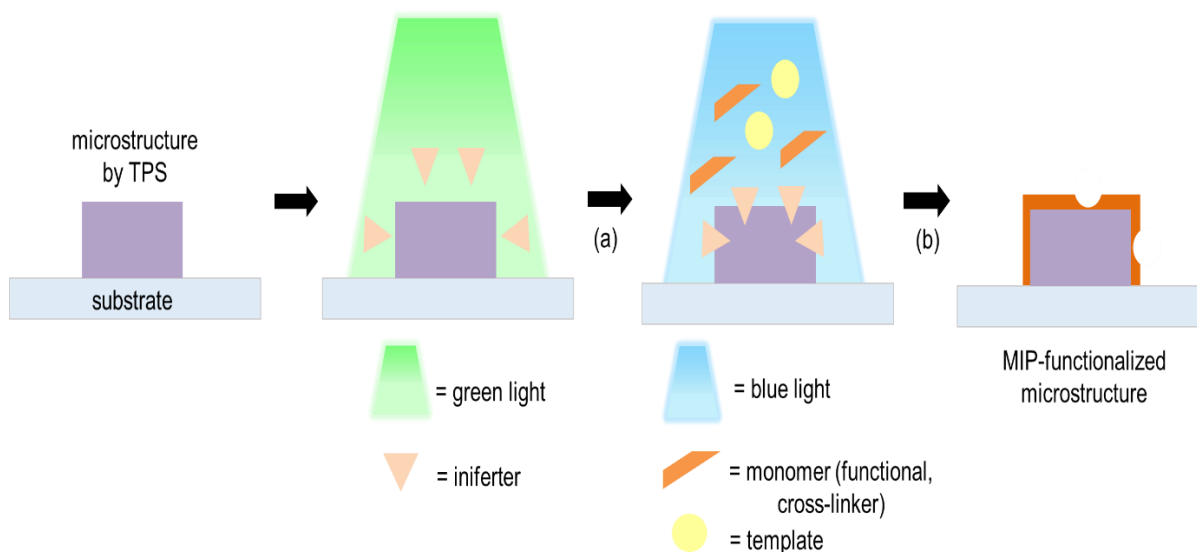


Figure 4. 1. Schematic representation of the functionalization with MIP of a TPS-written microstructure via photoiniferter-mediated polymerization. (a) The microstructure is immersed in a solution of the photoiniferter, which couples to its surface C=C upon activation by light. (b) The photoiniferter-coupled microstructure is washed and placed in a MIP precursor solution, which polymerizes at the microstructure surface, leading to MIP-functionalized microstructures.

Herein, repeating 2.5D micro-hexagons (honeycomb) were chosen as model microstructure, in order to use a simple yet edged structure which would allow appreciating the effect of growing a MIP on the geometrical features of a representative microstructure. A reduced axial (z) dimension was also achieved by positioning the center of the voxel at the substrate-resin interface.

The new strategy involves the determination of the smallest lateral and axial structural sizes for each photoresist, followed by writing 2.5D honeycombs using these parameters. The presence of unreacted double bonds on the honeycombs will be verified by Raman and FT-IR spectroscopy, before proceeding with anchoring 4-cyano-4-((dodecylsulfanylthiocarbonyl)sulfanyl)pentanoic acid (CDTPA) as a photoiniferter, for further polymerization.

## 2. Experimental

### 2.1. Materials

The photoresist IP-Dip and the fused silica substrates (3D SF DiLL) of dimensions 25 mm x 25 mm x 7 mm were acquired from Nanoscribe GmbH, Germany. 3-(trimethoxysilyl)propyl methacrylate (TMPM) ( $\geq 98\%$ ), propylene glycol methyl ether acetate (PGMEA) ( $\geq 99.5\%$ ), 2-propanol (99.9%), 4-cyano-4-((dodecylsulfanylthiocarbonyl)sulfanyl)pentanoic acid (CDTPA) (99%), N-(carbobenzyloxy)-(L)-phenylalanine (Z-(L)-Phe) (99%), methacrylic acid (99%), ethylene glycol dimethacrylate (EGDMA) (98%), 4-vinylpyridine (4-VP) (95%) and methyl methacrylate (99%) (MMA) were from Sigma-Aldrich. Methanol, glacial acetic acid, absolute ethanol and anhydrous toluene (99.8%) were from VWR Chemicals. Dansyl-(L)-phenylalanine (dansyl-(L)-Phe) was from MP Biomedicals, LLC, France. Methacryloxyethyl thiocarbonyl rhodamine B was from Polysciences, Inc., USA. N-(carbobenzyloxy)-(D)-phenylalanine (Z-(D)-Phe) was from Fluka Analytical, Switzerland. 3-(((1-carboxyethyl)thio)carbonothioyl)thio)propanoic acid (BM1429) was from Boron Molecular. 2-(dodecylthiocarbonothioylthio)-2-methylpropionic acid (DoMPAT) was kindly donated by Dr. Algi Serelis. EGDMA was passed through a column of aluminum oxide to remove the polymerization inhibitor. 4-VP was freshly distilled under reduced pressure before use.

### 2.2. Equipment and software

The TPS system used was a unit of Nanoscribe Photonic Professional GT 3D printer (Nanoscribe GmbH, Germany). It is equipped with a pulsed femtosecond laser source at a center wavelength of 780 nm. It also includes a Carl Zeiss Axio observer microscope, which focuses the laser beam via an objective into the photoresist and together with the live camera, allows the monitoring of the printing process. It has motorized stages for the coarse movement of the photoresist sample and piezoelectric stages for finer but slower movements. The scan modes for printing available are the galvo and the

piezo scan modes, the former of which was used throughout the study for its straightforward and rapid approach.

Two important software are associated with the Nanoscribe Photonic Professional GT. The first one is DeScribe which is an editor for General Writing Language (GWL) files. GWL is a script language developed by Nanoscribe that describes the trajectories to be followed by the laser focus and configures all the system parameters to be used during the writing process. DeScribe is used to design structures (in addition to third-party CAD software), to check syntax errors in the commands and to convert STL files to GWL files. The other software is called NanoWrite which presents a user interface to manipulate the Nanoscribe Photonic Professional GT. Through NanoWrite, the autofocus system is used to locate the interface between the photoresist and the substrate, and the printing process may be viewed online via a live camera.

### *2.3. Determination of the smallest lateral and axial printable feature*

A group of three horizontal lines of one-voxel width in the XY plane was designed on the Describe software and was replicated for every combination of various scan speed and laser power values. The scan speed values were from 1000  $\mu\text{m/s}$  to 10000  $\mu\text{m/s}$  with an interval of 1000  $\mu\text{m/s}$  while the laser power values were from 5 mW to 50 mW with an interval of 5 mW, totaling 100 groups of three one-voxel-wide lines. Each group was labelled to the right by scan speed (SS) and percent laser power (LP).

Each set of 100 groups of lines was 3D printed through Nanoscribe using either IP-Dip or IP-S. The printing of the one-voxel-wide lines was set to Dip-in Laser Lithography (DiLL) configuration. The center of the voxel was positioned at the photoresist-substrate interface to reduce the axial (z) dimension to half a voxel. The objective used was 63X NA 1.4. Either the IP-Dip or the IP-S was dropped on the center of a 2.5 cm x 2.5 cm x 0.07 cm fused silica substrate previously functionalized with 3-(trimethoxysilyl)propyl methacrylate (TMPPM). The GWL file were loaded into Nanowrite and printing was executed.

Development of the structures was performed by dipping the substrate in propylene glycol methyl ether acetate (PGMEA) for 20 minutes and then in 2-propanol for 2 minutes. The one-voxel-wide lines were visualized using scanning electron microscopy (SEM) on a QUANTA FEG 250 on gold sputter-coated samples. The width and the height of each line was measured through the ImageJ software.

#### *2.4. Writing of 2.5D honeycomb microstructures via TPS*

A basic unit of the honeycomb was designed in the XY plane on the DeScribe software such that the constituent lines were one-voxel wide and a half-voxel high along the +Z direction starting from 0 (another half-voxel in the corresponding -Z direction). The basic unit was then made to repeat over a 50  $\mu\text{m}$  x 50  $\mu\text{m}$  square of honeycomb. Sixteen squares were finally assembled together on the software to form a 200  $\mu\text{m}$  x 200  $\mu\text{m}$  honeycomb.

The writing of the 2.5D honeycomb microstructures was carried out using the Nanoscribe Photonic Professional (GT) printer in the DiLL configuration with the 63X NA 1.4 objective. Either the commercial photoresist IP-Dip or IP-S was used on a 25 mm x 25 mm x 7 mm fused silica substrate previously functionalized with 3-(trimethoxysilyl)propyl methacrylate (TMPPM) as previously described in Chapter 3. The scan speed (SS) used with IP-Dip was 6000  $\mu\text{m}/\text{s}$  while the laser power (LP) was 20 mW. The SS with IP-S was 2000  $\mu\text{m}/\text{s}$  while the LP was 35 mW.

Development of the microstructures was performed by dipping the substrate in propylene glycol methyl ether acetate (PGMEA) for 20 minutes and then in 2-propanol for 2 minutes. The 2.5D honeycomb microstructures were visualized using scanning electron microscopy (SEM) on a QUANTA FEG 250 on gold sputter-coated samples. The width and height of the constituent lines was measured through the ImageJ software.

#### *2.5. Assessment of C=C bonds on TPS-written microstructures*

The presence of C=C bonds on the microstructures was assessed using Raman spectroscopy on a Witec alpha300 RA (WiTec GmbH, Germany). The laser source (Ocean Optics, Innovative Photonic Solutions, USA) had a center wavelength of 785 nm (integration time: 20s, number of accumulations: 10, intensity: 0.250) and the objective used was 20X NA 0.4. Raman imaging was also performed over a 150  $\mu\text{m}$  x 150  $\mu\text{m}$  area including the microstructure with a final resolution of 100 pixels.

#### *2.6. Assessment of C=C bonds on conventionally photopolymerized photoresists*

A mass of around 500 mg of each photoresist was also photopolymerized by single photon absorption as follows. IP-Dip was polymerized by exposing to 435-nm LED (full width at half maximum or FWHM = 15 nm, LED435-66-60-110, Roithner LaserTechnik, Austria) at 4  $\text{mW}/\text{cm}^2$  for 26 h. IP-S was exposed to 365-nm UV lamp at 1  $\text{mW}/\text{cm}^2$  for 37 h. The polymers were washed in propylene glycol

methyl ether acetate (PGMEA) for 20 minutes followed by 2-propranol for 2 minutes. The polymers were then subjected to FTIR spectroscopy on a Nicolet iS50 FT-IR (Thermo Fisher Scientific, USA) with a scan range from  $675\text{ cm}^{-1}$  to  $4000\text{ cm}^{-1}$  and a resolution of  $4\text{ cm}^{-1}$  over 32 scans.

### *2.7. CDTPA decoration of the 2.5D honeycomb microstructure*

A substrate with the 2.5D honeycomb microstructures on its surface was cut in order to fit into a 4 mL glass vial and placed in an upright position. Each vial was then filled with 3 mL of 10 mM of 4-cyano-4-[(dodecylsulfanylthiocarbonyl)sulfanyl]pentanoic acid (CDTPA) in ethanol, submerging the piece of substrate inside. The vial was sealed and the solution purged with nitrogen for 10 minutes away from light. The vials were then exposed to 520-nm LED light (FWHM = 32 nm, LED520-66-60, Roithner LaserTechnik, Austria) at  $1\text{ mW/cm}^2$  for 24 h. After removing the solution, the substrate pieces were washed in ethanol for 10 minutes and in dichloromethane for another 10 minutes and left to dry.<sup>19</sup>

### *2.8. Growing of a fluorescent polymer on CDTPA-decorated 2.5D honeycomb microstructures*

A pre-polymerization mixture consisting of the fluorescent monomer methacryloxyethyl thiocarbamoyl rhodamine B (rhodamine B), the MMA and the crosslinker EGDMA in 1 : 91.9 : 289.9 molar ratio was prepared and dissolved in 4:1 methanol/water to give a final concentration of 2.67 mM of rhodamine B in the solvent. 2.5 mL of the mixture was then introduced to a vial containing the substrate piece of the CDTPA-decorated 2.5D honeycomb microstructures. The vial was sealed and purged with nitrogen for 10 minutes. It was then exposed to 435-nm LED (FWHM = 15 nm, LED435-66-60-110, Roithner LaserTechnik, Austria) at  $1\text{ mW/cm}^2$  for 24 h. Afterwards, the substrate piece was washed in 4:1 methanol/water several times and finally washed with methanol and left to dry.

The 2.5D honeycomb microstructure with the grown fluorescent polymer was inspected under a Leica DMI6000 B fluorescence microscope (Leica Microsystems, Germany) with a TX2 filter cube (excitation filter center wavelength: 560 nm; suppression filter center wavelength: 645 nm). The obtained fluorescence microscopy images were then processed using the software ImageJ to quantify the fluorescence intensity of the honeycombs. The intensity was then corrected against the background using the formula:<sup>20</sup>

$$\text{CTCF} = \text{Integrated Density} - (\text{Selected Area} \times \text{Mean fluorescence of background readings})$$



where CTCF is the background-corrected fluorescence intensity. The difference between the CTCF values after and before incubation ( $\Delta I_f$ ) was taken to be the response of the MIP (or the NIP) layer of the honeycomb to the target dansyl-(L)-Phe.

### *2.9. Growing of a MIP/NIP on CDTPA-decorated 2.5D honeycomb microstructures*

The MIP precursor formulation was adapted from Ref <sup>21</sup>. The formulation consisting of the template molecule Z-(L)-Phe, the functional monomers MAA and 4-VP, and the crosslinker EGDMA in 1 : 4 : 4 : 40 molar ratio was prepared and dissolved in acetonitrile so that the concentration of active bonds was either 0.99 M or 1.80 M. The corresponding NIP precursor solution had the same formulation but without the Z-(L)-Phe. The same volume of the precursor solution, i.e. 3 mL was introduced into the vials containing the substrate piece of the various and newly CDTPA-decorated 2.5D honeycomb microstructures. Each vial was sealed and purged with nitrogen for 10 minutes away from light. It was then exposed to 435-nm LED light (FWHM = 15 nm, LED435-66-60-110, Roithner LaserTechnik, Austria) at 1 mW/cm<sup>2</sup> for 24h for the precursor solution with 0.99 M active bonds while 5 h for the precursor solution with 1.80 M active bonds. After removing the solution, each substrate was washed for one hour with 40 mL each of methanol/acetic acid (9:1, v/v) (x3), ethanol (x2), methanol (x1) and dichloromethane (x3), and was left to dry.

The washed and dried 2.5D honeycomb microstructures decorated with MIP (or NIP) was inspected under a Leica DMI6000 B fluorescence microscope (Leica Microsystems, Germany) using the A4 filter cube (excitation filter center wavelength: 360 nm; suppression filter center wavelength: 470 nm). The obtained fluorescence microscopy images were then processed as before. The difference between the CTCF values after and before incubation ( $\Delta I_f$ ) was taken to be the response of the MIP (or the NIP) layer of the honeycomb to the target dansyl-(L)-Phe.

### *2.10. Binding and selectivity studies on the MIP (or NIP)-decorated honeycombs*

A substrate containing a MIP (or NIP)-decorated honeycomb microstructure was incubated in a 25-mL solution of either 1  $\mu$ M or 10  $\mu$ M dansyl-(L)-Phe in acetonitrile for two hours away from light and under gentle magnetic stirring. Thereafter, the substrate was rinsed with 500  $\mu$ L acetonitrile on each face to remove the unbound template. After letting it dry, the honeycomb microstructures was inspected under the Leica DMI6000 B fluorescence microscope (Leica Microsystems, Germany) with a A4 filter cube (excitation filter center wavelength: 360 nm; suppression filter center wavelength: 470

nm). The obtained images were processed using the software ImageJ to quantify the fluorescence intensity of the honeycombs. The intensity was corrected against the background using the formula in Section 5.2.8.<sup>20</sup>

For the selectivity study, the same procedure as that of the binding was followed but the solution in which the substrates were incubated was changed. Two kinds of solution were used for each study. The first one was a solution containing 10  $\mu\text{M}$  dansyl-(L)-Phe and 10  $\mu\text{M}$  of the template molecule, Z-(L)-Phe in acetonitrile. The second was a solution containing 10  $\mu\text{M}$  dansyl-(L)-Phe and 10  $\mu\text{M}$  of the enantiomer of the template molecule, Z-(D)-Phe.

### 3. Determination of the smallest voxel lateral and axial feature sizes

#### 3.1. Using IP-Dip

The parameters of our TPS system that favored the writing of the smallest achievable dimensions were determined by fabricating lines of one-voxel height and half-a-voxel width over ten different scan speeds and ten different laser power values using each photoresist, IP-Dip or IP-S. Starting with IP-Dip, the minimum lateral feature size achieved is shown as a function of the laser power at a fixed scan speed in Figure C1 (Appendix C). The thickest lines expectedly came from lower scan speeds and higher laser powers, which generated the highest number of radicals due to the length of exposure and the intensity of the activating wavelength. Conversely and more importantly, the thinnest lines and therefore the smallest lateral feature sizes were obtained at higher scan speeds and lower laser power values. The mean smallest lateral feature size was measured to be  $148 \pm 64$  nm and was achieved at  $SS = 6000 \mu\text{m/s}$  and  $LP = 20$  mW (Figure C1A, Appendix C). On the other hand, the mean smallest axial feature achievable was determined to be  $515 \pm 67$  nm ( $SS=9000 \mu\text{m/s}$ ,  $LP=20$  mW) (Figure C1B, Appendix C).

#### 3.2. Using IP-S

IP-S is another commercial photoresist like IP-Dip but is better suited for mesoscale printing using the 25x objective and the ITO-coated soda lime substrate.<sup>22</sup> Furthermore, its reactive group is declared to be methacrylate according to its data sheet, conversely to IP-Dip which is based on acrylates.<sup>23,24</sup> In any case, the printing with IP-S was still carried out with a 63x objective and a TMPM-functionalized fused silica substrate. For IP-S, mean smallest lateral size was measured to be  $270 \pm 35$  nm and was

achieved at  $SS=2000 \mu\text{m/s}$  and  $LP=35 \text{ mW}$  (Figure C2A, Appendix C). Meanwhile, the mean smallest axial size was  $533 \pm 166 \text{ nm}$  ( $SS=1000 \mu\text{m/s}$ ,  $LP=30 \text{ mW}$ ) (Figure C2B, Appendix C).

#### 4. Fabrication via TPS of 2.5D honeycomb microstructures

A 2.5D microstructure in the form of one layer of honeycombs (Figure 4. 2) was printed using the parameters that allowed the smallest lateral features as determined in the previous section (Section 1.2).

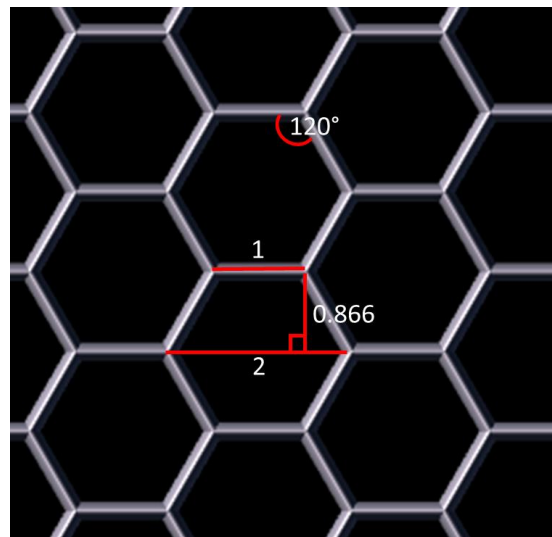


Figure 4. 2. The 2.5D honeycomb design (length measurements in  $\mu\text{m}$ ). The design is programmed to extend to an area of  $200 \times 200 \mu\text{m}^2$ .

Both photoresists IP-Dip and IP-S were used for writing these structures. Their absorbance spectra include the wavelength at  $390 \text{ nm}$  (Figure 4. 3), implying that they can be activated via two-photon absorption at  $780 \text{ nm}$ , which is indeed the center wavelength of the laser of our TPS system. As seen in Figure 4. 4, IP-Dip yielded an incomplete honeycomb since its repeating units did not connect with each other, which could be attributed to the low laser dose used. In contrast, IP-S yielded a complete honeycomb structure with its repeating units fully written, thereby allowing them to connect to each other.

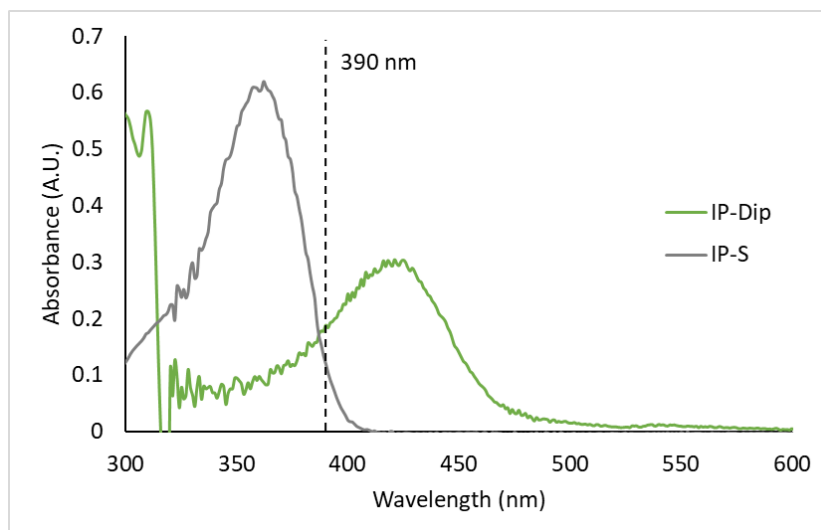


Figure 4. 3. Absorbance spectra of the unreacted photoresists IP-Dip and IP-S recorded in acetonitrile at a concentration of 69  $\mu\text{g}/\text{mL}$ .

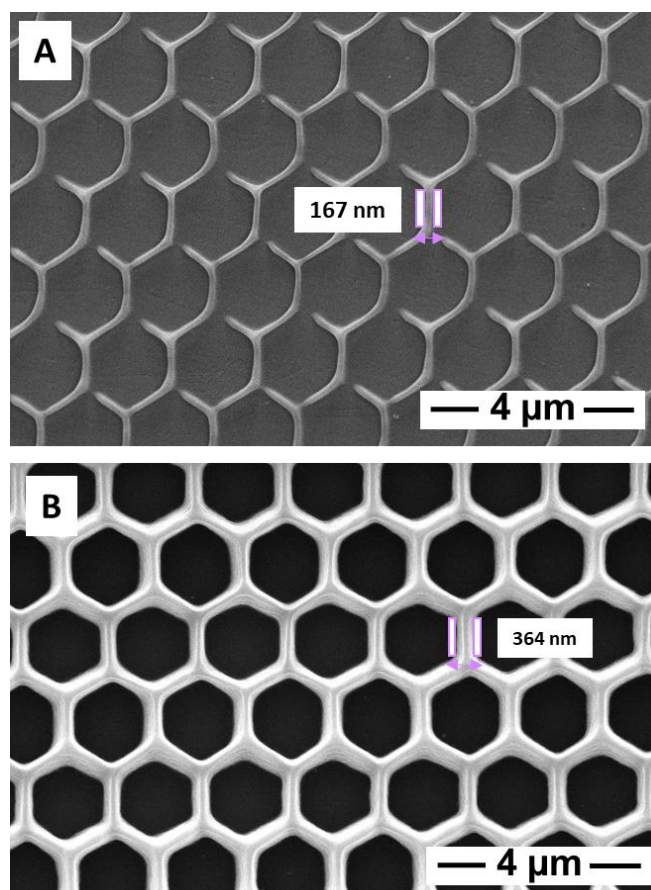


Figure 4. 4. Representative SEM images of TPS-written 2.5D honeycomb microstructures based on the commercial photoresists (A) IP-Dip and (B) IP-S.

The width and the height of the constituent lines were also measured ( $n=54$ ) and statistically compared to the previously observed minimum lateral or axial size of triplicate lines (Welch t-test,  $\alpha = 0.05$ ). The average line width from the IP-Dip honeycomb was  $167 \pm 31$  nm, which is statistically different from the expected  $148 \pm 64$  nm for  $SS = 6000 \mu\text{m/s}$ ,  $LP = 20$  mW. The height (presented here as twice the measured one to account for the whole voxel) was  $585 \pm 75$  nm, which is statistically different from the expected  $648 \pm 51$  nm. As for the IP-S honeycomb, the line width was  $364 \pm 44$  nm, which is statistically different as the previously observed  $270 \pm 35$  nm for  $SS = 2000 \mu\text{m/s}$ ,  $LP = 35$  mW. The height being  $2188 \pm 304$  nm was likewise different from the expected  $559 \pm 57$  nm.

## 5. Decorating 2.5D honeycomb microstructures with CDTPA

Once the substrate written, we investigated the feasibility of decorating its surface via a photoiniferter coupling. The chosen photoiniferter was CDTPA.<sup>19</sup> Upon activation by light (e.g. 520 nm), the trithiocarbonate moiety of CDTPA is expected to react with the residual C=C bonds on the honeycomb surface, possibly following a single-unit monomer insertion (SUMI) reaction especially on the IP-Dip.<sup>25</sup>

### 5.1. Residual C=C bonds at the surface of the 2.5D honeycomb microstructures

Raman spectroscopy was used to confirm the presence of residual C=C bonds on the surface of model 500- $\mu\text{m}$ -tall truncated cones (Figure 4. 5). These structures are easier to analyze compared to the honeycombs, but are expected to be chemically equivalent with the same concentration of unreacted C=C since the printing process was the same. As a reference, the monomer pentaerythritol triacrylate (PETA, which was found to be present in the IP-Dip photoresist) was used with its C=C bond yielding a peak at  $1635 \text{ cm}^{-1}$  (Figure 4. 6).<sup>26</sup> The unreacted photoresists, IP-Dip and IP-S, expectedly exhibited the same peak, which was also present on all truncated cones based on the various photoresists, confirming the presence of residual C=C bonds on the TPS-written structures (the cone of IP-S showed a much less intense peak which was probably due to fluorescence induced by the laser of the Raman spectrometer).

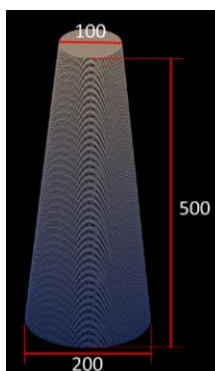


Figure 4. 5. The truncated cone design for the Raman spectroscopy of the photoresists polymerized via TPS (length measurements in  $\mu\text{m}$ ).

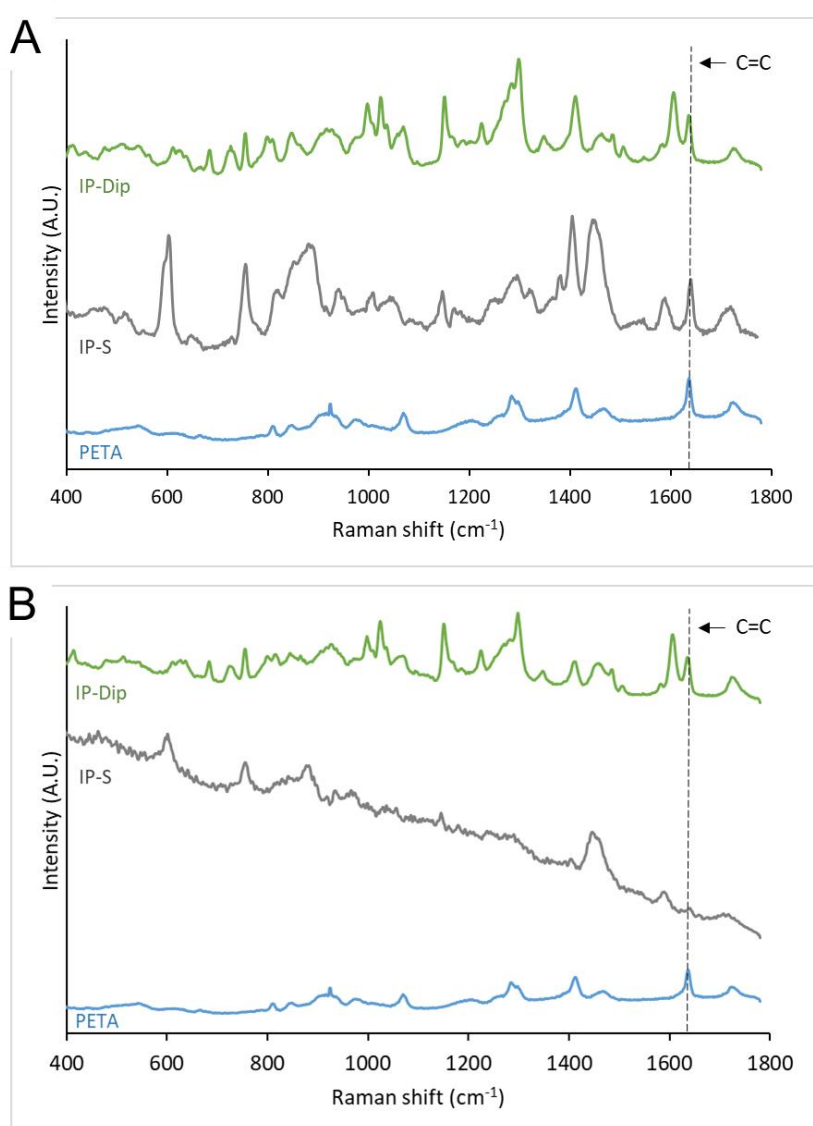


Figure 4. 6. Raman spectra of (A) unreacted photoresists and (B) TPS-written truncated cones based on these photoresists. PETA was used as the C=C bond-containing monomer reference.

Raman imaging was also performed on the top surface of each truncated cone. This allowed imaging of residual C=C on their surface without any preparation step for a more global inspection. Figure 4. 7 places side-by-side the brightfield image and the Raman image of the cones. The images also show the presence of residual C=C bonds on the surface of the polymerized photoresists, confirming the feasibility of CDTPA decoration and the subsequent growing of polymers on a TPS-written surface. It is noticeable that the Raman image of the polymerized IP-S has much less contrast between the C=C-filled and C=C poor zones. This could be attributed to the laser-induced fluorescence of the IP-S, which masks most of its peak at  $1635\text{ cm}^{-1}$ , as seen in Figure 4. 6.

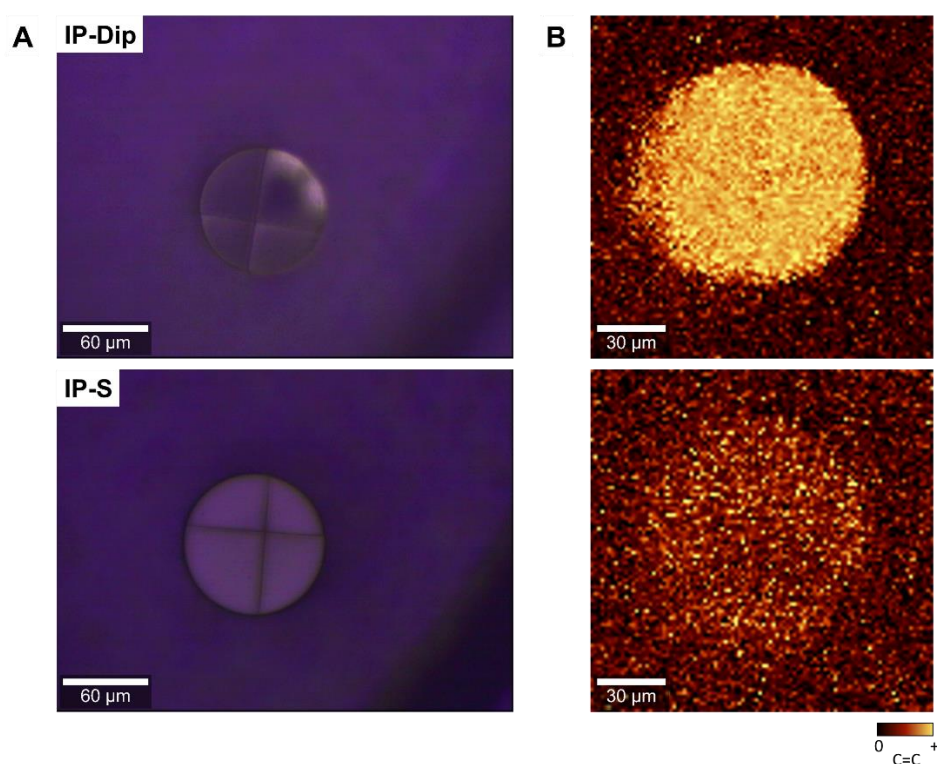


Figure 4. 7. The (A) brightfield image and (B) the Raman image of top surface of the TPS-written truncated cone of each photoresist.

The above results were confirmed by Fourier-transform infrared (FTIR) spectroscopy on unreacted photoresists, which all showed a peak around  $1635\text{ cm}^{-1}$  attesting their C=C bonds (Figure 4.8A). Since the microstructures were too small for FTIR measurements, the photoresists were conventionally photopolymerized instead. After photopolymerization, a residual C=C peak was still visible (Figure 4.8B), thus confirming the previous Raman results.

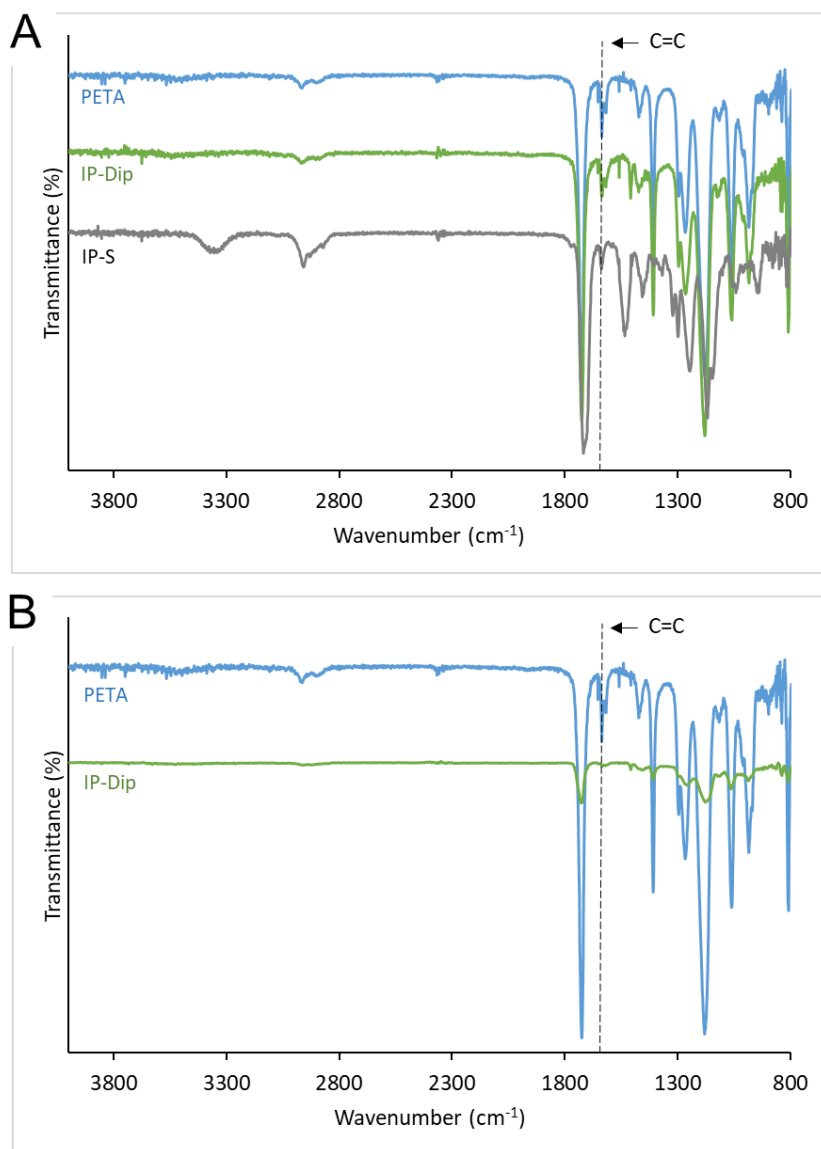


Figure 4.8. The FTIR spectra of (A) unreacted photoresists and (B) conventionally photopolymerized photoresists.

## 5.2. Grafting of CDTPA on the honeycomb via unreacted C=C

The 2.5D honeycomb microstructures were then decorated with CDTPA. This decoration was achieved by immersing the honeycomb in a solution of CDTPA and exposing it to 520-nm light, thereby activating the photoiniferter. Figure 4. 9 shows the absorption spectrum of CDTPA; it is noteworthy here that its absorbance tails at 520nm, which only allows weak excitation by the LED. However, upon coupling to an acrylic C=C, its absorption spectrum does blue shift (see BM1429 in Figure 4. 9), which makes the adduct insensitive to green light irradiation and thus preserves the grafted photoiniferter from further excitation (i.e. photobleaching and/or propagation to other C=C, though this second event is quite unlikely due to diffusion limitations). This principle does not apply to IP-S, since upon coupling



with a methacrylic C=C, the CDTPA absorption spectrum blue-shifts and broadens at the same time (see DoMPAT, in Figure 4. 9) and can thus still be excited by the green LED. In these conditions, photobleaching cannot be excluded<sup>27</sup> even though the low intensity applied ( $1 \text{ mW/cm}^2$ ) should lower it to a minimum.

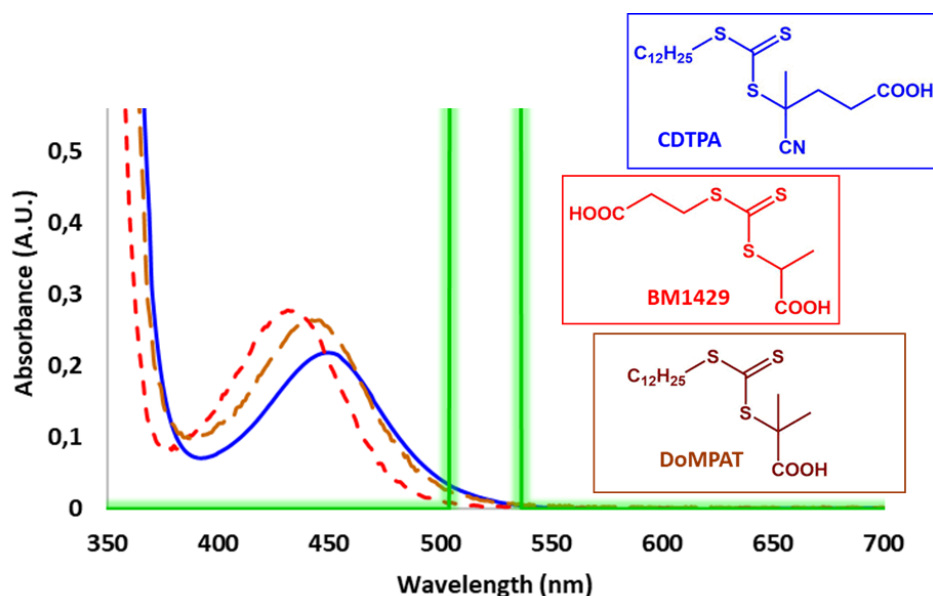


Figure 4. 9. Absorption spectra of CDTPA and the structural mimics of its SUMI adducts with acrylic acid (BM1429) and with methacrylic acid (DoMPAT). All the spectra were recorded in acetonitrile at a concentration of 7.5 mM.

Characterization of the CDTPA coupling by Raman or FTIR spectroscopy, however, was not possible since the width and the height of the lines of the honeycombs were too small to give meaningful responses. Thus, a fluorescent polymer based on a rhodamine B monomer was grown on the honeycombs to confirm the successful coupling of CDTPA, as discussed in the next subsection.

## 6. Honeycomb functionalization with a fluorescent polymer via a photoiniferter

In order to prove and validate the successful CDTPA coupling and set the feasibility of growing a polymer, honeycomb microstructure were functionalized with a fluorescent layer based on rhodamine B methacrylate. The polymerization was triggered by a blue LED ( $\lambda_{\text{max}}=435 \text{ nm}$ ) which matches the maximum absorption of the grafted CDTPA.

A bare IP-Dip honeycomb was first inspected under a fluorescent microscope in brightfield mode. The whole honeycomb appeared as a 4x4 square grid (Figure 4. 10A), not shown completely) consisting of a collection of 16 50  $\mu\text{m}$  x 50  $\mu\text{m}$  stuck together in order to cover a 200  $\mu\text{m}$  x 200  $\mu\text{m}$ -area, (i.e. exceeding the writing field of the 63X NA 1.4 objective of the Nanoscribe printer). When the area of a structure exceeds the writing field, its printing is performed by squares, “stitching” them together as one square is printed adjacent to another. The squares, however, did not precisely connect for the honeycombs, possibly because of the limited precision of the motorized stage when moving between writing fields, leaving considerable gaps between them that cannot be easily stitched especially given the thin dimensions of our structures.<sup>28</sup> The honeycomb also appeared faint due to its very small and thin constituent lines. Upon excitation under the fluorescence mode of the same microscope, virtually no fluorescence was observed from the bare honeycomb, as presented in Figure 4. 10B.

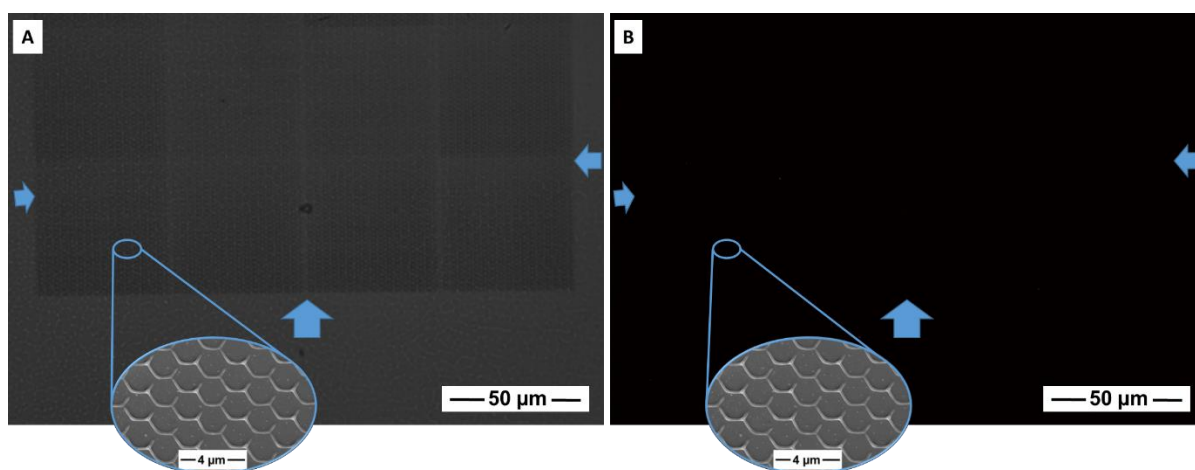


Figure 4. 10. (A) Brightfield and (B) fluorescence microscopy images of the bare IP-Dip 2.5D honeycomb microstructure. The arrows indicate the borders of the 200  $\mu\text{m}$  x 200  $\mu\text{m}$  area of the honeycomb.

On the other hand, upon excitation at 560 nm, honeycombs functionalized with rhodamine B-based polymer film actually exhibited fluorescence, although faintly owing to the miniscule dimensions of the constituent lines. It is important to note that the area of faint fluorescence moved along when the stage of the microscope was also moved, indicating that the fluorescence indeed emanated from the honeycomb. This indicates that the CDTPA was successfully anchored onto the surface of the honeycombs and it initiated the polymerization of the fluorescent polymer film. Figure 4.11 show images of (A) CDTPA-anchored and (B) rhodamine B modified honeycombs.

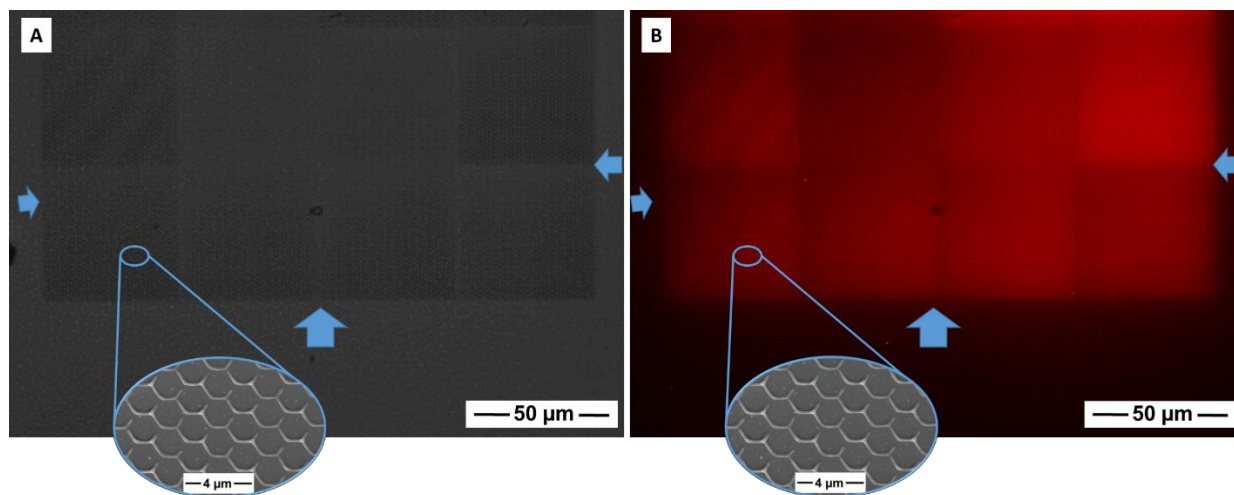


Figure 4.11. (A) Brightfield and (B) fluorescence microscopy images of the CDTPA-decorated IP-Dip 2.5D honeycomb microstructure after growing a fluorescent polymer. The arrows indicate the borders of the 200  $\mu\text{m}$  x 200  $\mu\text{m}$  area of the honeycomb. (Image enhanced)

A negative control was also prepared: in this case, a bare honeycomb (i.e. before the photoiniferter coupling step) was allowed to photopolymerize with rhodamine B, washed and inspected as above. Upon excitation at 560 nm, the negative control was poorly fluorescent (Figure 4. 12B), which possibly depends on some stuck/occluded rhodamine monomer and accounts for a negligible polymerization. We conclude that the photoiniferter coupling step was essential for further polymer grafting.

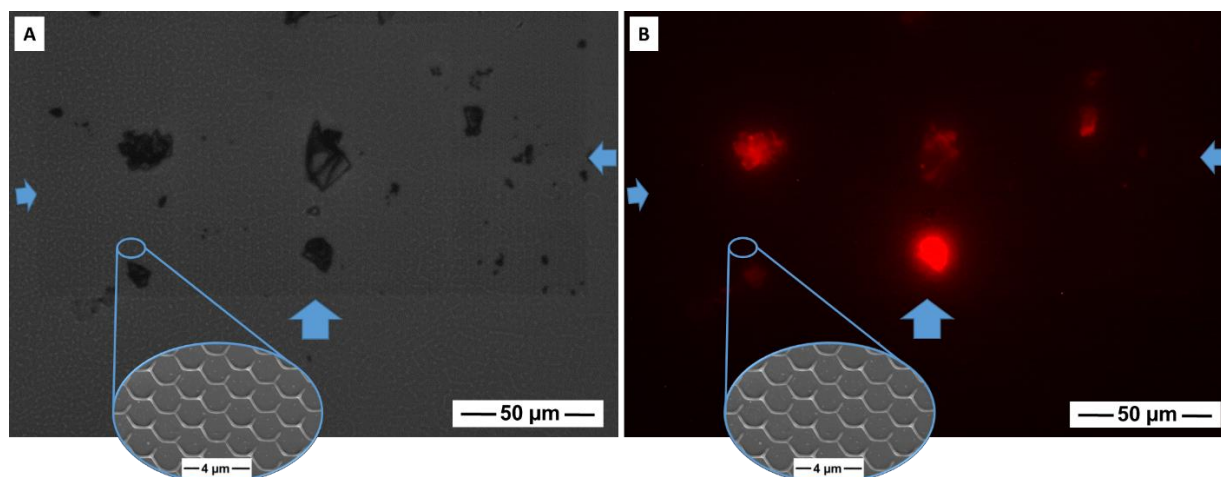


Figure 4. 12. (A) Brightfield and (B) fluorescence microscopy images of the negative control IP-Dip 2.5D honeycomb microstructure after growing a fluorescent polymer. The arrows indicate the borders of the 200  $\mu\text{m}$  x 200  $\mu\text{m}$  area of the honeycomb. (Image enhanced)

The same procedure was performed on the IP-S honeycombs and similar results were obtained (Figure 4. 13). The bare IP-S honeycomb did not show any fluorescence, while CDTPA-decorated IP-S honeycombs exhibited intense fluorescence, which indicated the successful polymerization of the

fluorescent monomer on its surface, thanks to the anchored CDTPA. Once again, the negative control (randomly) fluoresced to a limited extent which accounts for a negligible polymerization.

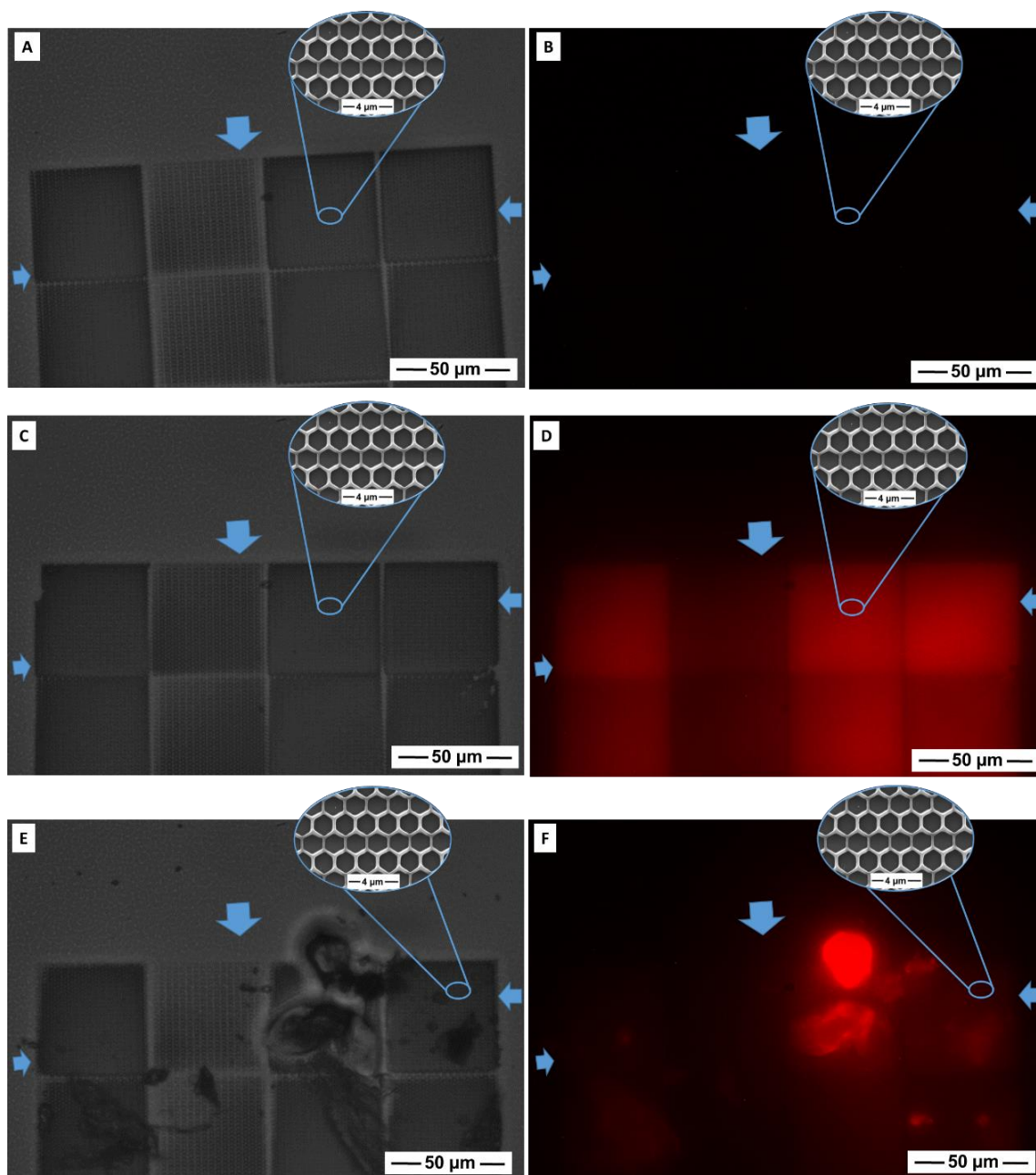


Figure 4. 13. (A, C, E) Brightfield and (B, D, F) fluorescence microscopy images of the (A, B) bare, (C, D) CDTPA-decorated, and (E, F) negative control IP-S 2.5D honeycomb microstructures after growing a fluorescent polymer. The arrows indicate the borders of the 200 μm x 200 μm area of the honeycomb.

## 7. Honeycomb functionalization with MIP via a photoiniferter

After confirming the successful grafting of CDTPA on structures printed using both photoresists, the honeycombs were surface-functionalized with a MIP (template Z-(L)-Phe) or a NIP by irradiating at

435-nm LED at rather concentrated monomer mixtures (with a total C=C concentration of 1.80 M). It was found that an irradiation time of 5 hours was necessary in order to grow the MIP (or NIP).

### 7.1. SEM characterization of the 2.5D honeycomb microstructures

SEM images of the honeycomb microstructures were captured in order to elucidate the effect of the post-polymerization on the feature size. As shown in Figure 4. 14 and Figure 4. 15, the general honeycomb pattern of all the microstructures was conserved and no extra features were created. The IP-S-based honeycombs, in particular, revealed a negligible increase in linewidth (Z test,  $\alpha = 0.05$ ). The linewidth of the IP-Dip-based honeycombs increased significantly, by 70 nm, which means that the thickness of the newly created polymer layer was roughly 35 nm. This is still much below the original linewidth. Different results on IP-S- and IP-Dip-based honeycombs may possibly relate to the varying groups present on their surface that could cause steric hindrance to entering monomer molecules.

Overall, these results illustrate that the post-TPS polymerization had no detrimental effects to the resolution (~few hundred nanometers) of the honeycomb microstructures and can be envisioned as a way of only tuning the surface properties of the printed structure.

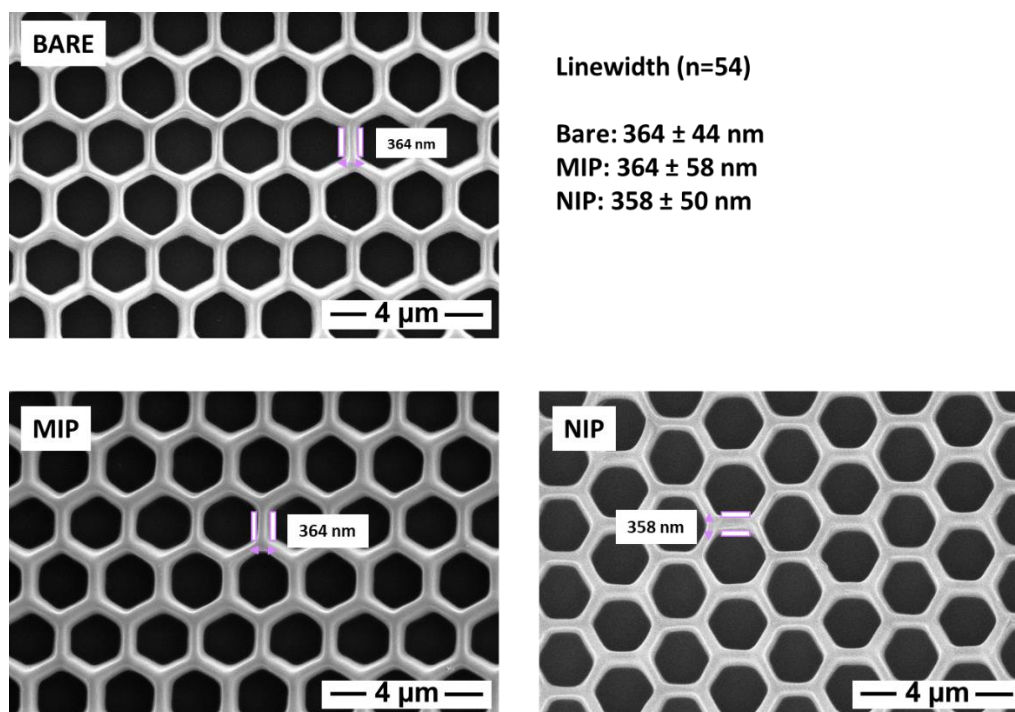


Figure 4. 14. Representative images of the bare, MIP- and NIP-decorated IP-S-based honeycomb microstructures.

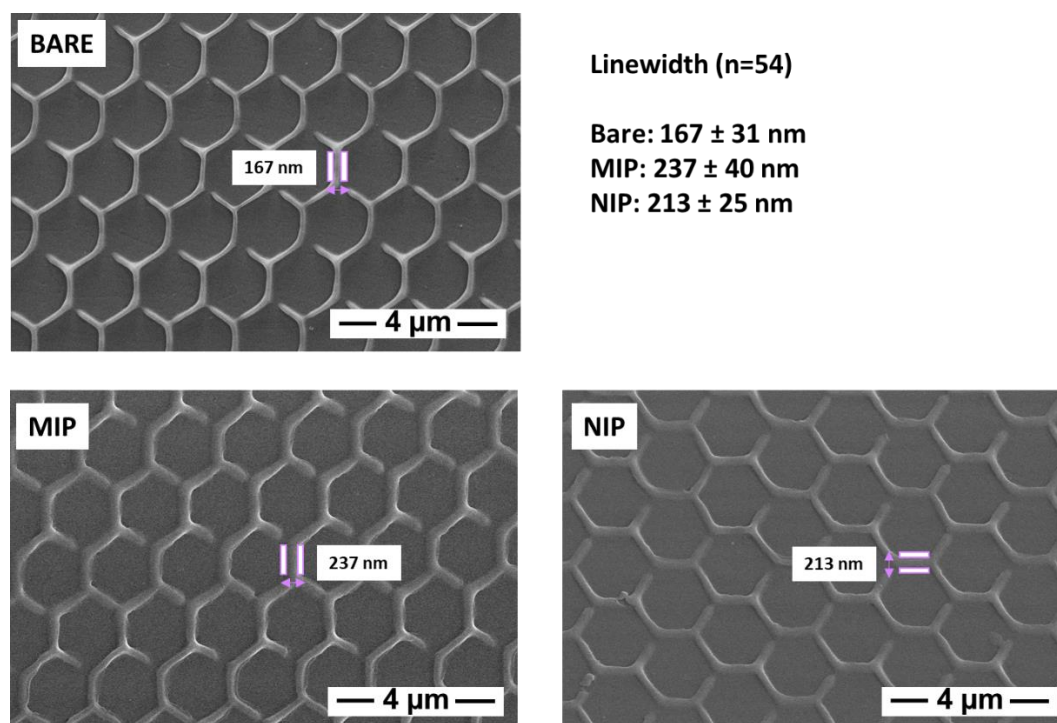


Figure 4. 15. Representative images of the bare, MIP- and NIP-decorated IP-Dip-based honeycomb microstructures.

## 7.2. Fluorescent binding test

Fluorescent binding test using the fluorescent target dansyl-(L)-Phe showed that the MIP layers generally featured an increase in fluorescent intensity. This is due to the target molecules captured in the binding sites of the MIP. On the other hand, the much less intense fluorescence observed with the NIP is attributed to non-specific binding. Since the structures were observed under a fluorescence microscope, the fluorescence intensities observed required quantification by image analysis (ImageJ was used in our case). The response of the MIP layer was thus expressed as the background-corrected  $\Delta I_f$  value which is the difference in the fluorescence intensity of the MIP layer between after and before incubation.

As shown in Figure 4. 16, MIP on the IP-Dip-based honeycomb yielded high fluorescence intensity after incubation with the target compared to the NIP. The intensity also increased when the concentration was raised tenfold, showing that the MIP layer not only responded to the presence of the analyte but also to a change in its concentration. The IF values were calculated to be 4.30 and 6.33 at  $1 \mu\text{M}$  and  $10 \mu\text{M}$  propranolol in acetonitrile, respectively. These values are higher compared to the IF of a MIP layer prepared with a formulation containing a total C=C of 0.99 M (Appendix C, Figure C3A), showing that 1.80 M C=C is the better choice for growing MIP layers.

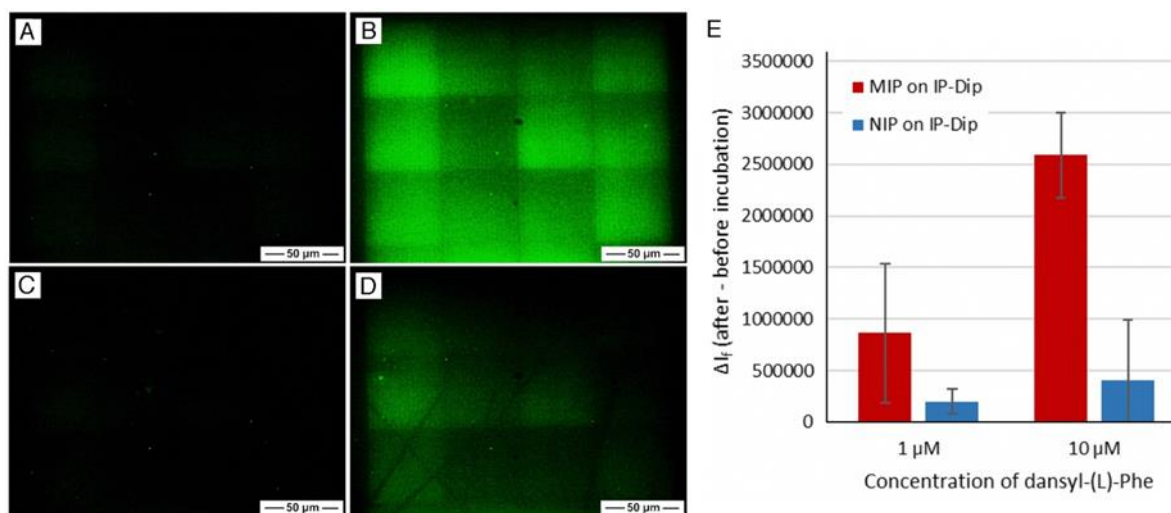


Figure 4. 16. Fluorescence microscopy image of the (A-B) MIP layer on the IP-Dip-based honeycomb microstructures (A) before and (B) after incubation, and of the (C-D) NIP layer (C) before and (D) after incubation in 10 μM dansyl-(L)-Phe in acetonitrile. (Image enhanced). (E) Background-corrected  $\Delta I_f$  of the MIP and NIP layer on the IP-Dip-based honeycomb microstructure after incubation in a solution of dansyl-(L)-Phe in acetonitrile ( $n = 3$ ). The concentration of polymerizable double bonds in the MIP and NIP precursor formulation was 1.80 M.

Similar results were also obtained on IP-S-based honeycomb microstructures, which allowed to calculate IF of 4.05 and 26.60 for 1 μM and 10 μM dansyl-(L)-Phe in acetonitrile, respectively (Figure 4. 17). These values were again better than the IF of a MIP prepared with 0.99 M total C=C (Appendix C, Figure C3B). **Erreur ! Source du renvoi introuvable.** shows the fluorescence microscopy images of the MIP- and NIP-decorated honeycombs before and after incubation in 10 μM dansyl-(L)-Phe.

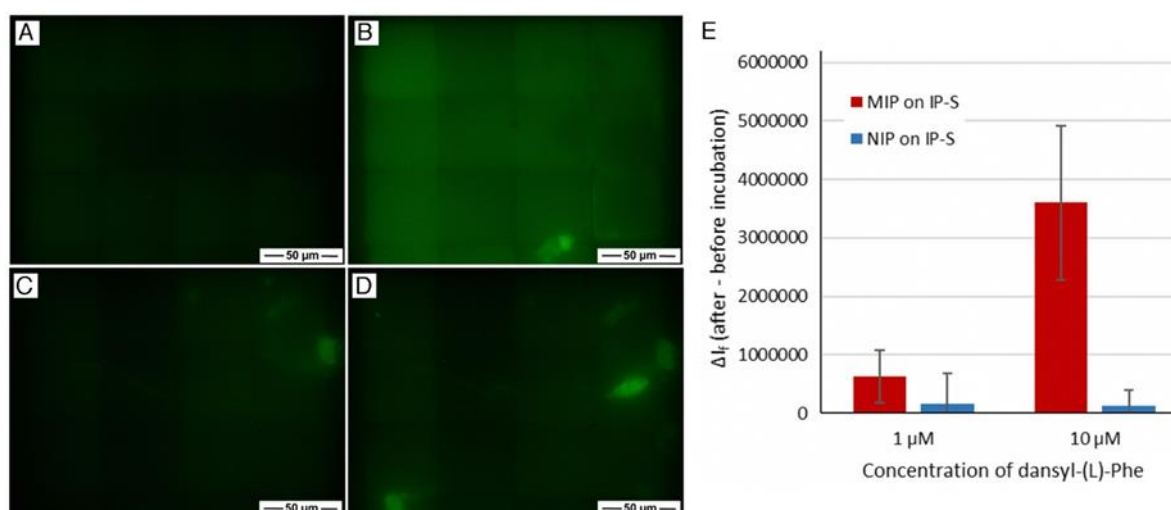


Figure 4. 17. Fluorescence microscopy image of the (A-B) MIP layer on the IP-S-based honeycomb microstructures (A) before and (B) after incubation, and of the (C-D) NIP layer (C) before and (D) after incubation in 10 μM dansyl-(L)-Phe in acetonitrile. (Image enhanced). (E) Background-corrected  $\Delta I_f$  of the MIP and NIP layer on the IP-S-based honeycomb microstructure after incubation in a solution of dansyl-(L)-Phe in

acetonitrile ( $n = 3$ ). The concentration of polymerizable double bonds in the MIP and NIP precursor formulation was 1.80 M.

### 7.3. Selectivity study

The MIP-decorated honeycombs were further investigated for their selectivity toward their target Z-(L)-Phe over the D-enantiomer. Since the template and its enantiomer are not intrinsically fluorescent, we used dansyl-(L)-Phe, as a fluorescent tracer, and selectivity tests were performed based on competitive equilibrium binding assays measuring the decrease in fluorescence due to dansyl-(L)-Phe displacement from the microstructures.

The IP-Dip- and the IP-S-based honeycombs were incubated first in a solution containing an equal concentration (10  $\mu$ M) of dansyl-(L)-Phe and Z-(L)-Phe. As seen in Figure 4. 18 , this resulted in a strong decrease of fluorescence intensity when compared to honeycombs incubated with dansyl-(L)-Phe alone. This was expected since Z-(L)-Phe is the actual template used for imprinting, meaning that the MIP's binding sites are tailored around its geometry. The honeycombs were also incubated in a solution containing both dansyl-(L)-Phe and the opposite enantiomer of the template molecule, Z-(D)-Phe. In this case, the decrease in fluorescence was less important, meaning that the binding sites are able to discriminate between the two enantiomers. As expected, the MIP has more affinity for the template enantiomer Z-(L)-Phe, which is more geometrically complementary to its binding sites. However, Z-(D)-Phe has the same functional groups as the template enantiomer Z-(L)-Phe, which is the reason for the decreased but still significant binding.



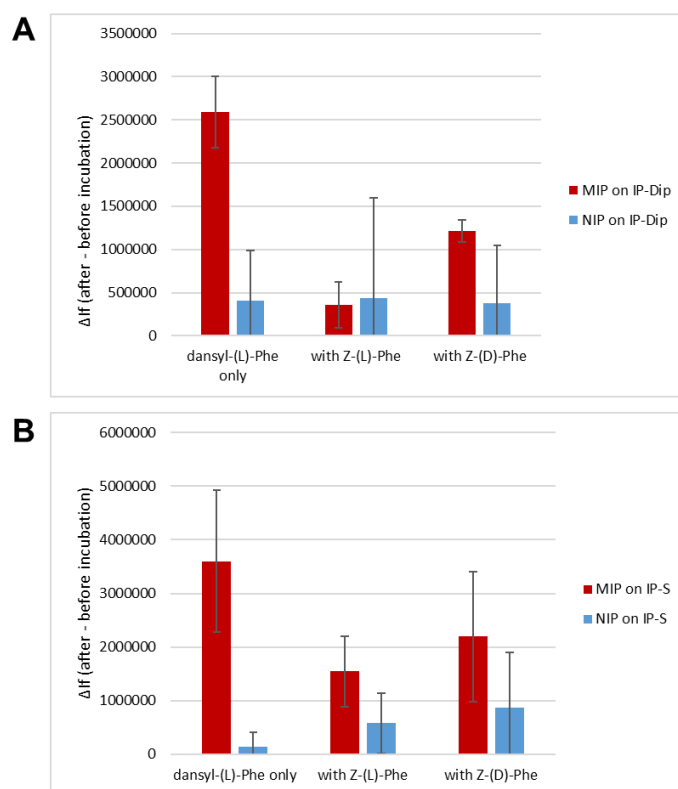


Figure 4. 18. Background-corrected  $\Delta I$  of the MIP and NIP layer on (A) the IP-Dip-, and (B) the IP-S-based honeycomb microstructures after incubation in a solution of dansyl-(L)-Phe alone, dansyl-(L)-Phe with Z-(L)-Phe or dansyl-(L)-Phe with Z-(D)-Phe in acetonitrile ( $n = 3$ ). The concentration of each molecular species in every solution was  $10 \mu\text{M}$ .

The results indicate that the MIP-decorated honeycombs are selective since they recognized and bound more the template molecule over its enantiomer.

## 8. Conclusions

As a sophisticated additive manufacturing technique, TPS has proven to be effective in directly and precisely fabricating polymeric microstructures according to its limits of resolution. Structures with dimensions as small as  $\sim 150$  nm in the XY plane and as short as  $\sim 325$  nm in the Z axis (half-voxel height) were fabricated using the acrylate-based photoresist IP-Dip and the methacrylate-based IP-S, granting them a large surface area-to-volume ratio. Taking advantage of the unreacted C=C bonds on the surface of the microstructures, the trithiocarbonate moiety of the photoiniferter CDTPA could be anchored, which allowed for the further surface-initiated polymerization of a thin MIP layer specific and selective for Z-(L)-Phe as model target. The honeycomb microstructures retained their original geometry and did not suffer drastic change in their linewidth upon functionalization with the MIP (or NIP). Also, no extra-features appeared, which is ascribed to the surface-initiated functionalization process.

Unlike its non-imprinted counterpart (NIP), the MIP showed intense fluorescence after binding the fluorescent target analog dansyl-(L)-Phe, and its fluorescence also increased with increasing concentration of target. Competitive binding experiments with the non-fluorescent target analogs Z-(L)-Phe and Z-(D)-Phe revealed a certain degree of enantioselectivity of the MIP. Taken together, these results confirm that our post-polymerization approach with a photoiniferter coupled to residual double bonds in the TPS-printed structure is a valuable strategy to functionalize microstructures with thin layers of (meth)acrylic polymers, such as MIPs.

## 9. REFERENCES

- (1) Haupt, K. Biomaterials: Plastic Antibodies. *Nat. Mater.* **2010**, *9*, 612–614.  
<https://doi.org/10.1038/nmat2818>.
- (2) Xie, Z.; Zhang, L.; Chen, Y.; Hu, X. Magnetic Molecularly Imprinted Polymer Combined with High-Performance Liquid Chromatography for the Selective Separation and Determination of Glutathione in Various Wild Edible Boletes. *Food Anal. Methods* **2019**, *12*, 2908–2919.  
<https://doi.org/10.1007/s12161-019-01646-w>.
- (3) Kurczewska, J.; Cegłowski, M.; Pecyna, P.; Ratajczak, M.; Gajęcka, M.; Schroeder, G. Molecularly Imprinted Polymer as Drug Delivery Carrier in Alginate Dressing. *Mater. Lett.* **2017**, *201*, 46–49. <https://doi.org/10.1016/j.matlet.2017.05.008>.
- (4) Medina Rangel, P. X.; Laclef, S.; Xu, J.; Panagiotopoulou, M.; Kovensky, J.; Tse Sum Bui, B.; Haupt, K. Solid-Phase Synthesis of Molecularly Imprinted Polymer Nanolabels: Affinity Tools for Cellular Bioimaging of Glycans. *Sci. Rep.* **2019**, *9*, 1–9. <https://doi.org/10.1038/s41598-019-40348-5>.
- (5) Nestora, S.; Merlier, F.; Beyazit, S.; Prost, E.; Duma, L.; Baril, B.; Greaves, A.; Haupt, K.; Tse Sum Bui, B. Plastic Antibodies for Cosmetics : Molecularly Imprinted Polymers Scavenge Precursors of Malodors. *Angew. Chem. Int. Ed.* **2016**, *55*, 6252–6256.  
<https://doi.org/10.1002/anie.201602076>.
- (6) Wang, R.; Pan, J.; Qin, M.; Guo, T. Molecularly Imprinted Nanocapsule Mimicking Phosphotriesterase for the Catalytic Hydrolysis of Organophosphorus Pesticides. *Eur. Polym. J.* **2019**, *110*, 1–8. <https://doi.org/10.1016/j.eurpolymj.2018.10.045>.
- (7) Rico-Yuste, A.; Carrasco, S. Molecularly Imprinted Polymer-Based Hybrid Materials for the Development of Optical Sensors. *Polymers* **2019**, *11* (7), 1173.  
<https://doi.org/10.3390/polym11071173>.
- (8) Ambrosini, S.; Beyazit, S.; Haupt, K.; Tse Sum Bui, B. Solid-Phase Synthesis of Molecularly Imprinted Nanoparticles for Protein Recognition. *Chem. Commun.* **2013**, *49* (60), 6746–6748.  
<https://doi.org/10.1039/c3cc41701h>.
- (9) Sharma, P. S.; Pietrzyk-Le, A.; D'Souza, F.; Kutner, W. Electrochemically Synthesized Polymers in Molecular Imprinting for Chemical Sensing. *Anal. Bioanal. Chem.* **2012**, *402*, 3177–3204.  
<https://doi.org/10.1007/s00216-011-5696-6>.
- (10) O'Shannessy, D. J.; Ekberg, B.; Mosbach, K. Molecular Imprinting of Amino Acid Derivatives at

- Low Temperature (0°C) Using Photolytic Homolysis of Azobisnitriles. *Anal. Biochem.* **1989**, *177* (1), 144–149. [https://doi.org/10.1016/0003-2697\(89\)90029-8](https://doi.org/10.1016/0003-2697(89)90029-8).
- (11) Chen, M.; Zhong, M.; Johnson, J. A. Light-Controlled Radical Polymerization: Mechanisms, Methods, and Applications. *Chem. Rev.* **2016**, *116* (17), 10167–10211. <https://doi.org/10.1021/acs.chemrev.5b00671>.
- (12) Corrigan, N.; Yeow, J.; Judzewitsch, P.; Xu, J.; Boyer, C. Seeing the Light: Advancing Materials Chemistry through Photopolymerization. *Angew. Chem. Int. Ed.* **2019**, *58* (16), 5170–5189. <https://doi.org/10.1002/anie.201805473>.
- (13) Fuchs, Y.; Soppera, O.; Mayes, A. G.; Haupt, K. Holographic Molecularly Imprinted Polymers for Label-Free Chemical Sensing. *Adv. Mater.* **2013**, *25* (4), 566–570. <https://doi.org/10.1002/adma.201203204>.
- (14) Boysen, R. I.; Li, S.; Chowdhury, J.; Schwarz, L. J.; Hearn, M. T. W. Selectivity Optimisation of Biomimetic Molecularly Imprinted Polymer Thin Films. *Microelectron. Eng.* **2012**, *97*, 81–84. <https://doi.org/10.1016/j.mee.2012.03.026>.
- (15) Gomez, L. P. C.; Spangenberg, A.; Ton, X. A.; Fuchs, Y.; Bokeloh, F.; Malval, J. P.; Tse Sum Bui, B.; Thuau, D.; Ayela, C.; Haupt, K.; Soppera, O. Rapid Prototyping of Chemical Microsensors Based on Molecularly Imprinted Polymers Synthesized by Two-Photon Stereolithography. *Adv. Mater.* **2016**, *28*, 5931–5937. <https://doi.org/10.1002/adma.201600218>.
- (16) Ertürk, G.; Mattiasson, B. Molecular Imprinting Techniques Used for the Preparation of Biosensors. *Sensors* **2017**, *17* (2), 288. <https://doi.org/10.3390/s17020288>.
- (17) Beyazit, S.; Tse Sum Bui, B.; Haupt, K.; Gonzato, C. Molecularly Imprinted Polymer Nanomaterials and Nanocomposites by Controlled/Living Radical Polymerization. *Prog. Polym. Sci.* **2016**, *62*, 1–21. <https://doi.org/10.1016/j.progpolymsci.2016.04.001>.
- (18) Garcia-Soto, M. J.; Haupt, K.; Gonzato, C. Synthesis of Molecularly Imprinted Polymers by Photo-Iniferter Polymerization under Visible Light. *Polym. Chem.* **2017**, *8* (33), 4830–4834. <https://doi.org/10.1039/C7PY01113J>.
- (19) Montagna, V.; Haupt, K.; Gonzato, C. RAFT Coupling Chemistry: A General Approach for Post-Functionalizing Molecularly Imprinted Polymers Synthesized by Radical Polymerization. *Polym. Chem.* **2020**, *11* (5), 1055–1061. <https://doi.org/10.1039/c9py01629e>.
- (20) McCloy, R. A.; Rogers, S.; Caldon, C. E.; Lorca, T.; Castro, A.; Burgess, A. Partial Inhibition of Cdk1 in G2 Phase Overrides the SAC and Decouples Mitotic Events. *Cell Cycle* **2014**, *13* (9), 1400–1412. <https://doi.org/10.4161/cc.28401>.

- (21) Fuchs, Y.; Linares, A. V.; Mayes, A. G.; Haupt, K.; Soppera, O. Ultrathin Selective Molecularly Imprinted Polymer Microdots Obtained by Evanescent Wave Photopolymerization. *Chem. Mater.* **2011**, *23* (16), 3645–3651. <https://doi.org/10.1021/cm2009829>.
- (22) Nanoscribe GmbH. Resins for printing: Resins Overview <https://support.nanoscribe.com/hc/en-gb/articles/360002486493-Resins-Overview> (accessed Jul 8, 2021).
- (23) Nanoscribe GmbH. Resins for Printing: IP-S <https://support.nanoscribe.com/hc/en-gb/articles/360001750353-IP-S> (accessed Jul 5, 2021).
- (24) Nanoscribe GmbH. Resins for Printing: IP-Dip <https://support.nanoscribe.com/hc/en-gb/articles/360001748953-IP-Dip> (accessed Jul 5, 2021).
- (25) Fu, C.; Huang, Z.; Hawker, C. J.; Moad, G.; Xu, J.; Boyer, C. RAFT-Mediated, Visible Light-Initiated Single Unit Monomer Insertion and Its Application in the Synthesis of Sequence-Defined Polymers. *Polym. Chem.* **2017**, *8* (32), 4637–4643. <https://doi.org/10.1039/c7py00713b>.
- (26) Jöhnck, M.; Müller, L.; Neyer, A.; Hofstraat, J. W. Quantitative Determination of Unsaturation in Photocured Halogenated Acrylates and Methacrylates by FT-IR and Raman-Spectroscopy and by Thermal Analysis. *Polymer* **1999**, *40* (13), 3631–3640. [https://doi.org/10.1016/S0032-3861\(98\)00596-5](https://doi.org/10.1016/S0032-3861(98)00596-5).
- (27) McKenzie, T. G.; Costa, L. P. da M.; Fu, Q.; Dunstan, D. E.; Qiao, G. G. Investigation into the Photolytic Stability of RAFT Agents and the Implications for Photopolymerization Reactions. *Polym. Chem.* **2016**, *7* (25), 4246–4253. <https://doi.org/10.1039/C6PY00808A>.
- (28) Dehaeck, S.; Scheid, B.; Lambert, P. Adaptive Stitching for Meso-Scale Printing with Two-Photon Lithography. *Addit. Manuf.* **2018**, *21*, 589–597. <https://doi.org/10.1016/j.addma.2018.03.026>.

# **GENERAL CONCLUSIONS AND PERSPECTIVES**

## GENERAL CONCLUSIONS

---

---

Molecular recognition is the underlying principle of many biochemical processes. In affinity technology, this specific biological recognition is employed for applications like bioseparation, bioimaging and biosensors. In 1993, the use of synthetic biomimetic materials, namely Molecularly Imprinted Polymers (MIPs) was reported for the first time as an antibody replacement in an immunoassay for drugs. Since then, the interest in MIPs as versatile affinity materials in general, and as recognition elements in chemical sensors in particular, has kept growing exponentially. In this context, the micro and nanostructuring of MIPs and their interfacing with transducers is of outmost importance, which was the main objective of this PhD thesis.

We explored several new routes for the synthesis and the micro and nanostructuring of molecularly imprinted polymers (MIPs). We used for the first time the radical-mediated thiol-yne reaction for the high-yield synthesis of MIPs based on common acrylic functional monomers and without any preliminary deoxygenation step. The resulting thiol-yne MIPs exhibited affinity for the target propranolol and selectivity over its structural analog atenolol. This demonstrated the feasibility of using the thiol-yne chemistry as an oxygen-tolerant polymerization method compatible with (meth)acrylic monomers for preparing selective MIPs. It could be useful in open-air setups of micro and nanofabrication, such as in two-photon stereolithography (TPS). Indeed, TPS was used on the thiol-yne formulations to fabricate MIP-based photonic crystals in the form of woodpiles that should function in the visible spectrum. However, the thiol-yne polymerization system was too reactive to produce finely resolved features, which prevented it from yielding woodpiles that could be interrogated with visible light. As an alternative, we also modified the commercial photoresist IP-Dip to make it suitable for imprinting with propranolol. Through TPS, color-generating MIP woodpiles were written which displayed in preliminary tests an decrease in brightness after incubation in a solution of propranolol. Despite these encouraging results, overall the use of modified IP-Dip was found to furnish structurally weak MIP woodpiles. We therefore adapted a new strategy, which entailed the TPS of microstructures based on the unaltered IP-Dip and on a second commercial photoresist, IP-S, and the subsequent functionalization of the microstructures with MIP by post-polymerization. The advantage of this approach is the decoupling of the photo-structuration and the MIP synthesis, which allows making fewer compromises and performing the two steps under their specific optimal conditions. A honeycomb pattern was chosen as the model microstructure, and linewidths as small as 167 nm were

achieved. As confirmed by Raman spectroscopy, the surface of the honeycombs contained unreacted C=C bonds which were exploited later in a reaction to anchor the photoiniferter CDTPA. Through CDTPA initiation, MIPs of a few nanometer thickness imprinted with N-(carbobenzyloxy)-(L)-phenylalanine (Z-(L)-Phe) were grown on the honeycombs in a controlled “living” photopolymerization. As evidenced by the SEM images of the MIP-decorated honeycombs, the post-TPS polymerization step did not drastically diminish the resolution of the honeycomb pattern. The MIP-decorated honeycombs showed affinity for the fluorescent target dansyl-(L)-phenylalanine (dansyl-(L)-Phe), which was indicated by the increase in the intensity of their fluorescence after incubation with the target. They also exhibited selectivity for Z-(L)-Phe over its enantiomer Z-(D)-Phe. Overall, the study brought new insights into the field of molecular imprinting through the thiol-yne chemistry and more importantly, into nanostructuring of MIPs through TPS and by living polymerization, culminating in the demonstration of a general approach for the TPS of arbitrarily designed microstructures and functionalizing them with MIPs through a photoiniferter for the selective recognition of target molecules. This paves the way for the future use in opto-chemical sensors of these synthetic affinity materials.



## PERSPECTIVES

---

---

This work allowed gaining precious insights for a deeper understanding of two-photon stereolithography (TPS) and its application in the field of molecular imprinting, in which it is still very much an uncharted technique. The relationship established between the various writing parameters and the resolution of our TPS system through our experiments can serve as a guide for the future fabrication of structures especially those that require submicron features. The behavior observed of our formulations as photoresists must be considered when designing novel ones to improve, for example, the control over polymerization and the durability of the resulting polymer. Most importantly, demonstrating that the surface of any structure fabricated with the IP-Dip and IP-S photoresists can be coupled with a photoiniferter through residual double bonds provides a general and straightforward approach for its post-functionalization with MIPs or with other functional layers. Given that this approach has been applied to model 3D structures, namely honeycomb microstructures with linewidths of a few hundred nanometers, further studies may finally lead to the construction via TPS of molecularly imprinted photonic crystals (PhCs) that work effectively as opto-chemical sensors in the visible range. By post-functionalizing the PhCs with hydrophilic MIPs, they could also be adapted for a use in an aqueous environment. Another possible application is in microfluidics, wherein TPS may be used for the development of microchannels or other elements. Each of this microchannel may have its inner wall modified via an iniferter with polymers of certain polarity different from the other microchannels. When assembled together on a platform, the microchannels may lead to the effective delivery of a liquid sample to a sensor through enhanced capillary action while potentially filtering out interferences along the way through polymer brushes found on their inner walls. Lastly, TPS may be used for the design and elaboration of nanobots. These nanobots would possess a suitable architecture and may be post-functionalized on their various regions with different kinds of MIPs, or other functional polymers, depending on their purpose. For instance, a nanobot may be functionalized with a MIP on a certain area for carrying a drug molecule, on another side with a MIP that can recognize a cell receptor and finally the rest of the surface of the nanobot with hydrophilic polymer brushes so that it can be injected into the bloodstream of a patient, unattacked by the latter's immune defense until it delivers the drug molecule to a diseased tissue for treatment. Indeed, the encounter between the fields of advanced additive manufacturing and molecular imprinting described in this thesis has opened new and exciting possibilities for sophisticated molecular recognition that can be applied to chemical sensing, bioimaging, molecular separation, drug delivery and many others.

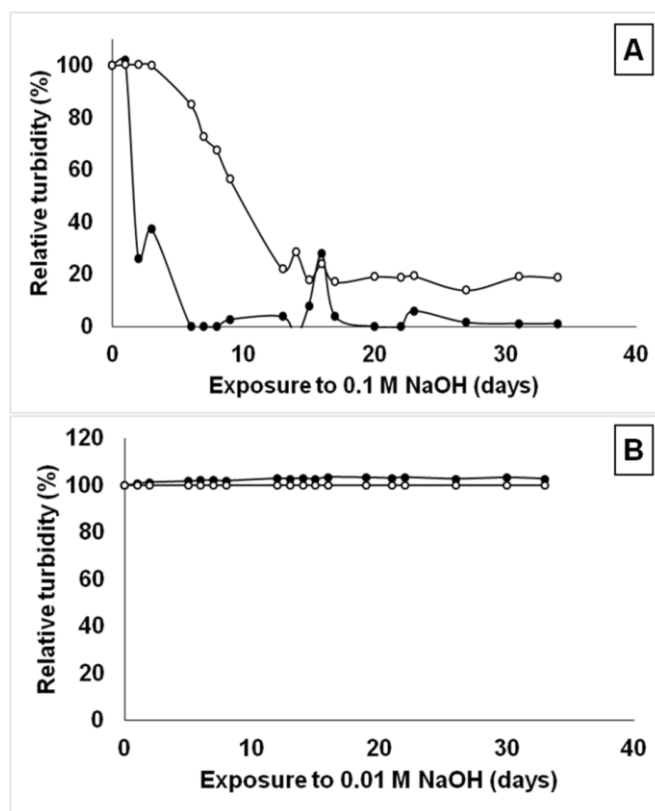
# **Appendices**

## **A to D**

## Appendix A

**Table A 1.** Alkyne and thiol conversions for thiol-yne polymerized p(AA-co-PETMP-co-DBC) and p(AA-co-diPETMP-co-DBC) as measured by FTIR.

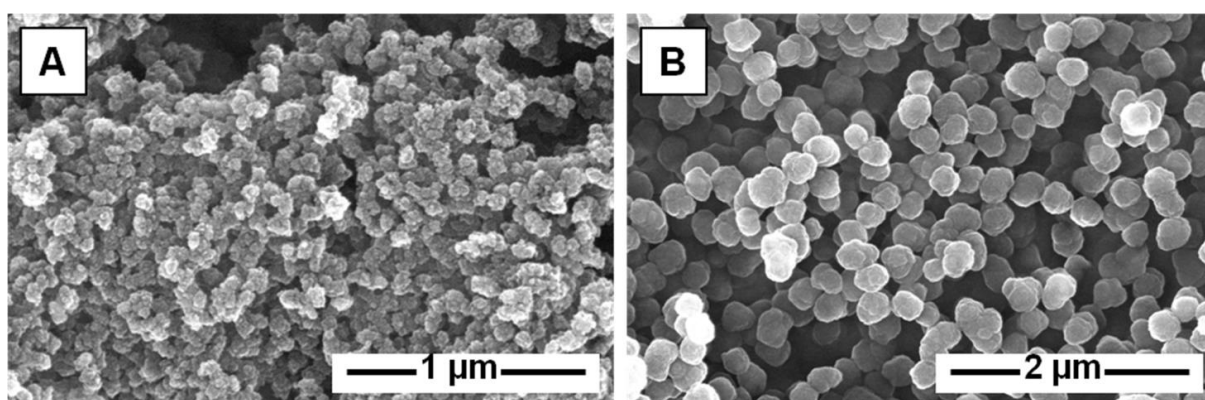
	Monomers			Polymers			Conv (%) ≡C-H
	peak height ≡C-H	peak height C=O	ratio	peak height ≡C-H	peak height C=O	ratio	
p(AA-co-PETMP-co-DBC)	26.5	74.2	0.357	0.9	62.4	0.014	96
p(AA-co-diPETMP-co-DBC)	26.8	74.5	0.360	0.7	41.9	0.017	95
	peak height S-H	peak height C=O	ratio	peak height S-H	peak height C=O	ratio	Conv (%) S-H
p(AA-co-PETMP-co-DBC)	4.1	83.6	0.049	0.7	62.4	0.011	77
p(AA-co-diPETMP-co-DBC)	3.6	79.9	0.045	0.5	41.9	0.012	73



**Figure A 1.** Hydrolytic degradation of p(AA-co-PETMP-co-DBC) (filled circles) and p(AA-co-diPETMP-co-DBC) (empty circles) in 0.1 molar aqueous NaOH (A) and in 0.01 molar aqueous NaOH (B) over time.

**Table A 2.** Mean particles size of the thiol-yne MIPs and NIPs and the FRP polymers as measured by SEM.

Polymer	Mean particle size (nm)
poly(AA-co-PETMP-co-DBC) MIP	2025 ± 446
poly(AA-co-PETMP-co-DBC) NIP	1147 ± 163
poly(AA-co-diPETMP-co-DBC) MIP	1922 ± 370
poly(AA-co-diPETMP-co-DBC) NIP	991 ± 148
poly(AA-co-PETA)	46.72 ± 11.63
poly(MAA-co-EGDMA)	329.7 ± 39.1



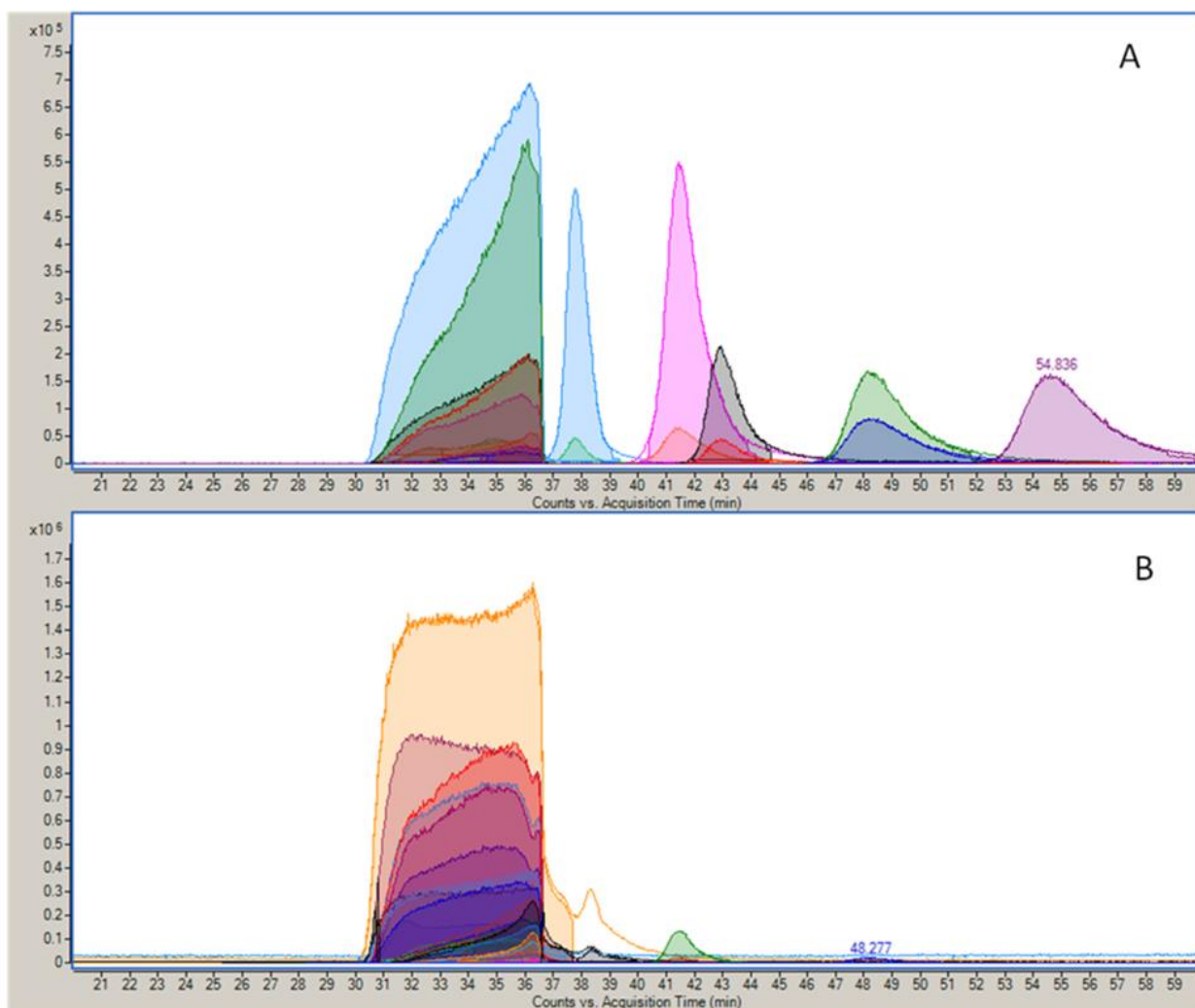
**Figure A 2.** Representative SEM images of (A) p(AA-co-PETA) and (B) p(MAA-co-EGDMA).

**Table A3.** Exact Mass (Mass), retention time (RT) and putative formula for the compounds identified by the algorithm "Find Bye Molecular Feature" (MASSHunter, Agilent) on signals generating more than 2000 counts, for p(AA-co-PETA). Corresponding chromatograms are presented in Figure A3.

ESI-			ESI+			ESI+		
Mass	RT	Formula	Mass	RT	Formula	Mass	RT	Formula
363.947	0.968		1589.64	34.192		206.118	1.1	
613.902	1.113		1259.73	34.22		973.801	32.528	
613.902	1.117		1589.64	34.224		273.12	34.767	
383.918	1.165		1453.66	34.237		117.078	34.888	
895.814	1.184		657.886	34.309		157.958	35.13	
285.939	1.184		793.859	34.328		837.827	35.21	
649.851	1.188		1453.66	34.345		565.882	35.306	
379.925	1.188		987.787	34.361		293.934	35.385	
363.947	1.188		113.993	34.386		480.256	35.532	C22 H40 O11
1161.75	1.189		2441.45	34.43		157.958	35.554	
895.815	1.19		1317.69	34.438		429.91	35.612	
191.952	1.191		987.787	34.473		1031.76	35.687	
645.859	1.201		521.914	34.499		436.23	35.743	C20 H36 O10
649.851	1.202		1317.69	34.561		895.785	35.824	
269.96	1.202		385.941	34.685		392.203	35.974	C18 H32 O9
285.938	1.203		1181.72	34.866		392.204	35.978	C18 H32 O9
645.859	1.204		1511.62	34.903		430.912	36.116	
911.793	1.212		851.815	34.904		623.839	36.122	
457.884	1.215		1181.72	35.097		348.177	36.213	C16 H28 O8
911.794	1.217		1375.65	35.242		157.958	36.472	
629.881	1.219		1045.74	35.331		293.934	36.541	
535.893	1.219		1045.74	35.381		565.885	36.635	
629.88	1.221		1239.67	35.539		157.958	36.647	
551.871	1.221		579.871	35.644		429.91	36.649	
175.974	1.223		715.843	35.651		429.91	36.65	
1177.73	1.227		1103.7	35.761		701.861	36.674	
1177.73	1.233		579.871	35.819		837.836	36.704	
298.054	1.951		1103.7	35.836		837.836	36.716	
515.9	2.472		443.898	35.843		701.86	36.725	
249.967	2.785		773.799	35.882		973.812	36.737	
365.129	3.492		969.726	35.956		973.812	36.739	
479.929	9.628		443.898	35.987		1109.79	36.762	
395.897	10.534		773.799	36.019		1109.79	36.765	
395.897	10.564		967.729	36.038		1245.76	36.772	
301.91	10.572		637.827	36.044		1245.76	36.78	
661.831	10.712		1163.66	36.106		1381.74	36.784	
661.831	10.722		637.828	36.134		1381.74	36.788	
927.764	10.852		1027.68	36.163		1517.72	36.8	
927.764	10.866		501.856	36.164		1517.72	36.801	

645.859	11.231		501.856	36.198		1653.69	36.806	
915.787	11.253		385.943	36.228		1653.69	36.812	
645.859	11.261		1085.64	36.243		1789.67	36.819	
911.794	11.336		521.918	36.587	C18 H2 O19	1925.64	36.835	
629.88	11.363		249.967	36.631		1789.67	36.835	
285.939	11.476		657.893	36.635		2061.62	36.844	
191.952	11.476		385.943	36.648		2333.56	36.845	
379.925	11.479		427.93	36.65		2061.62	36.848	
1443.66	11.53		155.981	36.653		1925.64	36.848	
379.925	11.532		657.893	36.682		2469.54	36.85	
1177.73	11.595		521.918	36.682	C18 H2 O19	2197.59	36.854	
1177.73	11.6		929.845	36.698		2469.54	36.856	
895.814	11.6		929.845	36.708		2605.51	36.857	
551.871	11.6		793.869	36.719		2197.59	36.858	
895.813	11.613		793.869	36.721		2741.49	36.861	
911.793	11.625		1065.82	36.73		2605.51	36.862	
649.851	11.626		1065.82	36.733		2333.57	36.862	
395.898	13.169		1201.8	36.753		460.267	37.292	
395.898	13.222		1201.8	36.754		273.121	37.534	
249.967	13.808		1337.77	36.763		172.072	37.541	C8 H12 O4
365.129	14.312		1337.77	36.764		273.121	37.614	
365.129	17.497		1473.75	36.769		118.063	37.806	
287.112	17.786		1473.75	36.774		136.075	37.829	
508.883	29.14		1609.72	36.777		136.075	38.118	C5 H12 O4
508.883	29.14		1609.72	36.791		288.156	38.653	C14 H24 O6
1881.64	31.648		1745.7	36.794		288.156	38.661	C14 H24 O6
1745.67	31.893		1881.68	36.797		346.198	39.216	C17 H30 O7
1065.8	33.69		1745.7	36.797		230.08	41.559	
385.941	33.701		2561.55	36.801		208.098	41.56	
1667.65	33.78		2425.58	36.803		230.077	41.726	C10 H14 O6
1531.68	33.847		2017.65	36.803		208.096	41.729	C8 H16 O6
1395.71	33.881		1881.68	36.803		269.148	42.203	
249.966	33.892		2425.57	36.804		134.095	42.997	
1939.6	33.907		2289.6	36.805		116.084	43.009	
155.98	33.928		2153.63	36.805		134.095	43.324	C6 H14 O3
1259.73	34		2153.62	36.806		116.084	43.376	C6 H12 O2
1725.61	34.066		2289.6	36.807		302.099	48.068	C13 H18 O8
1861.58	34.099		2017.65	36.808		280.117	48.072	C11 H20 O8
1803.62	34.103		385.943	37.354	C12 H2 O15	341.17	48.208	
1725.61	34.119		385.944	38.439		280.12	48.413	
1123.76	34.125		322.088	41.492		302.102	48.47	
657.887	34.188		208.094	41.502		228.098	54.766	
1123.76	34.189		280.116	48.277		206.116	54.818	C9 H18 O5
						206.118	54.836	

						267.169	55.052	
--	--	--	--	--	--	---------	--------	--



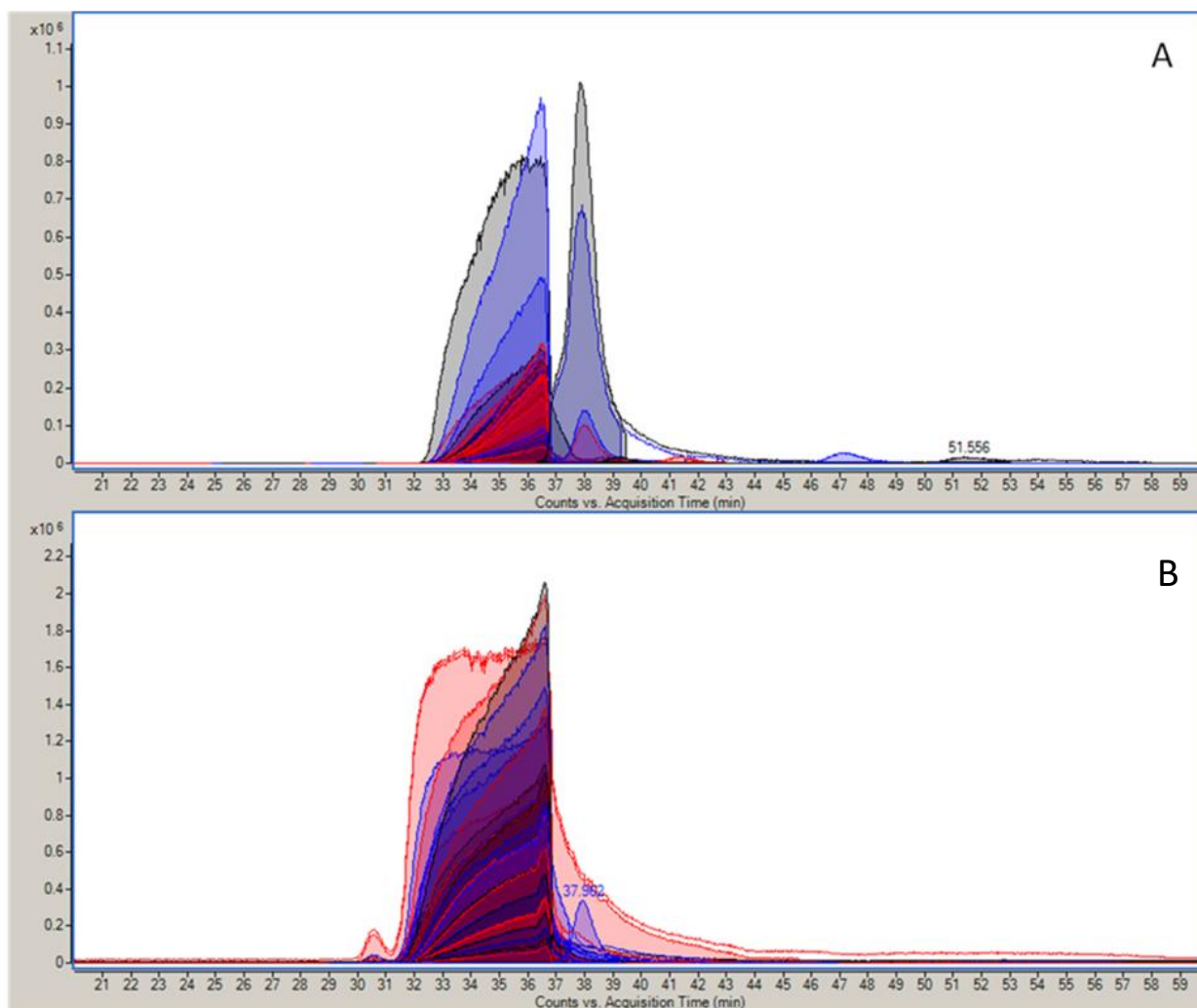
**Figure A3.** Major compounds found by SEC/HRMS with positive (A) et negative (B) ionisation for p(AA-co-PETA). Retention time, exact mass and putative formula was reported on Table A3.

**Table A4.** Exact Mass (Mass), retention time (RT) and putative formula for the compounds identified by the algorithm "Find Bye Molecular Feature" (MASSHunter, Agilent) on signals generating more than 2000 counts, for p(AA-co-diPETMP-co-DBC). Corresponding chromatograms are presented in Figure A4.

ESI-			ESI+		
Mass	RT	Formula	Mass	RT	Formula
155.980	34.51		368.131	37.96	C14 H24 O11
155.980	34.51		368.131	37.96	C14 H24 O11
249.966	34.59		157.959	35.44	
249.966	34.59		157.959	35.44	
385.941	34.66	C12 H2 O15	293.936	35.70	
385.941	34.66	C12 H2 O15	293.936	35.70	
113.993	35.03		429.912	35.91	C13 H2 O15 S
113.993	35.03		429.912	35.91	C13 H2 O15 S
155.980	35.18		565.886	35.93	
155.980	35.18		565.886	35.93	
249.966	35.25		701.860	35.99	
249.966	35.25		701.860	35.99	
385.941	35.32	C12 H2 O15	429.912	35.99	C13 H2 O15 S
385.941	35.32	C12 H2 O15	429.912	35.99	C13 H2 O15 S
521.914	35.39	C18 H2 O19	565.884	36.01	
521.914	35.39	C18 H2 O19	565.884	36.01	
521.914	35.41	C18 H2 O19	837.834	36.03	
521.914	35.41	C18 H2 O19	837.834	36.03	
657.887	35.43	C20 H2 O26	837.834	36.07	
657.887	35.43	C20 H2 O26	837.834	36.07	
427.928	35.46	C14 H4 O14 S	973.810	36.08	
427.928	35.46	C14 H4 O14 S	973.810	36.08	
657.887	35.46	C20 H2 O26	701.859	36.08	
657.887	35.46	C20 H2 O26	701.859	36.08	
929.833	35.49		1109.790	36.11	
929.833	35.49		1109.790	36.11	
929.833	35.51		973.810	36.11	
929.833	35.51		973.810	36.11	
1065.810	35.61		1109.790	36.12	
1065.810	35.61		1109.790	36.12	
1201.780	35.61		1245.760	36.14	
1201.780	35.61		1245.760	36.14	
793.860	35.64		1245.760	36.15	
793.860	35.64		1245.760	36.15	
1065.810	35.64		1381.740	36.15	
1065.810	35.64		1381.740	36.15	
793.860	35.68		1381.740	36.16	
793.860	35.68		1381.740	36.16	



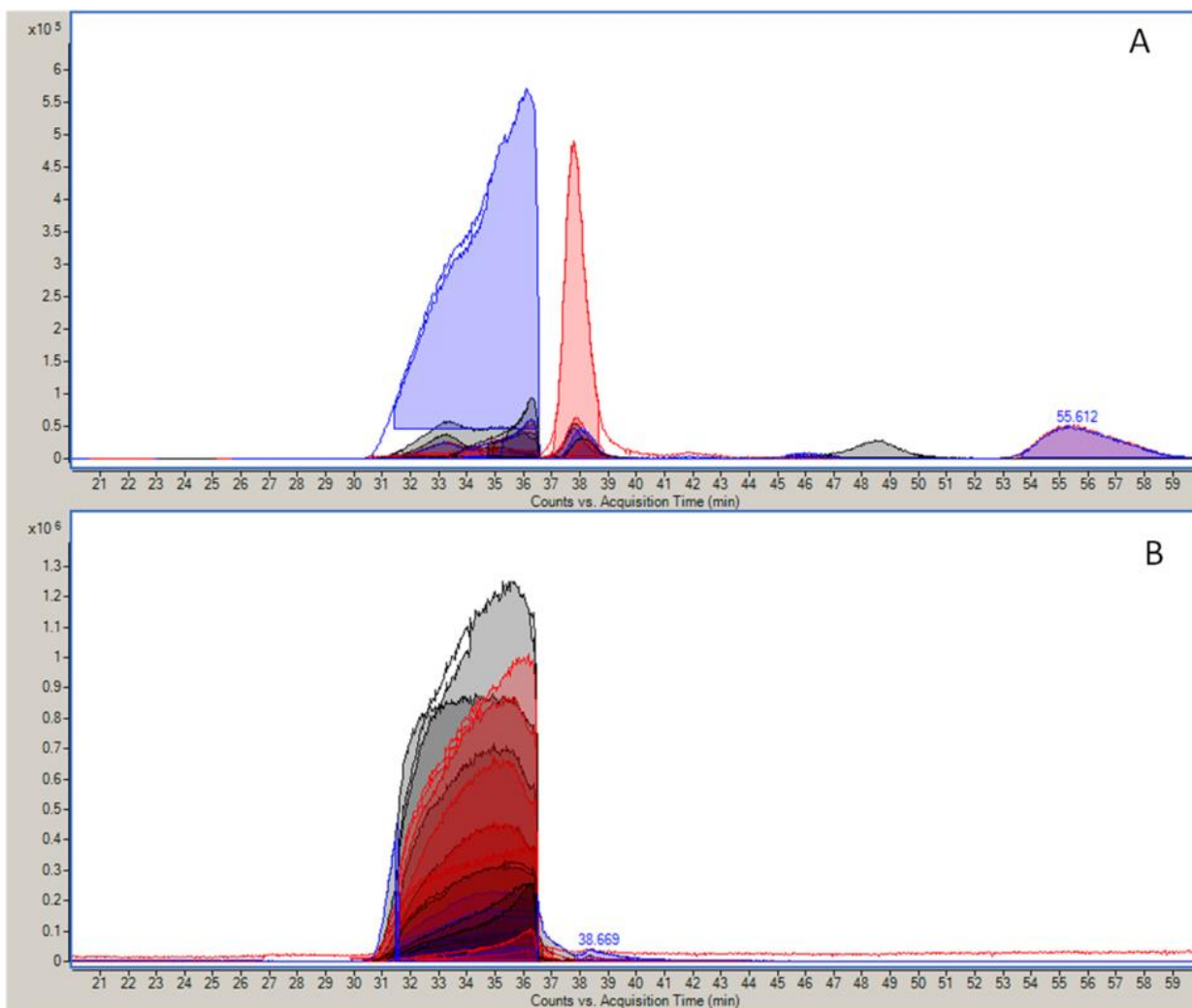
<b>1201.780</b>	35.74		<b>1517.710</b>	36.17	
<b>1201.780</b>	35.74		<b>1517.710</b>	36.17	
<b>1337.750</b>	35.75		<b>1517.710</b>	36.17	
<b>1337.750</b>	35.75		<b>1517.710</b>	36.17	
<b>1337.750</b>	35.81		<b>1789.670</b>	36.19	
<b>1337.750</b>	35.81		<b>1789.670</b>	36.19	
<b>1473.730</b>	35.81		<b>1789.670</b>	36.19	
<b>1473.730</b>	35.81		<b>1789.670</b>	36.19	
<b>1473.730</b>	35.88		<b>1653.690</b>	36.20	
<b>1473.730</b>	35.88		<b>1653.690</b>	36.20	
<b>1609.700</b>	35.89		<b>2061.620</b>	36.21	
<b>1609.700</b>	35.89		<b>2061.620</b>	36.21	
<b>1609.700</b>	35.94		<b>1925.640</b>	36.21	
<b>1609.700</b>	35.94		<b>1925.640</b>	36.21	
<b>1745.680</b>	35.97		<b>1653.690</b>	36.22	
<b>1745.680</b>	35.97		<b>1653.690</b>	36.22	
<b>1881.650</b>	35.99		<b>1925.640</b>	36.23	
<b>1881.650</b>	35.99		<b>1925.640</b>	36.23	
<b>1745.680</b>	36.01		<b>2197.590</b>	36.23	
<b>1745.680</b>	36.01		<b>2197.590</b>	36.23	
<b>2017.620</b>	36.04		<b>2061.610</b>	36.24	
<b>2017.620</b>	36.04		<b>2061.610</b>	36.24	
<b>1881.650</b>	36.04		<b>276.123</b>	37.89	C12 H20 O7
<b>1881.650</b>	36.04		<b>276.123</b>	37.89	C12 H20 O7
<b>2017.620</b>	36.08		<b>254.141</b>	37.90	
<b>2017.620</b>	36.08		<b>254.141</b>	37.90	
<b>2153.590</b>	36.12		<b>372.204</b>	38.04	
<b>2153.590</b>	36.12		<b>372.204</b>	38.04	
<b>2153.600</b>	36.13		<b>394.186</b>	38.04	C17 H30 O10
<b>2153.600</b>	36.13		<b>394.186</b>	38.04	C17 H30 O10
<b>2289.570</b>	36.17		<b>290.138</b>	39.21	C13 H22 O7
<b>2289.570</b>	36.17		<b>290.138</b>	39.21	C13 H22 O7
			<b>346.164</b>	41.37	C16 H26 O8
			<b>346.164</b>	41.37	C16 H26 O8
			<b>194.027</b>	47.19	C8 H12 Cl2 O
			<b>194.027</b>	47.19	C8 H12 Cl2 O
			<b>450.157</b>	51.56	C15 H30 O15
			<b>450.157</b>	51.56	C15 H30 O15



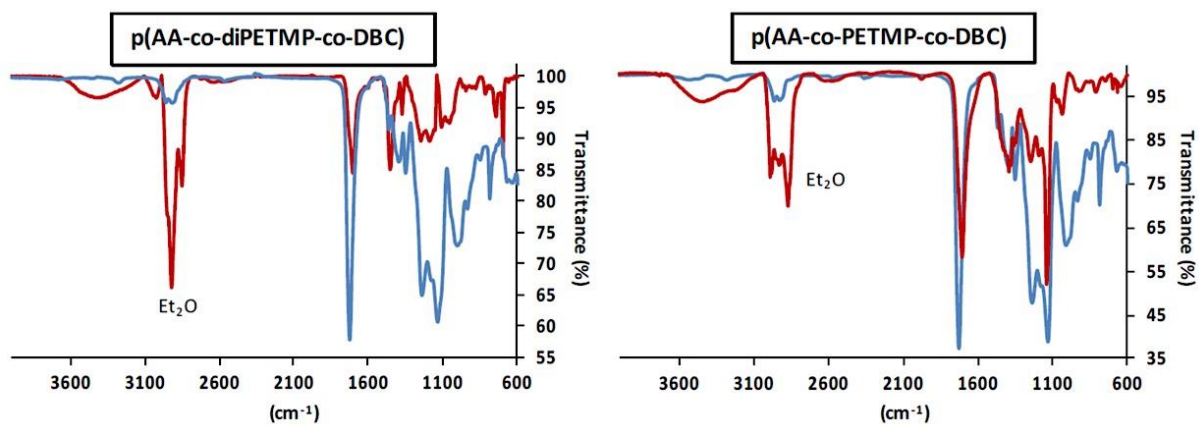
**Figure A4.** Major compounds found by SEC/HRMS with positive (A) and negative (B) ionisation for p(AA-co-diPETMTP-co-DBC). Retention time, exact mass and putative formulae were reported on Table A4.

**Table A5.** Exact Mass (Mass), retention time (RT) and putative formula for the compounds identified by the algorithm "Find Bye Molecular Feature" (MASSHunter, Agilent) on signals generating more than 2000 counts, for p(AA-co-PETMP-co-DBC). Corresponding chromatograms are presented in Figure A5.

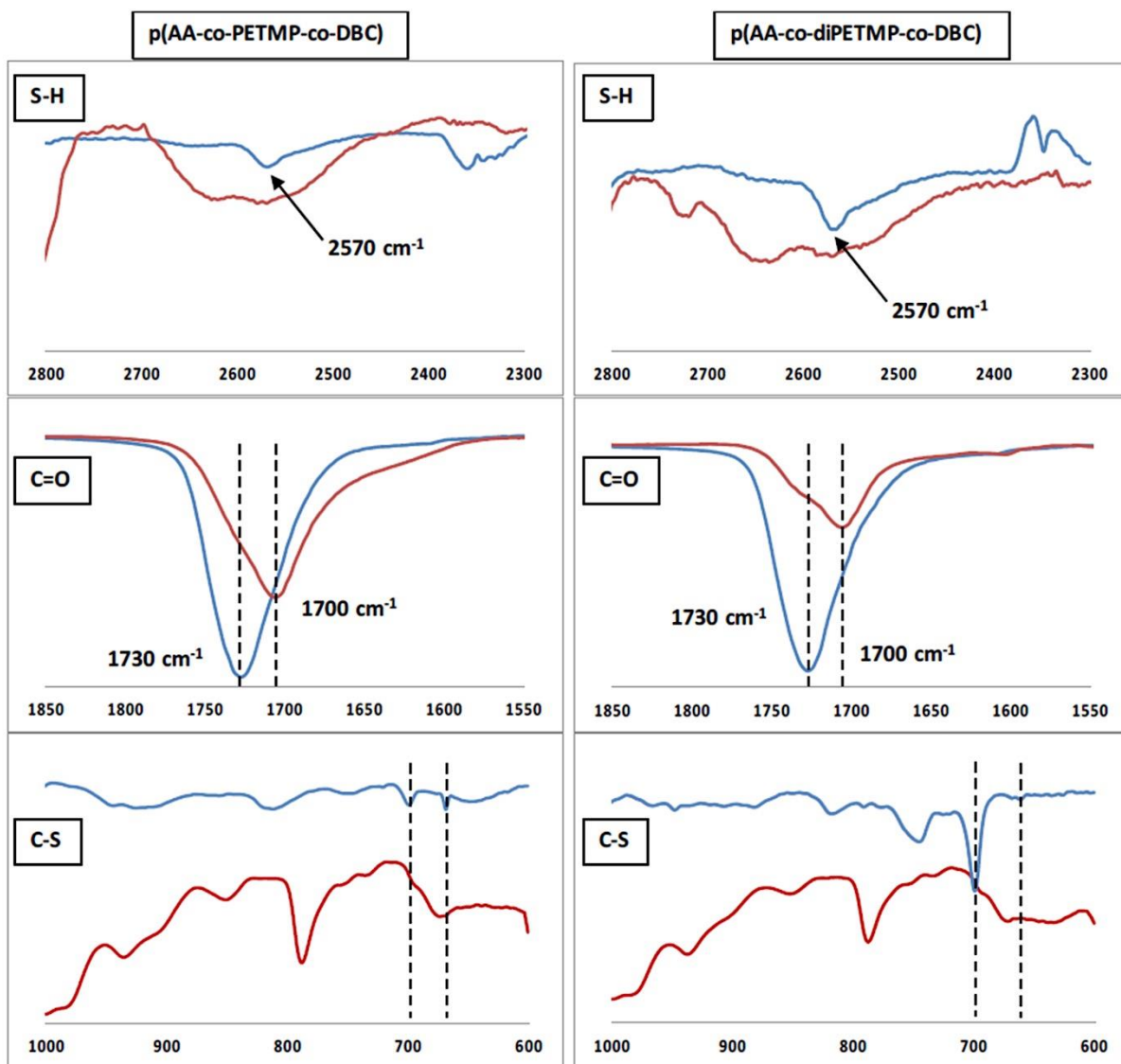
ESI-						ESI+		
Mass	RT	Formula	Mass	RT	Formula	Mass	RT	Formula
853.811	32.56		1453.660	34.92		1653.680	33.23	
386.943	32.73		1375.650	34.92		1381.730	33.28	
1181.720	33.47		1317.690	34.95		1517.700	33.44	
1201.780	33.94		249.966	34.99		973.804	34.21	
385.941	34.13	C12 H2 O15	1045.740	35.17		158.961	34.88	
987.787	34.50		579.871	35.59	C15 H13 Cl O12 S5	429.910	35.54	
1123.760	34.52		967.729	35.73		759.813	35.96	
657.886	34.57	C20 H2 O26	773.800	35.79		623.841	36.07	
1589.640	34.63		443.899	35.80	C9 H16 O6 S7	487.867	36.15	
1123.760	34.63		637.828	35.97	C19 H4 Cl2 O17 S2	351.893	36.21	
1395.710	34.64		385.944	38.67	C13 H6 O10 S2	136.075	37.81	
113.993	34.65		1653.680	33.23		118.063	37.82	
1259.730	34.68		1381.730	33.28		276.122	37.91	
657.886	34.69	C20 H2 O26	1517.700	33.44		254.140	37.92	
793.859	34.70		973.804	34.21		394.185	38.11	
1511.620	34.71		158.961	34.88		394.185	38.11	
1259.730	34.71		429.910	35.54		244.095	38.17	
929.831	34.74		759.813	35.96		206.082	46.08	
1453.660	34.75		623.841	36.07		194.027	48.47	
987.787	34.75		487.867	36.15		332.095	55.60	
793.859	34.75		351.893	36.21		332.095	55.61	
929.831	34.78		136.075	37.81				
1181.720	34.78		118.063	37.82				
521.914	34.79	C18 H2 O19	276.122	37.91				
1045.740	34.79		254.140	37.92				
715.843	34.79	C18 H20 O12 S9	394.185	38.11				
1531.680	34.80		394.185	38.11				
851.815	34.81		244.095	38.17				
521.914	34.85		206.082	46.08				
427.928	34.87		194.027	48.47				
1065.800	34.89		332.095	55.60				
385.941	34.90	C12 H2 O15	332.095	55.61				



**Figure A5.** Major compounds found by SEC/HRMS with positive (A) and negative (B) ionisation for p(AA-co-PETMTP-co-DBC). Retention time, exact mass and putative formulae were reported on Table A5.



**Figure A 6.** Comparison between the FTIR spectra of the thiol-yne MIPs (blue) and their products of hydrolysis (red) obtained by incubation in 1.0 M NaOH.



**Figure A 7.** Comparison between the FTIR spectra of the thiol-yne polymer (blue) and their products of hydrolysis (red) for different vibration modes (insets). Wavenumbers are in cm<sup>-1</sup>.

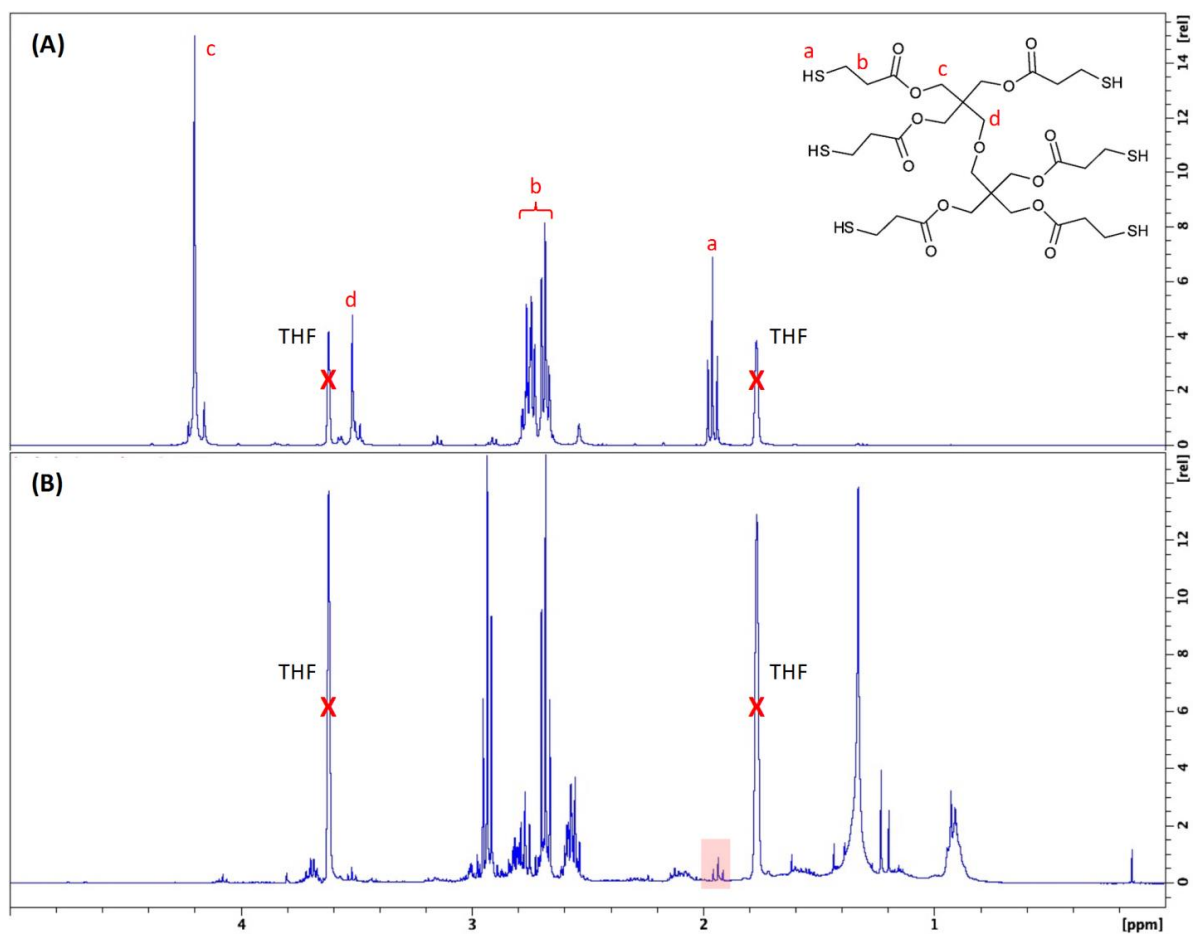
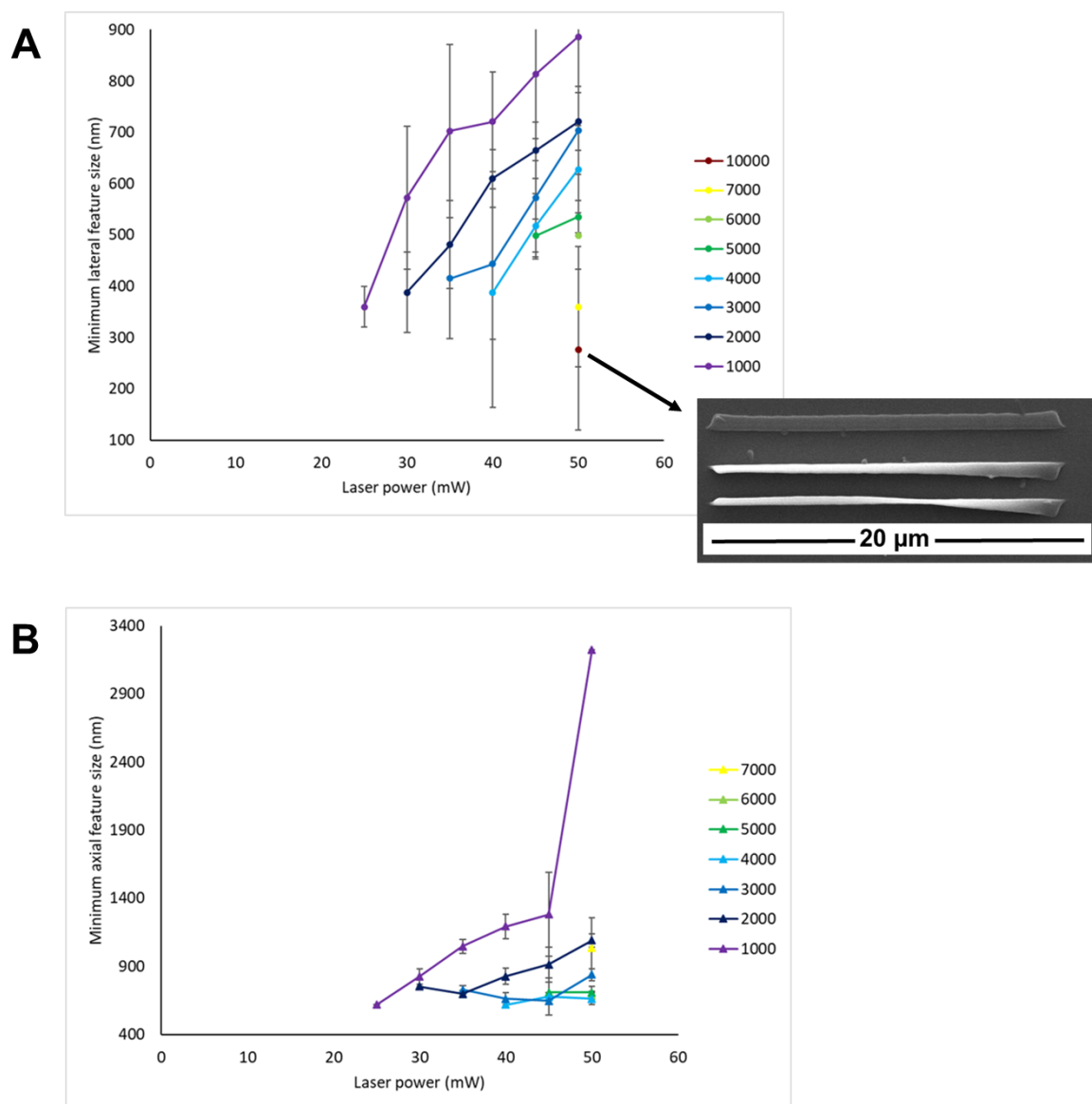


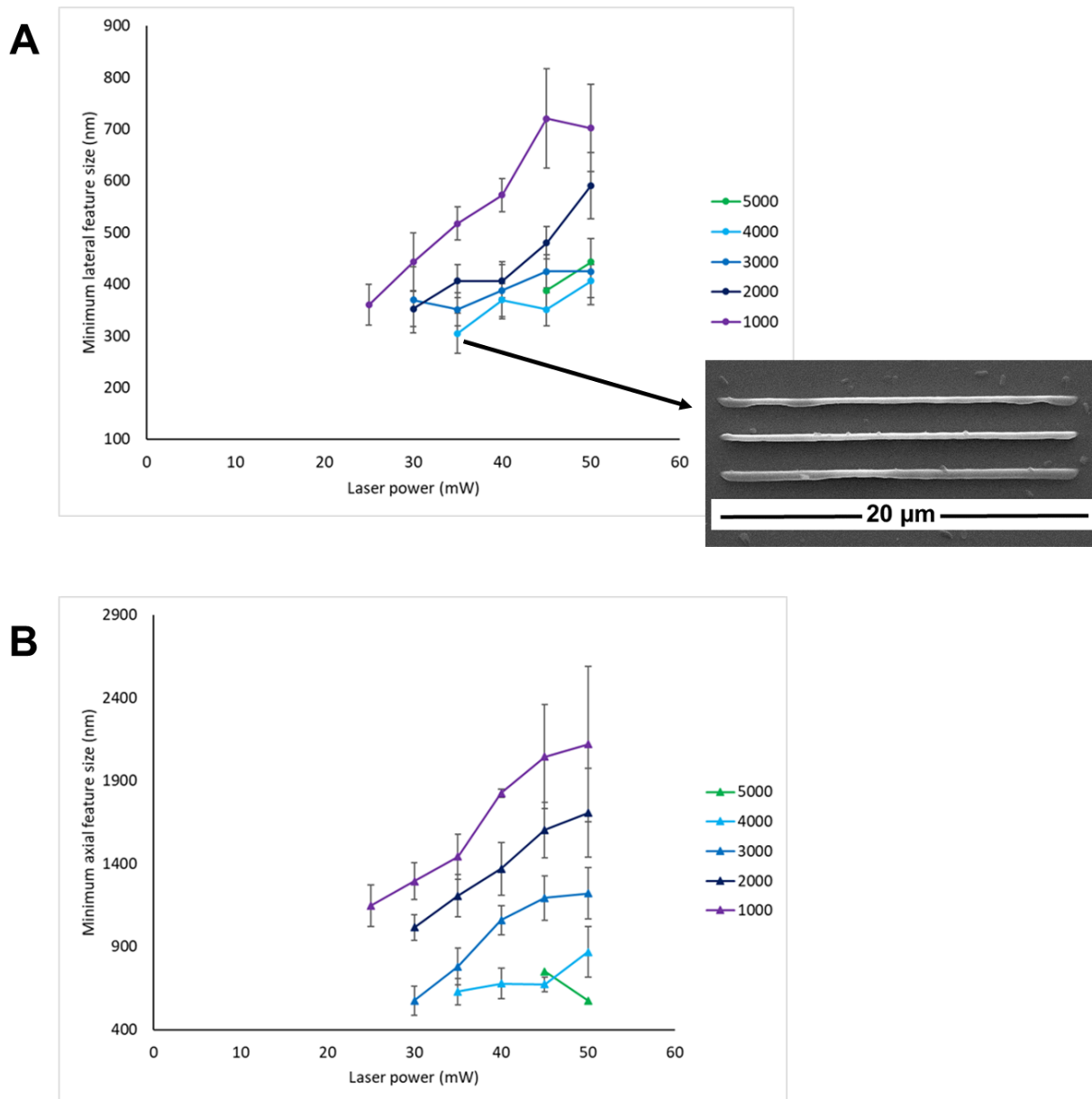
Figure A 8. Comparison between the <sup>1</sup>H-NMR spectra (in d<sub>8</sub>-THF) of (A) the polythiol diPETMP and (B) the products of the alkaline hydrolysis (pH = 14) for p(AA-co-diPETMP-co-DBC). The highlighted peaks in B (1.96 ppm) refer to the –SH group.

## Appendix B

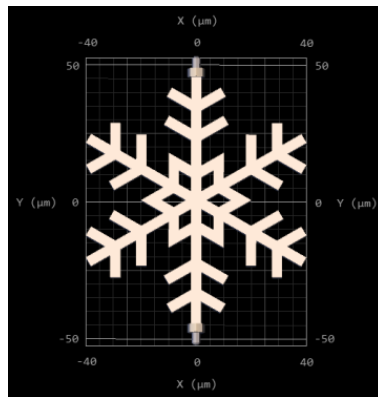


**Figure B1.** The minimum (A) lateral and (B) axial feature sizes as functions of laser power at a fixed scan speed using the IP-Dip MIP precursor formulation ( $n = 3$ ). Outset of A: SEM image of triplicates of one-voxel-wide line with the smallest average minimum lateral size ( $277 \pm 156$  nm) generated using  $SS = 10000 \mu\text{m/s}$  and  $LP = 50$  mW. Legend shows scan speed values expressed in  $\mu\text{m/s}$ .

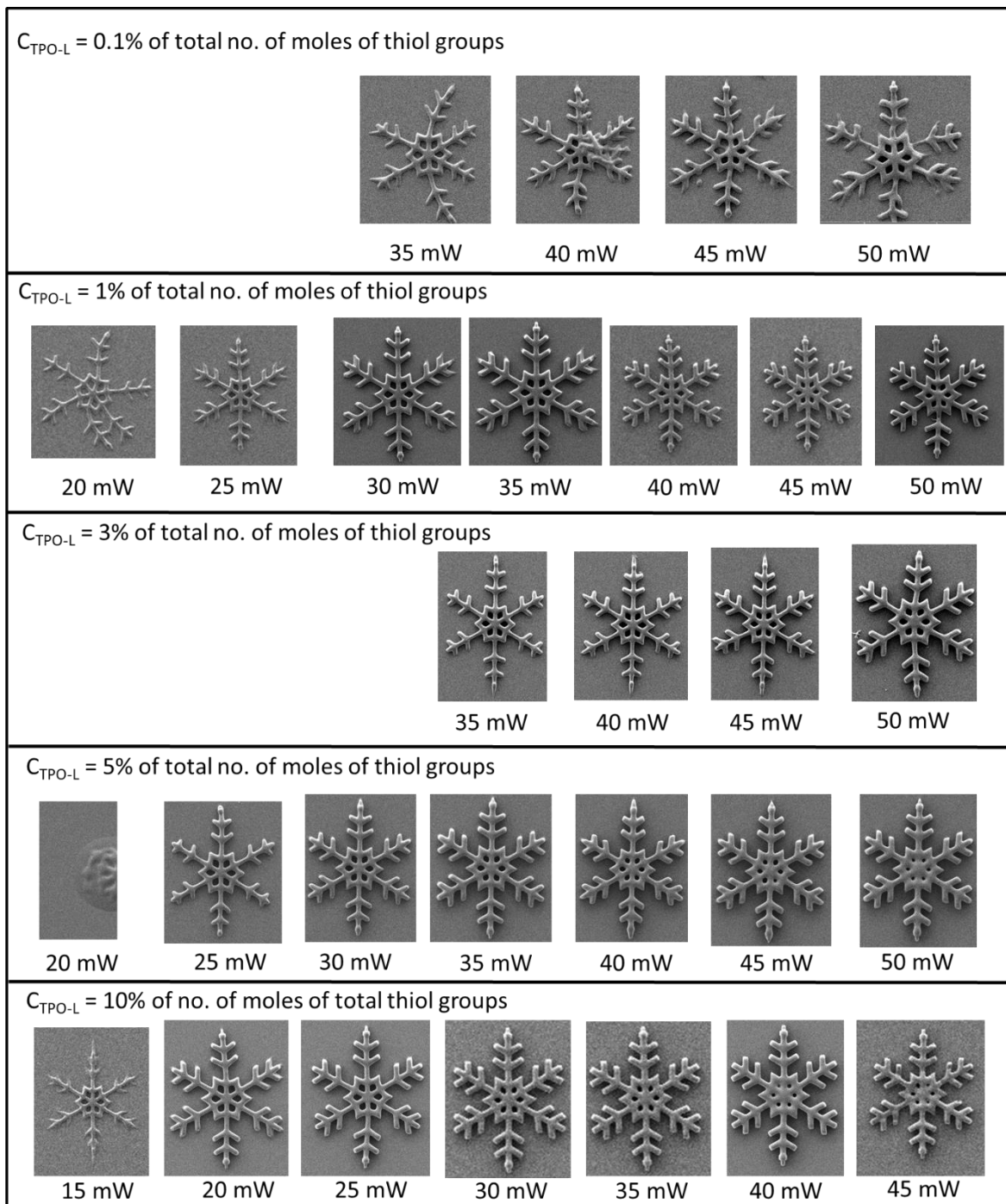




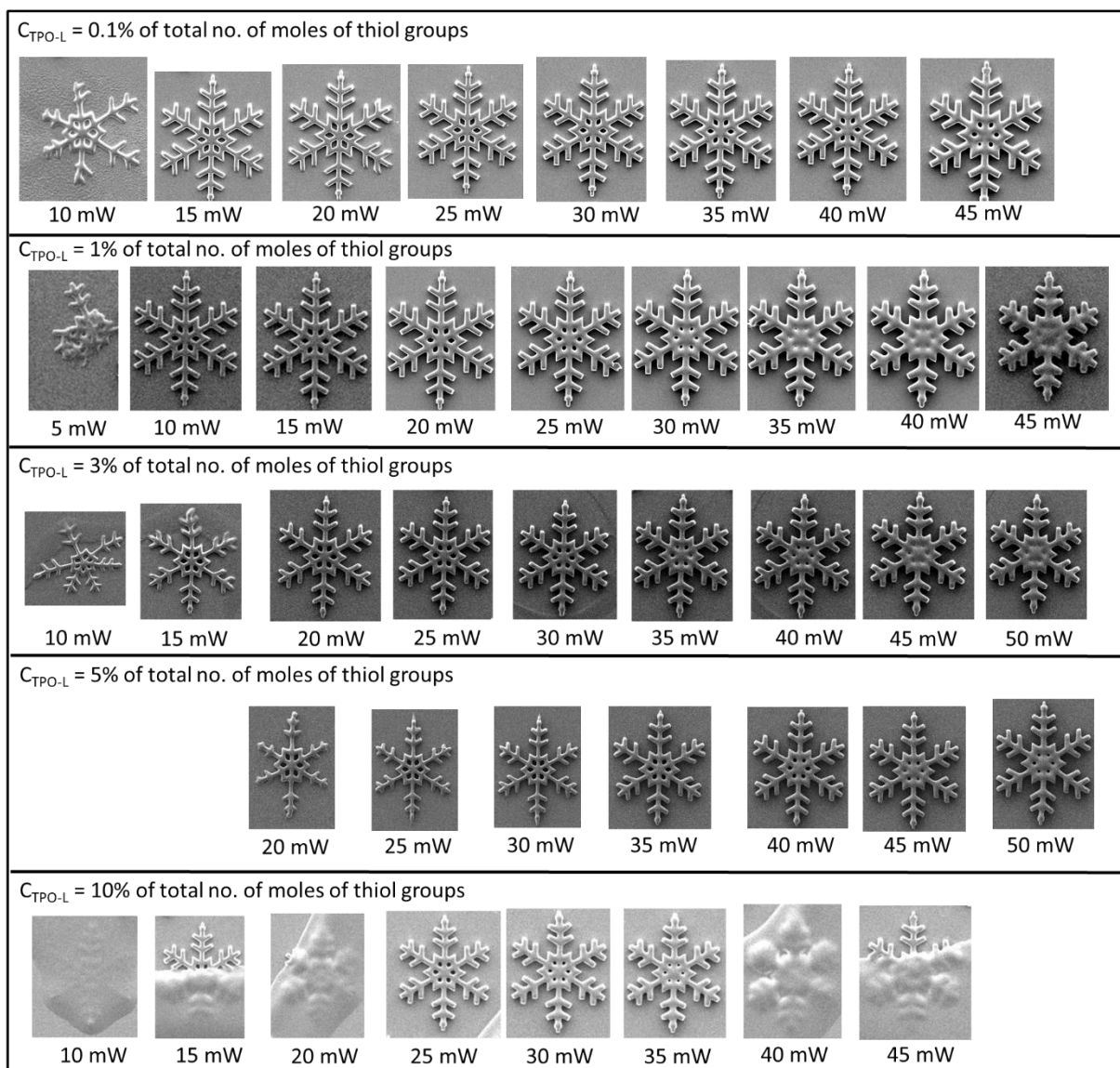
**Figure B2.** The minimum (A) lateral and (B) axial feature sizes as functions of laser power at a fixed scan speed using the IP-Dip NIP precursor formulation ( $n = 3$ ). Outset of A: SEM image of triplicates of one-voxel-wide line with the smallest average minimum lateral size ( $304.7 \pm 39.2$  nm) generated using  $SS = 4000 \mu\text{m/s}$  and  $LP = 35$  mW. Legend shows scan speed values expressed in  $\mu\text{m/s}$ .



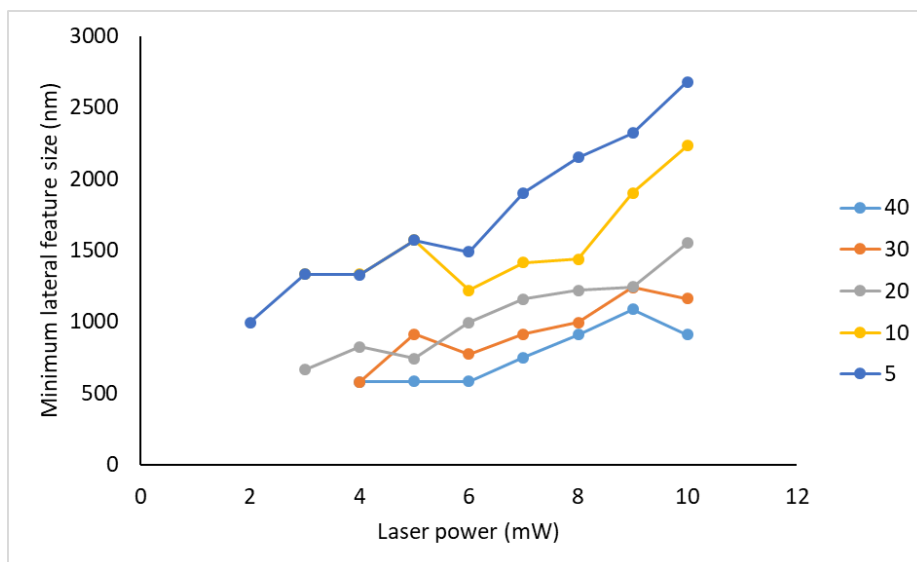
**Figure B3.** The computer-generated image of the snowflake microstructure.



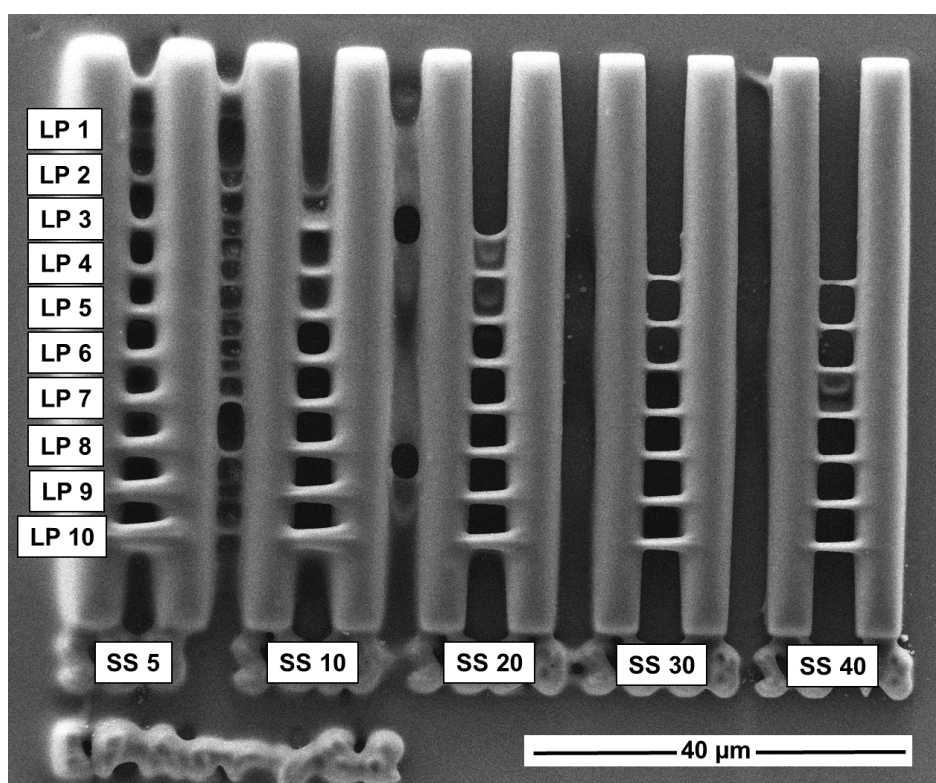
**Figure B4.** Effect of increasing TPO-L concentration and of increasing laser power at the same scan speed on the resulting written snowflake microstructures of poly(AA-co-PETMP-co-DBC).



**Figure B5.** Effect of increasing TPO-L concentration and of increasing laser power at the same scan speed on the resulting written snowflake microstructures of poly(AA-co-diPETMP-co-DBC).

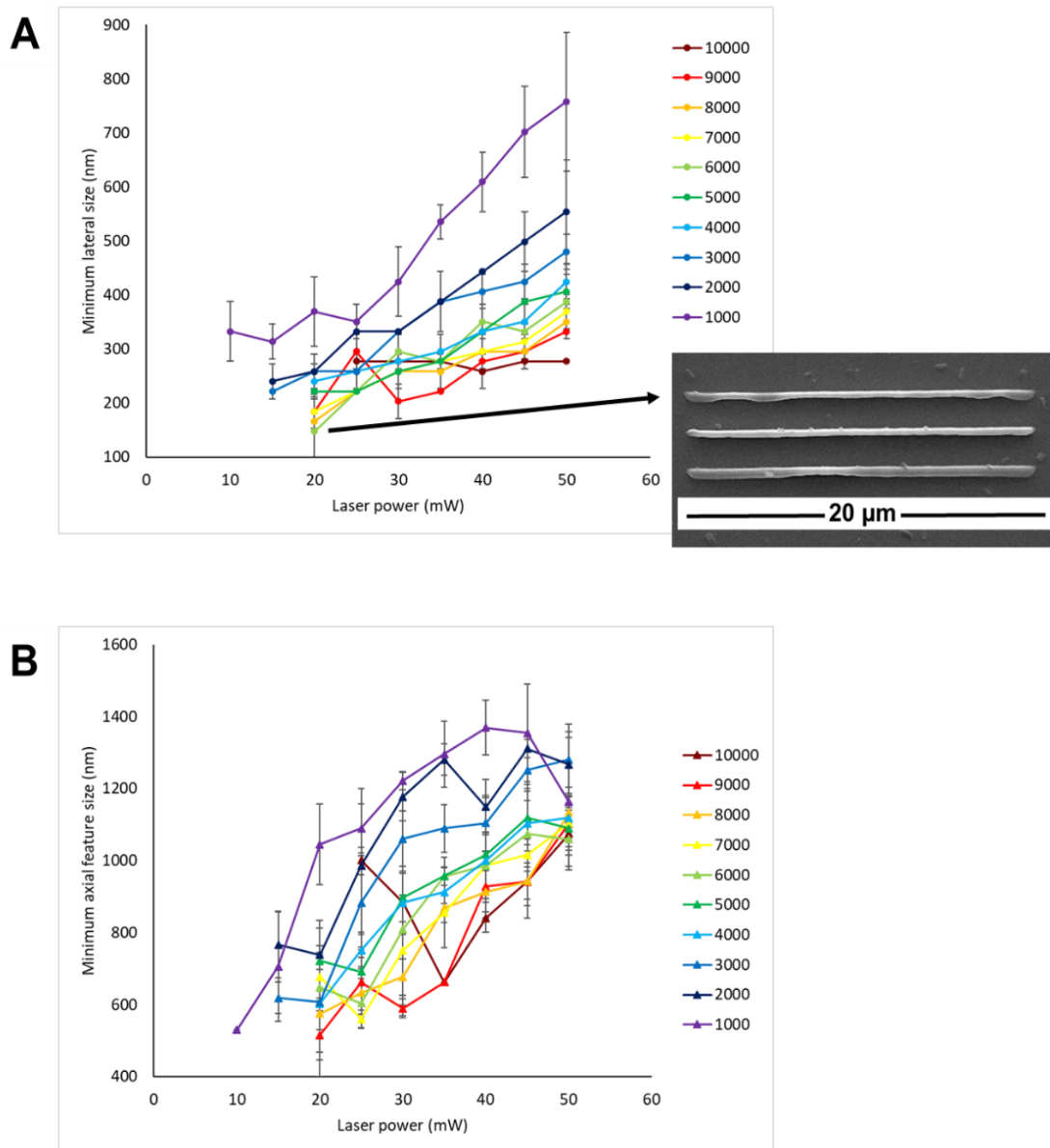


**Figure B6.** The minimum lateral feature size as a function of laser power at a fixed scan speed using Nanoscribe, 63x NA1.4 objective, DiLL configuration and AcryS2 formulation ( $n = 1$ ). Legend shows scan speed values expressed in  $\mu\text{m/s}$ .

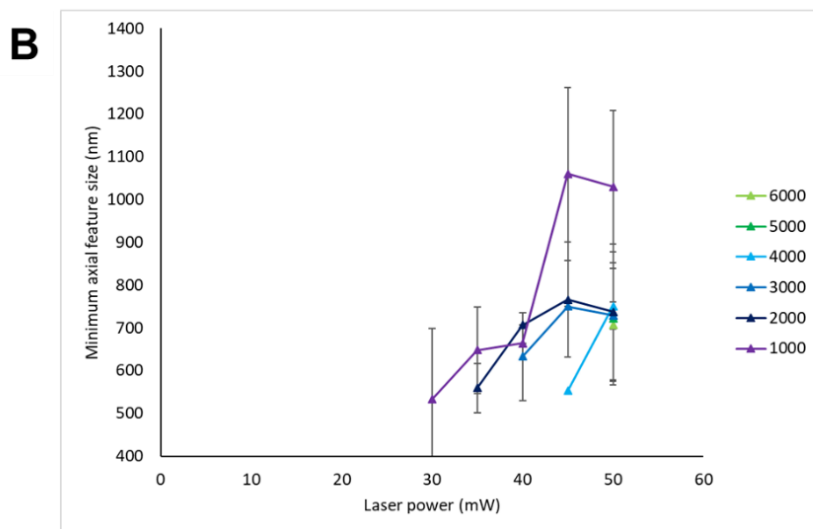
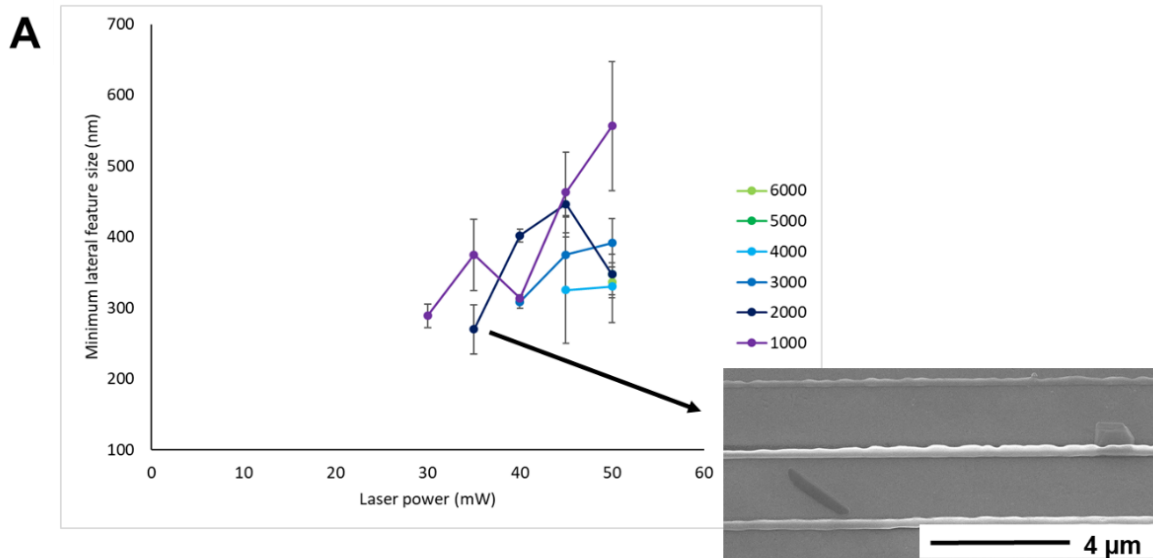


**Figure B7.** SEM image of suspended lines generated by varying scan speed and laser power using the AcryS2 formulation.

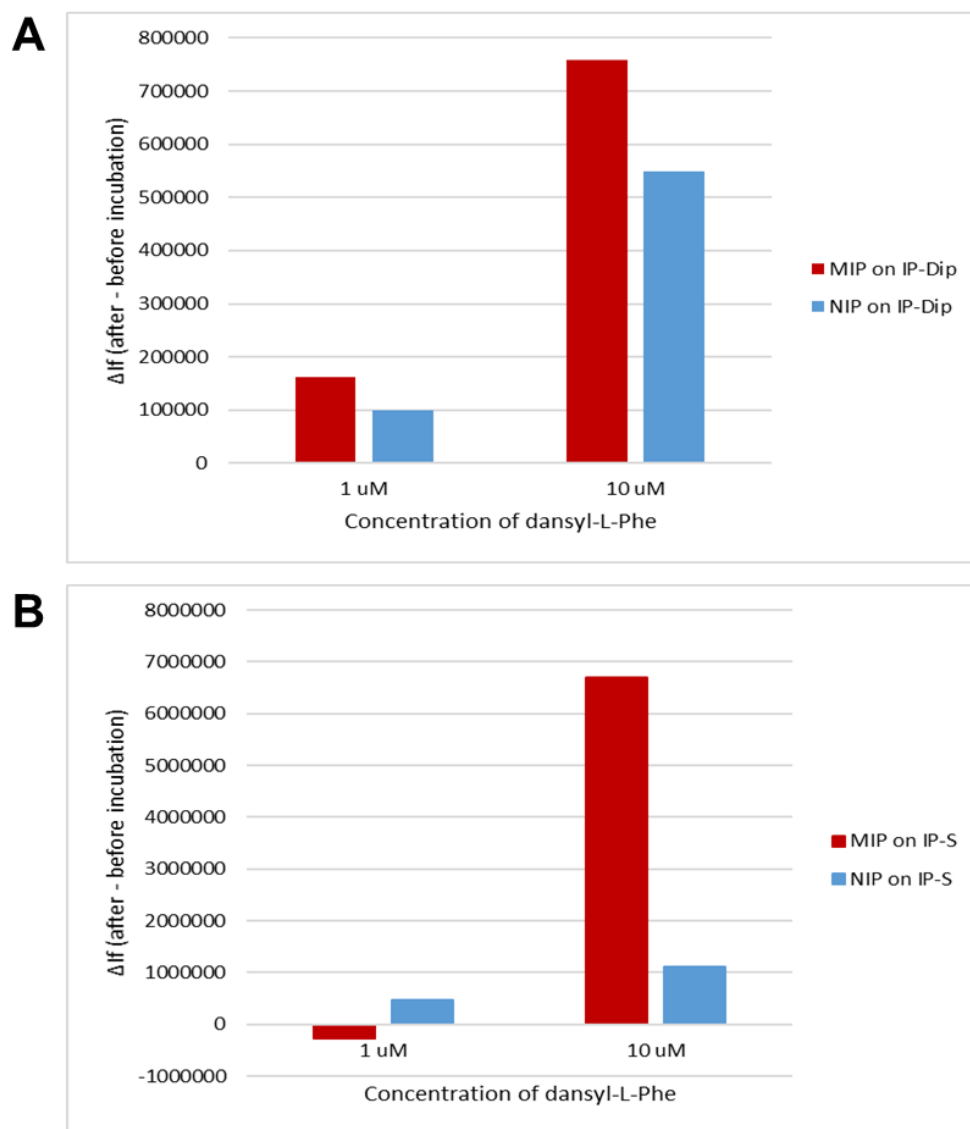
## Appendix C



**Figure C 1.** The minimum lateral feature size as a function of laser power at a fixed scan speed using the IP-Dip photoresist ( $n = 3$ ). Outset: SEM image of triplicates of one-voxel-wide line with the smallest average minimum lateral feature size ( $147.7 \pm 64.0$  nm) generated using  $SS = 6000$   $\mu\text{m/s}$ ,  $LP = 20$  mW. Legend shows scan speed values expressed in  $\mu\text{m/s}$ .



**Figure C 2.** The minimum lateral feature size as a function of laser power at a fixed scan speed using the IP-S photoresist ( $n = 3$ ). Outset: SEM images of triplicates of one-voxel-wide line with smallest ( $270.0 \pm 34.8$  nm) average minimum lateral feature size generated using  $SS = 2000 \mu\text{m/s}$ ,  $LP = 34$  mW. Legend shows scan speed values expressed in  $\mu\text{m/s}$ .



**Figure C 3.** Background-corrected  $\Delta I_f$  of the MIP and NIP layer on the (A) IP-Dip- and (B) IP-S-based honeycomb microstructure after incubation in a solution of dansyl-(L)-Phe in acetonitrile ( $n=1$ ). The concentration of the active bonds in the MIP (and NIP) precursor formulation was 0.99 M.



## Appendix D: Achievements

---

### Publications:

- **E. Paruli**, O. Soppera, K. Haupt, C. Gonzato. Photopolymerization and photostructuring of molecularly imprinted polymers. *ACS Applied Polymer Materials*. **2021**, 3 (10), 4769-4790. DOI: 10.1021/acsapm.1c00661
- **E. Paruli**, T. Griesser, F. Merlier, C. Gonzato, K. Haupt. Molecularly Imprinted Polymers by thiol-yne chemistry: making imprinting even easier. *Polymer Chemistry*. **2019**, 10 (34), 4732-4739. DOI: 10.1039/C9PY00403C
- In preparation: **E. Paruli**, V. Montagna, K. Haupt, C. Gonzato. Surface imprinting on two-dimensional nanostructures by two-photon stereolithography: a general approach toward the functionalization of 3D-printed platforms.

### Oral presentations:

- **E. Paruli**, T. Griesser, F. Merlier, K. Haupt, C. Gonzato. Thiol-yne chemistry as a novel approach to the synthesis of molecularly imprinted polymers. *Nature Inspires Creativity Engineering (NICE) 2020*. 12-14 October 2020. Nice, France
- **E. Paruli**, T. Griesser, F. Merlier, K. Haupt, C. Gonzato. Thiol-yne chemistry as a novel approach to the synthesis of molecularly imprinted polymers. *4ème Journée des Jeunes Polyméristes du Nord*. 27 June 2019. Lille, France

### Poster presentations:

- **E. Paruli**, C. Gonzato, K. Haupt. Two-photon stereolithography for the direct writing of 3D MIP photonic crystals. *The 9<sup>th</sup> International Workshop on Surface Modification for Chemical and Biochemical Sensing*. 08-12 Novembre 2019. Żelechów, Poland.
- **E. Paruli**, T. Griesser, F. Merlier, K. Haupt, C. Gonzato. Thiol-yne chemistry as a novel approach to the synthesis of molecularly imprinted polymers. *Imprinted Polymers and Sensors Seminar*. 27 September 2018. Bedford, United Kingdom.
- **E. Paruli**, T. Griesser, F. Merlier, K. Haupt, C. Gonzato. Thiol-yne chemistry as a novel approach to the synthesis of molecularly imprinted polymers. *The 10<sup>th</sup> International Conference on Molecular Imprinting*. 24-28 June 2018. Jerusalem, Israel.

### Awards:

- Poster award:  
**E. Paruli**, C. Gonzato, K. Haupt. Two-photon stereolithography for the direct writing of 3D MIP photonic crystals. *The 9<sup>th</sup> International Workshop on Surface Modification for Chemical and Biochemical Sensing*. 08-12 Novembre 2019. Żelechów, Poland.



Le projet PO2019M est cofinancé dans le cadre du Fonds Européen de Développement Régional et Régional (FEDER) 2014-2020.



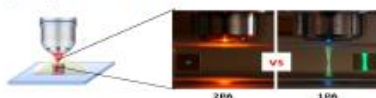
## TWO-PHOTON STEREO LITHOGRAPHY FOR THE DIRECT WRITING OF 3D MIP PHOTONIC CRYSTALS

Ernesto Paruli III<sup>1</sup>, Carlo Gonzato<sup>1</sup>, Karsten Haupt<sup>1</sup>

<sup>1</sup>Genie Enzymatique et Cellulaire, Sorbonne Universités, Université de Technologie de Compiègne, 60200 Compiègne, France  
✉ ernesto3.paruli@utc.fr

### Introduction

Rapid prototyping techniques are gaining interest thanks to the possibility to easily fabricate arbitrary 3D micro-/nanostructures. One of such techniques is the two-photon stereolithography (TPS) which, due to the high-energy densities required by two-photon absorption, allows the highly confined polymerization of a photoresist into the focal point of a microscope's objective. As so, microstructures of sub-micrometer resolution can directly and precisely be manufactured [1-2].

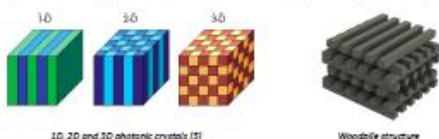


Two-photon absorption (2PA) versus one-photon absorption (1PA) [3]

In this study, TPS has been exploited for the direct writing of 3D photonic crystals in the form of molecularly imprinted woodpile microstructures for the recognition of the model target propranolol. Molecularly imprinted polymers (MIP) also known as plastic antibodies, are synthetic polymers featuring binding sites with high affinity and selectivity for a target [4]. Thus the polymerization of a MIP by TPS allows writing an all-in-one sensor: a recognition element and a transducer.

### Experimental - Direct writing of photonic crystals

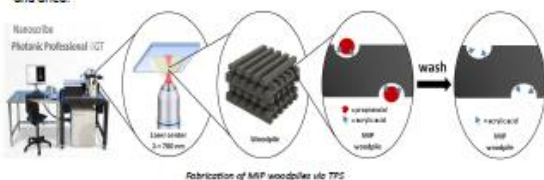
Photonic crystals are ordered structures featuring different refractive indices periodically arranged in one, two or three directions. As a result, they forbid the transmission of certain frequencies as an electromagnetic radiation goes through them, a phenomenon known as the photonic band gap. A woodpile structure is an example of a 3D photonic crystal.



1D, 2D and 3D photonic crystals [5]

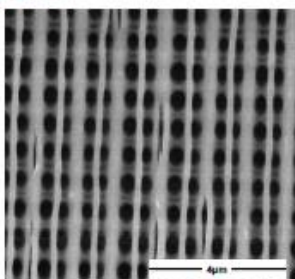
Woodpile structure

For making molecular imprinting woodpile structures, a commercial IP-Dip photoresist was modified by the addition of acrylic acid as functional monomer (functional photoresist) and propranolol as a template. A drop of such photoresist was then placed onto a functionalized fused silica substrate, which was then inserted into the Nanoscribe Photonic Professional GT for the 3D writing via TPS. The structures were then developed, washed and dried.



### Results

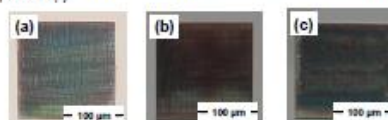
#### ✦ SEM



The architecture of the woodpiles was characterized by scanning electron microscopy (SEM). Faithful to its design, the intra-layer rods are spaced from each other by 450 nm whereas each layer are apart by 815 nm. These dimensions are within or close to the wavelength of the visible range of the electromagnetic spectrum.

Representative SEM image of woodpile by TPS

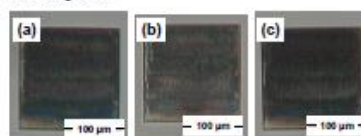
Three kinds of woodpiles were fabricated: (a) using the unaltered IP-Dip photoresist, (b) using the functional photoresist without propranolol (NIP woodpile), and (c) using the functional photoresist containing propranolol (MIP woodpile). The color transmitted by each woodpile after development was observed under transmitted-light polarization-mode (TL-POL) microscopy.



Microscopy images (TL-POL) of (a) woodpile using unaltered IP-Dip, (b) NIP woodpile and (c) MIP woodpile

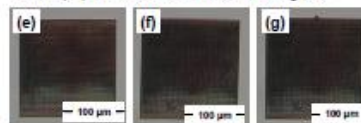
#### ✦ Preliminary binding test

After incubation with 1.0 mM propranolol in acetonitrile, the MIP woodpile changed its colour from pinkish-blue to dark blue. This can be attributed to the shift in the transmitted wavelength due to the change in the average refractive index of the structure caused by the binding event.



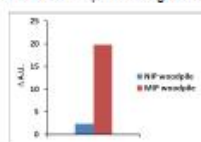
Microscopy images (TL-POL) of the MIP woodpile (a) before washing, (b) after washing and (c) after incubation with 1.0 mM propranolol in acetonitrile

In contrast, the NIP woodpile did not display a significant change in colour after incubation with the propranolol solution due to lack of binding sites.



Microscopy images (TL-POL) of the NIP woodpile (e) before washing, (f) after washing and (g) after incubation with 1.0 mM propranolol in acetonitrile

The difference in the dimness of the woodpiles after washing and after incubation with propranolol was also compared through the software images.



### Conclusions

- A woodpile-based optical sensor via TPS with fast response was successfully imprinted against propranolol.
- TPS allows the easy and quick fabrication of 3D molecularly imprinted microstructures for all-in-one optical sensors.

### Acknowledgements

The authors would like to thank the Hauts-de-France (Nord Pas de Calais-Picardie) region for equipment. We extend our gratitude to the Embassy of France in the Philippines and the Commission on Higher Education of the Philippines for the fellowship grant. We also acknowledge Mr. Frédéric Nadaud for the SEM images. KH acknowledges financial support from Institut Universitaire de France.

### References

- [1] L.P.C. Gomez, A. Spangenberg, X.-A. Ton, Y. Fuchs, F. Bokoeh, J.-P. Maival, B. The Sum Bu, D. Thueu, C. Ayela, K. Haupt, O. Soppers, *Adv. Mater.*, **2016**, *28*, 5931-5937.
- [2] A. Spangenberg, N. Hoobeika, F. Stehlin, J.-P. Maival, F. Wielder, P. Prabhakaran, P. Baldeck, O. Soppers, *Updates in Advanced Lithography*; Hosaka, S., Ed.; InTech, 2014; pp 35-63.
- [3] Retrieved from <http://microscopy.berkeley.edu/courses/TLM/2P/index.html>. Photo by S. Ruzin and H. Aaron. The University of California, Berkeley.
- [4] K. Haupt, *Anal. Chem.*, **2003**, *75*, 376A-383A.
- [5] J.D. Joannopoulos, S.G. Johnson, J.N. Winn, R.D. Meade, *Photonic crystals: Molding the flow of light*; Princeton Univ. Press, 2008; p. 4.

Poster presented at The 9<sup>th</sup> International Workshop on Surface Modification for Chemical and Biochemical Sensing (08-12 November 2019, Poland), Poster Award



Le projet POLYMER est cofinancé dans le cadre du Fonds Européen de Développement Régional (FEDER) 2014/2020.



## THIOL-YNE CHEMISTRY AS A NOVEL APPROACH TO THE SYNTHESIS OF MOLECULARLY IMPRINTED POLYMERS

Ernesto Paruli<sup>1,3</sup>, Thomas Griesser<sup>2</sup>, Karsten Haupt<sup>1</sup>, Carlo Gonzato<sup>1</sup>

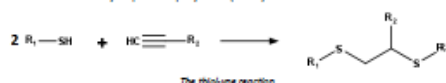
<sup>1</sup>Genie Enzymatique et Cellulaire, Sorbonne Universités, Université de Technologie de Compiègne, 60200 Compiègne, France

<sup>2</sup>Christian Doppler Laboratory for Functional and Polymer Based Ink-Jet Inks, University of Leoben, Otto-Glöckel-Strasse 2, A-8700 Leoben, Austria

<sup>3</sup>ernesto-3.paruli@utc.fr

### Introduction

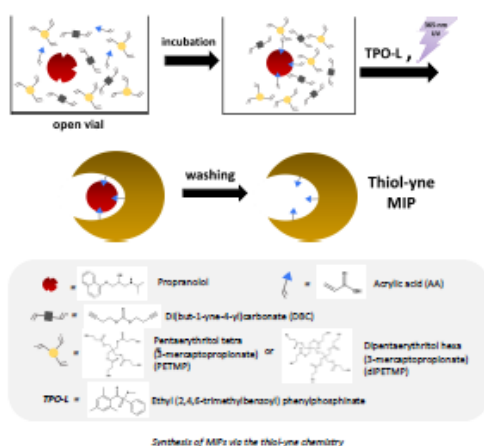
Thiol-yne chemistry as a means for polymerization offers several advantages over the more common free-radical technique (FRP). These include step-growth mechanism, oxygen tolerance, compatibility with meth(acrylic) monomers and generally much easier degradable matrices [1-4]. Despite these advantages, it has been scarcely applied to the synthesis of molecularly imprinted polymers (MIPs).



In this study, we have demonstrated using propranolol as model template that thiol-yne chemistry represents a convenient approach to the synthesis of MIPs.

### Synthesis

A formulation containing the dialkyne DBC and a polythiol as crosslinkers, acrylic acid (AA) as the functional monomer and acetonitrile as the solvent was used for the synthesis of MIPs. The polythiol was either PETMP or dPETMP. Without any prior degassing, the formulation in open vial was exposed to 365-nm UV with TPO-L as the photoinitiator of the polymerization reaction. The UV exposure was stopped after 3 minutes and the newly synthesized polymers were homogenized, washed and dried.

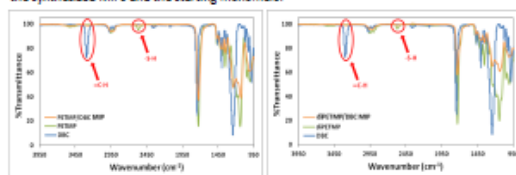


Synthesis of MIPs via the thiol-yne chemistry

### Results

#### FTIR and SEM

We produced MIPs for propranolol using the reaction between a dialkyne and a polythiol. The progress of the thiol-yne reaction was confirmed by the difference in the IR spectra of the synthesized MIPs and the starting monomers.



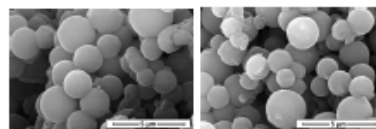
Comparison between the IR spectra of the thiol-yne MIPs and the starting monomers

#### Bond conversions after polymerization

The IR spectra show that the degree of conversion of the active bonds was high.

MIP	Triple bond conversion	Thiol bond conversion
PETMP/DBC	87%	98%
dPETMP/DBC	92%	92%

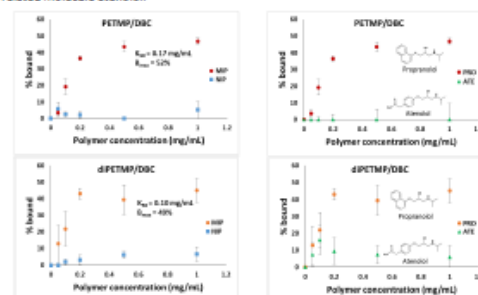
The structure of the MIPs produced from the thiol-yne reaction was also characterized using scanning electron microscopy (SEM). The images obtained show that the MIPs were composed of microspheres with sizes ranging from 1 μm to 2 μm.



SEM images of PETMP/DBC polymer (left) and dPETMP/DBC polymer (right)

#### Binding tests

The capacity of the thiol-yne MIPs to bind the target molecule propranolol was investigated. The fluorescence assay showed that the MIPs were highly specific while the reference non-imprinted polymers (NIPs) exhibited virtually no binding at all. The MIPs were also selective for the target propranolol since they showed no significant binding with the structurally related molecule atenolol.

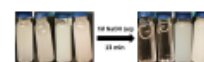
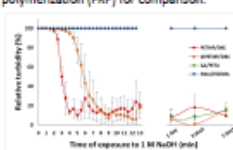


Binding isotherms of thiol-yne MIPs with propranolol

Selectivity study of thiol-yne MIPs with propranolol (PRO) and atenolol (ATE)

#### Hydrolytic degradation

The thiol-yne MIPs were immersed in 1 M NaOH (aq) simultaneously with the corresponding acrylate-based and methacrylate-based polymers obtained by free radical polymerization (FRP) for comparison.



Hydrolytic degradation of thiol-yne polymers in NaOH with time (left). Polymers after 12 minutes in NaOH (top, from left to right): PETMP/DBC, dPETMP/DBC, AA/PED and MAA/BDMA

#### Conclusions

MIPs that were highly specific and selective for propranolol were easily synthesized using the thiol-yne chemistry. This highlights the thiol-yne chemistry as a convenient approach to MIP synthesis in an open vial with no need for a preliminary degassing step. The easily degradable matrices of the MIPs also limits its environmental impact.

#### Acknowledgements

The authors would like to thank the Hauts-de-France (Nord Pas de Calais-Picardie) region and the European Regional Development Fund 2014/2020 for the funding of this work. We extend our gratitude to the Embassy of France in the Philippines and the Commission on Higher Education of the Philippines for the fellowship grant. We also acknowledge Bruno Bock and IGM resins for the polythiols and TPO-L as well as Mr. Frederic Nadaud for the SEM images.

#### References

- [1] Fairbanks, B., Scott, T., Kloxin, C., Anseth, K., Bowman, C. (2009). *Macromolecules* 42:211-217.
- [2] Acebo, C., Fernandez-Francos, X., Ramis, X., Serra, A. (2016). *RSC Advances* 6:61576-61584.
- [3] Lowe, A. (2014). *Polymer* 55:3517-3549.
- [4] Kade, M., Burke, D., Hawker, C. (2010). *Journal of Polymer Science: Part A: Polymer Chemistry* 48:743-750.

Poster presented at *Imprinted Polymers and Sensors Seminar (27 September 2018, United Kingdom)* and at the *10<sup>th</sup> International Conference on Molecular Imprinting (24-28 June 2018, Israel)*

